NUREG/CR–6203

Validation Studies for Assessing Unsaturated Flow and Transport through Fractured Rock

Manuscript Completed: April 1994
Date Published: August 1994

Prepared by
R. L. Bassett, S. P. Neuman, T. C. Rasmussen, A. Guzman,
G. R. Davidson, C. F. Lohrstorfer

Department of Hydrology & Water Resources
University of Arizona
Tucson, Arizona 85721

Prepared for
Division of Regulatory Applications
Office of Nuclear Regulatory Research
U.S. Nuclear Regulatory Commission
Washington, DC 20555–0001
NRC FIN L1282

DISCLAIMER

ABSTRACT

This is a progress report for a project of the U.S. Nuclear Regulatory Commission (sponsored contract, NRC-04090-51, FIN L1282 with The University of Arizona) for the time period of November 12, 1989 to November 11, 1992. The project manager is Thomas J. Nicholson, Office of Nuclear Regulatory Research. The objectives of this contract are to examine hypotheses and conceptual models concerning unsaturated flow and transport through heterogeneous fractured rock and to design and execute confirmatory field and laboratory experiments to test these hypotheses and conceptual models. Specific tasks have been identified to address these objectives.

The initial task identified physical and chemical properties that affect HLW transport in unsaturated fractured rock. Specific processes include thermal, liquid, vapor, and solute transport. Important new information is presented such as the application and evaluation of procedures for estimating hydraulic, pneumatic, and solute transport coefficients for a range of thermal regimes.

A field heater experiment was designed as part of the second task that focused on identifying the suitability of existing monitoring equipment to obtain required data. Important issues related to model evaluation for distinguishing between alternate conceptual models were also addressed.

Field research under Task 3 resulted in the development of a reliable method for conducting and interpreting tests for air permeability using a straddle-packer arrangement. Application of this procedure ensures repeatability and accuracy of the in-situ tests.

As part of Task 4, detailed studies of fracture flow from Queen Creek into the Magma Copper Company ore haulage tunnel have been initiated. These studies will provide data on travel time for transport of water and solute in unsaturated tuff. Samples of an intervening perched water table have an uncorrected radiocarbon age of near 3000 years BP. Methods are being developed to correct measured radiocarbon activity to approximate solute "age" so that travel time may be approximated in unsaturated systems. Ages are not valid for unsaturated hydrologic conditions, unless they include corrections for carbon derived from all sources that impact the mass balance, e.g., vadose zone gas, carbonate minerals, and organic material.

Task 5 includes the collection of rainfall, runoff, and infiltration data at two small watersheds at the Apache Leap Tuff Site to evaluate the quantity and rate of water infiltrating into the subsurface via either fractures or matrix. The data indicate that only a small proportion of precipitation results in overland runoff, even though the site is primarily devoid of vegetation and soil, possessing steep slopes with bare rock exposed at the surface. The importance of long-duration, low-intensity precipitation on the potential for large volumes of infiltration was identified as a critical circumstance controlling net moisture movement through the unsaturated zone.

Characterization methods for hydraulic parameters relevant to high-level waste transport, including fracture apertures, transmissivity, matrix porosity, and fracture wetting front propagation velocities, were developed in Task 7. Evaluations were conducted of analytic and numeric models for representing fluid flow and transport through fractured rock under isothermal conditions.

Workshop V was organized by The University of Arizona, the U.S. Geological Survey, and the NRC, and was convened in Tucson, Arizona in January 1991; more than 70 scientists attended. A field trip was conducted to the Apache Leap Research Site, followed by two days of technical presentations by the attendees. Summaries of the papers are published in a NUREG/CP-0040.

CONTENTS

CONTENTS (Continued)

CONTENTS (Continued)

CONTENTS (Continued)

FIGURES

FIGURES (Continued)

FIGURES (Continued)

TABLES

TABLES (Continued)

ACKNOWLEDGEMENTS

This report has been prepared to document work performed to date by researchers in the Department of Hydrology and Water Resources at The University of Arizona, under contract NRC-04-90-51, FIN L1282, entitled "Validation Studies for Assessing Unsaturated Flow and Transport Through Fractured Rock." The project manager is Thomas J. Nicholson who provided substantial input to the preparation of this report. The report is an independent product and does not necessarily reflect the views or regulatory position of the NRC.

FOREWORD

This technical report was prepared by The University of Arizona under their research projects with the Waste Management Branch in the Office of Nuclear Regulatory Research (FINs L1282 and L1283). The report outlines research findings for completed field testing and evaluations of site characterization methodologies, techniques, and instrumentation for unsaturated flow and transport in heterogeneous, fractured rock. The work reported focuses on field studies at the Apache Leap Tuff Site (ALTS) in central Arizona that represents a hydrologic field analogue to an unsaturated zone high-level radioactive waste (HLW) repository site. Data sets from the ALTS field studies are being used to evaluate various conceptual models of flow and transport through unsaturated fractured media. This document presents information which assists in identifying key technical uncertainties associated with confirmation of DOE's site characterization and performance assessment studies for an unsaturated zone HLW repository site.

NUREG/CR-6203 is not a substitute for NRC regulations, and compliance is not required. The approaches and/or methods described in this NUREG/CR are provided for information only. Publication of this report does not ncessarily constitute NRC approval or agreement with the information contained herein.

1. INTRODUCTION

This document provides a progress report for U.S. Nuclear Regulatory Commission sponsored contract, NRC-04090-51 (FIN L1282) with The University of Arizona. The contract was initiated on November 12, 1989 and expires on November 11, 1992, with an optional extension for an additional two years until November 11, 1994. The project manager is Thomas J. Nicholson, Office of Nuclear Regulatory Research. The Principal Investigator is R.L. Bassett.

This contract arises from a statement of work based upon NRC regulatory needs that originated in the technical review of DOE's Site Characterization Plan and research needs identified in two symposium peer reviews of the earlier research programs conducted at the University of Arizona (Evans and Nicholson, 1987). The broad objectives of this contract are to examine various hypotheses and conceptual models concerning unsaturated flow and transport through heterogeneous fractured rock and to design and execute confirmatory field and laboratory experiments to test these hypotheses and conceptual models. Conceptual models and hypotheses relevant to flow and transport processes in unsaturated fractured rock have been recently identified and prioritized through the Peer Review of the Yucca Mountain Site Characterization Project (Freeze et al., 1991). The specific objectives under this contract are to: (1) investigate continuum scales for predicting gas and liquid flow in matrix-fracture systems, (2) determine the relationships between relative permeability of air and water in unsaturated fractured tuff, (3) investigate the use of effective hydraulic, pneumatic and transport properties to predict transport, (4) investigate the use of isotope and reaction path studies to determine the rate and pathway of solute flux in an unsaturated fractured tuff, (5) investigate the role of fracture zones in unsaturated flow and transport in a region above the water table and (6) determine the relationships between measurements performed at different scales. Objectives (1), (3), and (6) are to be addressed in cooperation with another project also at The University of Arizona led by Shlomo P. Neuman (FIN L1283).

The research approach to the above objectives was divided into eight related tasks:

Task 1 Laboratory heater, hydraulic, pneumatic, and tracer tests
Task 2 Field heater tests: review and plan
Task 3 Field hydraulic, pneumatic, and tracer tests
Task 4 Geochemical studies: confirmation of groundwater travel time and flux estimation techniques
Task 5 INTRAVAL studies
Task 6 Infiltration, deep percolation, and recharge studies
Task 7 Fracture flow studies
Task 8 Workshops on fracture flow and transport studies

Progress reports for the above tasks are provided in this document.

2. TASK I: LABORATORY NONISOTHERMAL CORE EXPERIMENTS

by Todd C. Rasmussen and Shirlee Rhodes

This section summarizes research related to studies of coupled fluxes of water (as liquid and vapor), heat (latent and sensible), and a conservative liquid-phase solute in an unsaturated, unfractured rock core. A NUREG/CR is in preparation which summarizes the research results and compares the computer simulation model predictions to experimental observations. In addition, several manuscripts are in preparation for publication in peer-reviewed journals. Finally, one M.S. thesis is in preparation at The University of Arizona which summarizes the characterization procedures employed.

Experimental data presented in this research were developed for the purpose of evaluating the magnitude of physical processes of fluid flow under conditions of steady heat flux. One component of the experiment investigated the thermal and liquid changes in a partially saturated core, while a second component examined thermal, liquid, and solute changes in a partially saturated core. These laboratory data provide calibration and evaluation data sets for thermal, liquid, vapor, and solute transport as a result of a thermal gradient. The simulation objective was to compare observed time-varying core water content profiles and solute concentration profiles for the mother core against predicted profiles obtained independently using characterization data obtained from the daughter cores.

2.1 BACKGROUND

A thermal source dramatically affects air, vapor, water, and solute movement in geologic media, and unsaturated fractured rock in particular. The ability to understand and to predict the outcome of coupled fluid, heat, and solute transport experiments is essential for accurate modeling of water and solute migration near a subsurface thermal source, due to a geothermal gradient or solar heating at the Earth's surface. To investigate the coupled processes related to nonisothermal flow and transport, a cylindrically shaped core approximately 12 cm long and 10 cm in diameter was extracted from a block of Apache Leap Tuff (white unit). A larger core, termed the "mother" core, was used for the experiment, while smaller, "daughter" cores were also extracted from the block for characterization purposes. The mother core with a prescribed initial matric suction and solute concentration was sealed and insulated to prevent water, air, and solute gains or losses on all surfaces and to minimize heat loss along the sides of the core.

During a series of experiments, a horizontal temperature gradient was established along the long axis of the core. Thirteen thermistors were situated along the core at approximately 1-cm intervals to record temperature over time. A dual-gamma source was used to determine the water and solute content along the core over time.

The daughter cores were used to provide characterization data regarding porosity, moisture characteristic curves (including hysteretic effects), saturated and unsaturated hydraulic conductivity, and saturated and unsaturated air permeabilities. Similar data from 105 core segments at the Apache Leap Tuff Borehole Site were also available (Rasmussen et al., 1990).

2.2 CONCEPTUAL MODEL

The conceptual model forms the foundation for the mathematical and computer simulation models discussed below. The primary elements of the conceptual model focus on the influence of a heat source and sink maintained at constant temperatures during the course of the experiment. The flow domain is assumed to be one-dimensional and cartesian. Material properties are assumed to be uniform along the length of the core, except where noted. During the period of heating of the core, the following phenomena were anticipated:

(1) Liquid water near the warm end of the core vaporizes in response to an increase in the vapor pressure deficit, forming a zone of desiccation near the heat source.
(2) Water vapor moves away from the warm end of the core due to total pressure and vapor pressure gradients.
(3) Heat flux away from the warm end occurs as sensible heat conduction and latent heat transfer in the vapor phase.
(4) As the temperature decreases with distance from the warm end, the vapor condenses beyond the zone of desiccation, forming a zone of liquid water accumulation.
(5) Liquid water moves from the zone of accumulation toward drier regions due to liquid phase potential gradients.
(6) Solute concentrations affect the liquid and vapor potentials due to osmotic effects.

2.3 MATHEMATICAL MODEL

The conceptual model described above is more precisely defined mathematically using the formulations described here. The general conservation equation for uncoupled processes is:

$$\nabla \cdot q_i = \nabla \cdot (K_i \nabla \phi_i) = C_i \partial \phi_i / \partial t + Q_i \qquad (2.1)$$

where:

∇ = divergence operator;
q = flux rate;
K = conductance term;
C = capacitance term
ϕ = potential term;
Q = source or sink term; and
t = time.

For fluxes which are coupled (i.e., a potential gradient in one process induces flux in a different process), the corresponding constitutive relationships are:

$$q_i = \Sigma_j K_{ij} \nabla\phi_j \quad (2.2a)$$

$$C_i = f(\phi_j) \quad (2.2b)$$

$$K_i = f(\phi_j) \quad (2.2c)$$

This set of constitutive relationships states that flux of species i can be induced by a gradient of process j through the coupling term K_{ij}, and that both the uncoupled capacitance and conductance terms for species i can be affected by the potential term for process j. Combining Equations (2.1) and (2.2) yields a coupled processes relationship of the form:

$$\nabla\cdot[\Sigma_j(K_{ij}(\phi_k)\nabla\phi_j)]_i = C_i(\phi_k)\partial\phi_i/\partial t + Q_i \quad (2.3)$$

It should be noted that such parameters as the thermal conductivity and heat capacity are significantly affected by the water content and the solute concentration, yet only slightly affected by gas pressure. Two of the state variables (pressure head and vapor pressure) can be related to each other using Kelvin's equation, if the two potentials are in equilibrium.

2.4 DAUGHTER CORE EXPERIMENTS

Characterization of the hydraulic properties of volcanic tuff matrix is performed on oriented cylindrical cores taken from a rock sample. The cores drilled from the sample are 6 cm in diameter and range from 2.39 to 2.69 cm in height. Matrix properties were obtained using laboratory procedures, and the parameters estimated from those experiments apply to fractured rock and nonisothermal flow characterizations as described elsewhere in this report. A description of matrix hydraulic properties follows, including sorption/desorption characteristic curves, hydraulic permeability curves, and air permeability and thermal conductivity properties, along with data sets and procedures employed to collect the data.

2.4.1 Moisture Characteristic Curves

Moisture characteristic curves relate the water content or relative saturation of a rock sample to the matric potential (matric suction) of the water in the sample. The desorption portion of the moisture characteristic curve is obtained using a pressure extraction vessel for the wet region (i.e., matric suctions less than 500 kPa), while saturated salt solutions are used to obtain data for drier regions (i.e., matric suctions greater than 500 kPa). The sorption portion of the moisture characteristic curve is obtained by reversing the order of the pressure increments applied in the procedures just mentioned, with some modifications to the pressure extraction vessel setup.

For matric suctions less than or equal to 500 kPa, a pressure plate extractor is used to regulate the matric potential within a core segment (Klute, 1986). The system utilizes a computer-monitored on-off solenoid, pressure transducer, and bleed-off solenoid to control pressure in the extraction vessel to within 2 kPa. All experiments were done in a constant-temperature laboratory at 20°C. Beginning with a vacuum-saturated core segment, the procedure consists of placing the segment on the porous ceramic plate of the pressure extraction vessel (with a No. 42 Whatman

filter paper lying between the sample and the plate for good hydraulic connection), sealing the vessel, and applying pressure using nitrogen gas. The imposed external pressure of the gas will result in an equivalent matric suction within the core segment upon equilibration. Once the sample has reached equilibrium, the pressure is released, the vessel is opened, and the core sample is weighed to calculate volumetric moisture content. The core is returned to the extraction vessel, and a greater pressure is applied. Pressures of 10, 25, 50, 100, 300, and 500 kPa were applied to the cores using the method just described, and corresponding water contents and relative saturations were determined for the core samples.

For matric suctions greater than 500 kPa, saturated salt solutions were used to impose the desired potential on core segments. At saturation, different salt solutions will have different known potentials, which create specific relative humidities in their immediate environments. The water potential in the vapor phase associated with those relative humidities creates a vapor pressure gradient, which provides the mechanism for moisture sorption/desorption. Core samples were positioned just above a saturated salt solution on a lattice, within a closed Lucite desiccator chamber. This arrangement assures maximum exposed sample surface area and minimum separation between sample and osmotic medium, both factors in reducing equilibration time (Campbell and Gee, 1986). Samples were allowed to equilibrate and, again, weighed to determine volumetric moisture content. The salts used for this procedure were lead nitrate, $Pb(NO_3)_2$, zinc sulfate heptahydrate, $ZnSO_4 \cdot 7H_2O$, and potassium bromide, KBr, giving 2.7 MPa, 14.2 MPa, and 23.6 MPa, respectively. The water potentials associated with these specific salt solutions (the theoretical values) were used to plot the moisture characteristic curves for the drier regions. These theoretical values are listed for comparison in Table 2.1, along with the relative humidities/water potentials which were measured using a hygrometer or thermocouple psychrometer. NOTE: Care must be taken with hydrated salts. The crystals in the bottom of such a saturated solution may not be the exact composition of the original salt.

The sorption part of the characteristic curve was determined by reversing the order of the matric potential equilibration steps. In the case of saturated salt solutions, the cores were moved to a solution of higher humidity/less negative potential than that used for the previous step. For sorption at 500 kPa or less, the pressurized apparatus was used, with a ceramic pressure plate which was modified to allow deaired solution to be pumped through the bladder under the plate (Klute, 1986). A reservoir of solution and a slow-speed peristaltic pump provided the source and method. Here again, equilibration was in reverse order of the pressure steps used for desorption.

Tables 2.2 and 2.3 present summaries of water content and relative saturation data for pressure extractor and salt solution methods. The data presented indicate that the saturation of the matrix at a specified matric suction for these samples is consistent for 20 samples, with a coefficient of variation of the mean of less than 2%.

Table 2.1. Relative Humidity/Water Potential Values for Saturated Salt Solutions, Theoretical and Measured (hygrometer and thermocouple-psychrometer).

Salt	Lead Nitrate	Zinc Sulfate	Potassium Bromide
Relative Humidity (%)			
Theoretical	98	90	84
Hygrometer	97	91	88
Potential (MPa)			
Theoretical	2.73	14.2	23.6
Hygrometer	4.12	12.8	17.3
T.-Psychrometer	5.71		

Table 2.2. Summary of Laboratory Hysteresis Data for Apache Leap Tuff for 10 Samples Wetting from 500 kPa, % Water Content by Volume

	Matric Potential (kPa)					
	10	25	50	100	300	500
Mean	0.1317	0.1254	0.1120	0.1017	0.0917	0.0838
Coefficient Variation (m)	1.06%	1.91%	1.90%	2.19%	2.78%	2.48%
Minimum	0.1250	0.1074	0.1021	0.0919	0.0829	0.0753
Median	0.1319	0.1287	0.1113	0.1003	0.0887	0.0842
Maximum	0.1366	0.1334	0.1241	0.1132	0.1048	0.0958

Table 2.3. Summary of Laboratory Hysteresis Data for Apache Leap Tuff, for 10 Samples Sorbing from 500 kPa, % Relative Saturation

	Matric Potential (kPa)					
	10	25	50	100	300	500
Mean	92.77	88.30	78.88	71.70	64.74	59.08
Coefficient Variation (%)	0.805	1.43	1.8	2.35	3.38	2.54
Minimum	87.78	79.85	72.25	62.83	54.32	51.46
Median	92.85	89.47	78.57	71.99	64.35	61.15
Maximum	96.46	92.32	84.25	78.09	78.92	65.93

Calculated statistical variance, assuming consistent methods and equipment, embodies both measurement error and geologic variation. To obtain variance due to measurement error, ten saturated rock segments were equilibrated at 500 kPa, in the manner already described. The procedure was repeated, giving two sets of water content data for the same set of ten cores. Variance of the data produced by the two experiments was calculated for each sample. Because each variance value was calculated for a single sample, the variance must consist only of measurement error. A mean was determined for the ten variance values, based on volumetric water content, giving 1.25E-8. Subtracting this value from the total variance, as calculated for 20 samples at each pressure step, has no significant effect. It must be concluded that the relatively small amount of total variance observed in the set of samples examined here is due almost entirely to geologic variation.

2.4.2 Hysteresis

Hysteresis describes the phenomenon of inconsistent moisture content and distribution with respect to matric potential that occurs during the history of wetting and drying of matrix material. At any given potential, moisture content of a wetting matrix is less than that of a drying matrix. Just as moisture sorption and desorption curves are characteristic of the matrix material from which they are derived, hysteresis scanning curves are influenced, additionally, by the water content/matric potential status of the matrix material at the point the wet/dry cycle is reversed.

Ten volcanic tuff samples were vacuum saturated, then placed in a pressure outflow apparatus at 500 kPa to desorb as described previously. After equilibration at 5 bars, the cores were replaced in the pressure apparatus with a wetting plate designed to provide deaired solution as the cores sorbed solution under decreasing pressure, at steps 300, 100, 50, 25, and 10 kPa. Figure 2.1 shows the complete desorption/absorption curve, with the single hysteresis scanning curve. Tables 2.2 and 2.3 present the statistical summaries of the hysteresis data sets.

2.4.3 Hydraulic Permeability Curves

Hydraulic permeability for geologic materials decreases as moisture content decreases, or as matric potentials (suctions) increase. The outflow method was used to obtain data for both

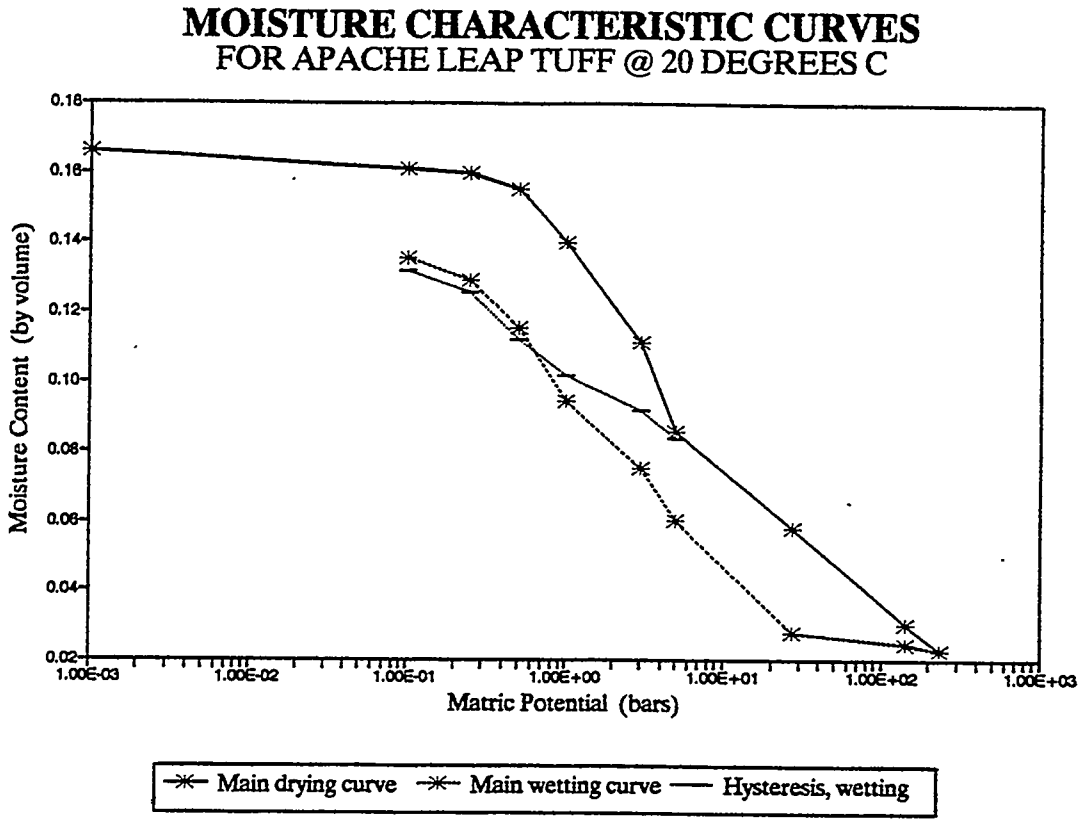

Figure 2.1. Apache Leap Tuff moisture characteristic curves.

saturated hydraulic conductivity and intrinsic permeability, with slight differences in technique. While all core segments were vacuum saturated, those used for saturated hydraulic conductivities were "packed" in a cylinder with water-proof caulking, leaving both upper and lower surfaces unobstructed (permeameter method). This arrangement allows flow through the core only. In the constant-temperature laboratory at 20°C, samples were placed in a Tempe pressure cell, and a pressure increment was applied, either as solution under pressure for saturated flow or as humidified gas for unsaturated flow. Rate of outflow from the pressure cell was monitored using a small capacity pipette and an injected air bubble, or by directly measuring accumulated outflow in a calibrated buret. Air trapped at the bottom of the porous plate was removed with a recirculation pump (Klute and Dirksen, 1986).

An analytical form of the cumulative outflow function:

$$1-\frac{Q(t)}{Q(\infty)} = \frac{8}{\pi^2} \sum_{m=0}^{\infty} \frac{1}{(2m+1)^2} \exp\left[\frac{-(2m+1)^2\pi^2\, Dt}{4L^2}\right] \tag{2.4}$$

was used to construct a theoretical plot of the quantities $\log[(1-Q(t)/Q(\infty)]$ versus $\log(Dt/4L^2)$. On the same log-log graph paper, the quantity $\log[1-Q(t)/Q(\infty)]$ versus log t was plotted for the experimental data. Curve-matching technique was employed by translating along the $\log(Dt/4L^2)$ axis only and reading the corresponding value of *t* from the experimental curve. If *w* represents the chosen value of $Dt/4L^2$ and *t* is the experimental value of time corresponding to the chosen value of w (Klute, 1964), then diffusivity is given by:

$$D = 4wL^2/t \tag{2.5}$$

For sample volume, V, and steady state outflow, $Q(\infty)$, the specific water capacity is given by:

$$C = Q(\infty)/V\Delta h \tag{2.6}$$

and the hydraulic conductivity is given by:

$$K = DC \tag{2.7}$$

Conductivity values were converted to hydraulic permeability values, for which summary and full data listings are found in Table 2.4.

Table 2.4. Summary of Hydraulic Permeability Values for Apache Leap Tuff, m^2, E-14.

	Matric Potential (kPa)				
	0	10	25	50	100
# of Repetitions	10.0	5.0	2.0	2.0	13.0
Mean	42.7	142.0	69.1	0.49	0.630
Coefficient Variation (m) %	14.9	68.7	70.0	89.1	29.2
Minimum	13.9	1.23	6.86	0.276	0.092
Median	39.6	73.3	6.91	2.49	0.410
Maximum	87.6	522.0	6.96	4.71	2.46

2.4.4 Pneumatic Permeability

Pneumatic permeability was measured using the permeameter setup described in Section 2.2, with the core segments sealed so as to allow no bypassing of flow around the outside of the sample. This test was performed in a constant temperature room at 20°C, on both oven-dried and partially saturated cores. In the latter case, nitrogen was bubbled through a reservoir to increase the humidity of the gas. Flow rate was obtained on oven-dried cores by applying a known pressure gradient longitudinally across the core segment, at total potential differences of 20 and 40 kPa, and measuring air flow volume with a calibrated bubble flowmeter. The partially saturated samples, equilibrated by the methods and at pressure steps to 100 kPa as described for moisture characteristic curves, were tested at 7, 20, or 40 kPa, always less than the equilibration status. Atmospheric pressure was monitored, and those values, ranging from 96 to 102.5 kPa on different days, were incorporated into the calculation of pneumatic permeability.

The pneumatic permeability at each matric potential is calculated using the measured air flow rate, cross-sectional area, and core segment length. The ideal gas law is employed with the realistic assumption of isothermal flow:

$$k_a = 2QLP_o\mu/A(2P_o\Delta P + \Delta P^2) \qquad (2.8)$$

where:

k_a = pneumatic permeability, m^2;
Q = measured flow rate, m^3/s;
L = core length, m;
A = core cross-sectional area, m^2;
μ = viscosity of nitrogen gas, Pa s;
P_o = outflow pressure head (atmospheric), Pa; and
ΔP = imposed pressure gradient, Pa.

Table 2.5 summarizes the test results. Theoretically, the air permeability of an oven-dried sample should be the same as the water permeability of the sample at saturation. In practice,

however, permeability estimates may not be similar due to the phenomenon of slip flow along the walls of pores (Klinkenberg, 1941). The importance of the Klinkenberg phenomenon can be evaluated by comparing the computed air permeability for oven-dried cores with the computed water permeability for completely saturated cores. The two values should be a function of the ambient air pressure used to conduct the air permeability test, as well as the mean free path of the gas molecules and the pore diameter. Moisture retention curve data are used to determine mean pore diameter. Data from saturated hydraulic conductivity and air permeability tests are then used to calculate the Klinkenberg coefficient (Klinkenberg, 1941):

$$k_a = k_w(1 + b/p) = k_w(1 + 8C\lambda/d) \quad (2.9)$$

Table 2.5. Pneumatic Permeability for Apache Leap Tuff Matrix, m^2.

Air Permeabilities (m^2, E-15)							
Matric Potential (kPa): At Equilibration							
	10	25	50	100	300	500	Oven-Dried
# of Repetitions	8.0	3.0	7.0	6.0	6.0	6.0	9.0
Mean	--	0.057	0.73	0.77	1.60	1.13	8.24
Coefficient Variation (%)	--	95.3	95.8	82.2	80.6	54.6	56.1
Minimum	--	0.00084	0.0012	0.0013	0.114	0.293	1.02
Median	--	0.0045	0.0592	0.0263	0.033	0.563	1.27
Maximum	--	0.166	4.93	3.90	8.01	4.17	33.3

where:

k_a = oven-dried air permeability, m^2;
k_w = saturated water permeability, m^2;
b = Klinkenberg slip-flow coefficient, Pa;
p = mean air pressure on the sample, Pa;
C = proportionality factor, ~1;
λ = mean free path at pressure p, m; and
d = mean pore diameter, m.

The Klinkenberg slip-flow coefficient is important because the Knudsen diffusion coefficient, D_k (m^2), can be derived from it using (Thorstenson and Pollock, 1989):

$$D_k = k_w b/\mu \quad (2.10)$$

where μ is the gas viscosity, Pa s.

2.4.5 Thermal Conductivity

Because thermal gradients can substantially affect the movement of water as liquid and vapor in the subsurface, characterization of the moisture-dependent thermal properties of the rock matrix is important for modeling the thermal effects on fluid and solute transport. This section presents laboratory data sets for thermal parameters corresponding to samples consistent with other data sets given in this report.

To estimate thermal properties of the rock matrix, modifications were made to a new method (Ashworth, 1990) where core segments were "sandwiched" between a set of copper disks with thermistors and a set of heat exchangers, as shown in Figure 2.2. The "heat flux meter" of copper/nylon/copper disks, positioned on the top surface of the core, was the mechanism by which the amount of heat flux entering the segment could be measured. A thermal gradient was imposed vertically through the sample, and the steady-state temperature of the core was evaluated with the thermistor/copper disk at the core's lower surface. By using materials of known thermal conductivity and low thermal resistivity where appropriate, Fourier's Law can be used to calculate thermal conductivity for core samples of known length.

First, obtain the amount of heat flux being applied:

$$F_h = K_{T\,nylon}\, dT/dx \qquad (2.11)$$

where:

f_h = heat flux;
$K_{T\,nylon}$ = thermal conductivity of nylon disk;
dT = change in temperature across nylon disk, T_1-T_2; and
dx = thickness of nylon disk.

Rearranging the equation to solve for thermal conductivity of the core segment yields:

$$K_T = f_h\, dx/dT \qquad (2.12)$$

where:

K_T = thermal conductivity of the core segment;
f_h = heat flux into the core segment;
dx = length of rock segment; and
dT = change in temperature across segment, T_2 - T_3.

It must be noted that some moisture loss due to evaporation did occur during the course of the thermal conductivity measurements. Table 2.6 summarizes laboratory thermal properties. Figure 2.3 shows the nonlinear aspect of the relationship between rock matrix thermal conductivity and volumetric water content.

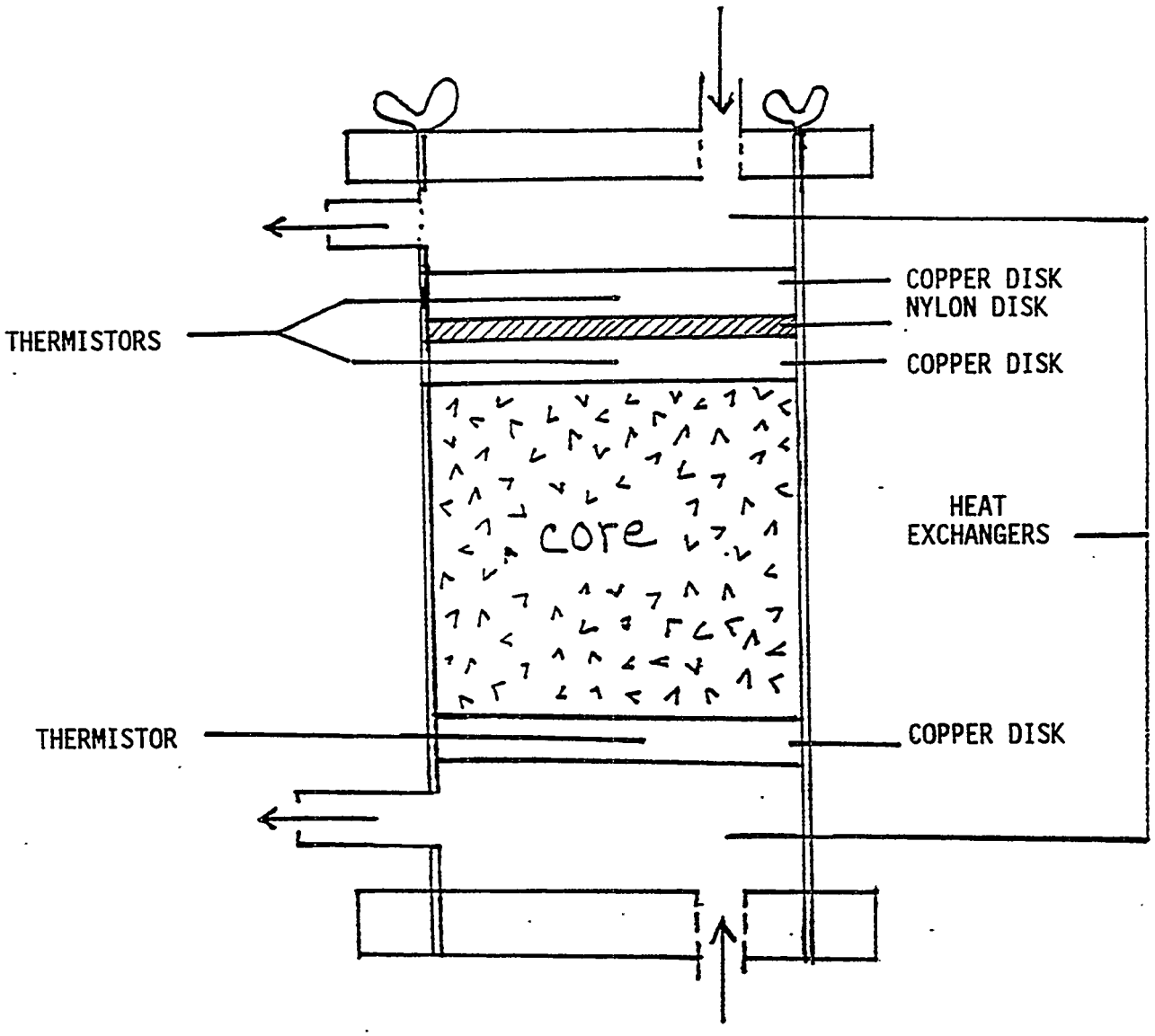

Figure 2.2. Thermal conductivity measurement device.

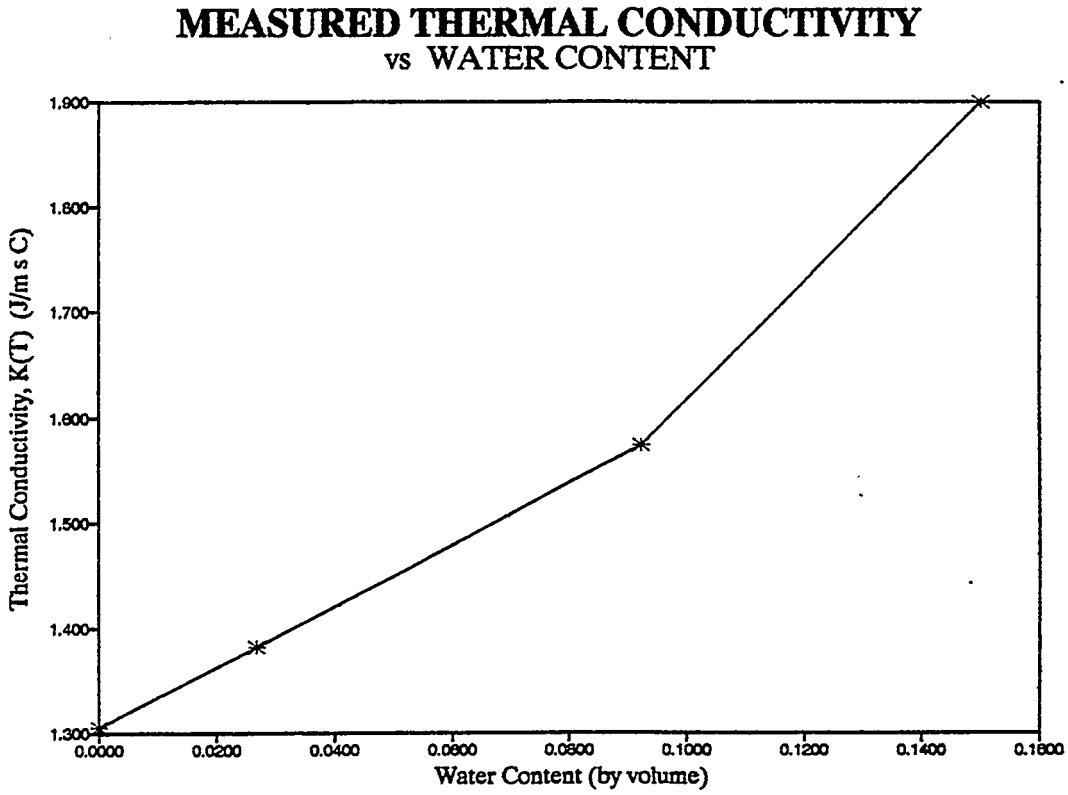

Figure 2.3. Dependence of thermal conductivity on water content for Apache Leap Tuff.

Table 2.6. Summary of Thermal Conductivities for Variably Saturated Apache Leap Tuff, J/sm°C

Water Content (Mean, Volumetric)				
	0.1502 (n_e)	0.0876	0.0267	0
# of Repetitions	10.0	9.0	3.0	9.0
Mean	1.899	1.574	1.382	1.305
Coefficient Variation (m) %	1.34	1.93	2.99	2.82
Minimum	1.786	1.470	1.341	1.168
Median	1.864	1.540	1.341	1.289
Maximum	2.027	1.703	1.465	1.533

2.5 MOTHER CORE EXPERIMENTS

Five nonisothermal experiments were conducted using the mother core. The mother core geometry measured 12.2 cm in length and 9.6 cm in diameter. The five experiments were proposed in order to provide a logical progression of experimental and theoretical complexity from one experiment to the next. Data obtained during the five experiments included water, temperature, and solute content profiles along the mother core. The same boundary conditions were employed in each case. Material properties were assumed to remain unchanged from one experiment to the next. The initial conditions were varied in the following manner:

(1) Oven dry, solute free;
(2) Water saturated, NaI solute absent;
(3) Partially saturated, NaI solute absent;
(4) Water saturated, NaI solute present; and
(5) Partially saturated, NaI solute present.

In addition to the changing initial conditions indicated above, the following mother-core initial conditions were employed:

(1) Air pressure was atmospheric at approximately 93 kPa.
(2) The initial core temperature was 22°C.

The initial conditions can be summarized as:

Experiment	1	2	3	4	5
ψ	∞	0	500	0	500
C_s	0	0	0	0.05	0.05

P_o = 93 kPa

T_o = 22°C

where:

ψ = matric suction, kPa;
C_s = solute molar concentration;
P_o = initial total gas pressure, kPa; and
T_o = initial core temperature, °C.

The mother-core boundary conditions during all heating experiments were:

(1) No flow water, air and solute boundary conditions on all surfaces.
(2) Steady temperatures of approximately 7 and 42°C at either end, with no flow thermal conditions along the sides of the core cylinder.

The boundary conditions can be summarized as:

$q_w = 0$ for $\forall$ surfaces
$q_a = 0$ for $\forall$ surfaces
$q_h = 0$ for $\forall$ sides of core cylinder
$T_1 = 7°C$ for cold end of core cylinder
$T_2 = 42°C$ for hot end of core cylinder

where:

q_w = water flux;
q_a = gas flux;
q_h = heat flux;
T_1 = temperature at cold end; and
T_2 = temperature at hot end.

2.6 SIMULATION MODEL

The simulation model used observed material properties from both the mother and daughter cores, mother-core geometry, and initial and final conditions. Estimates of material properties were obtained using two approaches:

(1) Generation of general phenomenological relationships using daughter cores. The daughter cores allowed for estimation of mean and variation-in-mean properties.

(2) Generation of specific material properties using the mother core. The spatial variability in porosity and bulk density were determined by means of gamma-ray attenuation. The bulk thermal conductivity was estimated using transient thermal responses of the mother core.

For steady water contents (dry, saturated, and partially saturated), the mother core thermal properties are estimated by applying step boundary conditions to both ends simultaneously. The temperature response at any location along the core can be estimated using (Carslaw and Jaeger, 1959):

$$v/V = 1 - 4/\pi \Sigma - 1^n/(2n+1) \exp[-(2n+1)^2 \pi^2 T/4] \cos[(2n+1)n\xi/2] \quad (2.13)$$

where:

$T = \kappa t/l^2$;
$\xi = x/l$;

and:

v = observed temperature;
V = applied temperature at ends of core;
κ = assumed constant thermal diffusivity;
x = distance along core; and
l = half-length of core.

Saturated and relative hydraulic conductivity functions for the daughter rock cores were obtained using osmotic solutions for dry conditions (matric suctions greater than 500 kPa). Pressure extraction vessels were used for wetter conditions (i.e., at potentials less than and equal to 500 kPa). Hysteresis relationships for the daughter cores were also determined.

Dual source (Am and Cs) gamma attenuation methods were employed to determine the water content and solute content at 1-cm intervals along the 12-cm mother core. The attenuation method uses the following relationships:

Americium Attenuation:

$$(C/C_o)_{am} = \exp(-\mu^r_{am} m^r - \mu^w_{am} m^w - \mu^s_{am} m^s) \quad (2.14)$$

Cesium Attenuation:

$$(C/C_o)_{cs} = \exp(-\mu^r_{cs} m^r - \mu^w_{cs} m^w - \mu^s_{cs} m^s) \quad (2.15)$$

where:

$(C/C_o)_{am}$ = ratio of americium counts through core to counts through the atmosphere;
m^r = mass of rock;
m^w = mass of water;
m^s = mass of solute;
$\mu_{am}{}^r$ = attenuation coefficient through rock for americium;
$\mu_{cs}{}^r$ = attenuation coefficient through rock for cesium;
$\mu_{am}{}^w$ = attenuation coefficient through water for americium;
$\mu_{cs}{}^w$ = attenuation coefficient through water for cesium;
$\mu_{am}{}^s$ = attenuation coefficient through solute for americium; and
$\mu_{cs}{}^s$ = attenuation coefficient through solute for cesium.

Due to the time required by the detector to respond to individual photon captures, a correction was made to each count to compensate for instrument dead time. This correction takes the form:

$$C_{am}^{corr} = C_{am}/(1-\tau_{am}C_{am}) \quad (2.16a)$$

and:

$$C_{cs}^{corr} = C_{cs}/(1-\tau_{cs}C_{cs}) \quad (2.16b)$$

where:

C^{corr} = corrected count;
τ_{am} = americium counting dead time, 1.32 μs; and
τ_{cs} = cesium counting dead time, 1.12 μs.

An additional complexity results from spurious americium photon counts generated within the detector by the cesium source. To correct for the spurious americium counts, a 5 M solution of NaI was used to eliminate any americium photons from entering the detector. The number of americium counts resulting from only the cesium source was obtained and used to correct the americium counts when the NaI solution was not present using the relationship:

$$C_{am}^{corr} = C_{am} - \alpha C_{cs} \quad (2.17)$$

where α is the ratio of spurious americium counts to cesium counts obtained using the 5 M NaI solution. This technique for removing the spurious counts was shown to be equivalent to removing the americium source and counting the false americium counts resulting only from the cesium source.

Porosity and initial water contents for the mother core were measured for 1-cm diameter cylinders situated perpendicular to the thermal gradient. Each estimate was obtained using americium and cesium gamma-attenuation counts located 0.5 cm apart along the 12 cm long core. The average porosity is 14.9 percent, and the average relative saturation is 53.1 percent. The initial saturation was not uniform, with a distinct trend from one end of the core to the other. The water saturation trend is a probable artifact of the single-step outflow procedure employed to induce the initial conditions. For the initial part of the experiment, the end nearest the number 1 position was heated, while the end nearest the number 22 position was cooled. Temperatures were measured using 13 precision thermistors placed at approximately 1-cm intervals along the length of the mother core, from position 0 cm to position 12 cm in increments of 1 cm. The initial temperature was 22°C.

Additional information was available from data collected during the desaturation of the mother core. Before thermal experiments were conducted, the circumference of the mother core was sealed, while the two ends were left open. The core was fully saturated and then one end of the core was placed on a pressure plate and a five bar (500 kPa) pressure was applied. The total weight of the core was measured on various dates and used to develop a time series of core saturations.

2.7 MODEL EVALUATION PROCEDURE

The model evaluation procedure examines the ability of the conceptual, mathematical, and simulation models to reproduce the observed water content profiles, solute concentration profiles, and temperatures profiles. Complete independence between the two data sets is maintained during the experimental and analysis phases by assuring that model predictions are generated without calibration to the observed data. Statistical analyses are then used to evaluate the ability of the prediction model to accurately reproduce the observed data.

The simulation output consists of mean water contents and solute concentrations at 0.5-cm increments along the length of the core for selected times. Each gamma-ray reading measured the mean water contents and solute concentrations across a 1-cm diameter cylinder of rock. Each reading was 0.5 cm apart and overlapped neighboring measurements. There were a total of 22 readings at each observation time. The output also consisted of predicted temperatures at 1-cm intervals. The temperature measurement was considered to be a point measurement. Each temperature measurement location was approximately 1-cm apart. There were a total of 13 temperature readings for each time.

2.8 SUMMARY AND CONCLUSIONS

Coupled processes related to high-level nuclear waste migration were examined on laboratory scales to support field heater test experiments at the Apache Leap Tuff Site. (The field heater test experiment design is described in Task 2, below). The physical and chemical processes relevant to unfractured rock over a range of fluid saturations and temperatures that affect HLW transport in unsaturated fractured rock include thermal, liquid, vapor, and solute transport. Experimental data presented as part of Task 1 were developed for the purpose of evaluating the magnitude fluid flow under conditions of steady heat flux. These estimates were then used to identify the influence of hydrogeologic parameters on HLW transport under field conditions.

One component of the laboratory experiments investigated the thermal and liquid changes in a partially saturated core, while a second component examined thermal, liquid, and solute changes in a partially saturated core. These laboratory data provide calibration and evaluation data for thermal, liquid, vapor, and solute transport as a result of a thermal gradient. The experimental objective was to compare observed time-varying core water content profiles and solute concentration profiles for the laboratory experiment against predicted profiles obtained independently using independently generated characterization data. The data have been made available to INTRAVAL studies. (INTRAVAL studies are described in Task 5, below.)

Characterization techniques to estimate the hydraulic, pneumatic, and solute transport coefficients were developed for a wide range of thermal regimes. Laboratory methods were established for estimating both wetting and drying characteristic curves (i.e., moisture content versus matric suction) for matric suctions ranging from 10 to 23,600 kPa. Modified pressure plate devices were employed for matric suctions between 10 and 500 kPa, while osmotic solutions were employed from 2,700 to 23,600 kPa. The characteristic curves were measured at three temperatures (5°C, 20°C, and 45°C) to observe the temperature dependence.

3. TASK II: FIELD HEATER EXPERIMENTS

by Todd C. Rasmussen and Daniel D. Evans

A generic experimental plan was developed that describes a long-term, field-scale nonisothermal experiment. The plan also includes the justification for conducting the experiment, a summary of related previous experiments, important processes expected to dominate coupled heat, liquid, vapor, gas, and solute flow during the experiment, material properties at the Apache Leap Tuff Site as an example heater site, simulations of water movement, water content changes, temperatures, gas fluxes and solute movement during the course of such an experiment, and critical design parameters that control expected outcomes of the experiment and maximize the ability to distinguish between alternate conceptual model forecasts. All details of the generic experimental plan have not been fully determined. Instead, the detailed plan is expected to result from interaction between modelers and experimentalists during the design phase.

The heater experiment plan provides a useful tool for designing a program to evaluate existing conceptual and computer simulation models related to fluid flow in a nonisothermal environment. The processes modeled include:

(1) two-phase liquid and vapor water fluxes;
(2) solute transport in the liquid water phase;
(3) bulk rock and rock fracture deformation due to thermal heating; and
(4) sensible and latent heat transfer.

Important characterization parameters required prior to application of computer codes to the interpretation of field-scale experiments include:

(1) saturation-, temperature-, and stress-dependent hydraulic conductivity and diffusivity for the bulk rock and embedded fractures;
(2) saturation-, temperature-, and stress-dependent pneumatic permeability and diffusivity for the bulk rock and fractures;
(3) saturation- and stress-dependent rock thermal conductivity and diffusivity;
(4) saturation-, temperature-, and stress-dependent solute diffusivity; and
(5) vapor pressure reduction due to osmotic potentials.

Previous laboratory, field, and laboratory nonisothermal experiments demonstrated the complexity associated with fluid flow in unsaturated fractured rock (Rasmussen et al., 1990). To avoid ambiguous and inconclusive experimental results, it was important that simulation modeling and site characterization be performed prior to conducting a field experiment. The design and implementation of a nonisothermal hydrologic transport study requires a concise and explicit statement of objectives, procedures, and tasks. The details of the experimental plan have been developed in consultation with INTRAVAL participants. (The INTRAVAL program is a multinational effort to compare numerical methods with field observations.)

A NUREG/CR document related to a field heater experimental plan was submitted to U.S. NRC for publication (Rasmussen and Evans, 1992). The field heater experimental plan presents methods for investigating hydrologic transport processes in unsaturated fractured rock related to the disposal of high-level radioactive waste (HLW) in an underground repository. The experimental plan also provides a methodology for obtaining data required for evaluating conceptual and

computer models related to HLW isolation in an environment where significant heat energy is produced. Coupled-process models are currently limited by the lack of evaluation data appropriate for field scales that incorporate relevant transport processes. An important motivation for conducting preliminary experiments and prototype heater experiments in general is to identify early in the study program previously unanticipated processes and events that may adversely impact the performance of high-level waste repositories.

The NUREG/CR document provides a discussion of previous nonisothermal experiments. Processes expected to dominate heat-driven liquid, vapor, gas, and solute flow during the experiment are explained, and the conceptual model for nonisothermal flow and transport in unsaturated, fractured rock is described. Of particular concern is the ability to confirm the hypothesized conceptual model, specifically, the establishment of higher water saturation zones within the host rock around the heat source, and the establishment of countercurrent flow conditions within the host rock near the heat source. Field experimental plans are presented using the Apache Leap Tuff Site to illustrate the implementation of the proposed methodology. Both small-scale preliminary experiments and a long-term experiment are described.

3.1 SUMMARY AND CONCLUSIONS

This task focused on the development of a field heater experiment in the Apache Leap Tuff Site that would use the information obtained from laboratory nonisothermal experiments. (Laboratory nonisothermal experiments were described in Task 1, above). Specific accomplishments included the design of a field heater experiment that focused on identifying the suitability of existing monitoring equipment to obtain required data. Important issues related to model evaluation for distinguishing between alternate conceptual models were also addressed. Previous field heater experiments related to HLW disposal were reviewed and evaluated. Important deficiencies in the previous experiments were identified, including the failure to focus on the effects of coupled processes.

Recommendations for a proposed heater test were developed using the review of previous studies as basis for future nonisothermal experimental design. An important recommendation was the establishment of an integrated modeling program that established the experimental techniques prior to field experimentation. A procedure was also developed for identifying unusual or unique processes that may indicate the possibility of events that are inconsistent with the conceptual model. It was shown that the ability to identify unanticipated events was an important component of field experimental data acquisition. A methodology for model performance evaluation was proposed and related to currently available data collection methods.

4. TASK III: FIELD HYDRAULIC, PNEUMATIC, AND TRACER TESTS: PHASE I

by Amado Guzman, Shlomo P. Neuman, Charles Lohrstorfer, and Randy Bassett

4.1 BACKGROUND

The objectives of Task 3, involving field hydraulic, pneumatic, and tracer tests are to: (1) investigate the role of fracture zones in unsaturated flow and transport, (2) determine relationships between the relative permeability of air and water in unsaturated fractured tuff, (3) investigate the applicability of the continuum approach to predict gas and liquid flow in fractured porous media, (4) determine the relationships between measurements performed at different scales, and (5) investigate the use of effective hydraulic, pneumatic and transport properties to predict transport in such media. To satisfy these objectives, an intensive program of pneumatic permeability measurements was initiated at the Apache Leap Tuff Site (ALTS). A full-time staff member, Mr. Michael Hendrich, is currently assisting us with the in-situ permeability determinations. Additional support for this work has been provided through NRC contract (NRC-04-90-052; FIN L1283). The theoretical aspects of this investigation are being developed under FIN L1283.

4.2 CURRENT STATUS

Currently, we are executing Phase I of Task 3 as described in the Experimental Research Plan (Bassett et al., 1992). During this Phase, the spatial structure of the pneumatic permeability at a scale of 1 meter is being characterized. The entire length of boreholes X2, V2, W2A, Z2, and Y3 are being scanned with our in-situ air-permeability instrument, resulting in about 160 meters of tested fractured rock. The data collected from the above-mentioned boreholes will allow us to obtain a three-dimensional representation of the spatial structure of air permeability. Combined with data obtained at the one-meter scale from borehole Y2, we should have a sample size large enough to allow the performance of meaningful statistical and geostatistical analyses. These analyses, in turn, should permit us to predict and design, through numerical simulation, cross-borehole injection and tracer tests for Phase II of our experimental research program.

A reliable method of conducting and interpreting straddle-packer air permeability tests has been developed and implemented. The present system, instrument, and method of interpretation has proved to provide a sound testing methodology. Repeated testing of several intervals during previous years resulted in highly reproducible permeability estimates. Air permeabilities together with dates, flow rates, corresponding steady-state pressure as obtained from injection/extraction tests in interval JH (15.85 m) in borehole Y2 (Table 4.1), were collected over a period of seven months and illustrate the consistency of the method. The estimates of permeability range from 206 to 246 x 10^{-16} m^2 with a mean of 227 x 10^{-16} m^2, excluding the two tests which did not reach steady state. These estimates have a standard deviation of 12.6 x 10^{-16} m^2 and a coefficient of variation of 5.6%. Appendix A includes the Field Operation Procedure (FOP) for the multi-rate injection tests and a schematic representation of the in-situ permeability apparatus.

An essential part of our testing technique is the quality assurance (QA) program. As part of this QA program, a procedure to periodically check the integrity of the straddle-packer arrangement was developed. This procedure was named the "Zero Permeability" test inasmuch as it is conducted within an impermeable PVC pipe having an inside diameter (ID) equal to that of our test boreholes at the ALTS. The FOP for this test is included as Appendix B. Under normal

conditions, the integrity of the packer system is checked every other week, each time a component is replaced or re-calibrated, or when the instrument is retrieved to the surface for maintenance. Periodic calibration of the pressure transducers and flow meter/controllers is also part of the QA program.

Table 4.1. Permeability Estimates from Multiple Testing in Interval JH (15.82 m) at Borehole Y2.

Date	Q(sccm)	$\Delta P_{steady\ state}$ (cm Hg)	k ($x10^{-16}$ m^2)
09/15/90	1,200	2.32[1]	287
09/19/90	1,500	3.25[1]	254
09/19/90	2,500	6.00	225
09/19/90	10,000	22.20	218
03/04/91	20,000	41.56	206
03/05/91	1,200	3.00	221
09/19/90	-6,000	-16.20	240
09/23/90	5,000	11.49	225
09/23/90	-6,400	-16.80	246
09/24/90	-2,500	-6.36	232

[1] In this test, pressure did not reach steady state.

A typical test consists of a sequence of constant flow rate periods, each of which lasts until the pressure in the test interval reaches steady state (defined for our purposes as a situation where pressure in the test interval remains within 1 mm of Hg for a period of 30 minutes). Pressure, flow rate, temperature, and relative humidity in the test interval are continuously monitored during the duration of the test pressure. A typical response of a multi-rate test, in which three different flows rates were imposed, is shown in Figure 4.1a. Figure 4.1b shows another typical pressure response to a single injection rate. The different behaviors in these two tests will be explained in Section 4.3.1. Initially, the multiple-rate testing was designed mainly to collect redundant information. However, it proved essential for understanding two-phase flow and inertial flow conditions that prevail during each test. Additional work is presently under way to further improve this understanding. A preliminary statistical analysis has been performed using all available information from boreholes Y2 X2,V2, Z2, and W2A. This report presents a summary of the method of interpretation, the currently available data, and the most relevant aspects of our statistical and geostatistical analyses to date. The report also points out issues that need further study to improve one's ability to characterize the permeability of unsaturated fracture tuff in-situ.

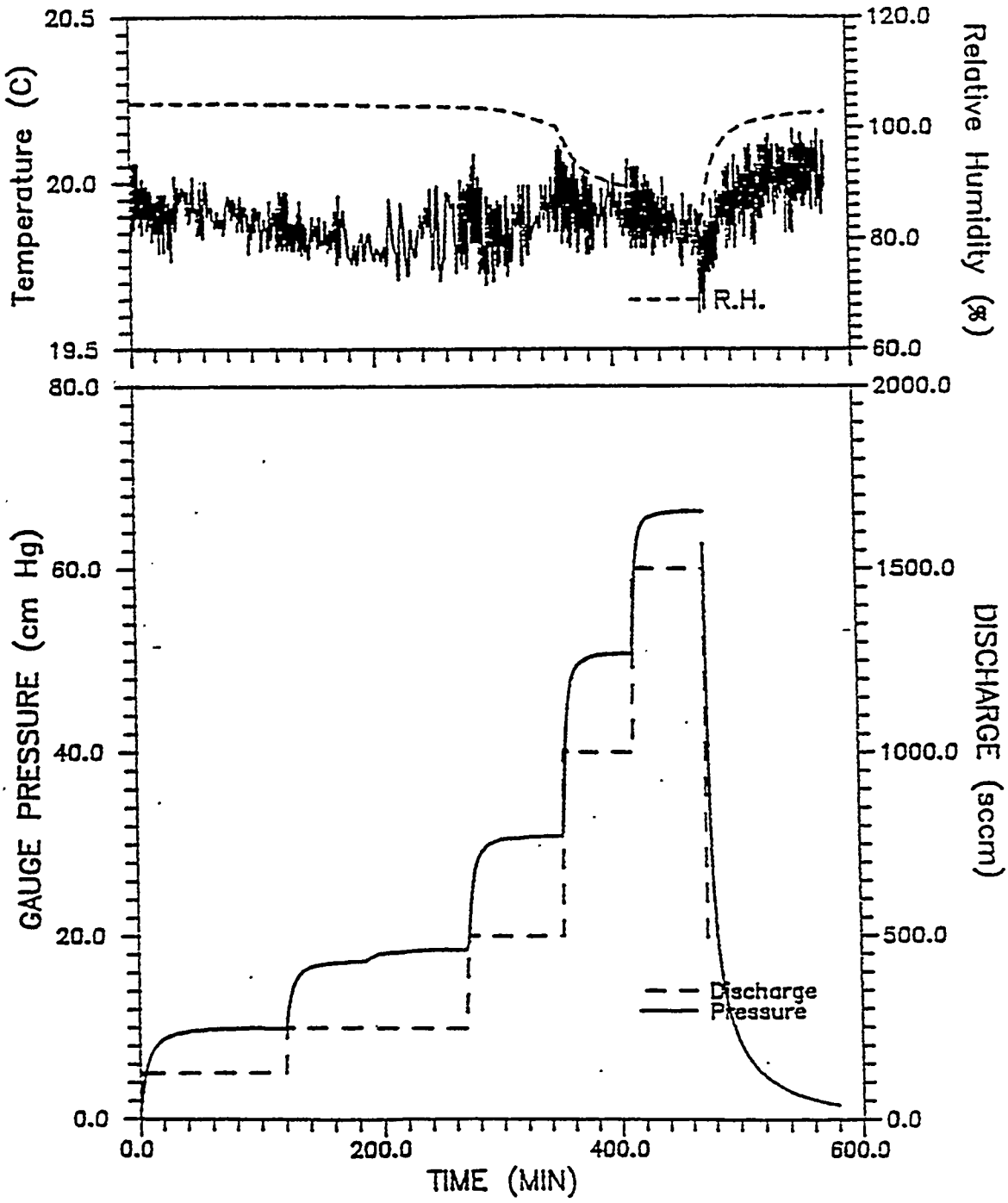

Figure 4.1. Typical multi-rate injection test.

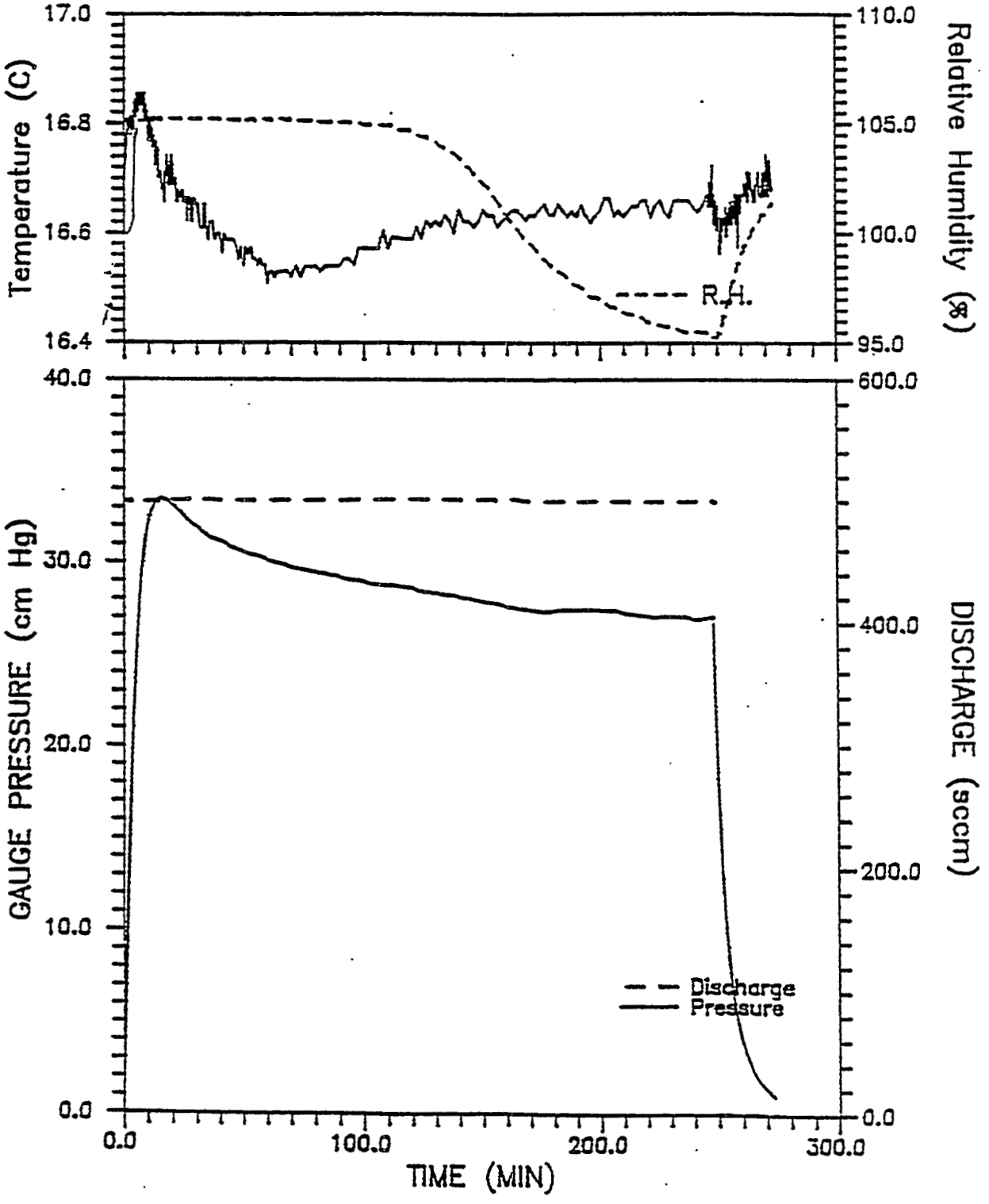
INJECTION TEST
Y2-JD3
04-08-91
Temperature (C)
17.0
16.8
16.6
16.4
Relative Humidity (%)
110.0
105.0
100.0
95.0
R.H.
GAUGE PRESSURE (cm Hg)
40.0
30.0
20.0
10.0
0.0
DISCHARGE (sccm)
600.0
400.0
200.0
0.0
Discharge
Pressure
0.0
100.0
200.0
300.0
TIME (MIN)

Permeability testing initially focused on borehole Y2 of the ALTS. Three different scales of measurement (distance between the straddle-packers) have been examined in this borehole: 0.5 m, 1.0 m, and 3.0 m. Early in our in-situ testing program, a comparison was made between injection and extraction tests which indicated consistent estimates of permeability (see Table 4.1). However, due to low permeability of the fractured rock in many intervals, vacuum extraction tests required unacceptably long times to stabilize (reach steady state). This happens because the low pressure developed in the test interval during vacuum extraction causes a reduction in air density, which in turn enhances borehole storage effects. To minimize this effect, the bulk of the in-situ determinations are performed by air injection rather than by air extraction.

Currently, two in-situ permeability instruments are available for testing at the ALTS. As of December 1993, boreholes Y2(30.5 m), X2 (32.5 m), and V2 (30.5 m) have been completely tested at the 1-meter scale. More than 20 intervals have been tested in borehole W2A (31.1 m) and more than 22 in borehole Z2 (30.5 m). The permeabilities in borehole V2 are generally smaller than those in the other boreholes, and the tests take longer to stabilize. It is foreseen that the remaining intervals in these two boreholes will be completed by late December 1993. Our next step (Phase I, Section (3) of the Experimental Plan) will be to investigate the relationship between apparent permeability and water content over a large range of liquid saturations in the G series of boreholes during early 1994 as well as cross-hole gas injection and tracer tests in the "covered site". Numerical analyses of two-phase flow under typical test conditions are underway, and the most relevant results are summarized in a later section of this report.

4.3 SUMMARY OF FINDINGS TO DATE

The experimental program at the ALTS has raised some very important and interesting issues concerning instrumentation, test procedure and methodology, conditions prevailing during the test, and test interpretation. An instrumentation problem that has proved difficult to resolve is the accurate measurement of the relative humidity of air in the injection interval. The behavior of our relative humidity cells under field conditions has been less than optimal in the high range of relative saturation (95 to 100%) observed at the ALTS, causing frequent downtime periods. Another instrument-related issue that has slowed down the field work relates to the detection and correction of leaks. Questions open to physical interpretation include the nature of the flow regime and the interaction between wetting and non-wetting fluids. Analytical issues concern test interpretation under steady-state and transient conditions, the geometry of the flow field, and the volume of rock (radius of influence) affected by each injection test. Many of these issues are being investigated through numerical simulation of typical test conditions.

Work completed to date addresses objectives (2), (3), and (4) and provides partial answers to Objectives (1) and (5). Information collected during subsequent stages of our program, as described in the Experimental Research Plan of March (Bassett et al., 1992), combined with the data accumulated during this Phase, should allow us to better address these latter two objectives.

4.3.1 Fluid Conditions in the Rock During Testing

The interpretation of injection tests is generally much simpler under steady-state than under transient conditions. Experience with hydraulic injection tests in saturated fractured crystalline rocks suggests that transient tests sometimes yield permeabilities that are too low (cf., Jones et al., 1985). We will see later that, at ALTS, both the transient and the steady-state parts of each test are strongly affected by two-phase flow phenomena. These phenomena render interpretation of

air injection tests difficult even under steady-state conditions, as will soon become apparent. We expect these difficulties to be much greater under transient conditions. For these reasons, our efforts are presently focused mainly on an interpretation of the steady-state record from each test.

Hvorslev (1951) and Hsieh et al. (1983) presented an analytical expression for the spatial distribution of steady-state water pressure around a hydraulic injection test interval which considers the equipotentials to form prolate spheroids. Modified for air, this expression takes the form:

$$Q_{sc} = 4\pi L \frac{k}{\mu} \frac{T_{sc}}{T p_{sc} Z} \frac{p^2 - p_o^2}{\sinh^{-1}\left[\frac{L/2+z}{r}\right] + \sinh^{-1}\left[\frac{L/2-z}{r}\right]} \tag{4.1}$$

where Q_{sc} is the volumetric flow rate at standard conditions, k is air permeability, μ is air viscosity, L is distance between the straddle packers, T is air temperature in the injection interval, p_{sc} is the pressure at standard conditions (1 atm), T_{sc} is the temperature at standard conditions (20°C), Z is air compressibility, p_o is ambient air pressure, p is air pressure in the rock at a radial distance, and r is vertical distance z from a point at the center of the interval. The pressure in the test interval, p_w, is usually associated with $z = 0$ and the borehole radius $r = r_w$. If $L/r_w >> 1$, flow is predominantly radial and Equation (4.1) simplifies to:

$$k = Q_{sc} \frac{\mu \mathrm{Ln}(L/r_w)}{\pi L(p^2 - p_o^2)} \frac{T p_{sc} Z}{T_{sc}} \tag{4.2}$$

Equation (4.2) has the advantage over standard radial flow equations in that it does not require introducing a fictitious radius of influence. The derivation of Equation (4.2) is presented in Appendix C. It can be rewritten as:

$$Q_{sc} = C\Delta p^2 \tag{4.3}$$

where:

$$C = \frac{\pi k L}{\mu \mathrm{Ln}(L/r_w)} \frac{T_{sc}}{T p_{sc} Z} \tag{4.4}$$

and:

$$\Delta p^2 = p_w^2 - p_o^2 \tag{4.5}$$

At the ALTS, air injection has to date been conducted on scales (in terms of L) of 0.5 m, 1.0 m, and 3.0 m. As the radius of each borehole is about 0.05 m, the smallest aspect ratio in our test is $L/r_w = 10$. Figure 4.2 shows how the ratio of k^R from the radial flow Equation (4.2) and k^P from the prolate spheroidal flow Equation (4.1) varies with L when $r_w = 0.05$ m. It follows from this figure that, under our test conditions, working with the radial flow Equation (4.2) differs from working with Equation (4.1) by not more than 0.5%.

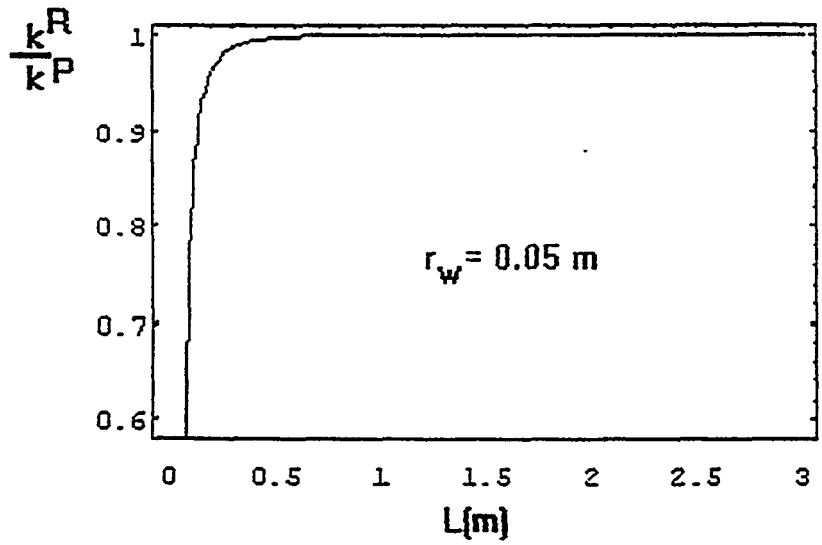

Figure 4.2. Interpretation of individual-rate injection tests.

Local heterogeneities (layers, lenses, fractures, other) and anisotropy may alter the steady-state flow regime around the test interval. When layers or fractures intersect this interval, flow in the rock may be predominantly two-dimensional. If preferential flow channels exist in such layers or fractures, flow in them may be predominantly one-dimensional. Intermediate flow regimes corresponding to non-integer (fractal) dimensions may also develop in some cases (Barker, 1989). A method to identify the prevailing integer-dimensional flow during oil extraction from a rock has been described by Ersaghi and Woodbury (1985). According to them, plotting the recorded differential pressure in the test interval versus time during the transient part of the test should help diagnose the dimensionality of flow. In the absence of borehole storage effects, plotting p versus $t^{-1/2}$ should yield a straight line under spherical (three-dimensional) flow; plotting p versus log t should yield a straight line under radial (two-dimensional) flow; and plotting p versus $t^{1/2}$ should yield a straight line under linear (one-dimensional) flow. For air injection, one should develop such curves in terms of squared differential pressure as shown in Figure 4.3. Unfortunately, the pressure square trace appears linear over the middle segment of each of these plots, rendering the diagnosis of flow geometry by this method ambiguous.

It is clear from Equations (4.3)-(4.5) that, when these equations apply, knowledge of the flow rate, pressure, and temperature in the test interval allow computing Δp^2, C, and hence k. In multiple flow rate tests such as ours, one can compute a k for each flow rate. In most of our tests, such k values either decrease (Figure 4.4a) or increase (Figure 4.2b) consistently with increasing mean pressure, taken as the arithmetic average of p_w and p_o. In other words, our tests indicate that in-situ air permeability as obtained by means of Equations (4.3)-(4.5) is nonunique, depending strongly on the applied mean pressure.

Theoretically, Equations (4.3)-(4.5) should apply under strictly Darcian flow conditions of a pure air phase. The effect of non-Darcian behavior on well testing has been studied in the natural gas (Katz et al., 1959) and oil industries (e.g., Lee, 1982). Deviations from ideal conditions as a result of inertial flow effects were recognized and taken into account by Rawlins and Schellhart (1936), Missbach (1937), and later by Hiles and Mott (1945), De Sorcy (1978), and Donohue and Ertekin (1982). Schellhart (1936) proposed modifying Equation (4.3) to read:

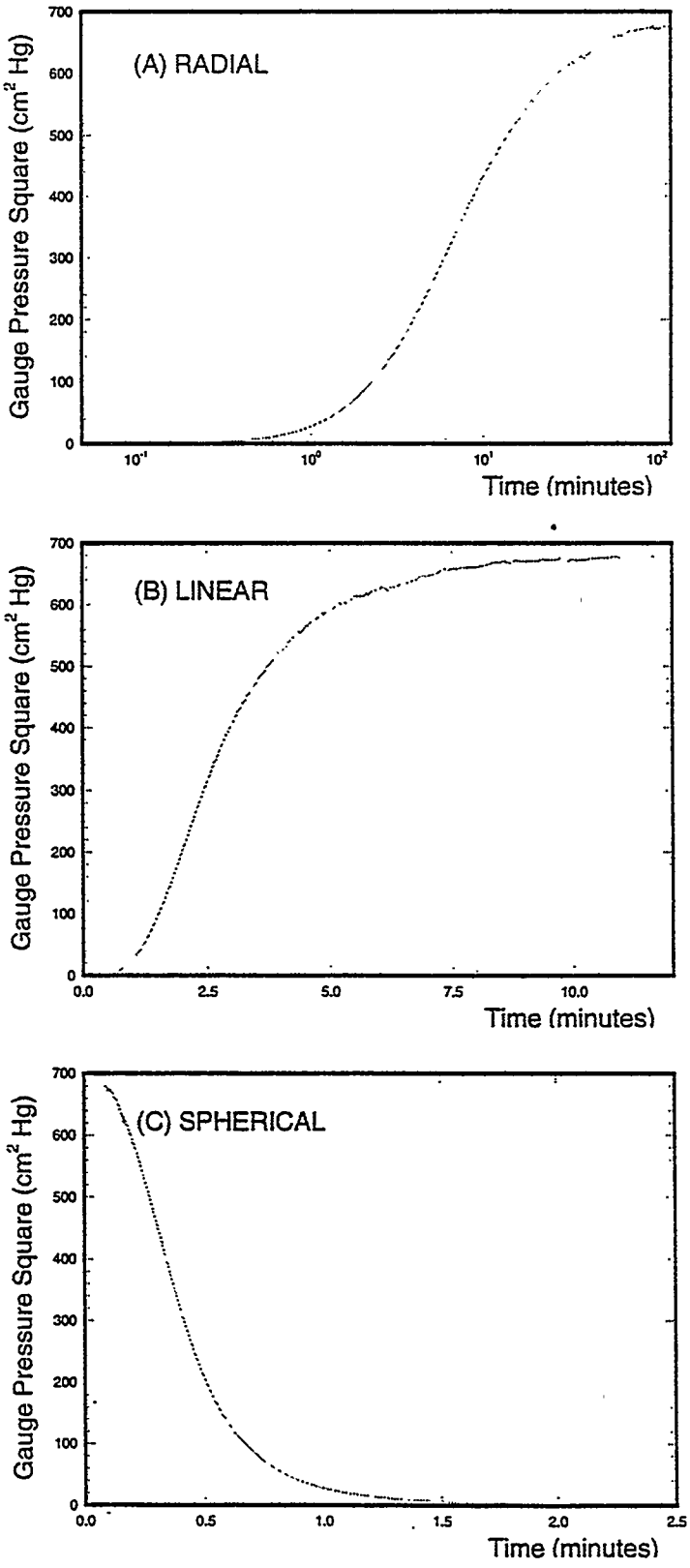

Figure 4.3. Flow geometry versus ratio between radius and length of test

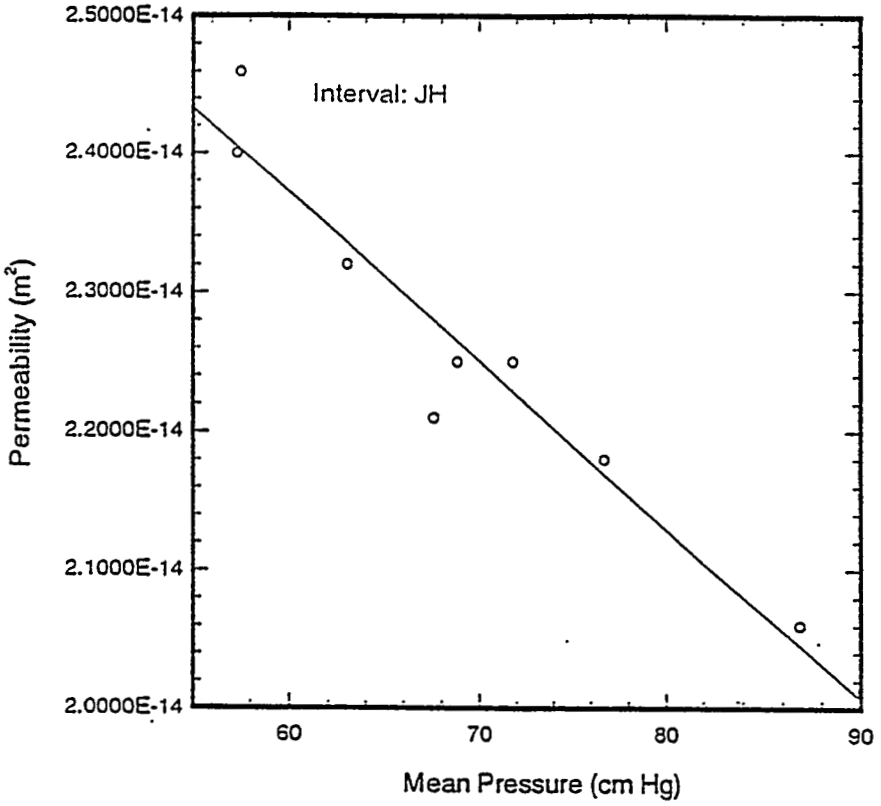

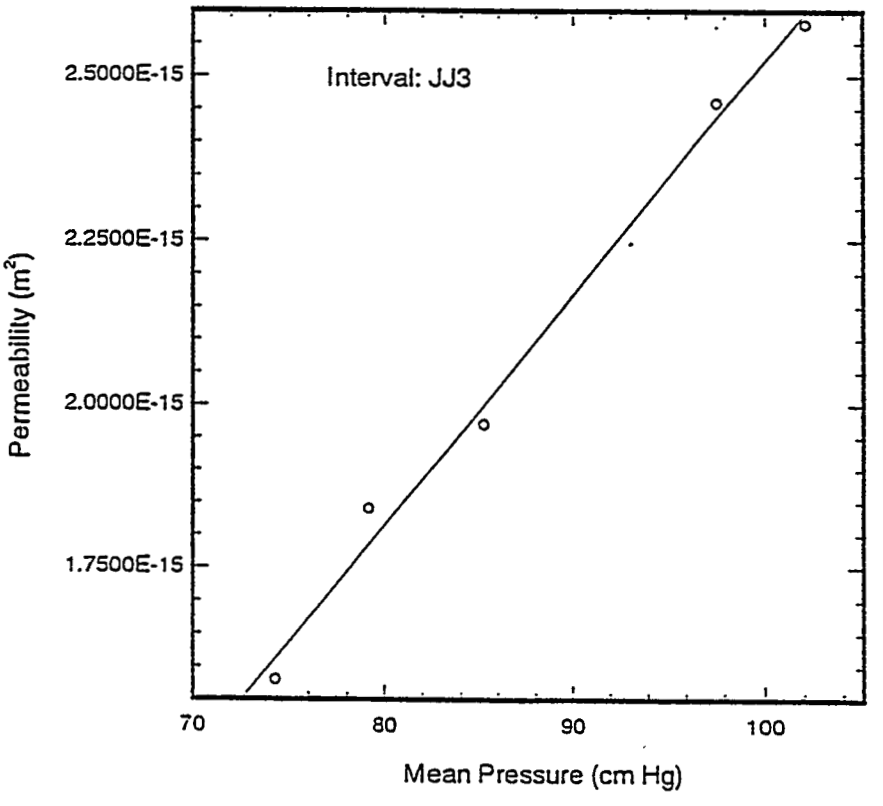

Figure 4.4. Interpretation of individual-rate injection tests

$$Q_{sc} = C(\Delta p^2)^n \tag{4.6}$$

where n accounts for possible inertial effects. As the pore velocity increases, inertial flow effects become significant, and n decreases from its Darcian value of 1.0 toward 0.5. Theoretically, in the limit when the flow becomes turbulent, n becomes 0.5. The same follows from the last term in the well-known equation of Forchheimer (1901):

$$\frac{\Delta p^2}{\Delta x} = Aq + Bq^2 \tag{4.7}$$

where 1/A is proportional to the permeability, B is a coefficient of turbulent head loss, and q is the gas flux.

Nonlinear behavior during air injection tests has been reported in the hydrology literature by Trautz (1984) and Schrauf and Evans (1986). Montazer (1982) interpreted air injection tests in the G-Tunnel at the Nevada Test Site individually for various flow rates and observed that, in most cases, the permeability decreased with increasing mean pressure. He attributed this behavior to "slip flow" (first reported by Klinkenberg, 1941), failing to recognize that it occurred primarily in the more permeable test intervals. Because slip flow results from a combination of low pressure and relatively small pore sizes, one would expect it to occur preferentially in the less-permeable intervals. We believe that the mechanism responsible for the decrease in permeability with pressure, observed by Montazer, is inertial flow. The permeability trends reported by Montazer (1982) are similar to those observed by us in a few high-permeability test intervals at the ALTS.

Equation (4.6) forms the basis for the so-called "deliverability test" used in the natural gas industry (Dranchuk and Kolada, 1968; De Sorcy, 1978). Deliverability tests are interpreted by plotting empirical Q_{sc} versus Δp^2 on log-log paper and determining the coefficients C and n by fitting Equation (4.6) to these data points. The purpose of the test is to estimate the rate at which gas can be produced under a given differential pressure. As C is theoretically unique, one should be able to obtain from it a unique value of k by means of Equation (4.4). Equation (4.6) offers an advantage over Equations (4.3) and (4.7) in that it covers flow regimes intermediate between linear (n = 1) and fully turbulent (n = 0.5). Therefore, we have initially adopted this approach to obtain unique k values for each of our test intervals. We now know, however, that this method of interpretation is inappropriate when n > 1, as is the case in most of the test intervals at the ALTS. The reason, as will become clear later, is that values of n larger than 1.0 are indicative of two-phase flow conditions in which the air permeability varies with saturation and, hence, with applied pressure. Application of the "deliverability" Equation (4.6) to the extensive injection test data base indicates that the relationship between the volumetric flow rate and the differential pressure square Equation (4.5) is well-represented by such a power model. Using the "deliverability" method to interpret multiple flowrate injection tests when n > 1.0 yields, however, k values that are too low by orders of magnitude. The deliverability equation is useful to study the dominant flow regime, but it should not be used to estimate air permeability for pressure values out of the range of applied field pressures.

Values of n greater than one imply an increase in apparent permeability with flow rate and pressure. This kind of permeability increase was observed by Wentworth (1944) during gas flow through thin cracks in lava rock. He attributed the phenomenon to an enhancement of permeability due to gas adsorption on the rock surfaces. Estes and Fulton (1956) observed a

similar enhancement in permeability when studying slip phenomena in sandstone and limestone cores. They attributed the increase in permeability with flow rate to experimental difficulties at higher liquid saturations due to redistribution of the liquid phase within the cores. Montazer (1982) briefly mentioned the possible effects of moisture on his permeability measurements. We suspect that the enhancement of permeability observed by these authors, and by us in numerous intervals at the ALTS, may be attributed to displacement of water, which partially blocks air movement, by air. Other mechanisms such as rock deformation, leakage around the packers, or gas diffusion are in our view less likely to act as the primary causes of this phenomenon at the ALTS. That two-phase flow causes n to attain values greater than 1.0 is strongly supported by our numerical experiments, described later. These experiments also reproduce the behavior observed in Figure 4.1b, where the pressure during a constant flow rate injection test first increases to a maximum and then decreases slowly toward a steady-state value.

Other behavior which suggests two-phase flow effects, and is reproduced in part by our numerical experiments, is that observed during a number of specially designed field experiments. Two types of experiments were conducted for this purpose. In the first type, air was injected at a step-wise increasing flow rate followed by a step-wise decrease back to the initial value. In the second type, air injection started at a very low flow rate and increased gradually to the maximum allowed by our equipment. Figure 4.5 shows the results of two experiments of the first type completed in boreholes Y2 and X2 at scales of 0.5 m and 1.0 m. The arrows in this figure indicate directions of change in the flow rate and mean pressure. For example, the test described in Figure 4.5a was completed under the following sequence of flow rates: 500, 750, 1000, 1200, 750, and 500 sccm. It is seen that equilibrium pressures during the flow rate increase are consistently larger than those during flow rate decrease. On the other hand, air permeabilities are smaller during flow rate and mean pressure increase than during their decrease. This hysteretic behavior has the following simple two-phase flow explanation. When air is injected into the medium, some water evaporates and some is forced out of larger voids into smaller voids during displacement by air. Increasing applied air pressure and flow rate increases the void space occupied by air and thereby enhances permeability to air. Except for evaporation, this is analogous to the porous plate method used to determine water release curves in the laboratory. When the flow sequence is reversed and the applied mean air pressure decreases, some water moves back toward the borehole. Some of it, however, remains in vapor phase, and some has difficulty returning from small to larger voids due to the ink-bottle effect and differences between receding and advancing capillary angles. Hence, the void volume available for air flow is larger than it was during the drying portion of the test, requiring lesser pressure to maintain a given flow rate and resulting in a larger permeability.

It is difficult to see how similar hysteresis might be caused by leaking equipment or gas diffusion. Although rock deformation is known to be hysteretic, the magnitude of such hysteresis is small compared to that observed at the ALTS. However, to fully settle this issue, there is a need to reliably measure changes in liquid saturation at the scale of the tests during injection. We strongly recommend that future research be conducted to develop methods for such measurement.

The second type of test was designed to cover as large a pressure and permeability range as allowed by the field equipment, with the hope of determining the critical air entry pressure at which drainage starts to occur. Pressure responses for two of these tests are depicted in Figure 4.6. Twelve flow rates were imposed during these one-meter scale tests in boreholes Z2 and W2A. We see that the pressure stabilized "rapidly" (within 100 to 200 minutes) at low flow rates, but took significantly longer to stabilize at higher flow rates. At small flow rates, the pressure increases monotonically toward stable values, whereas at larger flow rates the pressure first increases to a

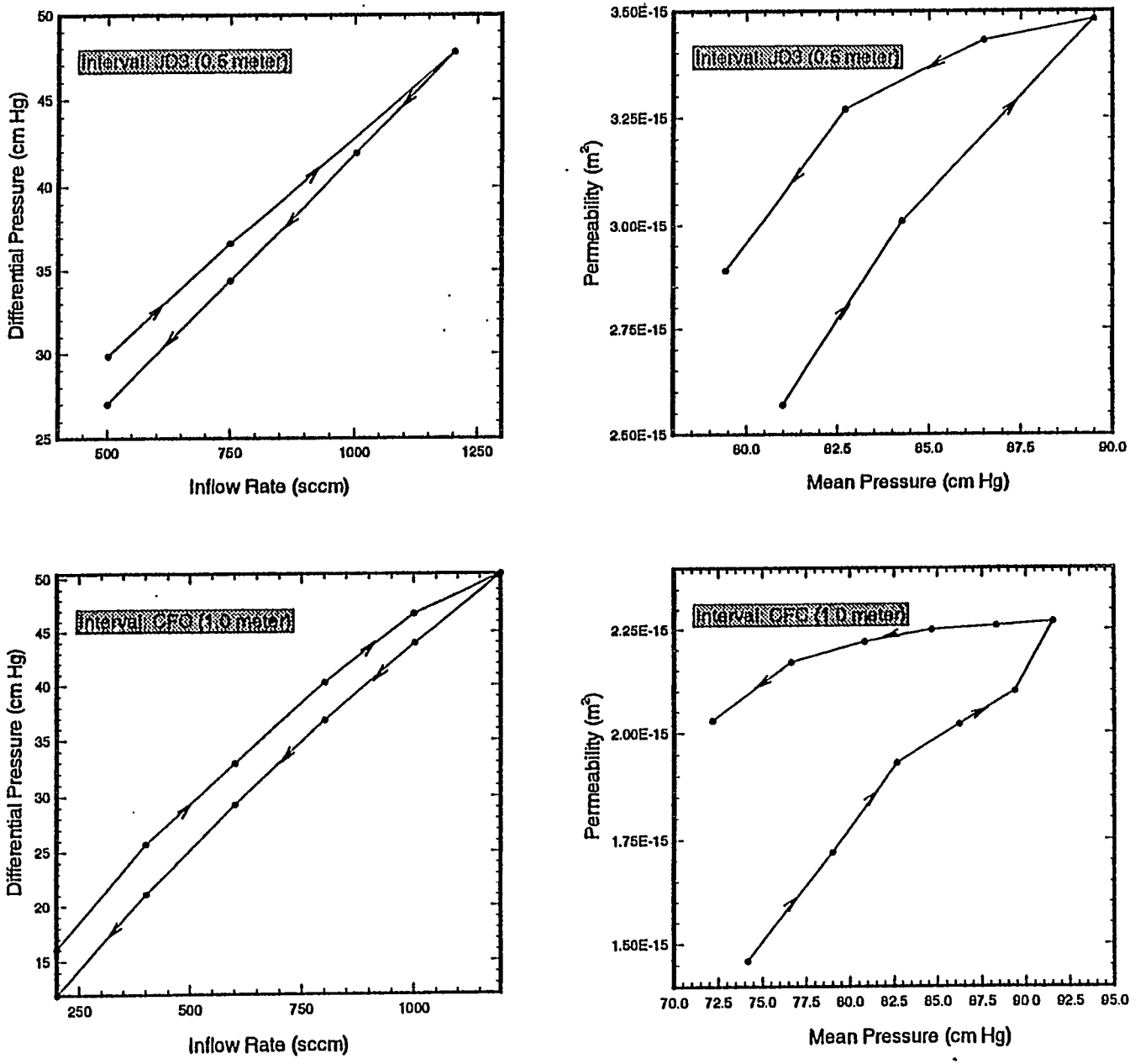

Figure 4.5. Hysteretic behavior of multi-rate tests

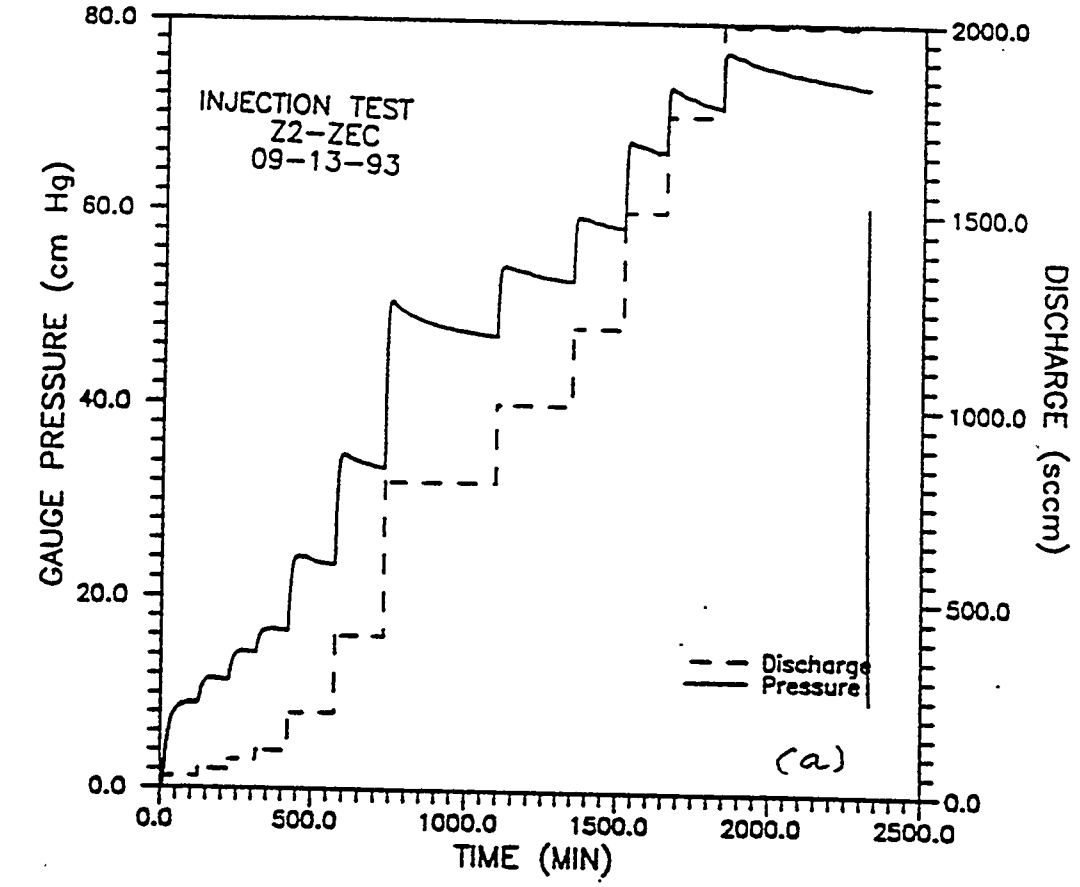

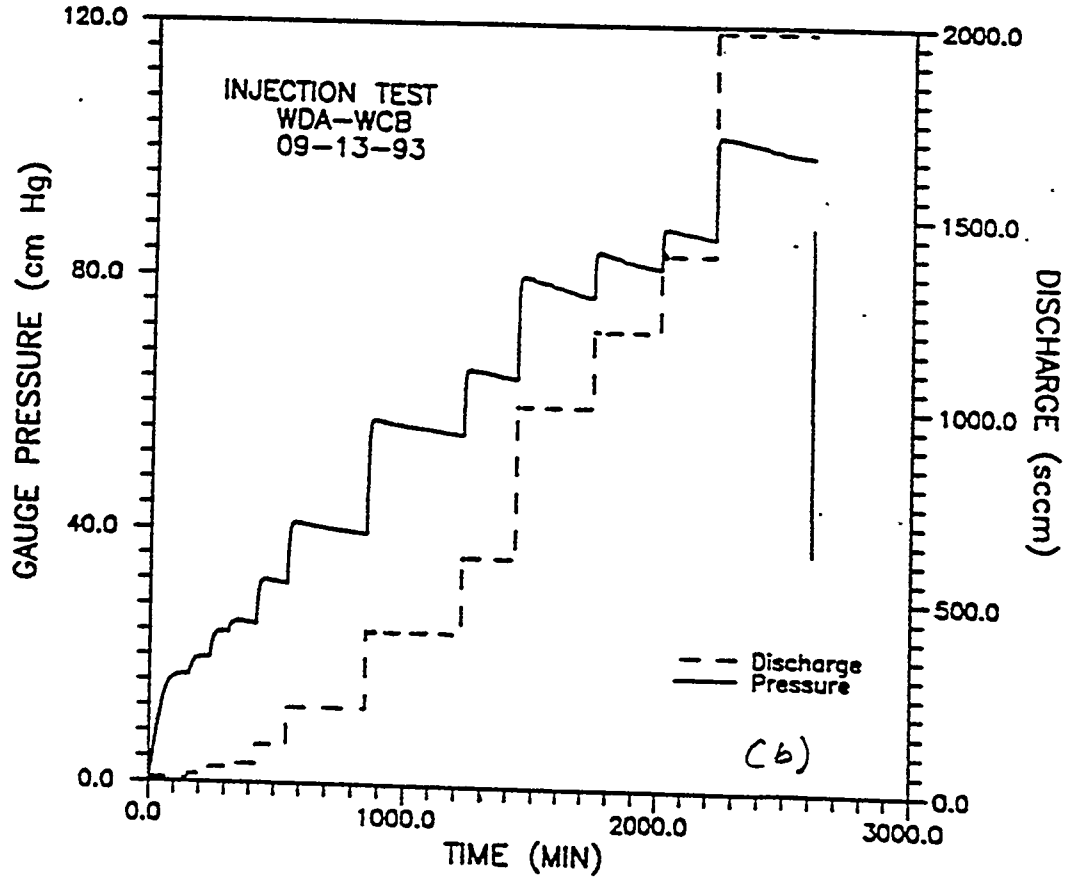

Figure 4.6. Pressure response of a multi-rate injection test

maximum and then decreases monotonically to a steady value. It appears that drainage occurs at all pressure levels but resistance to drainage varies in a nonlinear fashion, frustrating our hope of establishing a unique air entry value for the rock mass.

Figures 4.7 and 4.8 show plots of: (a) deliverability, (b) air permeability versus $\log(\Delta p^2)$, (c) log of air permeability versus Δp^2, and (d) log of air permeability versus $\text{Log}(\Delta p^2)$ corresponding to the above two tests. Plot (a) in these two figures shows that the deliverability equation fits the data quite well and results in an n parameter of 1.653 and 2.231 for these two tests, respectively. The plots of permeability versus $\log \Delta p^2$ flatten gradually to the left, suggesting an asymptotic approach towards values that correspond to ambient (undisturbed) levels of saturation. The plots of log air permeability versus Δp^2 flatten gradually to the right, suggesting an asymptotic approach toward log k values corresponding to maximum air pressure (or minimum water saturation). The log-log curves, however, make clear that log k corresponding to maximum air saturation cannot be determined by means of single-hole injection tests unless the ambient water saturation is very low.

Hence, air permeabilities from rocks partially saturated with water are lower than the permeability that controls single-phase air or water flow in the rocks. To determine these latter permeabilities, it may be necessary to conduct water injection tests.

The above discussion suggests that (a) deliverability plots and the corresponding n values may be used as a diagnostic tool to identify the prevalent flow regime during a test, inertial or two-phase; (b) plots of air permeability versus $\log (\Delta p^2)$ may be used to diagnose approach to k values at ambient saturation; (c) plots of log k versus Δp^2 may be used to diagnose approach to maximum k values at full air saturation; and (d) plots of log k versus $\log (\Delta p^2)$ may be used to ascertain the degree to which this asymptotic value has actually been reached. One thing is absolutely clear from our results: Conducting an air-injection test at a single pressure and/or flow rate (as is often done) is useless and misleading, yielding a k value that corresponds to unspecified air saturation somewhere between ambient and 100%. Equally unreliable are k values derived from steady-state formulae without ensuring that both the flow rate and the air pressure in the injection interval have stabilized as clearly depicted by the first two entries in Table 4.1. These tests did not reach pressure stabilization and result in overestimation of the permeability. The period required for stabilization depends on in-situ rock and fluid conditions as well as on the applied pressure. At the ALTS, pressure stabilization may at times require several hours.

In the following section, we describe some preliminary numerical simulations of single-hole air injection which support our interpretation of the field data.

4.3.2 Numerical Simulation of Air Injection

A three-dimensional axi-symmetrical, two-phase computer flow model was constructed to better understand the water displacement mechanism and observed behavior during air-injection tests. The model domain consists of a 15° wedge having a radius of 3.0 meters and a vertical extent of 3.0 meters (Figure 4.9). Due to flow symmetry, the wedge represents the upper half of a larger wedge extending 6.0 m vertically and including the entire injection interval (Figure 4.9a). The wedge is subdivided into 289 elements that increase geometrically in size with radial distance from the air source. Atmospheric constant pressure is maintained at all boundaries except the axis of the wedge, where a range of constant air-injection rates is imposed and along the bottom boundary where no vertical flow is assumed. The injection interval is 0.10 m in diameter and 0.3 meter long. Initially, air pressure is everywhere atmospheric and liquid saturation is uniform, varying from 0.05

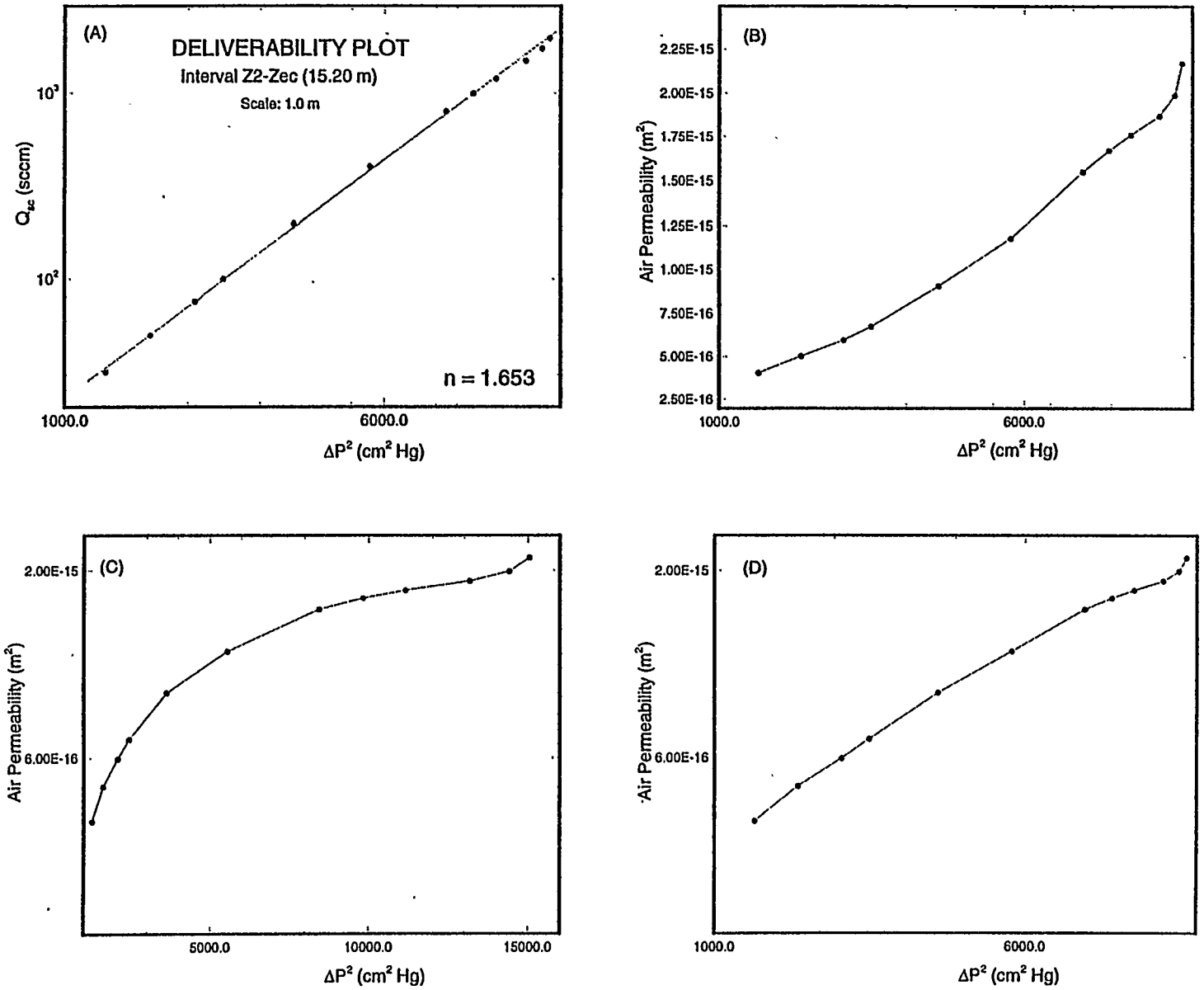

Figure 4.7. Interpretation of injection test in Z2-Zec

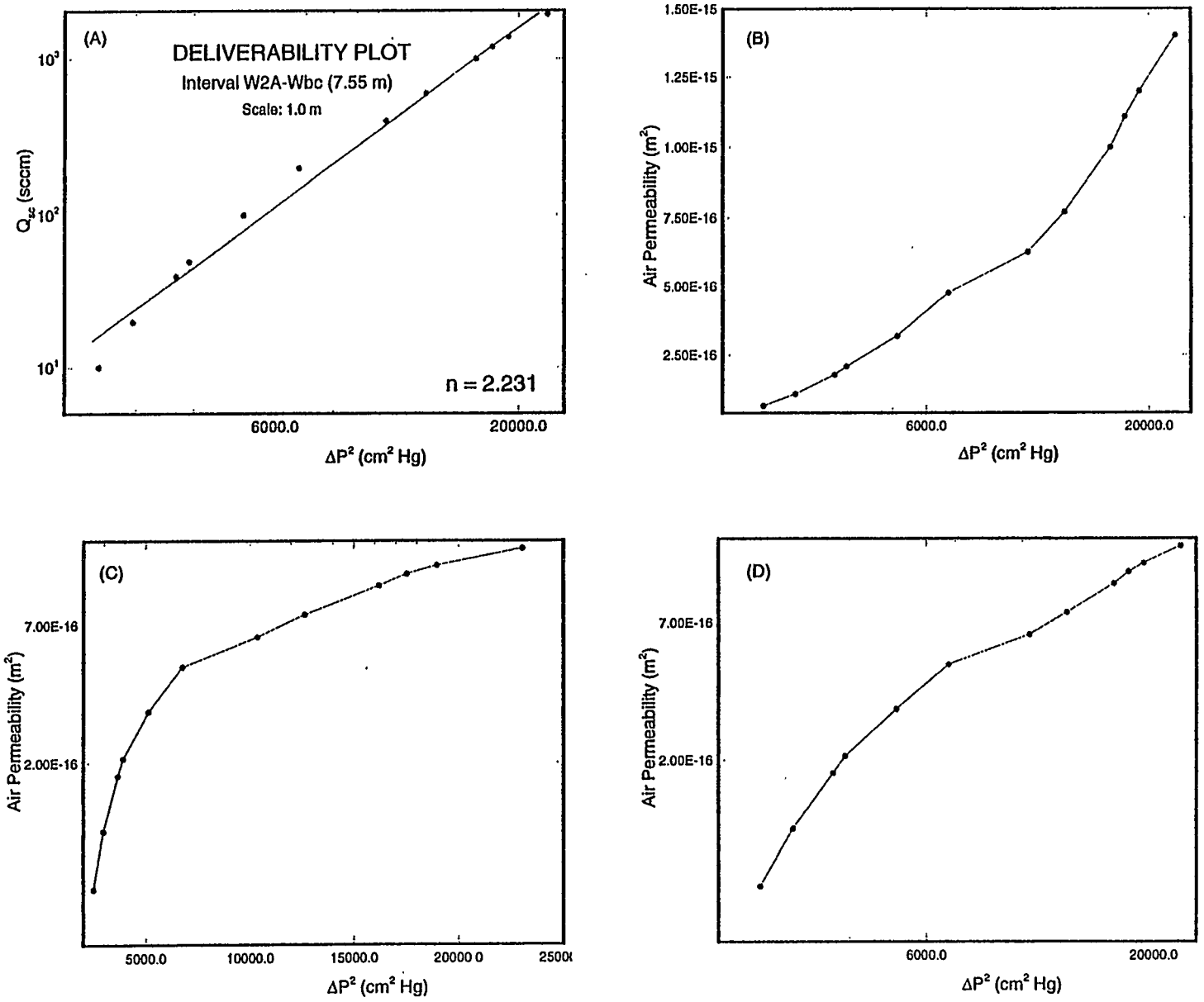

Figure 4.8. Interpretation of injection test in W2A-Wbc

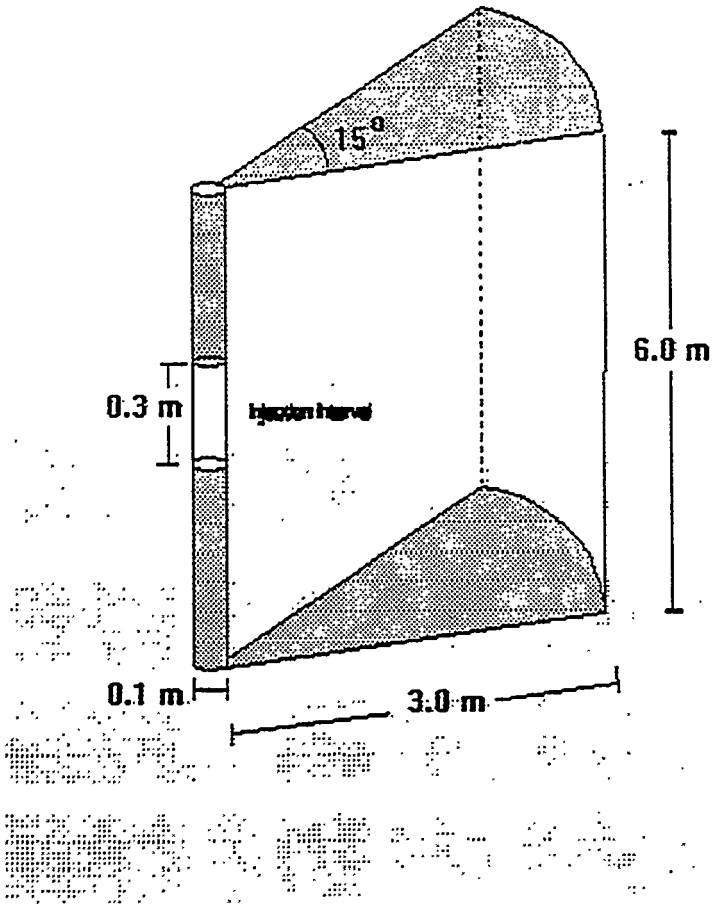

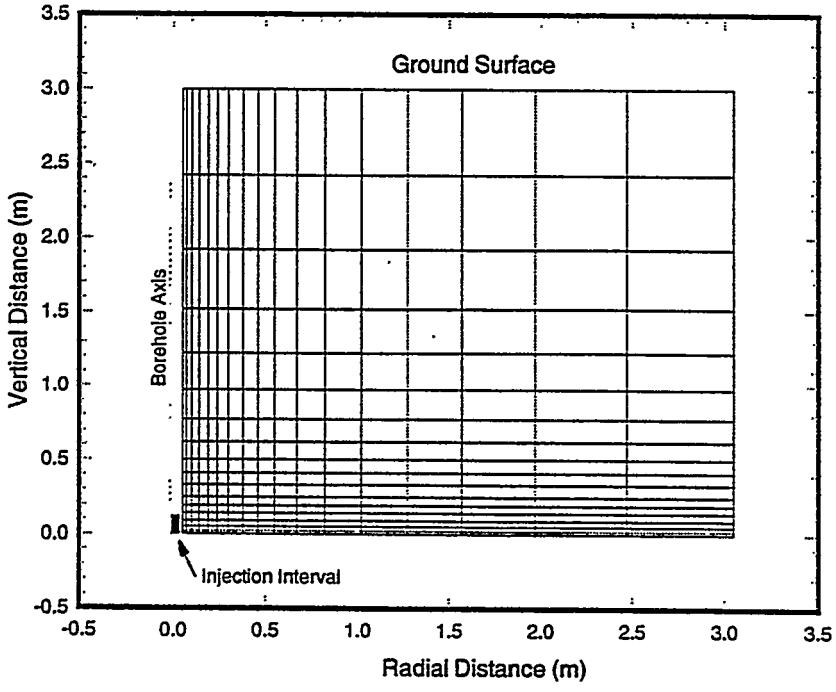

Figure 4.9. Simulation flow domain and computational grid.

to almost 1.0 m between simulations. The rock is homogeneous with hydraulic properties similar to those of a typical matrix core from the ALTS, as reported by Rhodes (1993). The relative air and water permeabilities as functions of water saturation, and saturation versus pressure head relationship, are given by the van Genuchten formulae (Parker et al., 1987):

$$k_{ra} = (1-S_e)^{1/2} (1-S_e^{1/m})^{2m}$$

$$k_{rw} = S_e^{1/2} [1-(1-S_e^{1/m})^m]^2 \qquad (4.8)$$

where:

$$S_e = [1+(\alpha\psi)^\beta]^{-m}$$

and k_{ra} is the relative air permeability, k_{rw} is relative hydraulic permeability, S_e is the reduced saturation, ψ is the suction, α and β are the van Genuchten parameters, and $m = 1-1/\beta$. Water release data from Rhodes (1993) yielded the following best fit parameters: $\alpha = 0.8653 \times 10^{-5}$ Pa^{-1}, $\beta = 1.36$ and a residual water content, θ_r, of 7.5×10^{-3}. We set porosity equal to 0.1754 (Rassmusen et al., 1989) and varied parameter β from 1.2 to 4.0. Based on our field data, we set saturated permeability equal to 25×10^{-16} m^2 in all simulations. Figure 4.10 shows how the relative permeabilities for water and air vary with β. The VTOUGH code (Nitao et al., 1992) was modified to include Equation (4.8) and used in our simulations.

Figure 4.11 presents computed air pressure and phase saturations (S_g and S_l; where $S_g + S_l = 1$ anywhere) in the immediate vicinity of the test interval for $\beta = 3.00$, and an initial water saturation $S_L^\circ = 0.75$. Nineteen injection rates ranging from 4.0×10^{-8} scms (standard cubic meter per second) to 1.33×10^{-5} scms were imposed during this simulation. This range of injection rates is representative of that used during our field injection tests. At the higher injection rates, the pressure response increases to a maximum and then decreases asymptotically to a steady value as do the field pressure responses in Figures 4.1b and 4.6.

This behavior is clearly a two-phase flow phenomenon. Initially, the imposition of elevated air pressure in the test interval causes capillary pressure in the adjacent rock to increase. This causes a reduction in liquid saturation and an increase in air permeability. Air now moves more easily from the test interval into the rock, and pressure in the former decreases.

While the above phenomenon can be reproduced numerically, we presently do not have at our disposal analytical formulae that would mimic the observed transient pressure response in the test interval due to two-phase phenomena. This means that we do not, at present, have appropriate analytical tools to interpret the transient (buildup and recovery) portions of our test pressure records. It is possible that, with time, we will learn how to interpret these records with the aid of numerical models such as VTOUGH or newly developed analytical solutions. In the meantime, we shall continue focusing our attention on the steady-state part of the available test record.

The spatial distribution of liquid saturation and pressure at the end of the last injection period are shown in Figure 4.12. A nearly spherical desaturation bulb is seen to have developed around the injection interval due to the relatively short length of the latter. When comparing the flux of the liquid phase with that of the vapor phase, one finds that initially water movement in the bulb

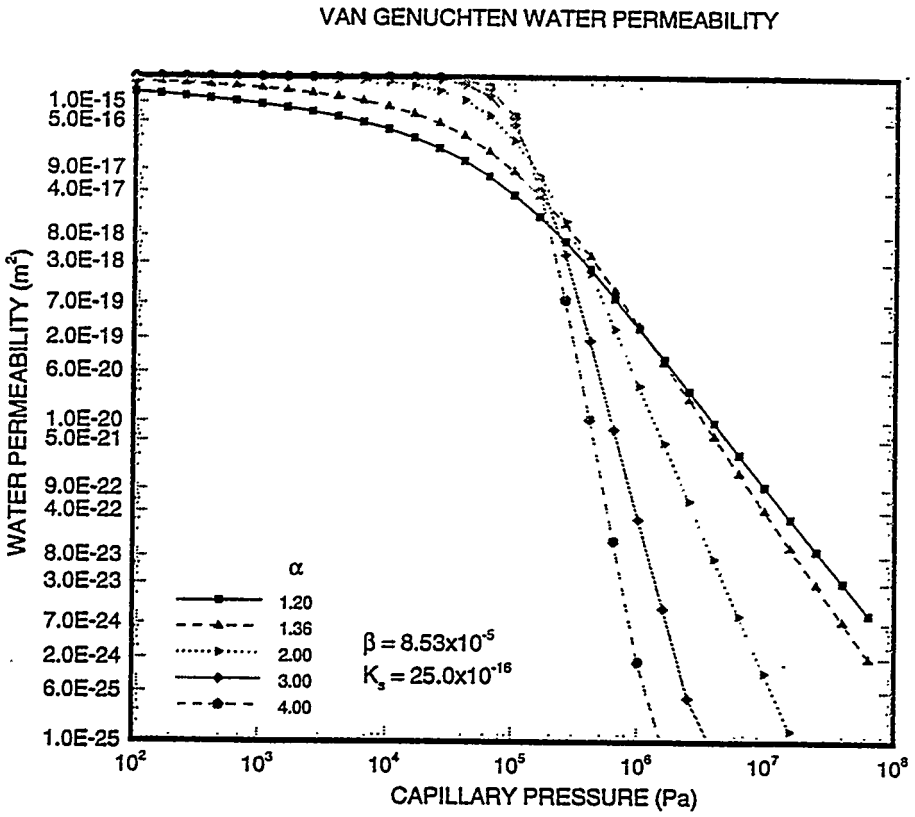

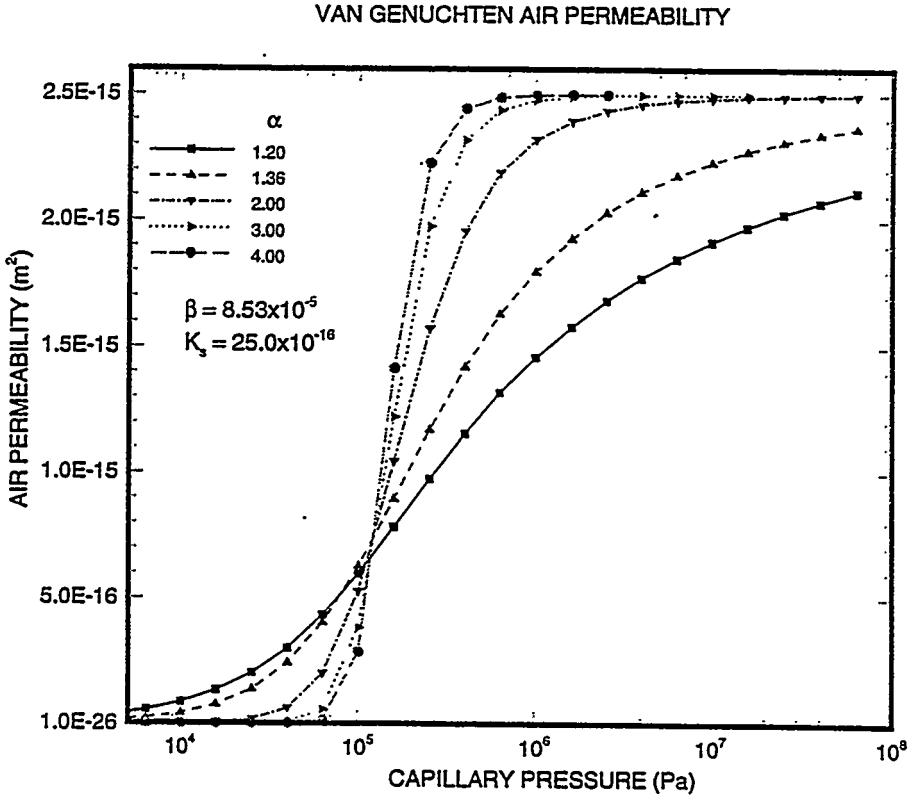

Figure 4.10. Relative air and water permeability curves

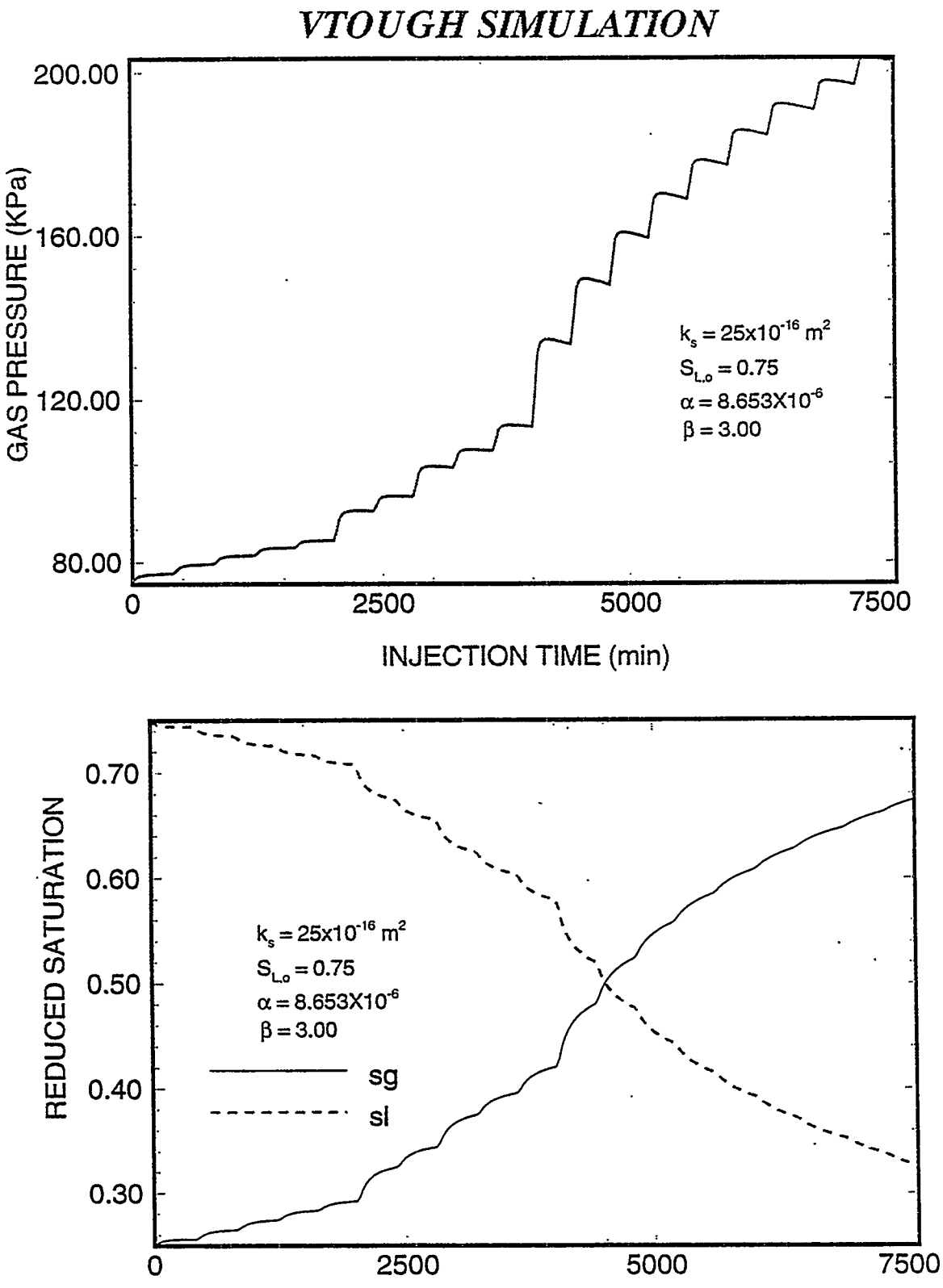

Figure 4.11. Air pressure and saturations as a function of time

VTOUGH-SIMULATED LIQUID SATURATION

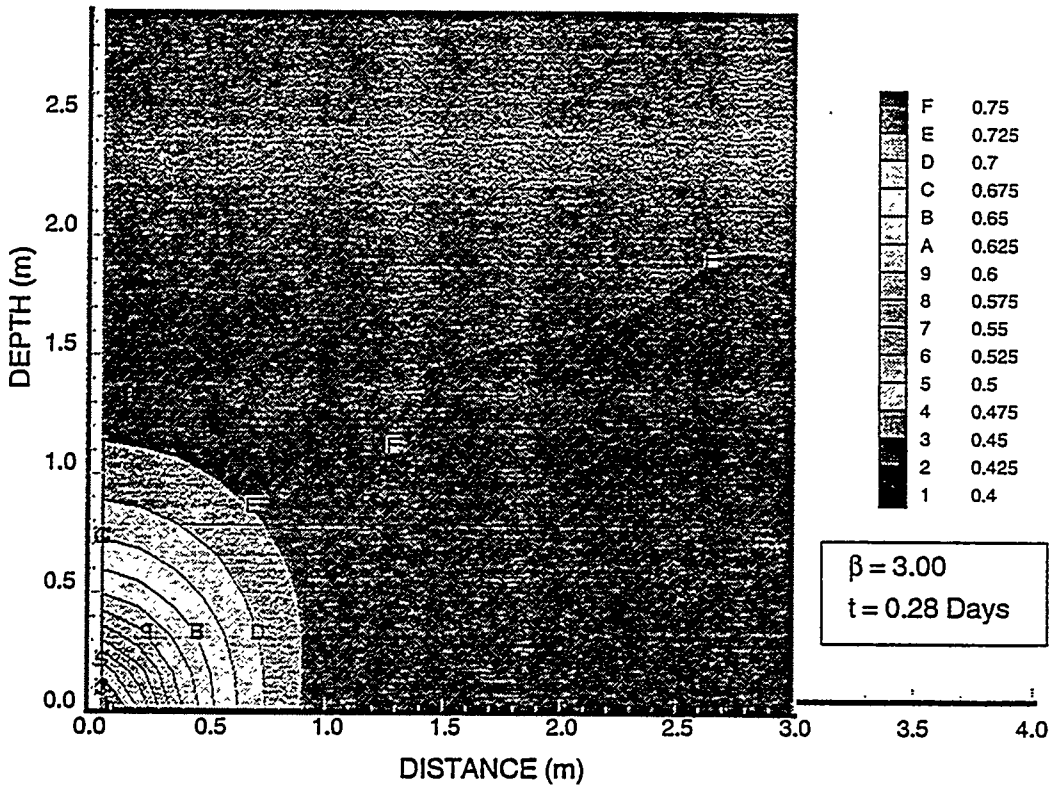

VTOUGH-SIMULATED AIR PRESSURE

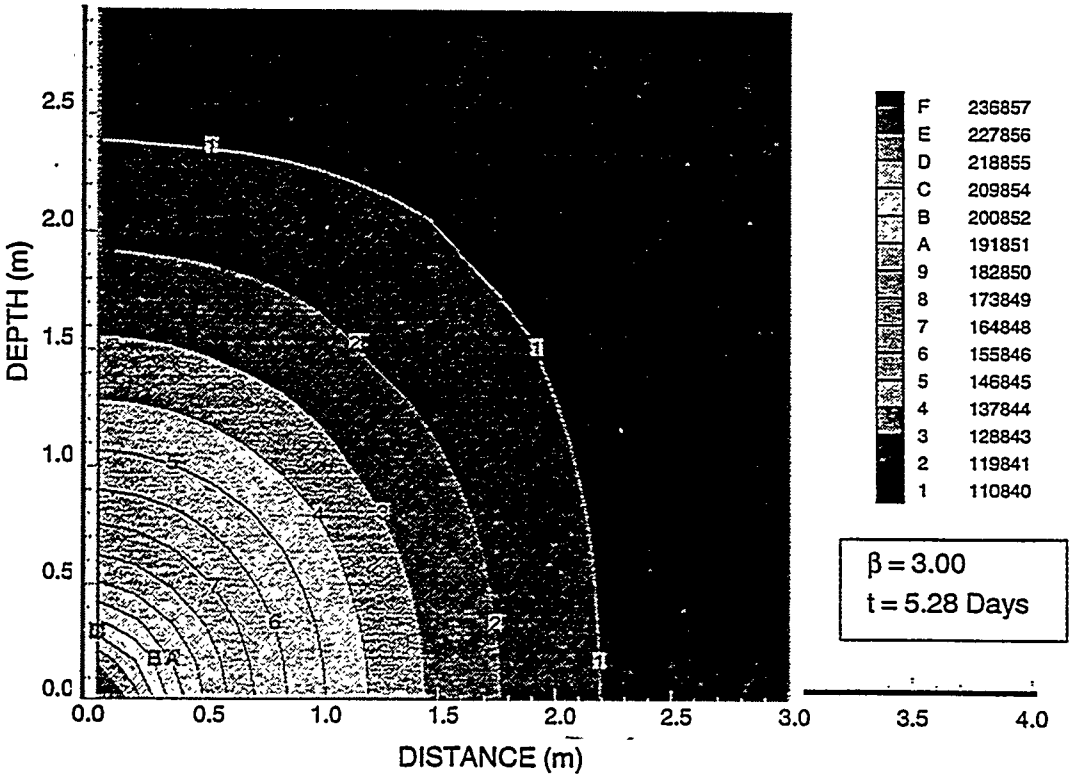

Figure 4.12. Distribution of liquid saturation and pressure after 5.28 days of injection

results mainly from displacement by air, the effect of evaporation being relatively minor. With time, the porous medium dries out near the borehole where vapor flux now becomes important and countercurrent liquid flow may occur due to capillary pressure gradients. At early times, the combination of these two mechanisms, evaporation and water displacement by air, results in drying around the injection source. Eventually, a state of quasi-equilibrium develops between evaporation and vapor flow on one hand, condensation and liquid flow on the other hand. During these simulations, a problem with the mass balance calculations in VTOUGH was encountered and reported to J.J. Nitao. Once this problem is resolved, a more accurate calculation of the magnitudes of these water-moving mechanisms will be prepared.

Figure 4.13 shows a deliverability plot derived from simulated steady-state pressures and flow rates, using Equation (4.6). The deliverability plot can be closely approximated by a straight line with a slope (n) equal to 1.32. This confirms that a value of n greater than one is indicative of the ease with which water is displaced by air as the injection pressure increases and thus the change in permeability with applied air pressure. Computed air permeabilities using Equation (4.2) are plotted on log scale versus Δp^2 in Figure 4.14a (circles), and on an arithmetic scale versus log (Δp^2) in Figure 4.14b. Also displayed are the air permeabilities computed with the van Genuchten equation (squares) based on simulated capillary pressure in the immediate borehole vicinity. The borehole vicinity undergoes the maximum amount of drying; thus, application of the van Genuchten equation yields the maximum permeability within the flow domain. The computed air permeabilities are consistently lower than the van Genuchten estimates but approach the latter asymptotically as Δp^2 decreases. This asymptotic value represents air permeability at ambient saturation. The observed difference between the circles and squares results from the fact that Equation (4.2), in contrast with the local van Genuchten estimate, provides an average estimate of permeability near the test interval. To see more precisely what is the meaning of permeability obtained by our test procedure, we plotted in Figure 4.15 profiles of simulated air pressure and air permeability versus radial distance from the injection interval for ten of the 19 injection rates. Permeabilities obtained using Equation (4.2) are indicated by open circles. It is clear that Equation (4.2) does not yield the maximum air permeability near the injection interval but somewhat lower values as found at a short distance into the rock. This distance is seen to increase very slightly with increased test flow rate.

Even though the circles in Figure 4.14 appear to tend asymptotically to the maximum permeability as Δp increases, they lie much below this value, and the maximum log permeability cannot be attained with workable applied pressure. On the other hand, the simulated behavior is very similar to that observed in the field and lends strong support to our test methodology and interpretation of test results.

4.3.3 Klinkenberg Effects

The Klinkenberg effect has been put forth to explain the observed behavior of laboratory (Rasmussen, 1993) and field (Montazer, 1982) air permeability variations with pressure. As part of our initial literature survey (Guzman, 1994), we summarized the findings of Klinkenberg (1941) concerning gas permeability variations in the laboratory. He reported that such variations can be represented by the relationship:

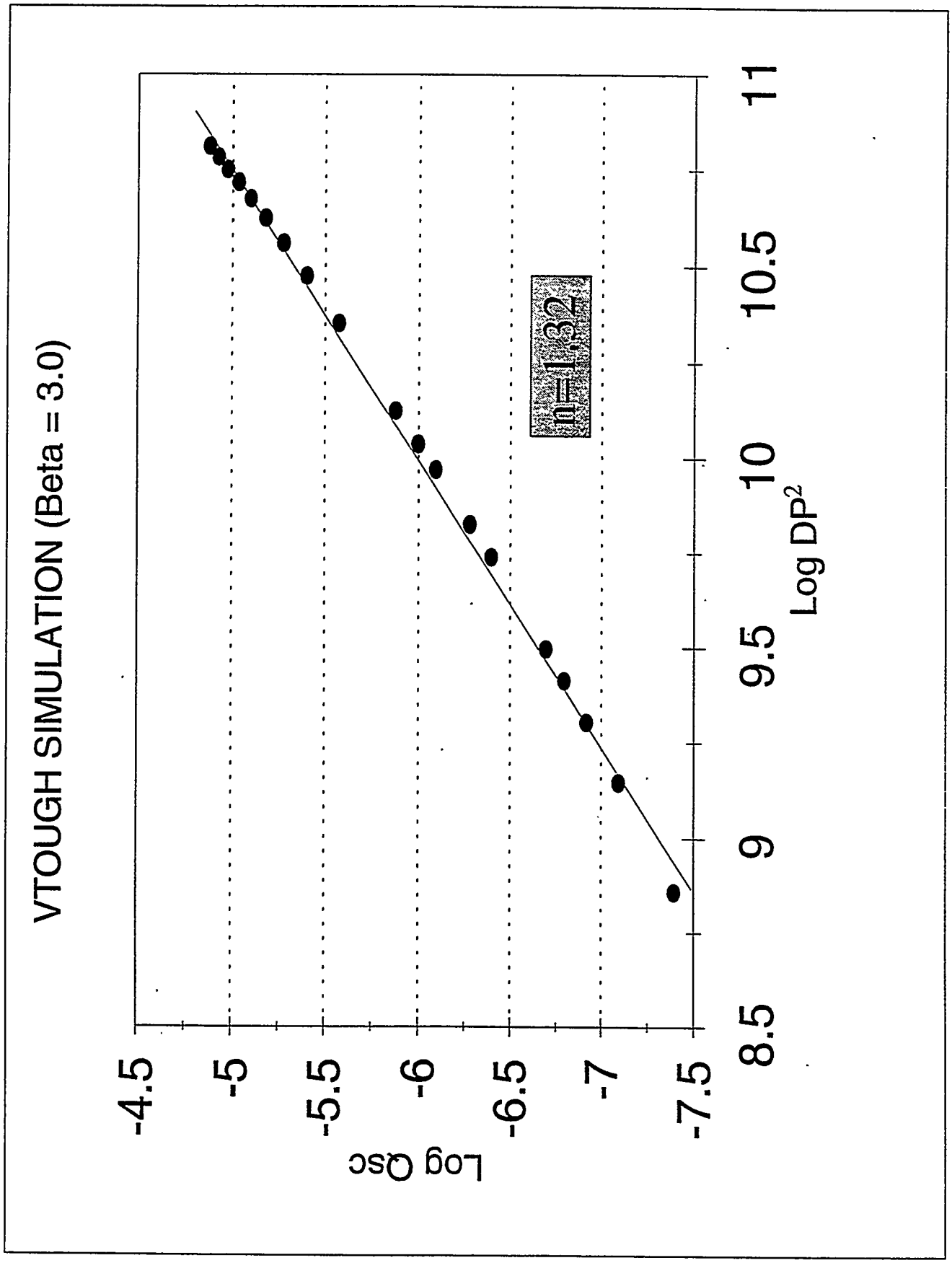

Figure 4.13. Deliverability plot for simulated air injection test

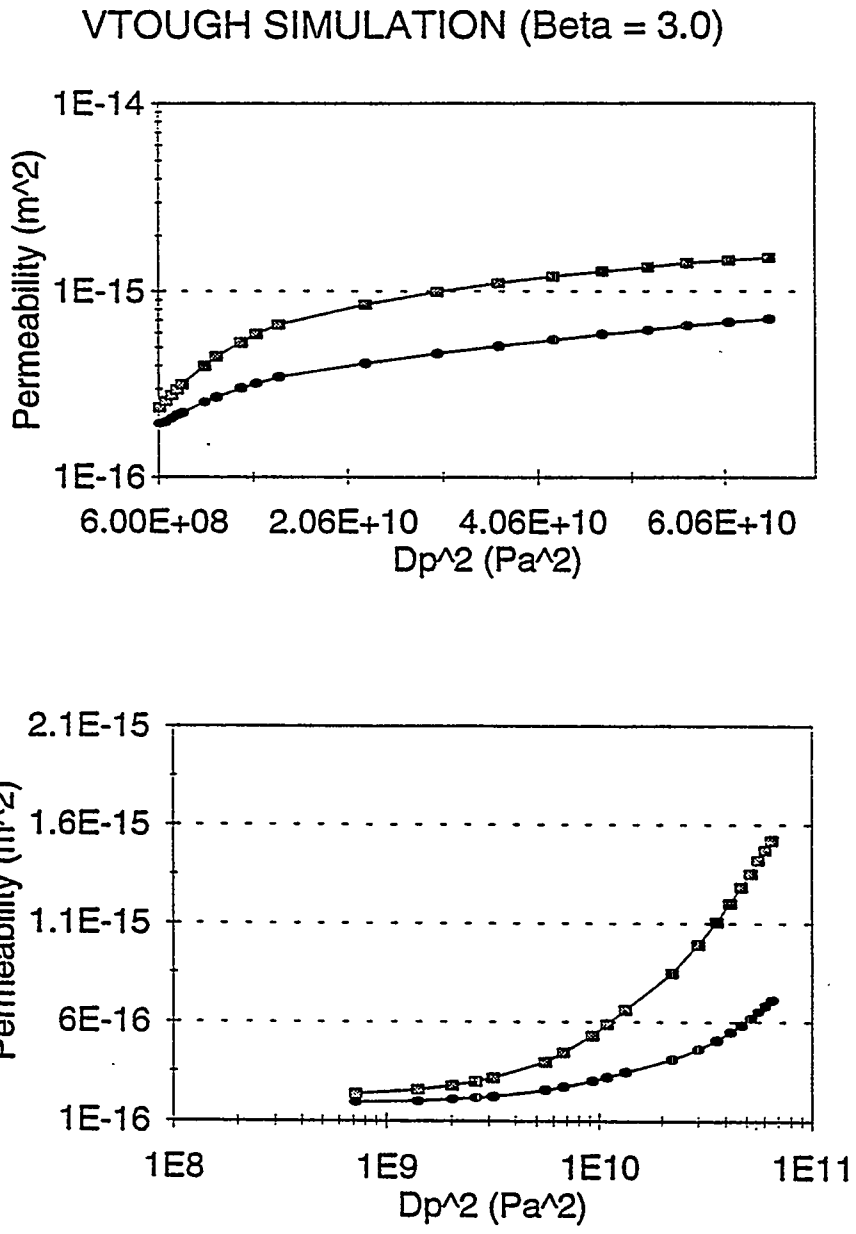

Figure 4.14. Permeability as a function of injection pressure

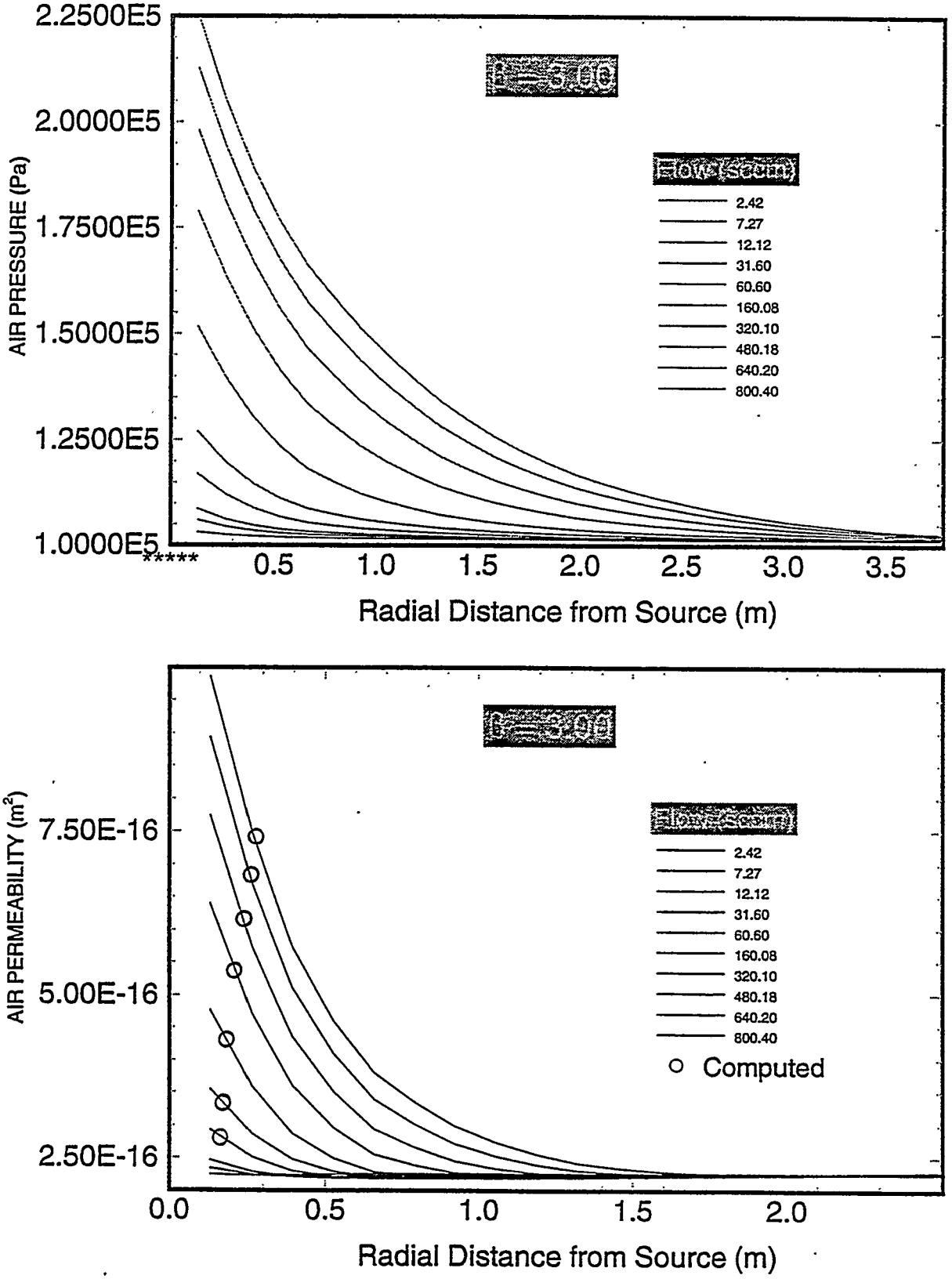

Figure 4.15. Simulated permeability profiles versus analytical estimates

$$k_a = k_\infty \left(1 + \frac{b}{p_m}\right) \tag{4.9}$$

where k_a is the apparent (Klinkenberg) gas permeability, p_m is the mean pressure across the sample, b is a parameter (now called the Klinkenberg parameter), and k_∞ is the gas permeability at very high mean pressure where the gas behaves more like a liquid. We found it surprising that the Klinkenberg permeability in Equation (4.9) is not a function of the pressure gradient across the sample or air saturation. We would expect that, even if the mean pressure was held constant, different flow regimes might develop under different pressure gradients. As the pressure gradient is increased, the flow should vary from viscous, through visco-inertial, through inertial to turbulent. To test this, we conducted laboratory experiments (not as part of this NRC contract) to study the dependence of k_a on the imposed gradient of square pressure during air permeability tests on samples of a loamy fine sand. The results support Klinkenberg's equation whenever the gradient across the sample is kept constant at a given saturation. In these experiments, b oscillated between 0.773 and 1.020 for liquid saturations less than or equal to 20% (including oven-dried samples) and increased drastically to values between 1.929 and 2.001 for a liquid saturation of 25%. At the ALTS, no evidence for the Klinkenberg effect has been noticed during the injection tests. It appears that inertial and water displacement effects overshadow slip flow.

4.4 EXPERIMENTAL RESULTS AND PRELIMINARY STATISTICAL ANALYSIS

Table 4.2 gives an example of the summary of steady-state data collected during a multiple-rate injection test. The entries in this table refer to interval identification name (see Appendix A), flow rate in standard cubic centimeter per minute (sccm), atmospheric pressure (cm Hg), permeability (m^2), mean pressure (cm Hg), mean pressure square (cm^2 Hg), and the deliverability estimates from the experimental data. The deliverability parameters (C and n, Equation (4.6)) are obtained through least squares. Their error of estimation (Sc and Sn) and the resulting χ^2 are also reported in this table. One sees that, for n values larger than unity, the difference between the deliverability estimate of k by means of Equation (4.6) and that estimated from Equation (4.2) becomes significant, indicating the failure of Equation (4.6) to provide an accurate estimate of k.

Due to the strong pressure dependence of the permeability, sample statistics presented in this section and summarized in Table 4.3 are computed using the arithmetic mean of the minimum and maximum permeabilities determined for each test interval. Note that 10^{-15} m^2 equal to about 1 milli-Darcy. Histograms and normal probability plots for the permeability data were prepared and showed that, as usual, k does not follow a normal distribution. A clear example of such non-Gaussian behavior of k is provided in Figure 4.16 for 0.5-m scale data. From now on, we consider only the behavior of ln k, the natural logarithm of k. We shall refer to these as log permeabilites.

More than 45 injection rates were imposed on the nine 3.0-meter test intervals in borehole Y2. The corresponding permeabilities ranged from 1.425×10^{-16} to 2.867×10^{-14} m^2. Figure 4.17 shows how these 3-meter permeability estimates vary with position along the borehole. The data are presented in the form of rectangles which delineate depth intervals and ranges of computed permeabilities. Also shown are the minimum (solid curve) and maximum (light curve) pressures applied during each test. The data vary over more than two orders of magnitude and show no obvious systematic trend (consistent increase or decrease) with position along the 45° borehole. However, there is a suggestion of periodicity which we shall see becomes accentuated as the length of the tests interval decreases. The sample mean and variance of the 3.0 meter log permeability

Table 4.2. Sample of Steady-State Data Summary from Injection Tests on Borehole Y2.

Test ID	Q(sccm)	P_{atm}(cmHg)	P_{ss}(cm Hg)	k(m^2)	Δ P^2	Mean P	Mean P^2
jda0219a	502.00	65.70	6.220	0.954E-14	856.0	68.81	97.41
jda0219b	951.50	65.650	11.350	0.958E-14	1619.08	71.32	101.19
jda0219c	1402.20	65.60	15.850	0.980E-14	2330.74	73.52	104.58
jda0219d	1904.10	65.580	20.740	0.985E-14	3150.41	75.95	108.41
ID = jda Num= 4 C = 0.493E+00 Sc = 0.0635 N = 1.025 Sn = 0.085 Chi2= 0.001 Tm =15.70					Del. Estimate of K (m^2) = 0.8031E-14		
jdb0225a	755.00	65.660	33.070	0.227E-14	5436.38	82.20	118.57
jdb0225a	100.80	65.630	42.220	0.224E-14	7324.33	86.74	126.25
jdb0311c	170.00	65.60	54.910	0.272E-14	10219.3	93.05	137.21
ID = jdb Num= 3 C = 0.109E-01 Sc = 1.6536 N = 1.292 Sn = 0.1855 Chi2= 0.069 Tm =16.96					Del. Estimate of K (m^2) = 0.1779E-15		
jdc0325a	399.50	65.060	57.590	0.607E-15	10810.22	93.85	138.84
jdc0325b	499.50	65.070	63.230	0.670E-15	12226.79	96.68	143.86
jdc0325c	620.70	65.10	71.450	0.707E-15	14407.89	10.82	151.27
ID = jdc Num= 3 C = 0.292E-03 Sc = 1.2992 N = 1.523 Sn = 0.1378 Chi2=0.008 Tm =17.91					Del. Estimate of K (m^2) =0.4786E-17		

Table 4.3. Summary Statistics of Steady-State Permeability Data in m^2.

Borehole ID	Scale of Measurement (m)	Number of Samples	k			ln k		
			Mean (10^{-15})	Median (10^{-15})	Variance (10^{-30})	Mean	Median	Variance
Y2	0.5	54	3.01	0.85	110.2	-34.75	-34.70	2.25
	1.0	28	5.00	1.38	147.9	-34.47	-34.22	3.07
	3.0	9	4.30	1.07	60.4	-34.04	-34.47	1.99
X2	1.0	23	6.41	1.65	342.3	-34.19	-34.04	2.25
Z2	1.0	24	9.13	0.36	363.4	-34.55	-35.55	5.38
W2A	1.0	20	1.72	0.77	4.2	-34.64	-34.80	1.49
V2	1.0	21	2.12	0.11	55.8	-36.21	-36.71	3.87

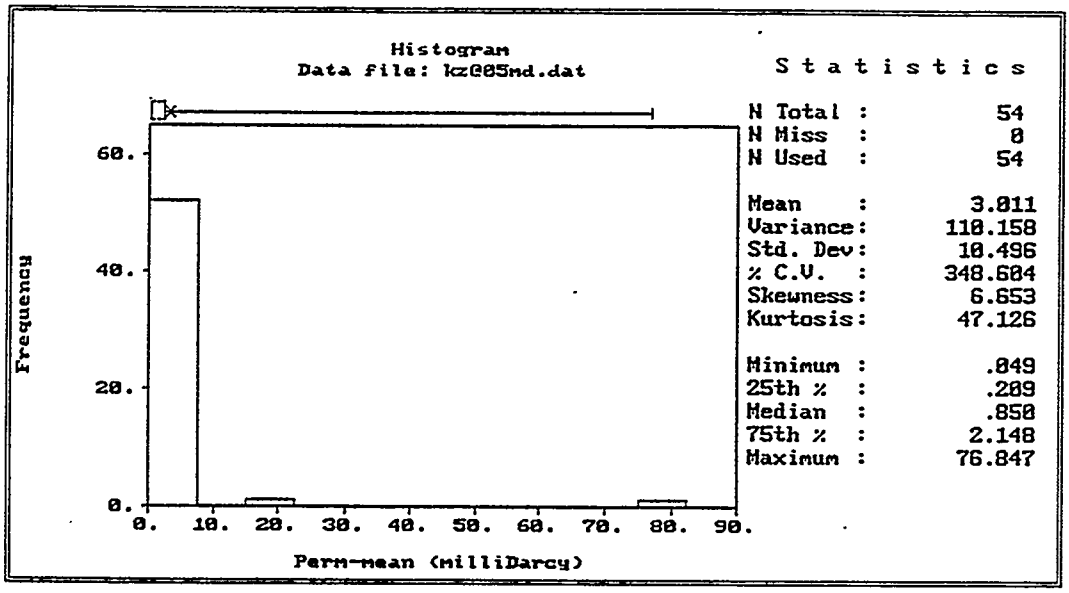

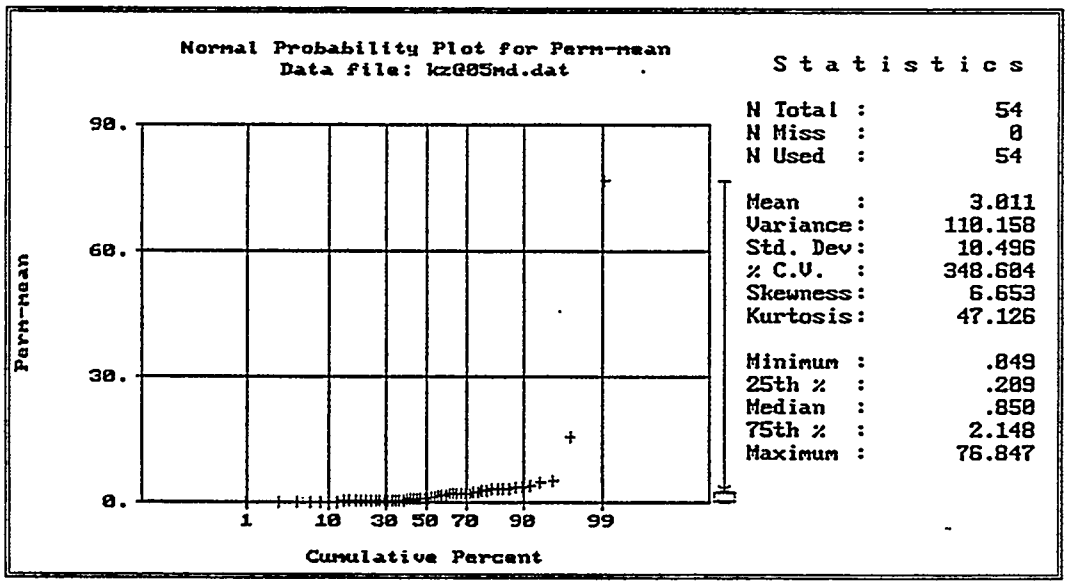

Figure 4.16. Statistics for data collected at a 3-meter scale for borehole Y2

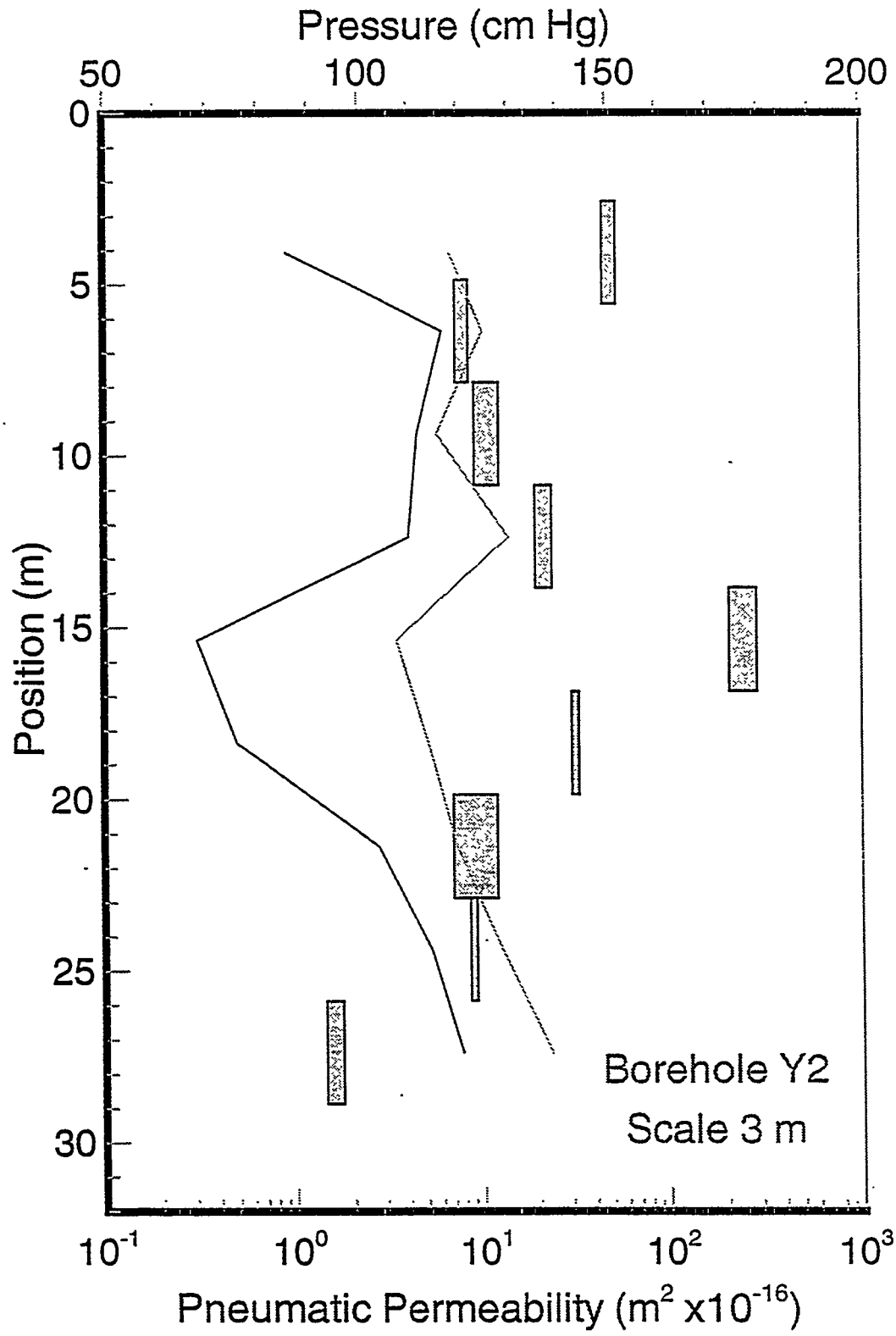

Figure 4.17. Spatial distribution of permeability at a 3-meter scale along borehole Y2

are -34.04 and 1.99, respectively. Notice that, because variability with pressure within each interval is much smaller than spatial variability from one interval to another, the former has only a minor adverse effect on these statistics. The same will be true about the statistical and geostatistical analyses given below.

Permeability measurements in borehole Y2 at a scale of 1 meter involved more than 105 individual flow rates applied to 28 intervals. The permeabilities range from 5.627×10^{-17} to 4.943×10^{-14} m^2. Permeability as a function of position and its variation with injection pressure are shown in Figure 4.18. The permeability data span three orders of magnitude and exhibit a conspicuous periodicity along the 45° borehole. The mean of the log-transformed permeability is -34.47 and its variance is 3.07.

Measurements of permeability in borehole Y2 were also made at a 0.5-meter scale. Here, about 245 individual injection rates were imposed along 54 intervals. Permeabilities as functions of position and injection pressure are shown in Figure 4.19. They range over more than three orders of magnitude from 4.411×10^{-17} to 8.182×10^{-14} m^2 and again show a distinct slow periodic variation with position along the 45° borehole. The sample mean of ln k is -34.75 and their sample variance is 2.25.

It is clear from Figures 4.17, 4.18, and 4.19 that, as the length of the test interval decreases, the level of detail revealed by the permeability data about rock heterogeneity increases. Both the amplitude and the frequency of spatial variations in permeability increases as the test interval decreases. Even though the rock is discontinuous as evidenced by the fracture traces in Figure 4.20, this is not reflected directly in the measured permeability values. The fracture trace data were obtained by Evans (1987) by inspection of oriented core and the use of subjective judgement as to which fractures are likely to conduct fluid. The highest permeability at position 16.5 m in Figure 4.19 indeed corresponds to a known, near horizontal fracture at a depth of about 12 meters in borehole Y2. Nevertheless, many other fractures originally considered conductive are associated with much lower permeabilities. There does not seem to be a direct correlation between fracture occurrence and permeability in borehole Y2, although high permeabilities are expected to be associated with some degree of fracturing.

Four additional 30-meter boreholes (X2, Z2, W2A, and V2) have been tested at a scale of 1 meter. Permeabilities as functions of pressure and position along these boreholes are shown in Figures 4.21 through 4.24, respectively. The boreholes are oriented as follows: X2 45° E-W (where the angle is measured with respect to the horizontal, top of casing is toward E, bottom toward W), Z2 45° W-E, W2A 45° N-S, and V2 is a 90° borehole (see also Figure 4.20). Two and six intervals are yet to be tested in boreholes W2A and Z2, respectively. A comparison between permeabilities on borehole X2 and fracture locations (Figure 4.20a) does not suggest an obvious correlation except perhaps between the highest permeability detected at about 11 m and a reported "major" fracture at the same position. The sample mean and variance of ln k in borehole X2 are -34.19 and 2.25, respectively. Figure 4.20c suggests the existence of highly fractured clusters (originally considered "major flow paths") along the length of borehole Z2. The highest measured permeabilities in Z2, encountered at 13.5, 17.5, and 22.5 m along the borehole (Figure 4.23), do not seem to coincide directly with these clusters. Similar comments apply to other boreholes tested. We conclude that a visual identification of open fractures is a poor predictor of permeability, which must therefore be measured directly by means of pneumatic (or hydraulic) tests.

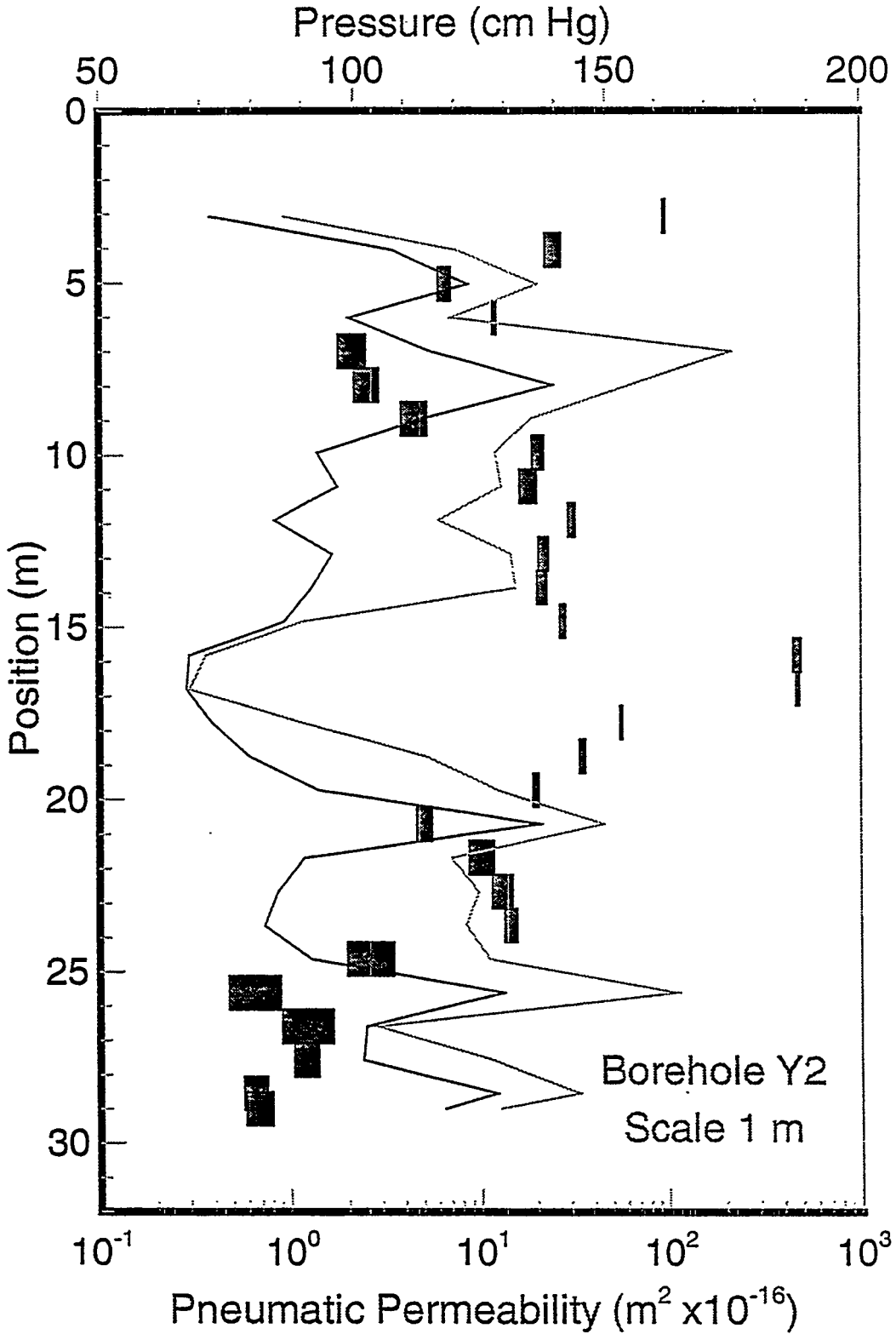

Figure 4.18. Spatial distribution of permeability at a 1-meter scale along borehole Y2

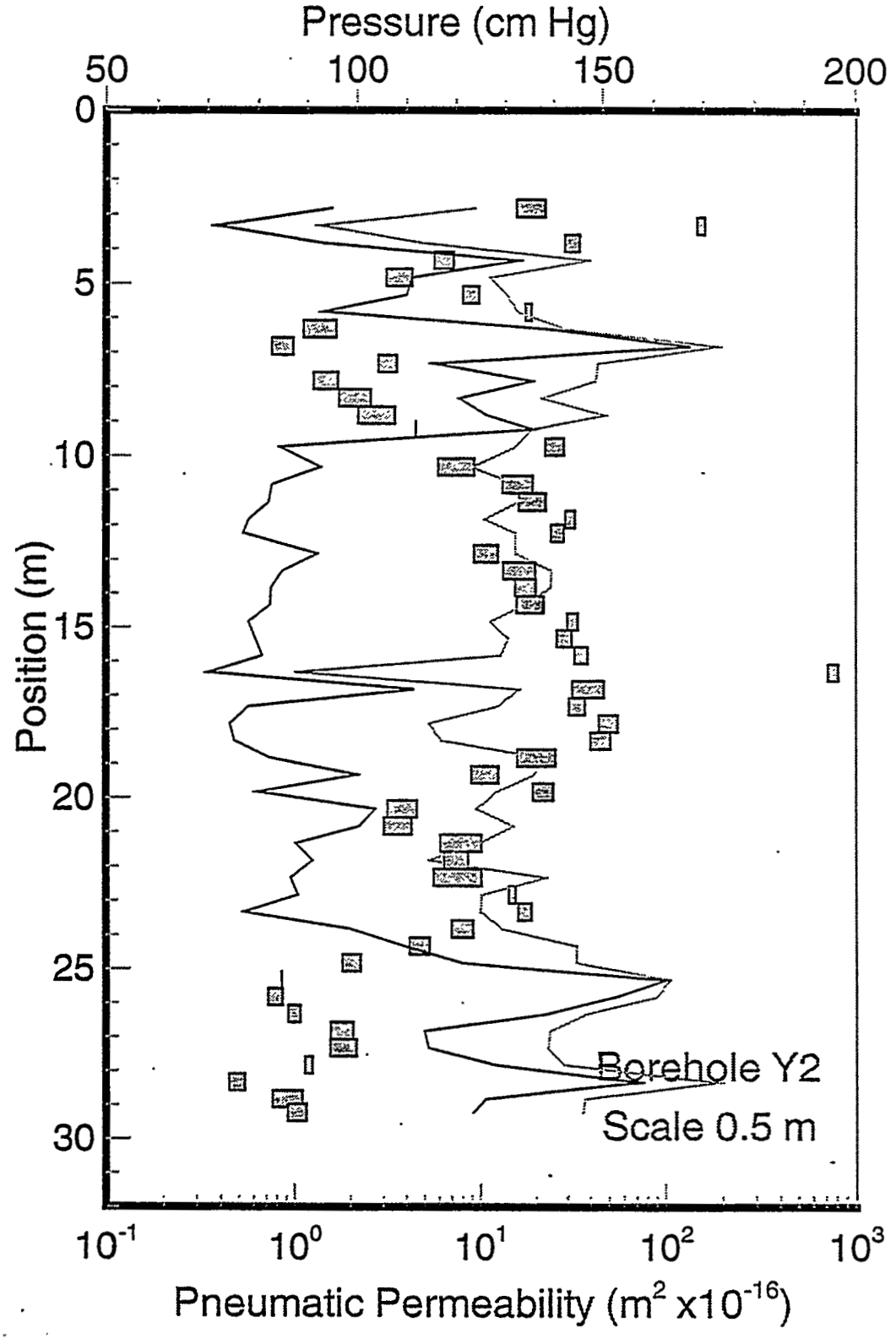

Figure 4.19. Spatial distribution of permeability at a 0.5-meter scale along borehole Y2

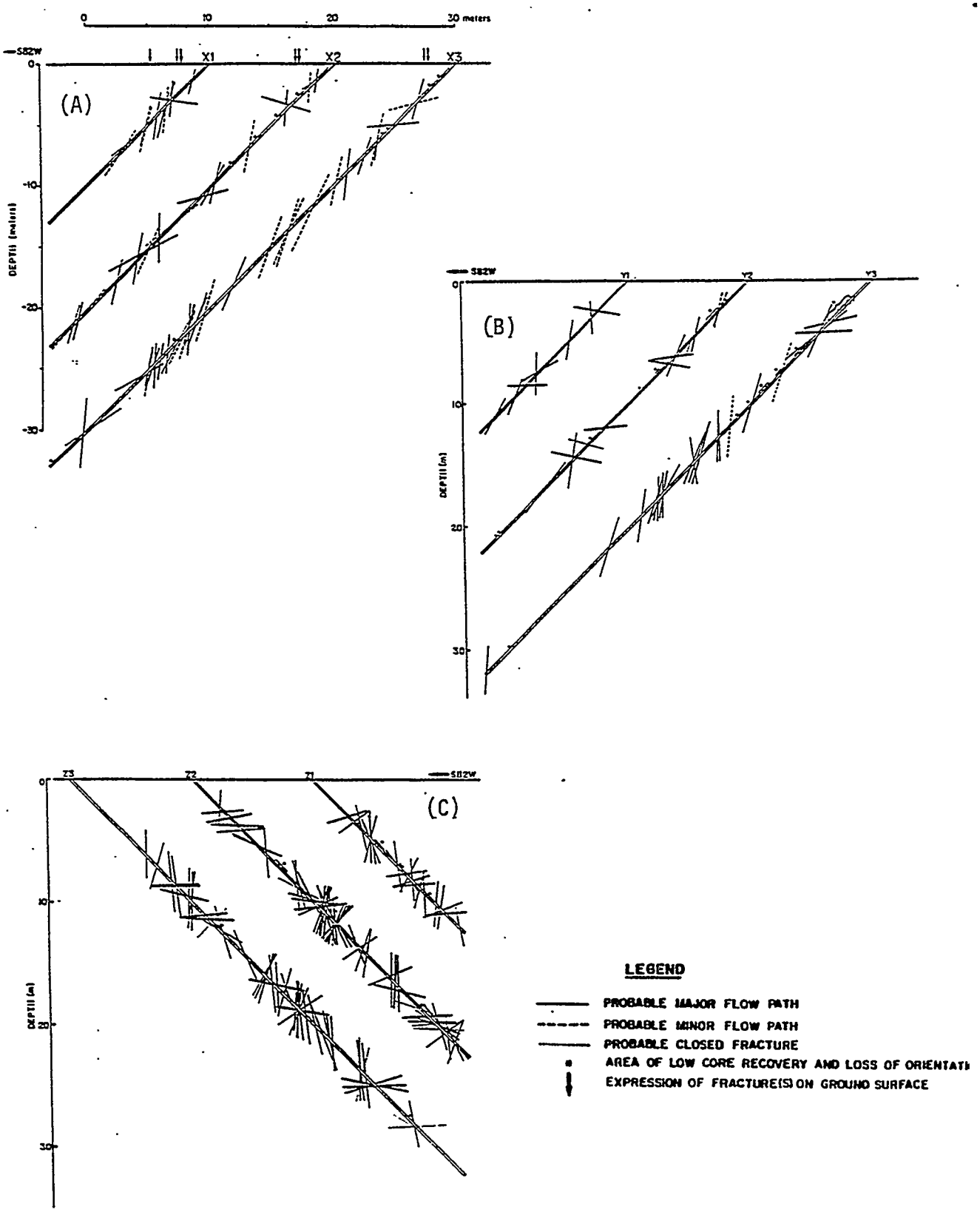

Figure 4.20. Fracture locations and orientation for boreholes series X, Y, and Z

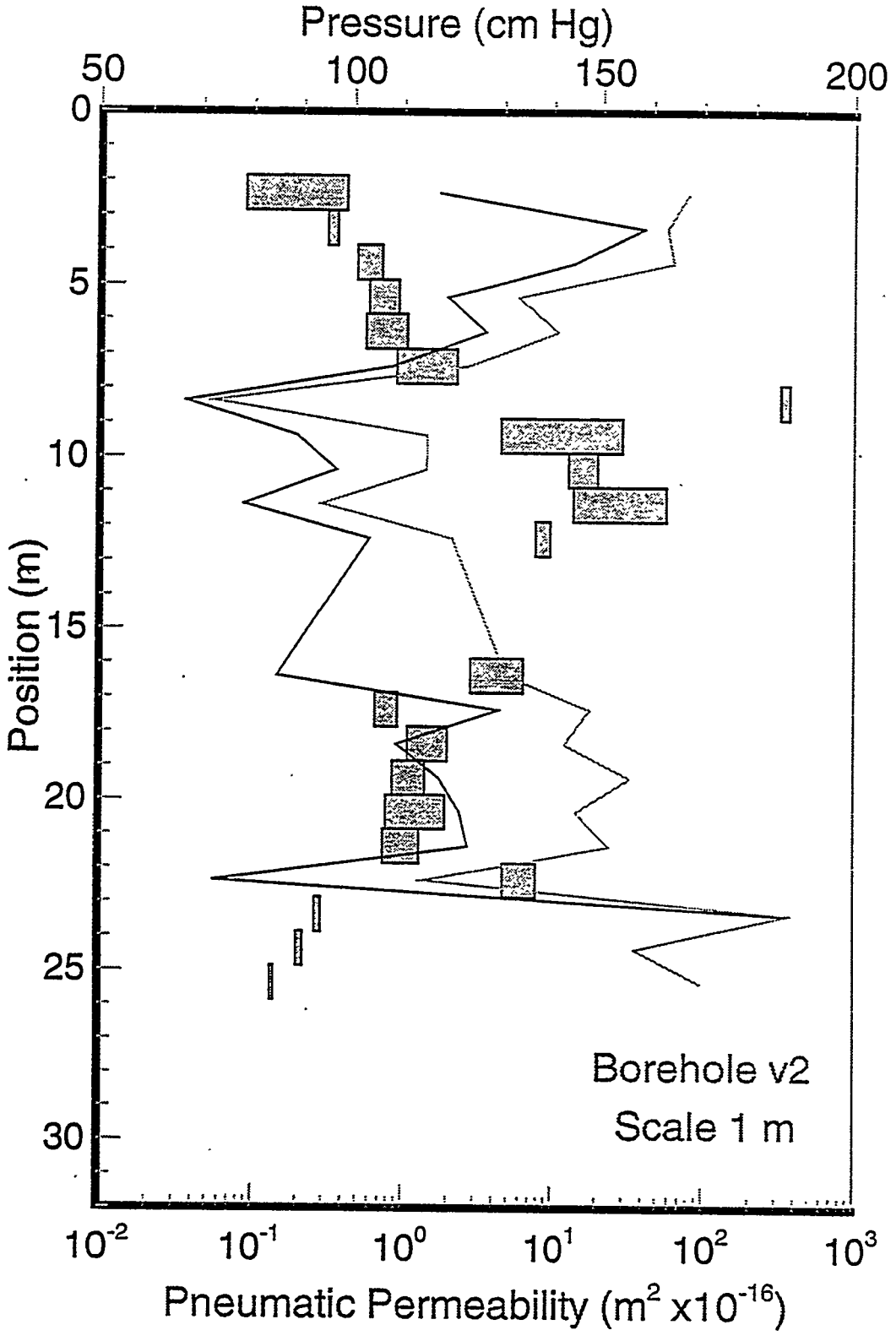

Figure 4.21. Spatial distribution of permeability at a 1-meter scale in borehole V2

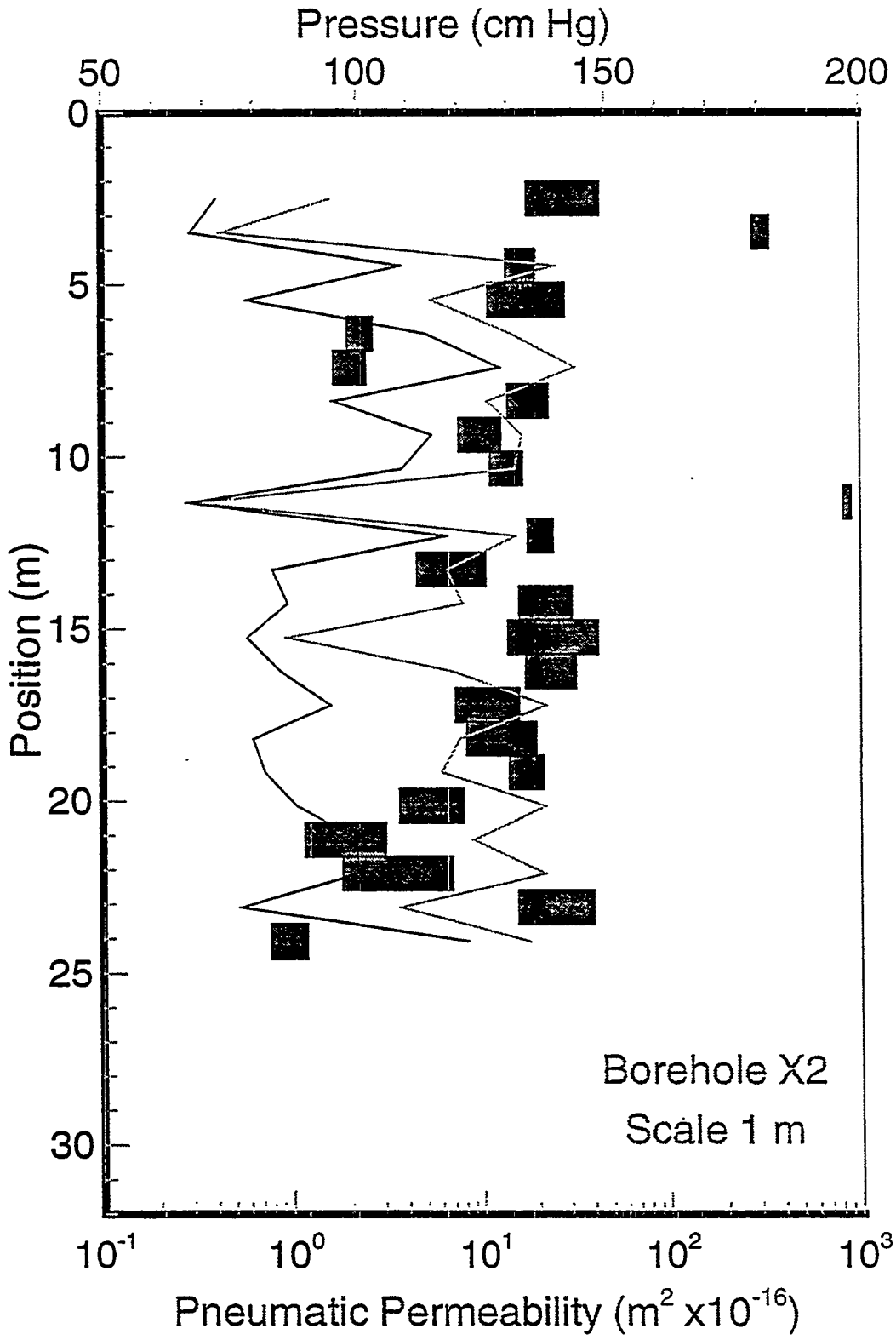

Figure 4.22. Spatial distribution of permeability at a 1-meter scale in borehole X2

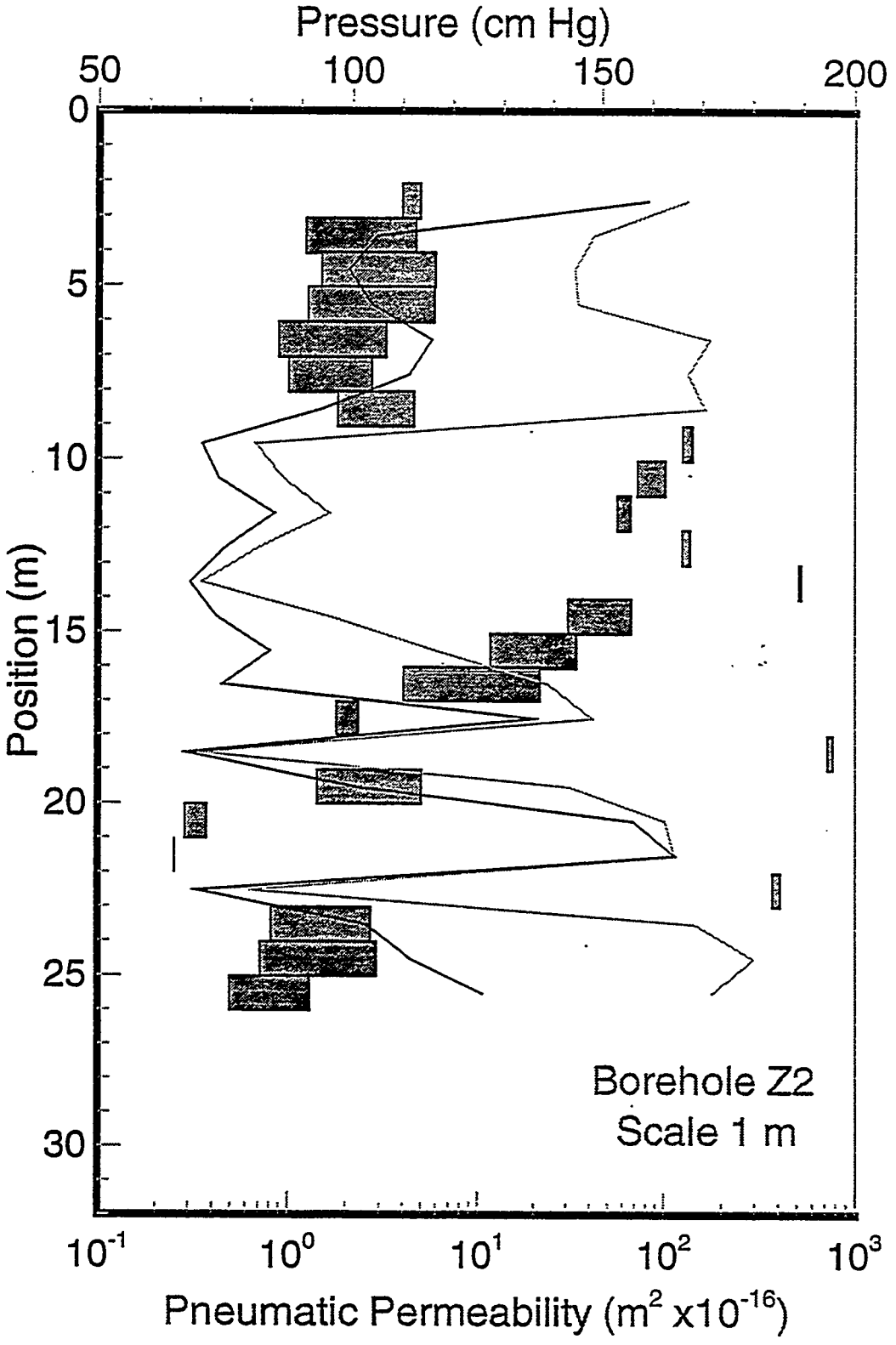

Figure 4.23. Spatial distribution of permeability at a 1-meter scale in borehole Z2

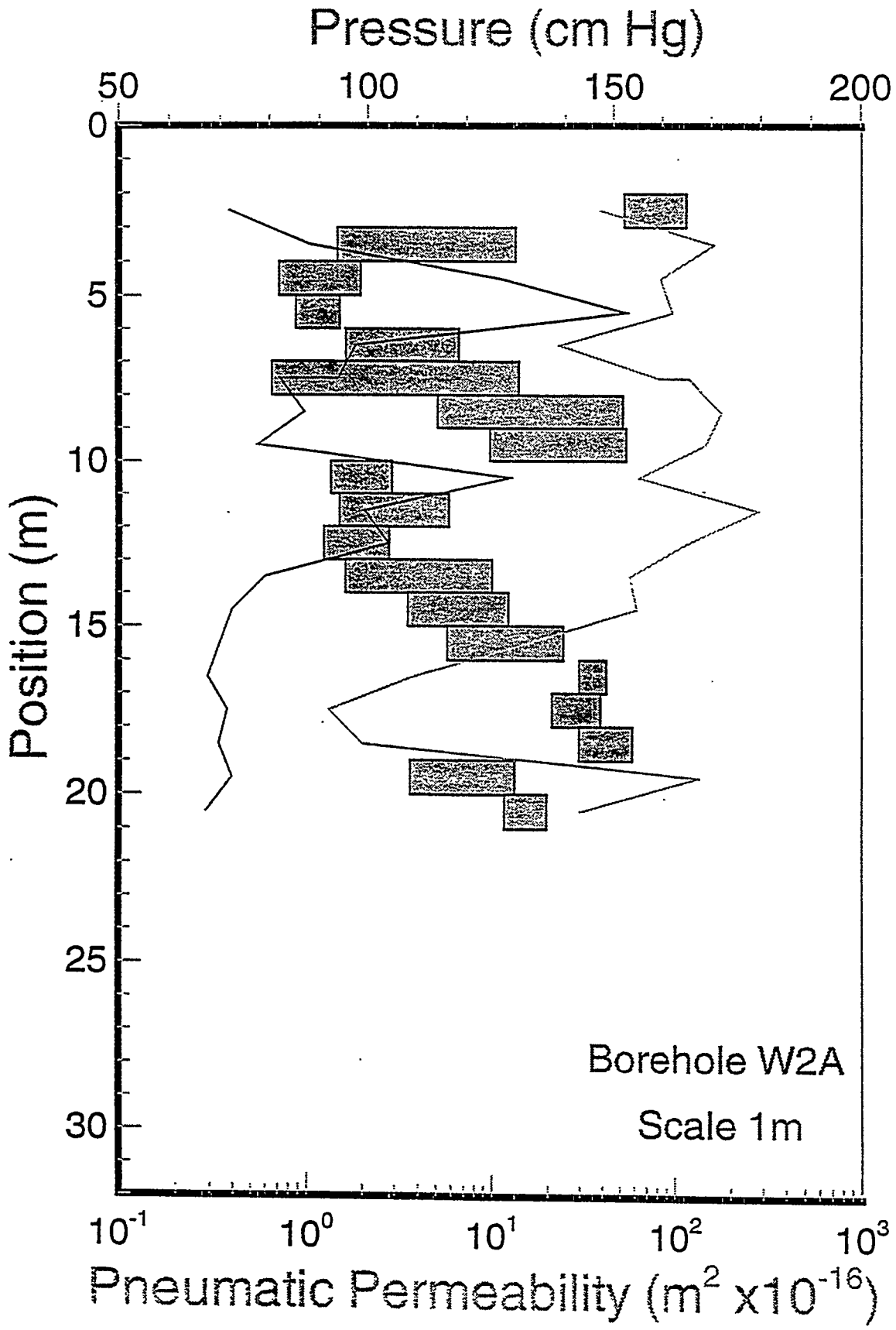

Figure 4.24. Spatial distribution of permeability at a 1-meter scale in borehole W2A

In borehole W2A, the measured permeabilities in a given interval vary with pressure over wider ranges than do those in other boreholes (Figure 4.24). Ranges of up to 1.5 orders of magnitude are observed over the applied injection pressures near the surface, but they decrease at depth. The surface above these intervals is exposed to the atmosphere (not covered by plastic) and may thus be affected by fluid and energy exchange with the latter. The effect of seasonal variability on moisture distribution, and in turn on permeability, needs to be studied further.

Table 4.3 summarizes the statistics of average (of minimum and maximum observed) permeabilities and corresponding ln k values for all tests conducted to date. The number of samples and their mean, median, and variance are reported for seven data sets: three for borehole Y2 at scales of 0.5, 1.0, and 3.0 m, and one for each of boreholes X2, Z2, W2A, and V2 at a scale of 1.0 m. At the 1.0-m scale, the mean of ln k for the 45° boreholes varies from -34.64 to -34.19 for boreholes W2A and X2, respectively. The ln k variances range from 1.49 for borehole W2A to 5.38 for borehole Z2. The vertical borehole (V2) has a sample mean for ln k of -36.21 and a variance of 3.87. As shown in Figure 4.20, fracture sets in the ALTS are preferentially oriented in an quasi-vertical direction. Sampling bias, due to borehole orientation, is thought responsible for the low mean permeability in borehole V2. Mean values and variances vary widely from one borehole to another, reflecting the strong heterogeneity of air permeability at the ALTS.

Permeability estimates obtained from Equation (4.2) assume that the tested medium behaves as a continuum at the scale of the test and does not necessarily represent the permeability of individual fractures. Therefore, we ask whether the fractured-porous tuff at the ALTS can be treated, on scales of 0.5 m or more, as a continuum. One way to address this question is to check how well do the data lend themselves to analysis by geostatistical methods which are based on the continuum concept. In classical geostatistics, the spatial correlation of a random variable is commonly represented by a semivariogram. These geostatistical techniques are optimal when applied to variables which are distributed normally. We saw that this is not the case for k values at the ALTS; therefore we examined the extent to which it may be true for ln k. Histograms and probability plots of log-transformed permeabilities from borehole Y2 are presented in Figures 4.25 to 4.27. Although far from being perfectly normal, they are much closer to a Gaussian distribution than are the k data, their skewness being close to zero and kurtosis near 3.0. Similar results are found for boreholes X2, Z2, V2, and W2A as seen in Figures 4.28 through 4.31.

4.5 GEOSTATISTICAL ANALYSIS

Sample semivariograms of ln k data from borehole Y2 at the three measurement scales are shown in Figure 4.32. As there are only nine data points at the 3.0-m scale, the sample semivariogram in Figure 4.32a is poorly defined. The semivariograms corresponding to 0.5-m and 1-m test intervals reveal a very definite structure (Figure 4.32b and c). Both show two distinct plateaus, suggesting the presence of two (multi-scale) nested semivariograms. We believe that the lower plateau (or sill) is associated with rock matrix and smaller fracture properties, whereas the higher sill is representative of more conductive fractured intervals. The structure with the lower sill exhibits a correlation scale (range) of about 6.0 m, the other about 9.0 m. The observed nested structure is similar to that discussed by Neuman (1990, 1991, 1993) in connection with his scaling theory according to which the variance (sill) and correlation scale (range) of log permeabilities increase consistently with separation distance. Semivariograms of ln k at 1.0 m scale for boreholes V2, X2, Z2, and W2A are shown in Figures 4.33 and Figure 4.34, respectively. These semivariograms seem to involve elements of a nugget, a nested structure, and periodicity. We tentatively attribute the differences between these semivariograms to sampling errors (the 1.0-m samples are

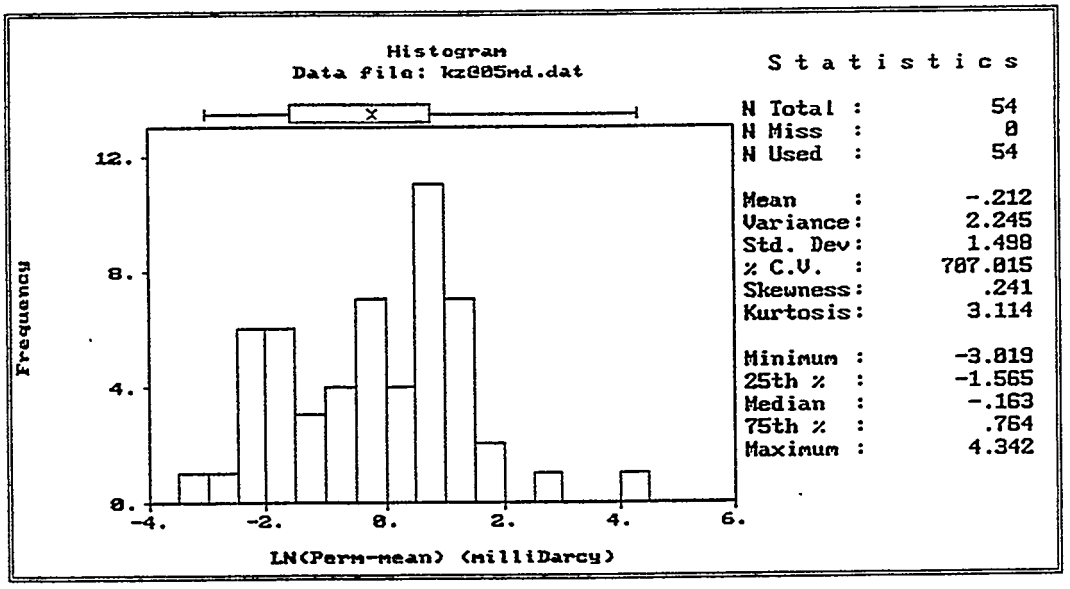

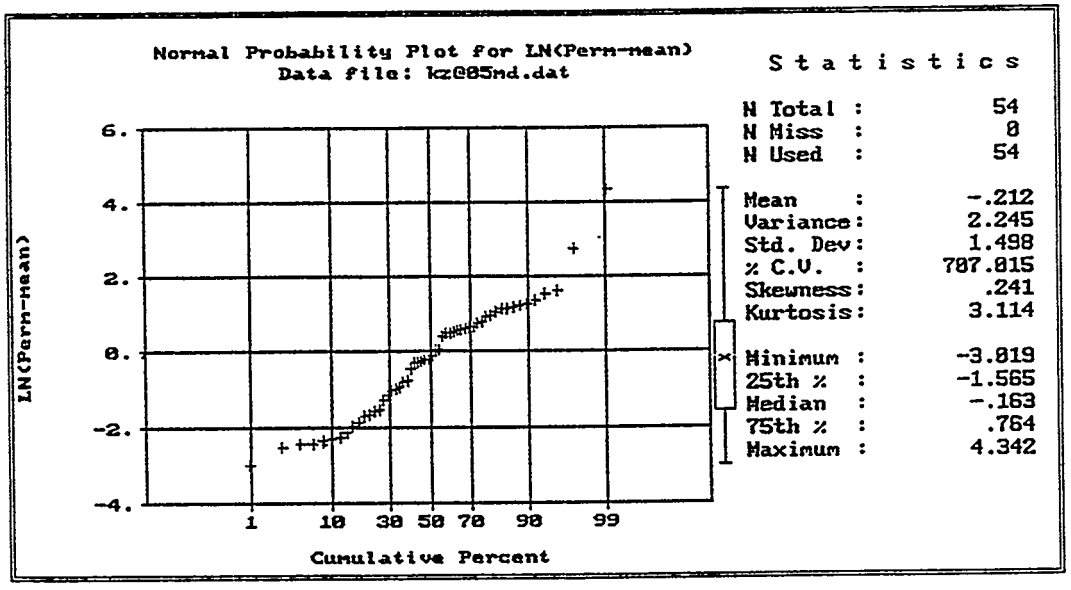

Figure 4.25. Statistics for log transformed data at a 0.5-meter scale for borehole Y2

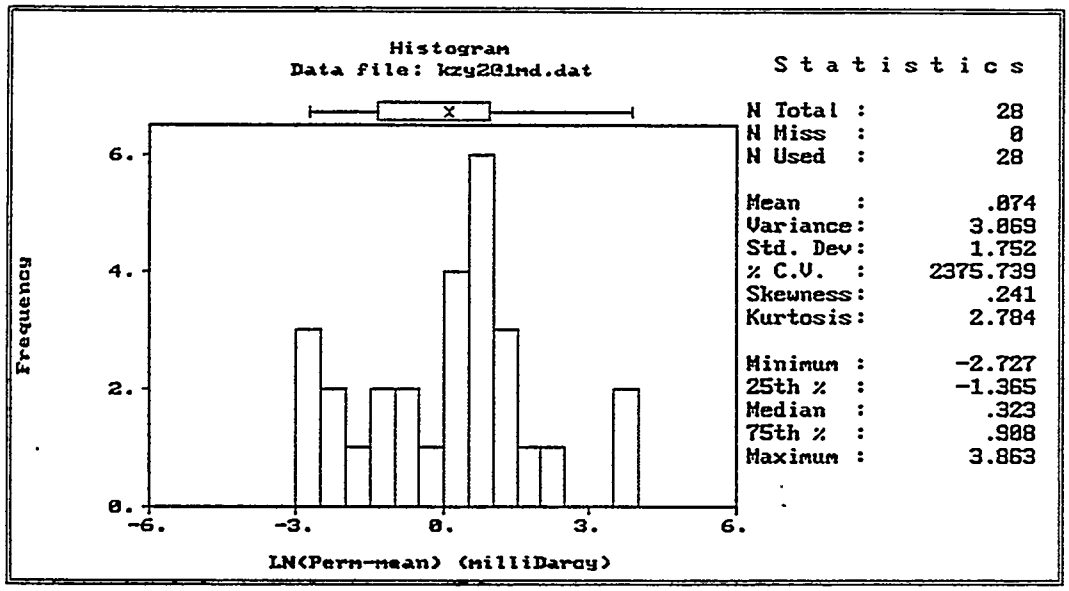

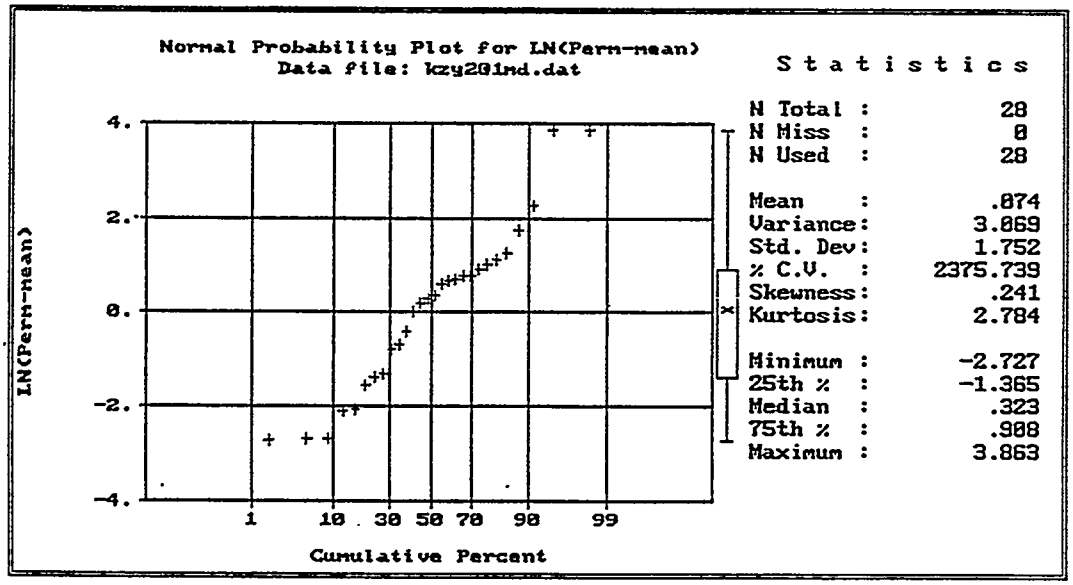

Figure 4.26. Statistics for log transformed data at a 1.0-meter scale for borehole Y2

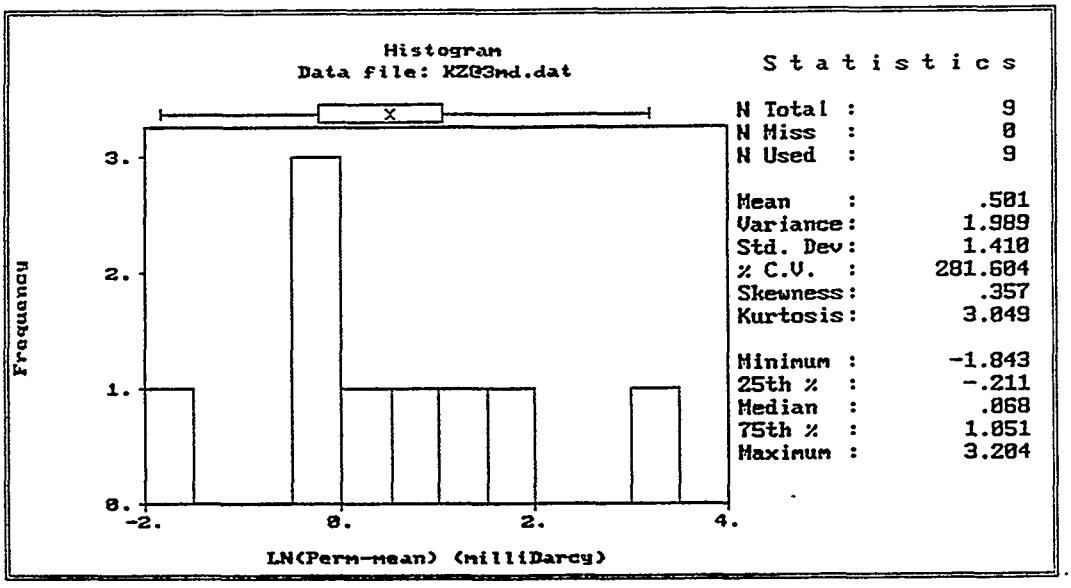

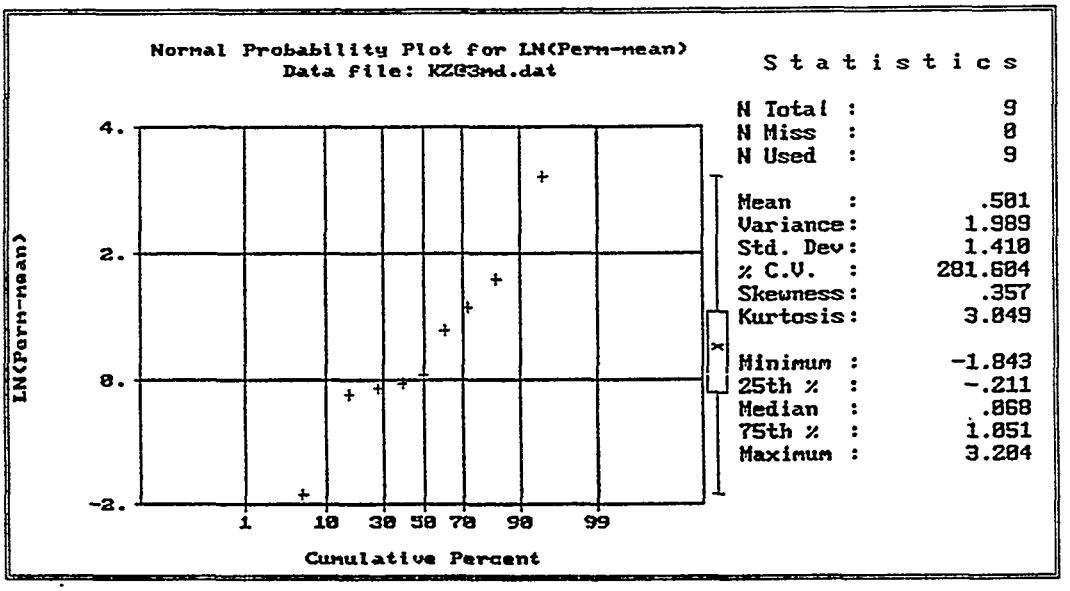

Figure 4.27. Statistics for log transformed data at a 3.0-meter scale for borehole Y2

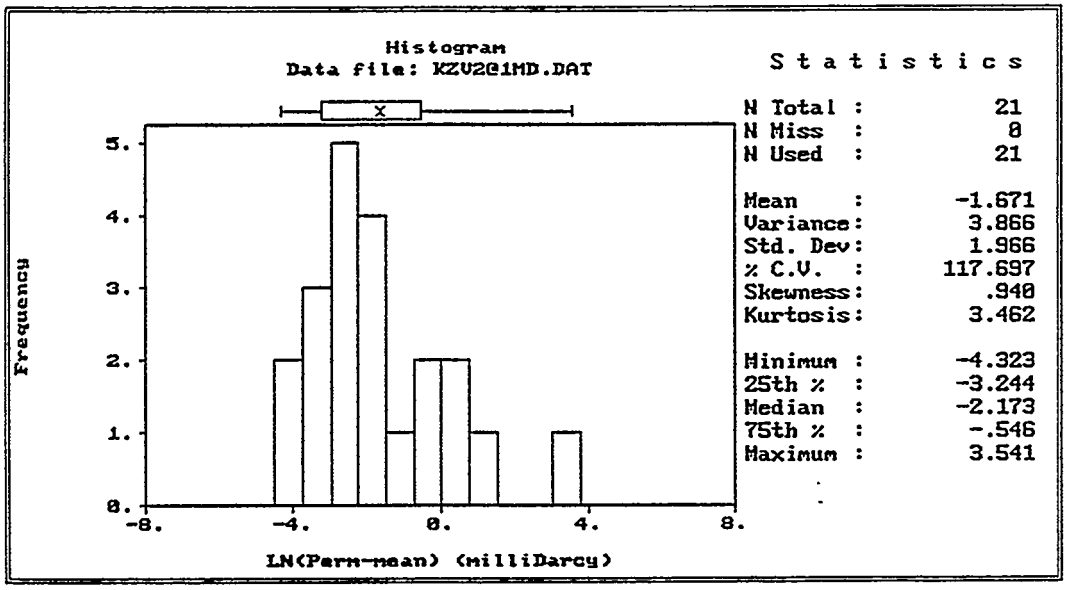

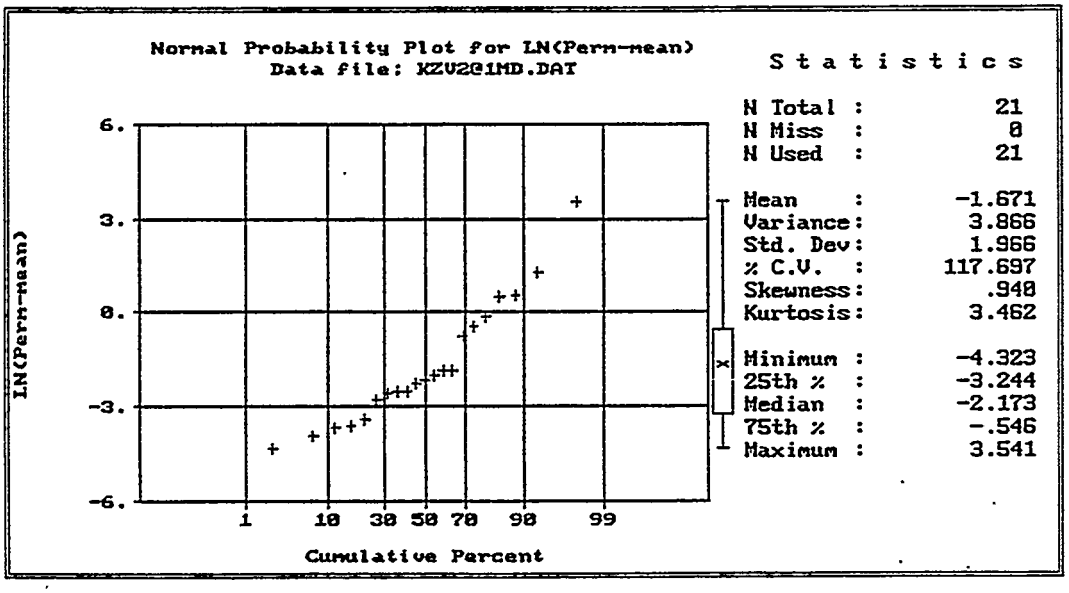

Figure 4.28. Statistics for log transformed data at a 1.0-meter scale for borehole V2

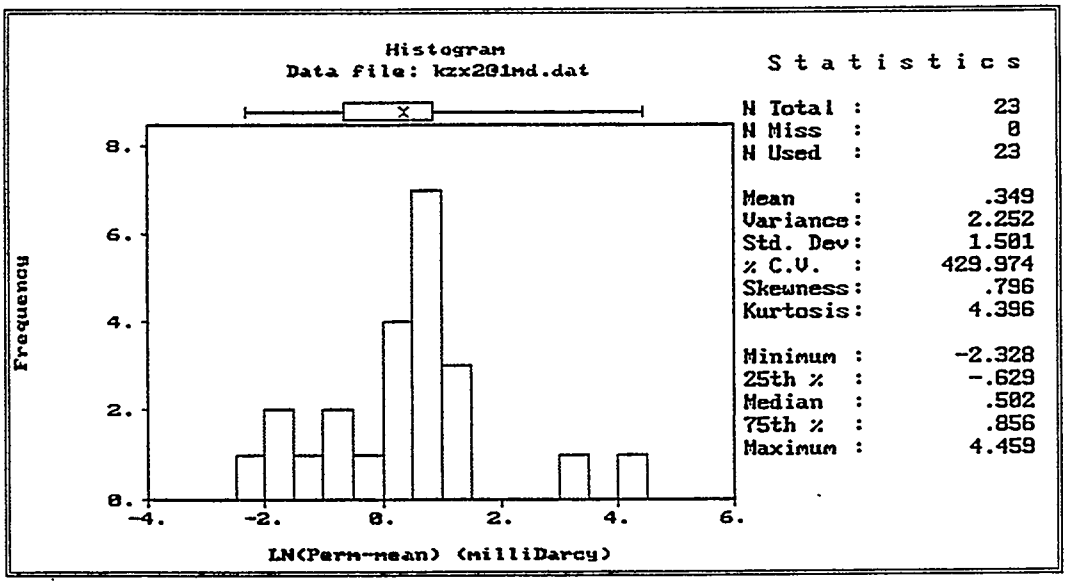

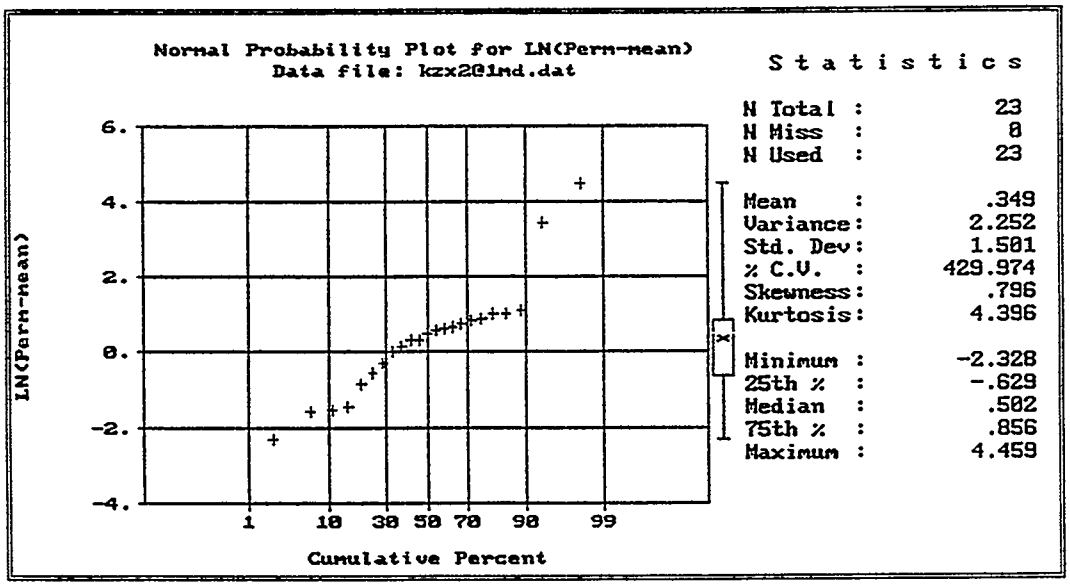

Figure 4.29. Statistics for log transformed data at a 1.0-meter scale for borehole X2

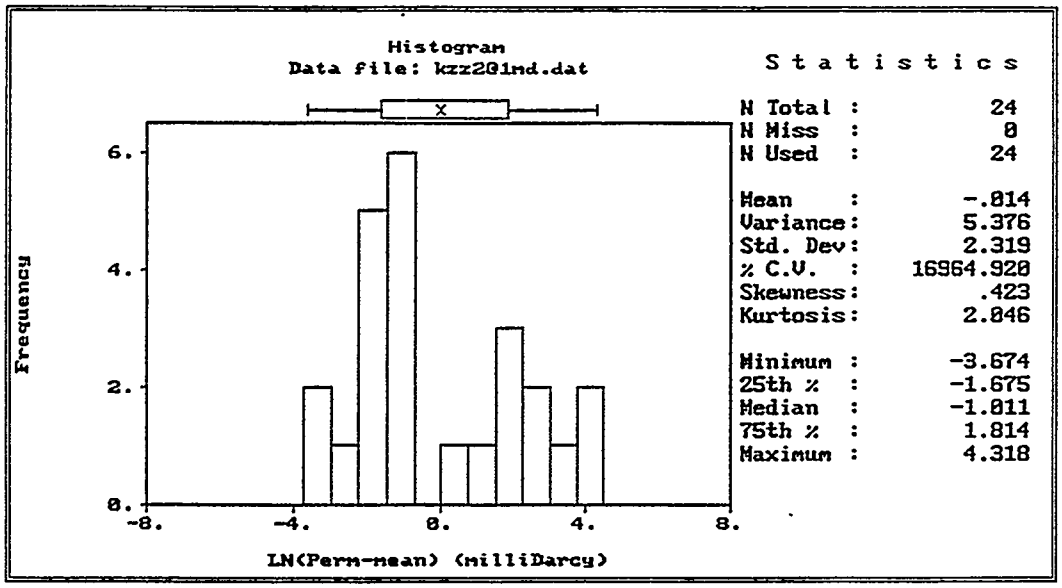

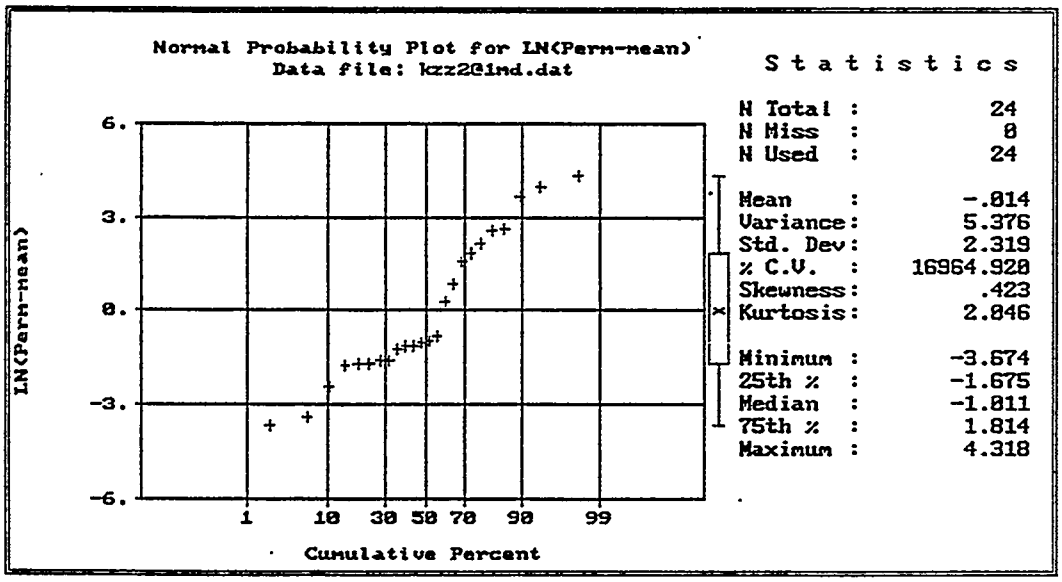

Figure 4.30. Statistics for log transformed data at a 1.0-meter scale for borehole Z2

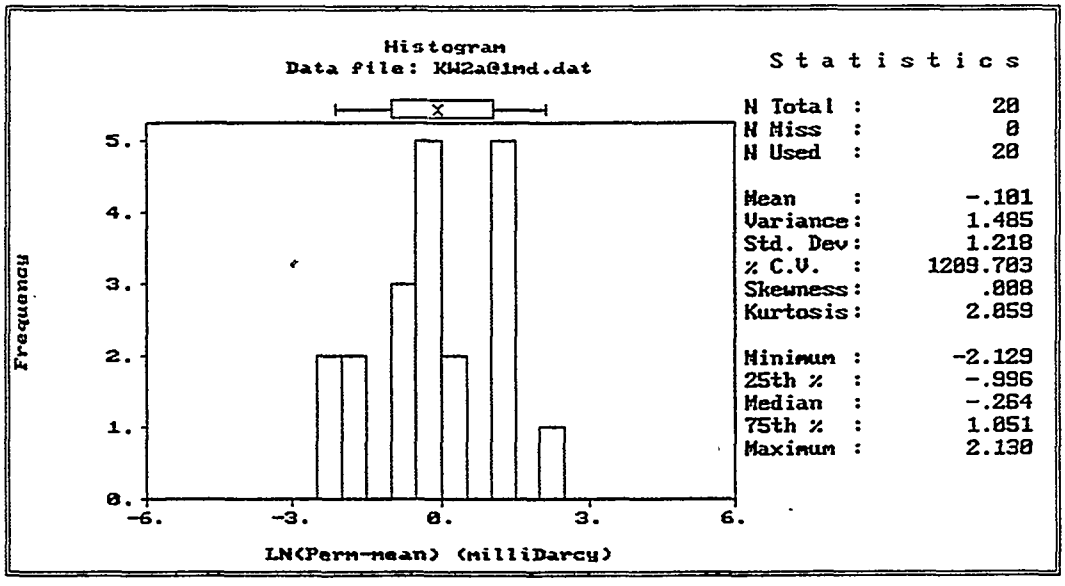

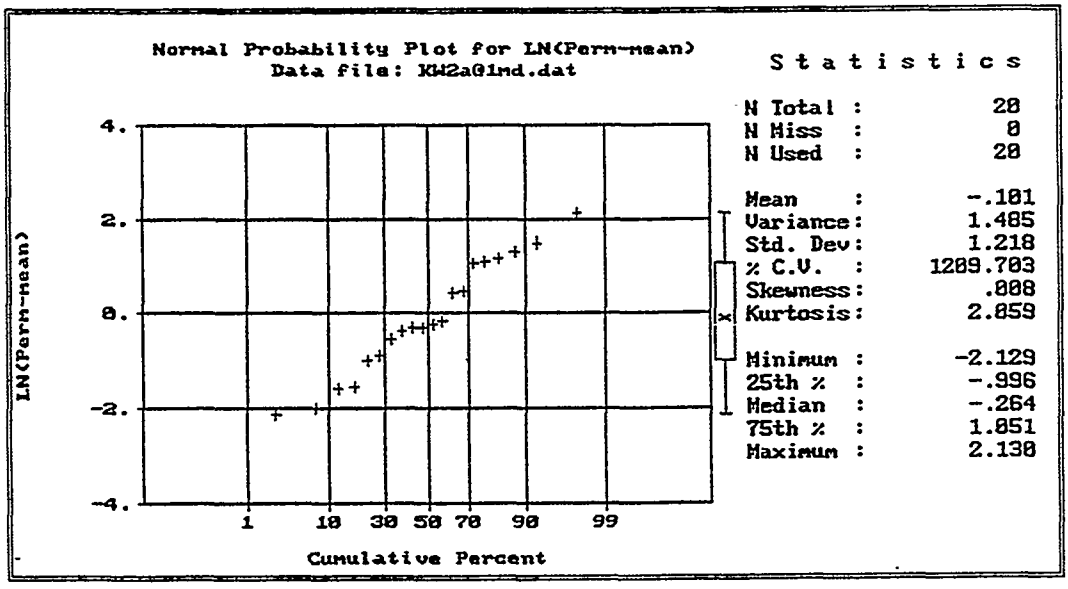

Figure 4.31. Statistics for log transformed data at a 1.0-meter scale for borehole W2A

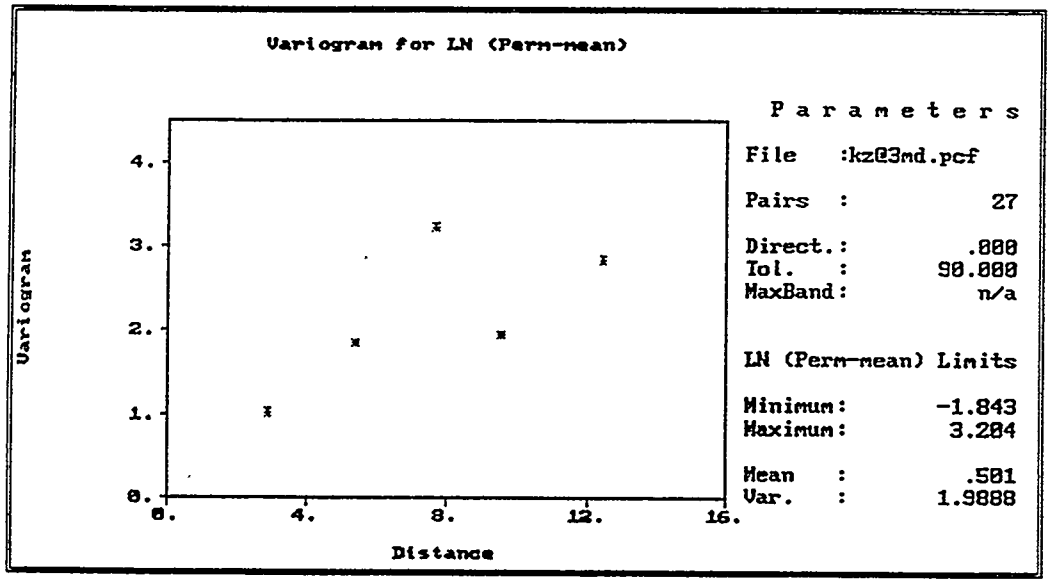

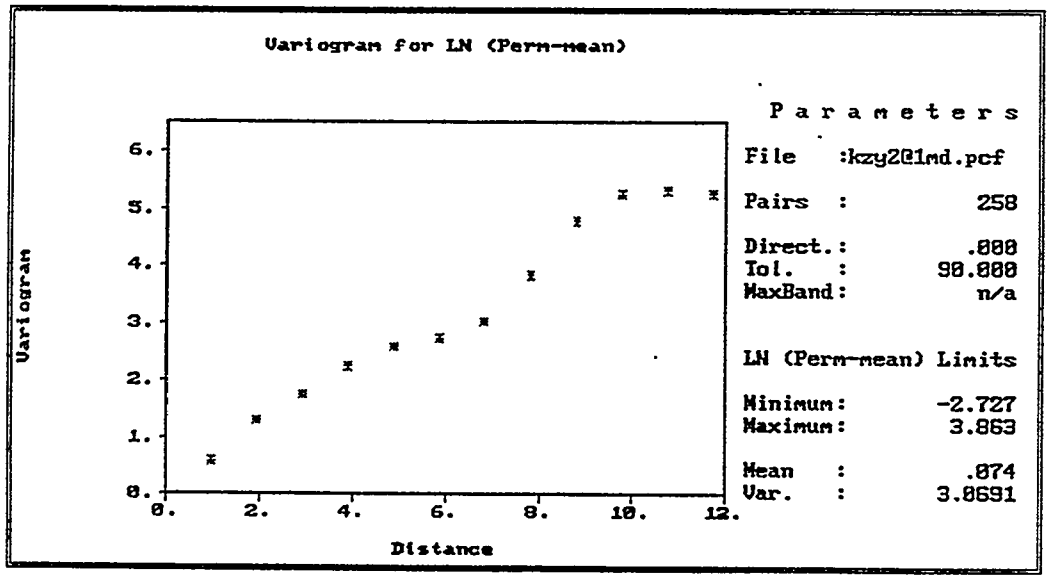

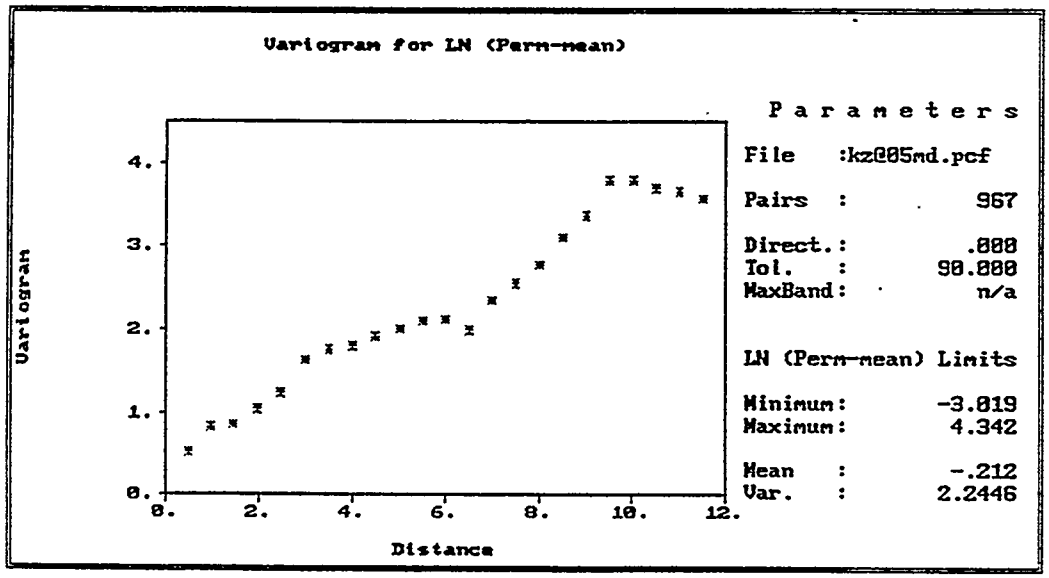

Figure 4.32. Experimental semivariogram of ln k for three scales in Y2

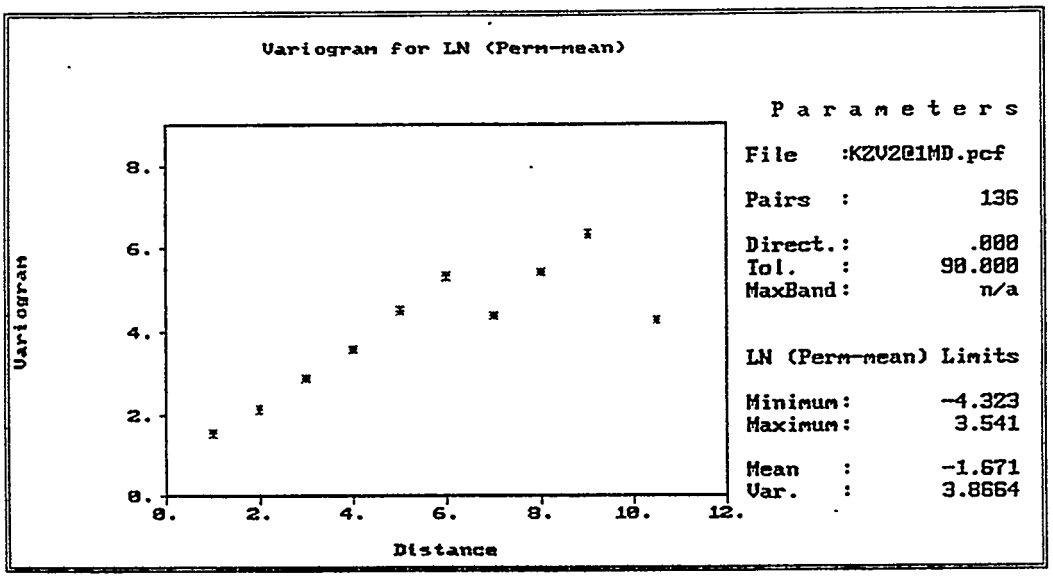

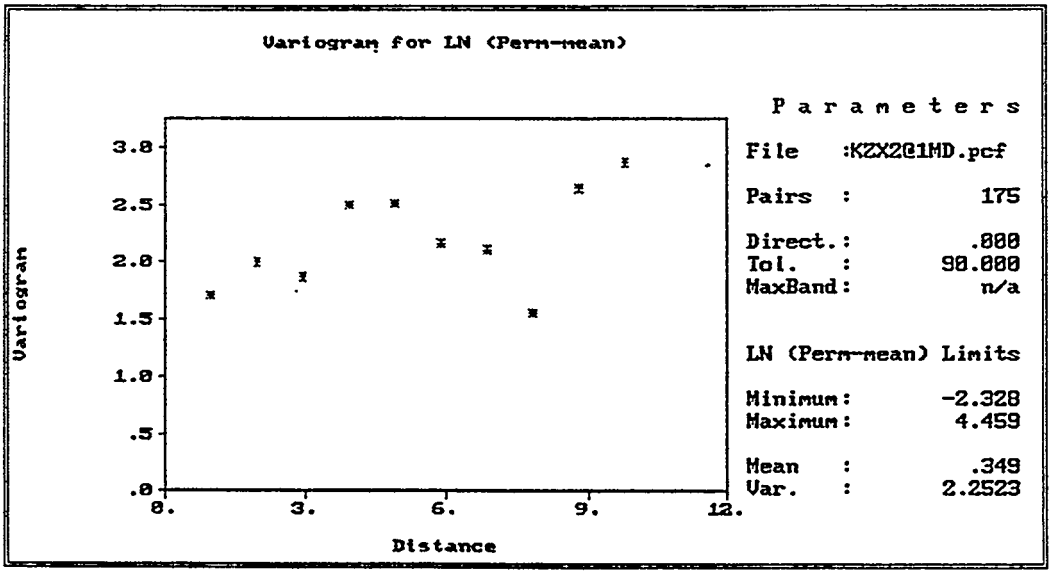

Figure 4.33. Experimental semivariogram of ln k for three scales in V2 and X2

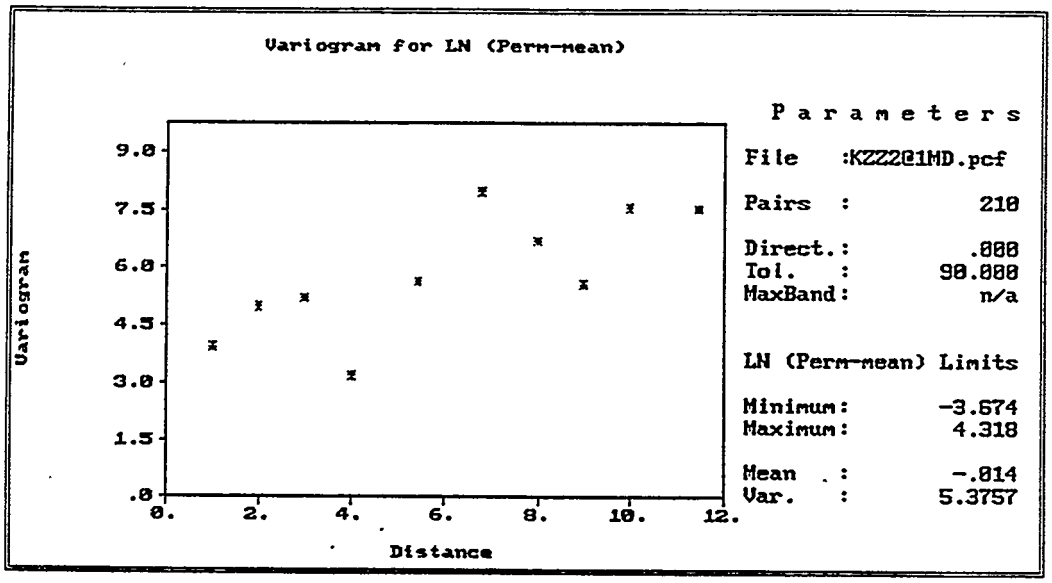

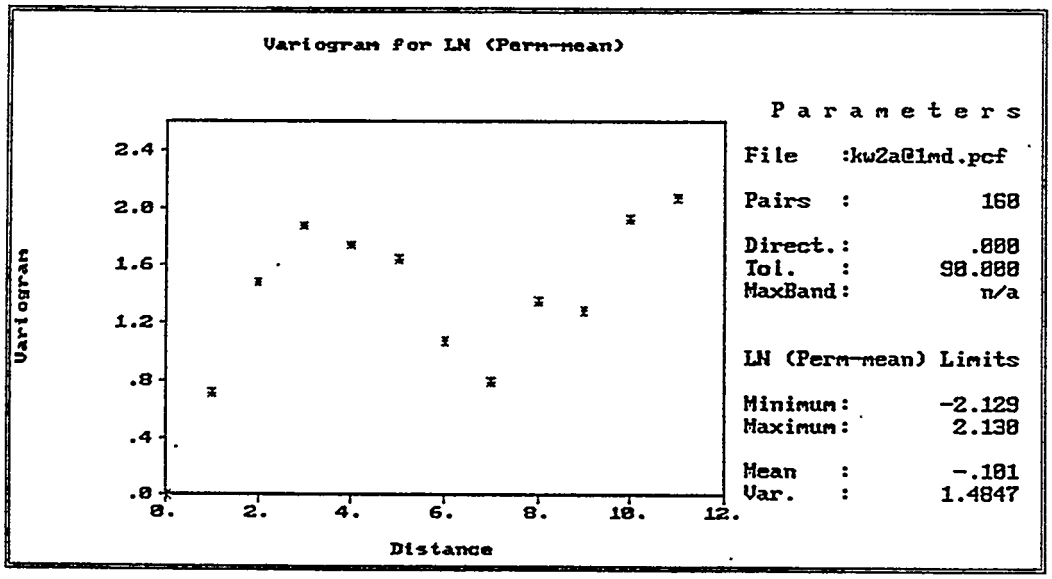

Figure 4.34. Experimental semivariogram of ln k for three scales in Z2 and W2A

relatively small) as well as to differences in borehole orientation. Regardless of these differences, our semivariograms are similar to those typically obtained in many heterogeneous porous media. This suggests to us that the air permeability data from ALTS behave, for all practical purposes, as if they represented a continuum. The same has been found true for log permeabilities from various other fractured rock sites including granites at Finnsjon in Sweden. Our data support an earlier conclusion by Neuman (1987, 1990) that one can often treat the permeability of fractured rocks as a random (stochastic) field defined over a (possibly multi-scale) continuum.

A joint semivariogram for 1.0-m data from the parallel boreholes Y2 and X2 was computed according to:

$$\bar{\gamma}(h_i) = \frac{1}{n_i + m_i}\left[n_i \gamma_{Y2}(h_i) + m_i \gamma_{X2}(h_i)\right] \qquad (4.10)$$

where n_i and m_i are the number of pairs at lag distance h_i, and γ_{Y2} and γ_{X2} are the semivariograms for Y2 and X2, respectively. This semivariogram (Figure 4.35) displays the same nested structure as shown by the individual borehole data.

A basic assumption behind the concept of flow and transport through porous media is that the partial differential equations used to describe these processes apply on some macroscopic scale. The precise magnitude of this scale is rarely, if ever, specified or mentioned. Although the dependence of permeability on the scale of measurement is often recognized, evidence for such scale dependence is usually circumstantial.

Our systematic measurement of k at the ALTS on three different scales (supports) provides a unique opportunity to observe the variation of permeability with such scale. We see in Figure 4.36a that the arithmetic mean of k increases from 3.01×10^{-15} m^2 at the 0.5-m scale (length of test interval) to 5.0×10^{-15} m^2 at the 1.0-m scale, then drops somewhat at the 3.0-m scale. As the flow is predominantly radial in all three cases, one would normally expect the arithmetic averages to be independent of measurement support. We attribute the increase in mean k from 0.5- to 1.0-m scales partly to sampling error and partly to the nested semivariogram structure observed in borehole Y2; a theoretical explanation of this phenomenon can be found in a recent paper by Neuman (1994). We believe that the subsequent drop in mean k from 1.0 m to 3.0 m scales is an artifact of the small sample at the 3.0 m scale; theoretically, we expect mean k to either stabilize or to continue increasing with the length of the support. Sample size decreases from 54 at 0.5 m to 28 at 1.0 m to 9 at 3.0 m test intervals.

Theoretically,. the variance of k should decrease as the support length increases. Instead, it increases from 0.5 to 1.0 m scales, then decreases. We again suspect that part of this is due to the small size of our samples, especially at the 1.0 and 3.0 m scales in borehole Y2.

Figure 4.36 shows a consistent increase in the sample mean of ln k in borehole Y2, but an increase and subsequent decrease in the sample variance.

Existing stochastic theories of flow and transport in heterogeneous media rely heavily on a knowledge of the mean and variance of log permeabilites. It is clear from our data that both the mean and the variance of ln k may vary with the scale of measurement in a way which may or may not be theoretically predictable. This emphasizes the need to perform site characterization on a wide range of well-defined scales of measurements, both in terms of support (dimension of rock

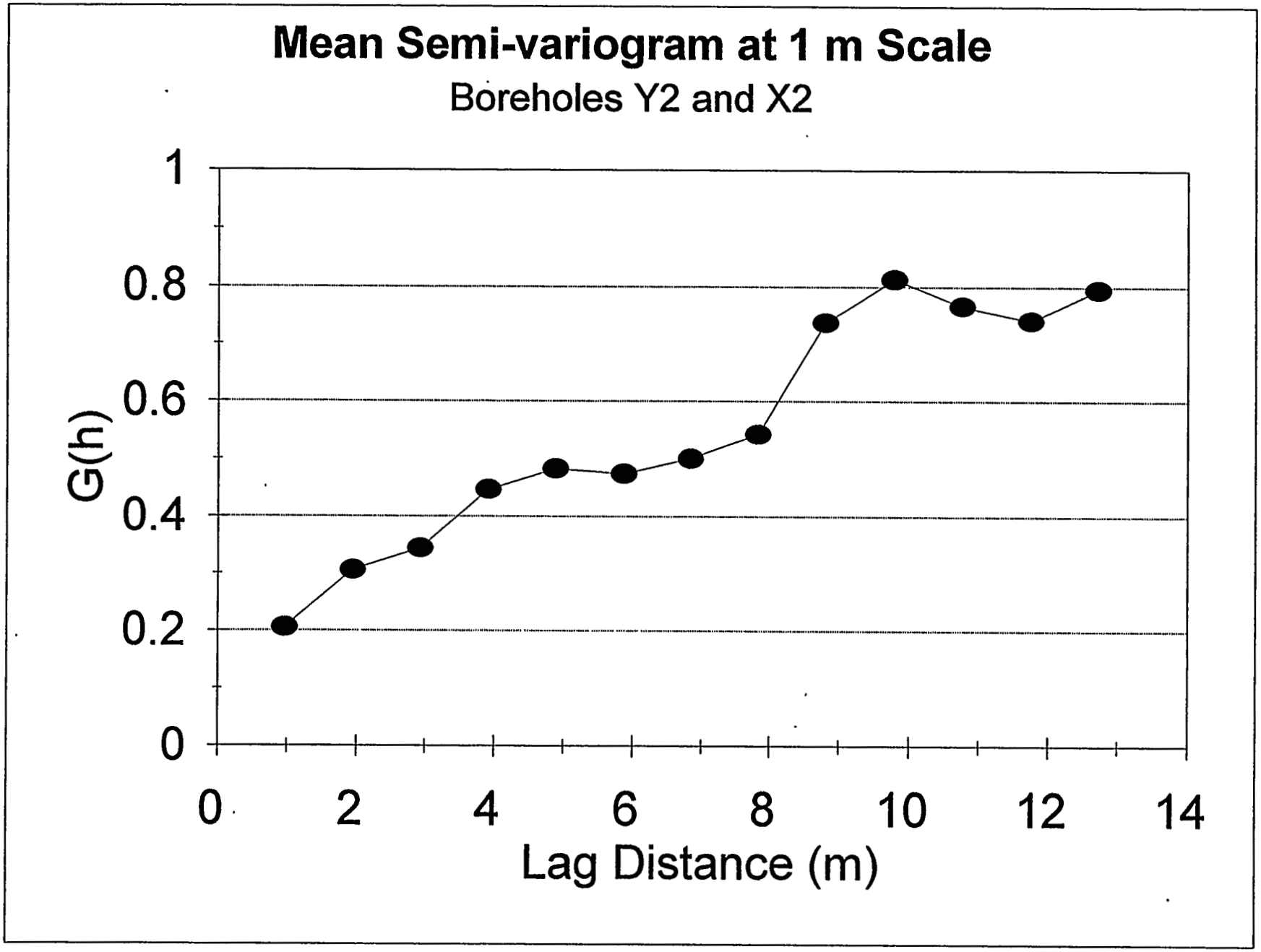

Figure 4.35. Mean semivariogram for boreholes Y2 and X2

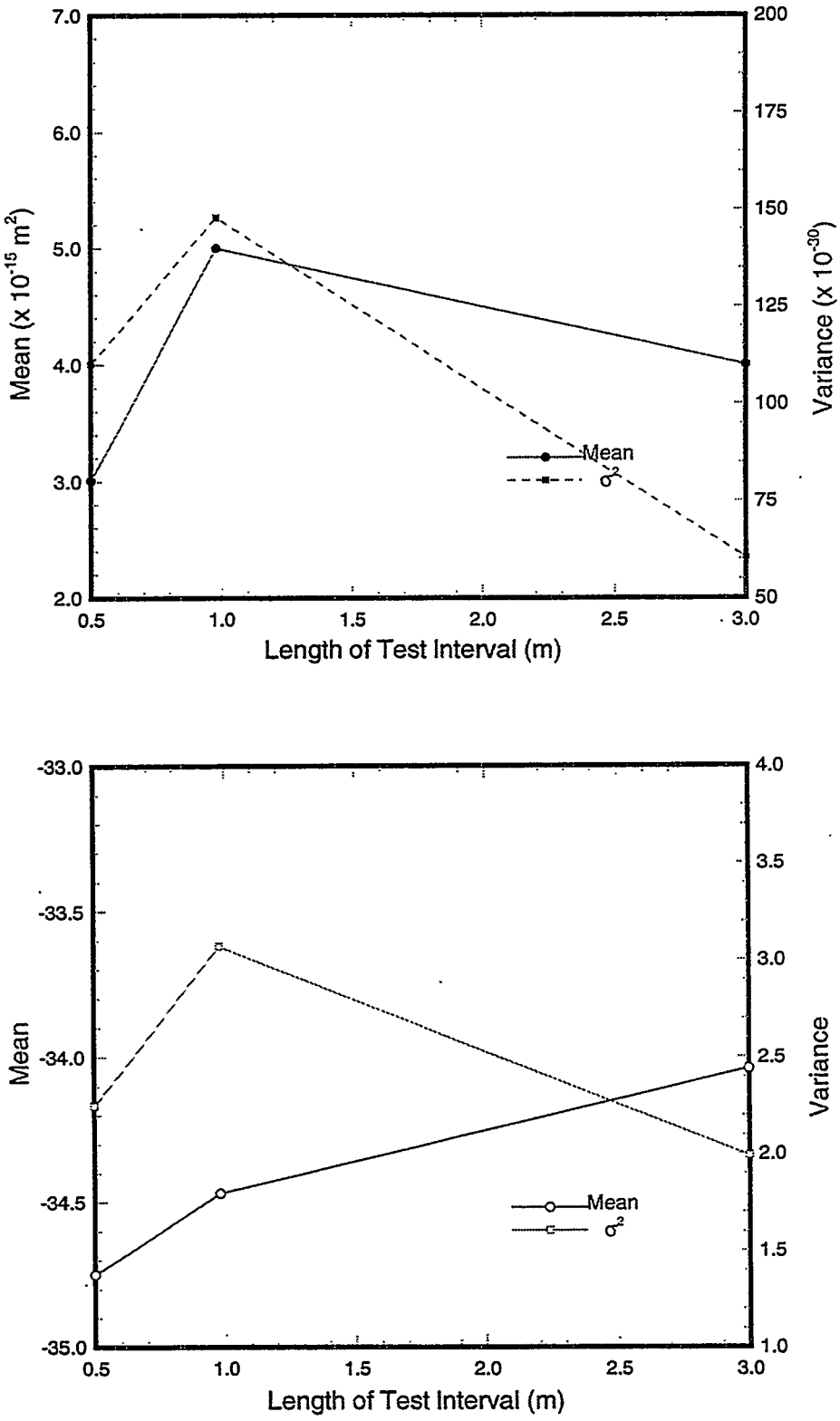

Figure 4.36. Scale effect on the experimental mean and variance of k for borehole Y2

sample tested) and in terms of correlation distanced between supports (to reveal semivariogram structures such as the nested forms in Figures 4.32 and 4.35).

To study further the relationship between our measurements at different scales, and to verify further that flow in our tests is predominantly radial, we computed spatial weighted averages of the 0.5- and 1.0-meter permeability data over test intervals of 1.0 and 3.0 m. We then compared these local spatial averages, arithmetic and geometric, with k values actually measured at the 1.0- and 3.0-m scales. The exact distance between the straddle-packers corresponding to the 1.0-meter scale was 0.98 m. Weighting was performed according to:

$$k_a = \sum_1^n \frac{l_i}{L} k_i \quad \text{and}$$
$$k_g = \prod_1^n (k_i)^{l_i/L} \quad \text{where } L = \sum_1^n l_i, \tag{4.11}$$

l_i being the portion of the particular interval completely contained within a larger interval L, and k_a and k_g being the arithmetic and geometric averages, respectively. Three different estimates were obtained in this way: 3-meter values based on 0.5- and 1.0-meter data, and 1-meter values based on 0.5-meter data. Figure 4.37a compares 1-meter averages based on 0.5-meter data with actual 1-meter data. The 1:1 slope line represents a perfect match between estimated and measured values. We see that arithmetic averages provide better estimates than geometric averages, the latter generally underestimating the measured values. Both averages underpredict the measurements at high permeabilities, but the arithmetic averages do so to a lesser extent than do the geometric means. Figure 4.28b compares 3-meter averages based on 0.5-meter data with actual 3-m measurements. Here again, arithmetic averages are better than geometric means which consistently underestimate the measured permeabilities. Both averages underpredict higher permeabilities. A comparison between 3-meter averages based on 1-meter measurements and actual 3-meter data is shown in Figure 4.37c. Once again, arithmetic averages match the measured values better than do geometric averages. The fact that the arithmetic averages produce better estimates supports our earlier contention that flow during the straddle-packer injection tests at the ALTS is predominantly radial.

Table 4.4 lists the variance and mean of permeability and log permeability for both the measured and the upscaled values. The differences between the values reported in Tables 4.3 and 4.4 for the 1.0-m permeabilities stem from the number of data points used in each of these tables. Upscaled permeabilities were computed for only 27 out of the 28 available test intervals. When using the 0.5-meter scale data to predict 1.0-meter and 3.0-meter values, the upscaled mean permeability consistently underestimates the average measured permeabilities (except for one instance). The difference between the mean of the measured and upscaled data is always within the same order of magnitude for both k and ln k. The variance of the upscaled permeabilities underpredicts that of the measurements in all but one case (1.0-m data to predict 3.0-m data for both k and ln k). The mean resulting from the upscaling of 1-meter data to the 3-meter scale brackets that obtained from the 3-m measurements; the arithmetic mean is larger and the geometric mean is smaller. In all cases, the arithmetic mean seems to better estimate the mean of the measured permeabilities than does the geometric mean. Moreover, upscaled permeabilities seem superior to upscaled ln ks. Based on these results, one may conclude that upscaling our straddle-packer permeabilities via weighted arithmetic spatial averaging yields reasonably good permeability estimates but a variance that is much too low.

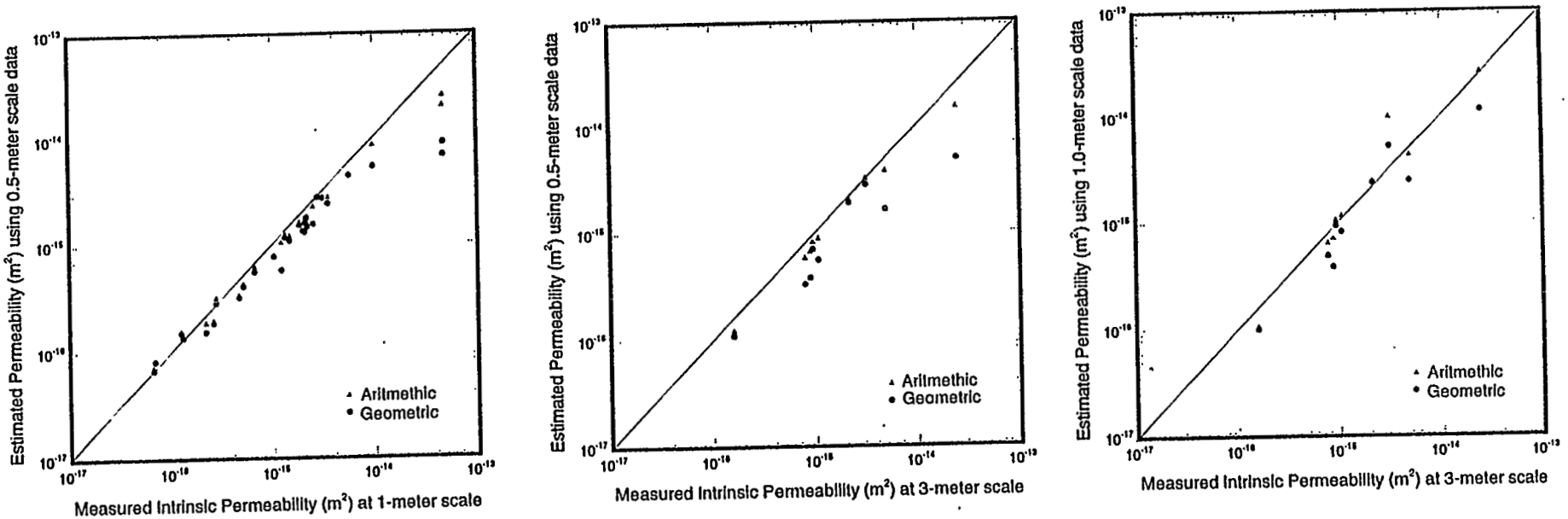

Figure 4.37. Comparison between upscaled and actual permeability measurements

Table 4.4. Moments of Measured and Upscaled Permeabilities in m^2.

ln Permeability Measured Data			Upscaled ln-Permeability			
			using 0.5 m		using 1.0 m	
			Arithmetic	Geometric	Arithmetic	Geometric
1.0 m (27)[2]	Mean	-34.36	-34.53	-34.71		
	Variance	2.855	2.337	1.860		
3.0 m (9)	Mean	-34.04	-34.26	-34.70	-33.99	-34.36
	Variance	1.99	1.914	1.441	2.665	2.083

Permeability Measured Data			Upscaled Permeability			
			using 0.5 m		using 1.0 m	
			Arithmetic	Geometric	Arithmetic	Geometric
1.0 m (27)	Mean (10^{-15})	5.18	3.07	1.78		
	Variance (10^{-30})	152.6	34.13	4.83		
3.0 m (9)	Mean (10^{-15})	4.30	3.03	1.48	5.10	2.69
	Variance (10^{-30})	60.36	22.53	2.43	69.12	13.44

[2] Number of measured data points used in the calculations

4.6 SUMMARY AND CONCLUSIONS

The following preliminary conclusions can be drawn from our single-hole air permeability tests at the ALTS:

A reliable method of conducting and interpreting straddle-packer air-injection permeability tests has been developed and implemented. The present system, instrument, and method of interpretation has proven to provide a sound testing methodology. Repeated testing of several intervals during previous years resulted in highly reproducible permeability estimates where seasonality effects could be discounted.

Vacuum extraction tests require an unacceptably long time for pressure to stabilize in low-permeability test intervals. Therefore, we abandoned this method of testing early in our program.

In air-injection tests, the time required for pressure to stabilize typically ranges from 30 to 60 minutes. This time increases with flow rate and may at times be as long as 24 hours or more. Permeability values published in the literature on the basis of much shorter air-injection tests may not be entirely reliable.

Test interpretation based on the assumption of radial flow is acceptable for intervals of length equal to or greater than 0.5 m in boreholes having a radius of 5 cm at the ALTS.

Both steady-state and transient air injection tests at the ALTS are strongly affected by two-phase flow phenomena. At present, we do not have at our disposal a reliable method to interpret the transient part of an injection test under such conditions. Much more theoretical work needs to be done to develop such method (or methods).

Computing air permeability on the basis of formulae which consider air to move through the rock at steady state, as a single phase, may be misleading. Such formulae predict a unique value of air permeability, k, regardless of the applied rate of air injection and pressure. Under two-phase flow, the computed k is nonunique, depending strongly on the applied pressure and exhibits a hysteretic effect. Hence, air permeabilities reported in the literature without specifying the manner in which k varies with pressure must be considered ambiguous.

Air permeabilities calculated by means of single-phase steady-state formulae show a decrease with applied pressure when inertial effects dominate over two-phase flow effects. In contrast, when two-phase flow effects dominate, the calculated k values increase with applied pressure. Hence, it is very important to conduct air injection tests at several applied flow rates and/or pressures.

During air-injection tests in rocks which contain both water and air, a steep gradient of permeability may develop in the immediate vicinity of the injection test interval. Calculation of air permeability by means of single-phase steady-state formulae under such conditions yields values which correspond neither to the minimum nor to the maximum k values that develop in the rock. Instead, one obtains intermediate k values representative of conditions very close to the test interval. In general, these intermediate values are higher than air permeability under ambient conditions of water-air saturation and lower than the equivalent single-phase rock permeability to either water or air.

If such calculated air permeabilities are available at a number of applied pressures (as is the case with our data), it may be possible to determine whether or not the values at lower pressure come close to representing ambient conditions. Likewise, it may be possible to determine whether or not the maximum attainable air permeability is being approached at the higher end of the applied pressure range. Both methods of determination rely on suitable graphical representation of the data.

Slip flow (Klinkenberg effect) appears to be of little relevance to our interpretation of single-hole air-injection tests at the ALTS.

In most boreholes tested thus far, the spatial variability of k determined from single-hole air-injection tests is much greater than the variability of k with pressure in any given interval. Hence, it is possible to perform a meaningful statistical and geostatistical analysis of how k varies spatially by considering a single representative value for each test interval. We have elected to perform such analyses on the arithmetic averages of the minimum and maximum k values from each interval.

The mean k values from the available test intervals are represented better by a log-normal than by a normal univariate probability distribution. This is typical of permeabilities in most geologic media.

In most boreholes, the permeabilities exhibit random fluctuations about a quasi-periodic background trend. Unusually high values of k are in some cases associated with known fracture traces along the boreholes. However, the presence of observable "fluid-conducting" fractures is not necessarily an indication of high permeability; in general, correlation between fracture density and permeability is low. The same was found true in many other fractured rocks worldwide, including our former granitic site near Oracle, Arizona.

Despite the lack of correlation between fracture density and permeability, there is a strong indication that fracture orientations exert an influence on permeability. The mean permeability in the only vertical borehole we have tested is lower than that in the inclined boreholes, most probably due to the fact that fractures at the ALTS tend to be steeply dipping. A vertical borehole "sees" fewer of these fractures than an inclined borehole.

The mean k values in several of our boreholes give rise to relatively well-defined semivariograms, not much different from those typically seen in heterogeneous porous media. This means that one is justified viewing the available k data as a sample from a random (stochastic) permeability field defined over a continuum. The same was found true in many other fractured rocks worldwide, including our former granitic site near Oracle, Arizona.

The semivariograms of data from two inclined, parallel boreholes at the ALTS exhibit a nested structure with two distinct plateaus (sills) and correlation scales (ranges). We attribute the smaller plateau and shorter correlation scale to the rock matrix and smaller fractures, the higher plateau and longer scale to larger fractures. This phenomenon of variance and correlation scale increasing with the scale of heterogeneities is consistent with that deduced on the basis of worldwide tracer test data by Neuman (1990, 1991, 1993).

The arithmetic average of all mean k values in borehole Y2 increases as the length of the test interval increases from 0.5 to 1.0 m, then decreases slightly as the test interval increases further to 3.0 m. The increase is anticipated on theoretical grounds (Neuman, 1994) when multi-scale

phenomena (of the kind exemplified by our nested semivariogram structure) are present. We believe the decrease is an artifact of sampling errors (the number of data in each sample decreases sharply as the length of the test interval increases).

Weighted averages of permeabilities from short injection test intervals over longer intervals underestimate permeabilities actually measured in these longer intervals. The actual error of estimation is, however, much smaller for arithmetic than for geometric averages. This provides additional support to our contention that flow around the injection intervals is predominantly radial.

The availability of a reliable method to quantitatively determine the degree of rock saturation around an injection test interval would greatly enhance reliability of permeability determinations by such tests. We strongly recommend that research be conducted to develop such a method.

All the information gathered under this Phase will be used to predict and design cross-hole and tracer tests during Phase 2 of our Research Plan. The design will be based on conditional stochastic flow simulations.

5. TASK IV: GEOCHEMICAL STUDIES: CONFIRMATION OF GROUNDWATER TRAVEL TIME AND FLUX ESTIMATION TECHNIQUES

by R.L. Bassett, Gregg Davidson, Elizabeth Lyons, Dan Cherry, and Charles Lohrstorfer

The activities of this research task as stated in the contract may be summarized as follows. The University of Arizona will design, conduct, and analyze field and laboratory studies to identify the geochemical and isotopic data required for calibrating and validating flow and transport models.

The objective of the task is to utilize indicator solutes at the Apache Leap Research Site to determine groundwater infiltration and recharge rates.

5.1 BACKGROUND

The location map for the Apache Leap Research Site (ALRS) is given in Figure 5.1. In the previous contract, work for this task focused on the covered borehole location (Weber, 1986); the principal location of task activity for this contract has been shifted (1) to the Magma haulage tunnel less than a kilometer to the west, and (2) to the new deep slant borehole site less than a kilometer to the southwest.

Access to the Never Sweat Tunnel, the principal ore haulage tunnel of the Magma Copper Company, has provided an unusually opportune circumstance for us to fulfill the requirement of this research task in a three-dimensional setting, by allowing us to monitor fluid movement from the surface to sampling points in the tunnel.

Magma Copper Company has given us access to the Never Sweat Tunnel which penetrates the tuff and passes underneath the Queen Creek watershed, terminating only 700 m from the covered borehole site. We now believe that, through our monitoring activities, we have defined two flow systems through the unsaturated tuff. The first is a fracture network that is intermittently recharged by runoff in Queen Creek, some of which emerges in the middle portion of the tunnel. The second is a local perched water table recharged through the unsaturated zone over a broad area of the tuff escarpment. This perched zone presently extends at least over the east end of the tunnel, providing a relatively constant discharge through boreholes and fractures in the ceiling and walls as discussed below.

5.2 REGIONAL GEOLOGY

The Apache Leap study area, in southcentral Arizona, is shown in Figure 5.1. Situated at the western edge of the mountainous region of the central and eastern part of the state, the Pinal Mountains bound the study area on the east while the Superior basin is directly west.

Local relief is moderate to high. Deeply cut canyons and pillar-capped ridges, as well as broad flat basins, characterize the terrain. Kings Crown Peak is the highest peak in the area, with an elevation of 1690 m above sea level, while basin elevations at Superior are about 830 m. The dominant geomorphic feature is the Apache Leap escarpment, a steep, west-facing wall which divides the highlands and the adjacent Superior basin. It rises abruptly from the basin floor to an elevation greater than 1,400 m, a gain of about 500 m.

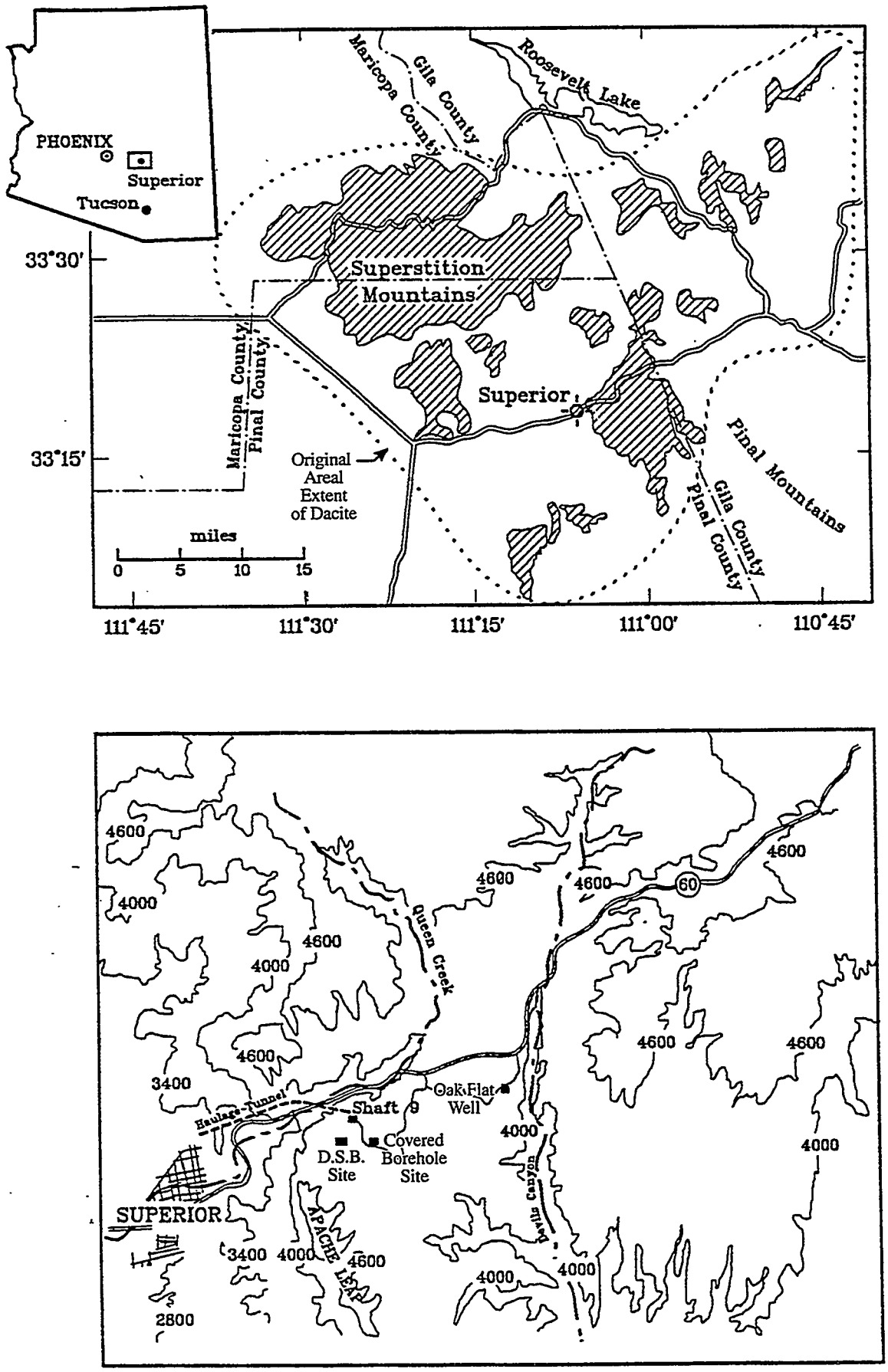

Figure 5.1. Map of principle features in the vicinity of the 3 Apache Leap Research Sites. 1) Covered Borehole Site, 2) Magma Haulage Tunnel and 3) Deep Slant Borehole Site.

The town of Superior is at the base of the escarpment in the Superior basin, while the study area proper is in the highlands directly east.

5.2.1 General Description of the Apache Leap Tuff

Apache Leap Tuff refers to the mid-Miocene ash-flow tuff capping the Apache Leap study area. The rock is part of a larger ash-flow sheet that occurs from 16 km west of the Superstition Mountains to the Salt River near Cherry Creek and from 1.5 km east of Globe to the vicinity of Ray. Figure 5.1 shows current areal extent and the original extent of the sheet as hypothesized by Peterson (1961).

Maximum exposed thickness is 600 m at the Apache Leap escarpment and thicknesses of greater than 300 m are common (Peterson, 1968). In general, the sheet is thickest near its center, thinning toward the margins. Thicknesses vary considerably, depending on irregularities of the surface on which the ash was deposited and on subsequent erosion.

The tuff was deposited on a surface of considerable relief. At the Apache Leap study area, it overlies primarily Paleozoic limestones, the Devonian Martin Limestone, the Mississippian Escabrosa limestone, and the Pennsylvanian Naco limestone. The locally derived Whitetail Conglomerate of Tertiary age underlies the tuff where it was deposited in depressions in the limestone units. Tertiary rhyolite flows underlie the tuff at a few locations where flows capped the Whitetail and limestone units (Peterson, 1969).

5.2.2 Zoning and Subunits

The ash-flow sheet comprises an undetermined number of flows which occurred in rapid succession and cooled as a single unit. Almost everywhere the sheet is a simple cooling unit, displaying the characteristic zones of welding and recrystallization associated with simple cooling units (Peterson, 1961). In ascending order, zones of welding are (1) lower zone of no welding, (2) lower zone of partial welding, (3) zone of dense welding, (4) upper zone of partial welding, and (5) upper zone of no welding. Zones of recrystallization are superimposed on the zones of welding. These are (1) devitrification, (2) vapor-phase crystallization, and (3) granophyric crystallization (Smith, 1960).

Peterson (1961) subdivided the rock into recognizable field units based on character of the groundmass. From bottom to top the units are: (1) basal tuff--poorly to moderately consolidated, non-welded tuff; (2) vitrophyre--streaky to uniform, partially, and densely welded tuff with black glassy groundmass; (3) brown unit--densely welded tuff with light brown aphanitic groundmass; (4) gray unit--partially welded tuff with pale red to light brownish gray aphanitic groundmass; and (5) white unit--partially to non-welded tuff with light gray to white aphanitic groundmass. Figure 5.2 shows correspondence between Peterson's subunits and the more general zones of welding and crystallization.

5.2.3 Mineralogical and Chemical Composition

Based on geochemical composition, the tuff is a quartz latite, although early studies led to a dacite classification which has remained ingrained in local usage and in the literature. Plagioclase is the major phenocryst. Position in the plagioclase series is uncertain, but studies of extinction angles suggest a composition of An_{35-40}, while examination of indices of refraction indicates a

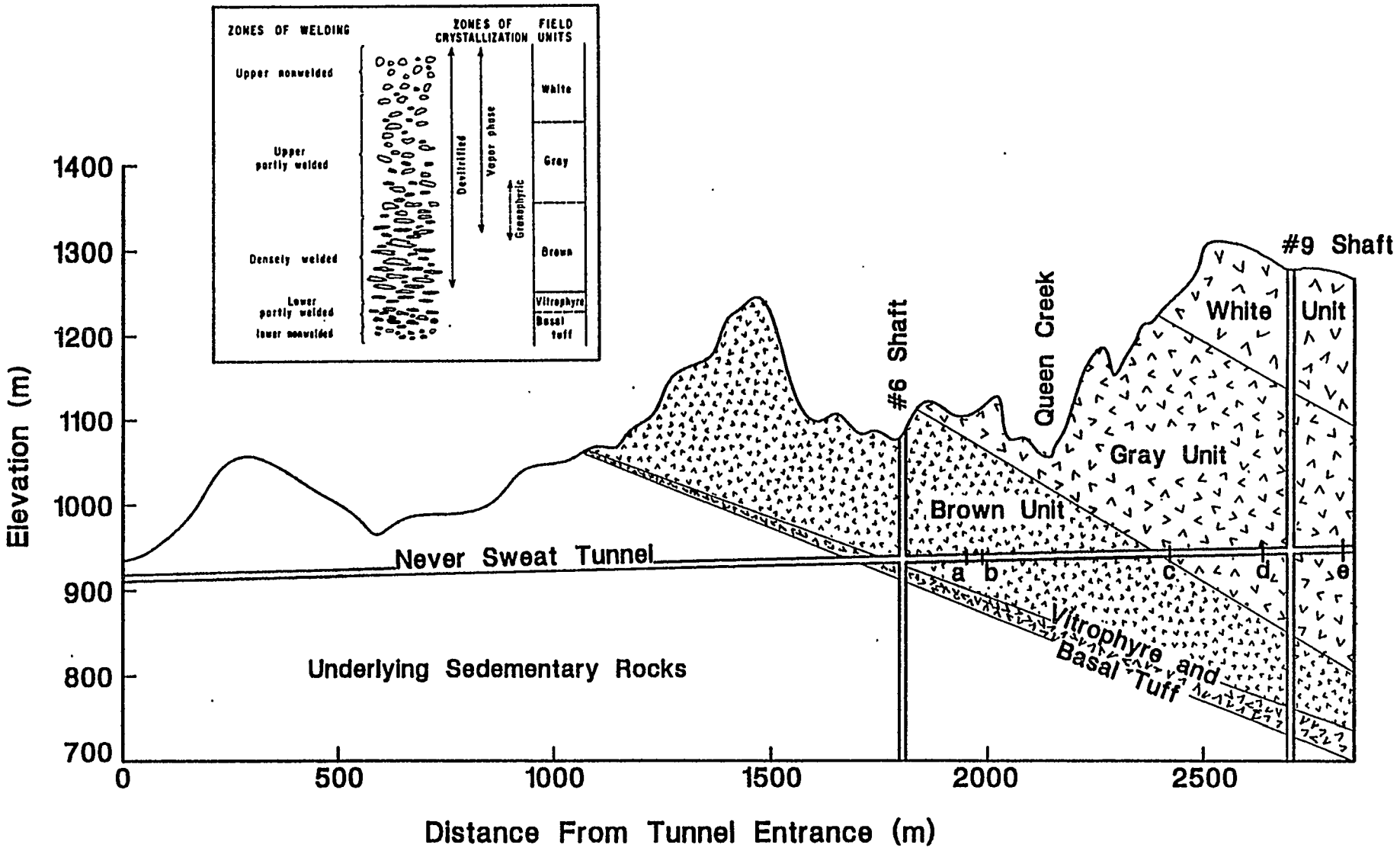

Figure 5.2. Cross section from tunnel entrance to terminus just beyond Shaft 9. Inset is tuff classification after Peterson (1961).

Table 5.1. Mineralogical Composition of Phenocrysts and Groundmass of Subunits of the Apache Leap Tuff (after Peterson, 1961). Concentration units given in mg/L unless otherwise noted.

	Basal Tuff	Vitrophyre	Brown Unit	Gray Unit	White Unit
% Total Phenocrysts	36.5	38.8	36.8	42.7	41.0
% Phenocryst					
Plagioclase	73.9	71.2	73.7	71.4	67.1
Sanidine	2.4	2.1	2.2	3.5	7.0
Quartz	8.9	9.2	9.9	11.9	14.1
Biotite	8.7	10.4	8.9	9.0	6.2
Magnetite	3.0	3.4	4.3	2.9	3.4
Hornblende	2.5	3.4	0.9	0.7	1.8
TOTAL	99.4	99.7	99.9	99.4	99.6
% Groundmass	63.5	61.2	63.2	57.3	59.0
Description of Groundmass	Vitroclastic material with k-feldspar and cristobalite	Glassy	Cryptocrystalline and microcrystalline cristobalite and k-feldspar with minor quartz and plagioclase	Cryptocrystalline cristobalite and k-feldspar with minor quartz and plagioclase	Cryptocrystalline cristobalite and k-feldspar with minor quartz and plagioclase

composition of An_{22-25} (Peterson, 1961). Groundmass minerals are mainly cristobalite and K-feldspar (Peterson, 1961). Tables 5.1 and 5.2 summarize mineralogical and chemical data.

Table 5.2. Whole-Rock Chemical Analyses of Specimens from Each Subunit of the Apache Leap Tuff (after Peterson, 1961). Concentration units in mg/L unless otherwise noted.

	Basal Tuff	Vitrophyte	Brown Unit	Gray Unit	White Unit
SiO_2	66.4	67.8	67.7	68.0	68.7
Al_2O_3	14.4	15.3	16.3	16.5	16.7
Fe_2O_3	2.1	2.1	2.5	2.6	2.7
FeO	0.34	0.77	0.13	0.12	0.1
MgO	0.80	0.72	0.76	0.52	0.38
CaO	2.3	2.3	2.5	2.4	2.2
Na_2O	1.8	4.0	4.1	4.2	4.2
K_2O	4.3	3.6	3.6	3.5	3.6
H_2O^-	7.1	2.3	1.8	1.8	1.4
H_2O^+	na[1]	na	na	na	na
TiO_2	0.41	0.46	0.43	0.40	0.40
CO_2	0.05	0.05	0.05	0.05	0.50
P_2O_5	0.10	0.14	0.16	0.14	0.15
MnO	0.09	0.09	0.08	0.08	0.08
TOTAL	100.2	99.6	100.1	100.3	101.1

[1] na = not analyzed

Lithic inclusions generally make up 1 or 2% of the tuff, but are much more abundant in the lower part of the sheet (Peterson, 1968). Pumice fragments comprise as much as 25% of the rock in the upper part of the sheet while scarce or absent in the lower part of the sheet. Their original glassy textures have been obliterated by recrystallization, and most carry the same assemblage of phenocrysts in the same proportion as the matrix (Peterson, 1961). Researchers for the United States Department of Energy (DOE) described locally zoned vugs and/or lithophysae which tended to be mineralized with clay, zeolites and other minerals (Sample Management Facility, 1990).

5.2.4 Structure

The Apache Leap Tuff is highly fractured. Considerable spatial variability exists in fracture sets; however, trends have been observed. Vertical or near vertical joints are ubiquitous. Most are 1.5 to 4.5 m apart, but may be spaced as closely as a few centimeters or as far apart as 10 m (Peterson, 1961). Thornburg (1990) described three distinct joint sets that strike (1) ENE with a mean azimuth of 67° to 77°, (2) N with a mean azimuth of 9° to 19°, and (3) NW with a mean azimuth of 136° to 145°. The first set appears to have formed from flexing around pre-existing topography, while the second and third sets appear to be derived from tectonism associated with basin and range deformation. Near horizontal joints (Thornburg, 1990) and polygonal cooling joints (Peterson, 1968) have been identified, although the latter are extremely rare.

Faults in Apache Leap Tuff are mostly unmapped. Hammer and Webster (1960) described two principal fault systems, one striking ENE and one striking NNW. The former are pre-Cenozoic and often mineralized with manganese and iron oxides (Hammer and Webster, 1962). The latter are younger, cutting Cenozoic and older rocks and most are not very mineralized.

5.2.5 Hydrologic Parameters

Measurements of hydrologic parameters demonstrate significant spacial variability. In general, porosity is inversely proportional to degree of welding. Peterson (1961) calculated porosity from powder density and bulk specific gravity data and reported values that range from 0.4% in the vitrophyre to 16% in the basal tuff. Vogt (1988) measured effective porosity by a mercury intrusion method. From 105 samples that were primarily in the white unit, values ranged from 9.2% to 47.6%, with a mean of 14.6%. From four samples, each taken from one location in the gray unit and one location in the brown unit, he determined mean effective porosities of 5.91% and 7.22%, respectively.

Researchers at The University of Arizona (Rasmussen et al., 1990) characterized rocks from the white unit at the Apache Leap Tuff Site. Their laboratory measurements of saturated hydraulic conductivity range from 0.69×10^{-9} m/s to 438.3×10^{-9} m/s, with a median value of 4.2×10^{-9} m/s.

5.3 MAGMA MINE

The underground workings at the Magma Copper Mine consist of a network of tunnels, drifts, and shafts east of Superior, Arizona. Currently, mine workings extend from Superior to 450 m east of #9 shaft and from 985 m north of #9 shaft to 900 m south of it.[1] The workings are almost entirely in the Paleozoic units underlying the Apache Leap Tuff. At their deepest, they extend beyond an elevation of 435 m below sea level, but at #9 shaft, where mining is currently active, depth is 1470 m below surface which is 200 m below sea level.

Although ore recovery is from units below the tuff, two shafts, #6 shaft and #9 shaft, and the ore haulage tunnel, known as Never Sweat Tunnel, pass through the tuff providing access to the interior of the rock. Never Sweat Tunnel is at the "500 level" of Magma Mine (500 ft below a reference elevation of 3,569 ft above sea level). Intercepted fractures circumscribe the walls and many discharge water into the tunnel. Discharges range from barely detectable seeps to flows of over 10 L/s. Many discharges have been observed to vary temporally.

---

[1]Personal communication. Gronland, F., 1991, Project Engineer, Magma Copper Company, Superior, Arizona.

The tunnel traces a curved path from Superior to a point 122 m from Magma Mine's #9 shaft. Total length is 2,842 m. Although the western section is in Paleozoic limestone units stratigraphically below Apache Leap Tuff, more than half of the tunnel, the eastern portion, is constructed in tuff (Figure 5.2). As shown in Figures 5.1 to 5.3, the tunnel roughly parallels Queen Creek and passes directly under it at a point 720 m from its eastern end, where creek and tunnel begin divergence.

Tunnel depths below the surface range from 0 m at the tunnel's western end to 370 m near the east end termination. At the point where the tunnel is nearest the creek, it lies 110 m directly below. Figures 5.2 and 5.3 illustrate the location of the tunnel and the overlying topography.

5.4 REGIONAL GEOHYDROLOGIC SETTING

The block diagrams shown in Figures 5.4 and 5.5 illustrate the watershed surface and its relationship to the tunnel. Queen Creek flows intermittently through a steep-walled canyon transecting the tunnel.

5.4.1 Surface Water

Most surface water in the Apache Leap area occurs as ephemeral streams or as runoff captured in stock ponds. Streamflow is intermittent, flowing after precipitation events for periods of days or weeks, although seasons of heavy rainfall may induce temporary baseflows. At least two springs have been located in the region. Flow is limited to seasonal discharge and is unreliable during periods of drought.

Only two drainage systems, Devil's Canyon and Queen Creek, serve the region. Devil's Canyon is a north-south trending valley cut 6 km east of Superior. Flowing southward, the stream has incised into the tuff section greater than 150 m in some places. Water as streamflow or pools is present in parts of Devil's Canyon most of the time.[2]

The Queen Creek watershed drains the region from Superior to the highlands about 7 km northeast of Superior. Queen Creek cuts into the tuff, creating a canyon that in some places is more than 180 m deep. At Superior and further westward, the creek drainage is in basin fill and becomes more washlike. The section of Queen Creek east of Superior is important for this study. For that reach, drainage basin area is about 18 km^2, and nearly all of this is in Apache Leap Tuff. Although Queen Creek is considered an intermittent stream, some stretches in the uppermost reaches are springfed and flow most of the time.

5.4.2 Groundwater

There are no known studies of groundwater conditions published for the Apache Leap region; however, drilling records from mining and ranching activities provide some information about the local hydrogeologic system. Local alluvial aquifers overlie the tuff in small, closed basins and valleys, providing a water source as shallow as 2.5 m below the surface (Arizona Department of Water Resources, 1990). Water levels, however, fluctuate rapidly in response to pumping and precipitation events such that wells in alluvial aquifers are unreliable during dry years.[2]

---

[2]Personal communication. Clary, T.A., 1991, Geologist and resident, Miami, Arizona.

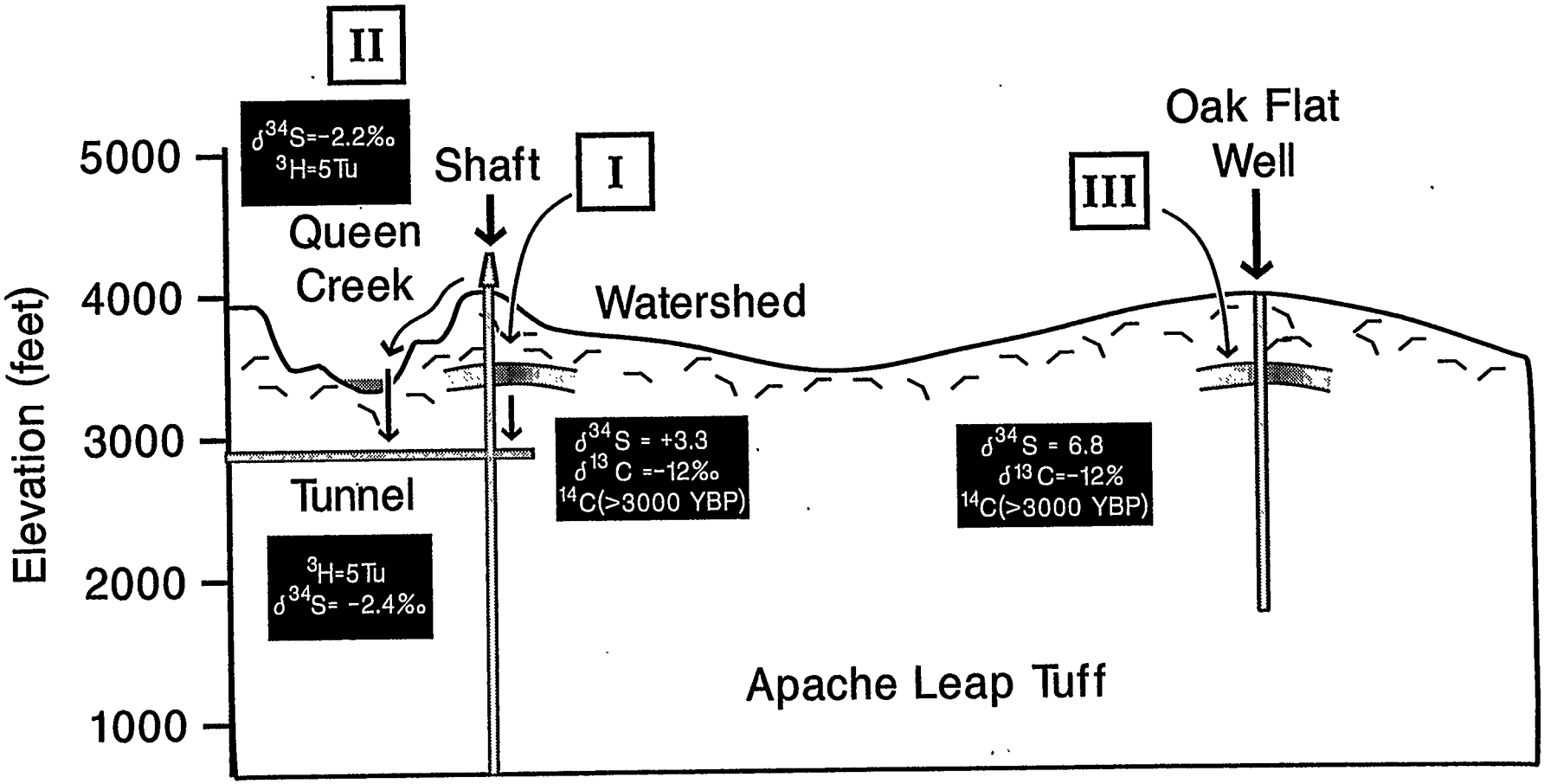

Figure 5.3. Regional schematic cross section from the Never Sweat Tunnel to the DOE Oak Flat Well (Figure 5.1). Roman numerals indicate three different flow pathways for surface water to recharge the perched water zone.

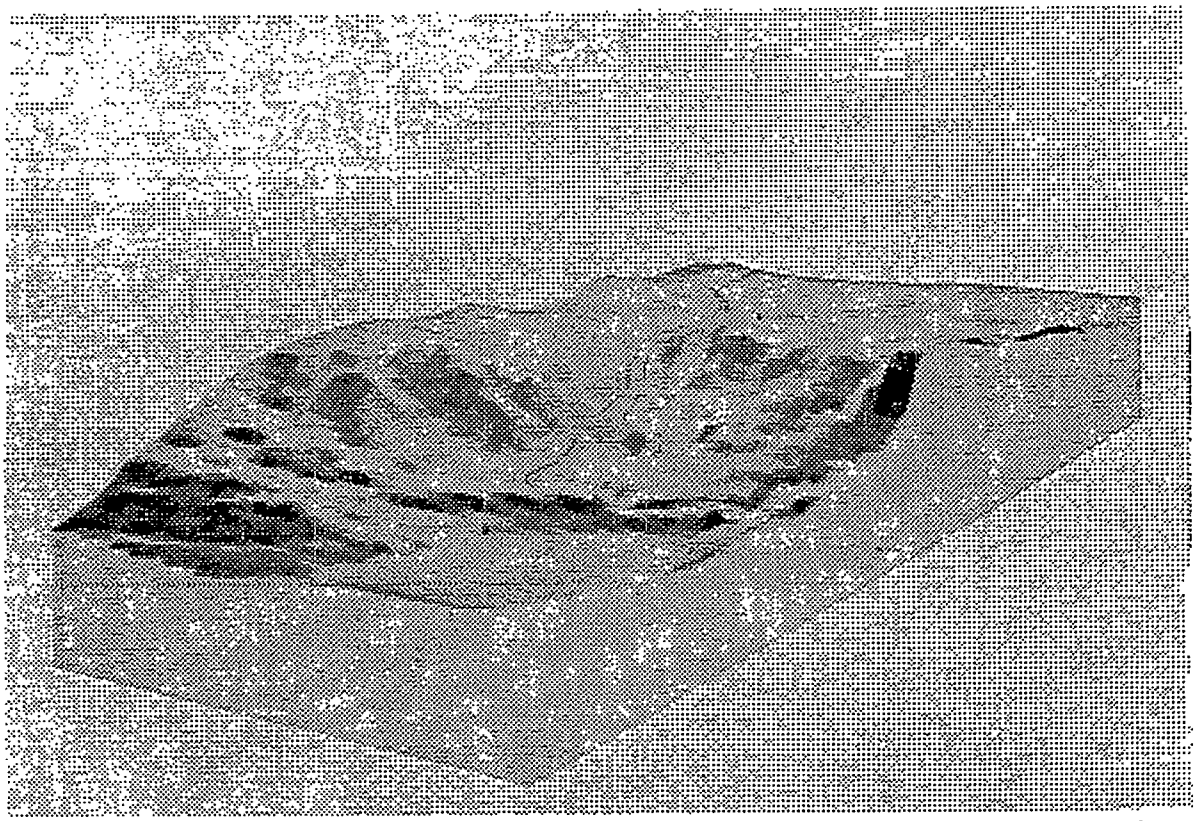

Figure 5.4. Computer generated image of the land surface at the research site, observed toward the northeast, illustrating the Queen Creek Watershed. The tunnel entrance is shown as the black rectangle in the foreground.

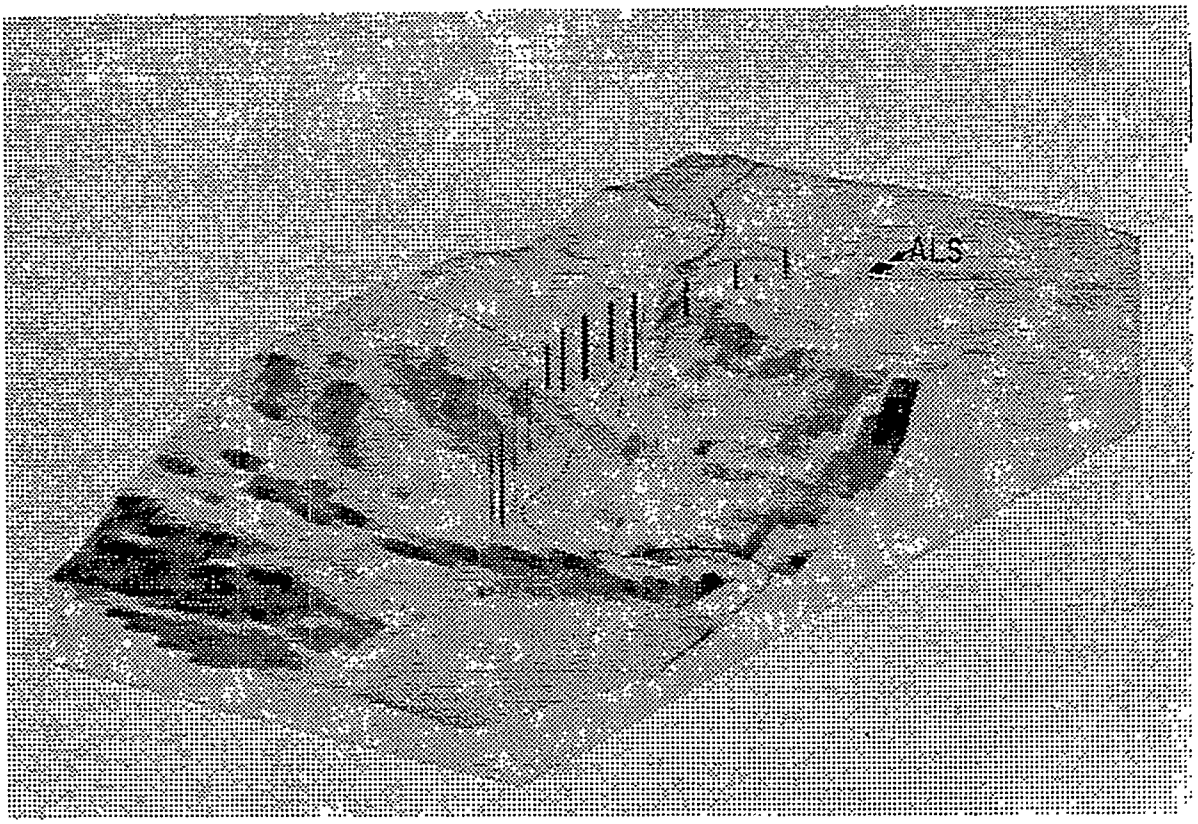

Figure 5.5. Computer generated image of the topography from higher angle then in Figure 5.4. The tunnel traverse is identified by equidimensional flags emerging vertically from the tunnel. The covered borehole site is also identified (ALS). (not to scale)

At present, data have been obtained from 25 wells and boreholes drilled into the Apache Leap tuff. Most recently, at Oak Flat, information about groundwater conditions was acquired by DOE during experimental drilling of a borehole. The well is 2.8 km east of #9 shaft and penetrates 522 m of tuff. Drilling was done using air, without addition of water. Cuttings and groundwater were continuously removed by air circulation; thus, discharge from the borehole reflected groundwater flow into the well (Sample Management Facility, 1990).

In the first 110 m, most core retrieved from the borehole was dry but some sections were damp, suggesting partial saturation. At 110 m below land surface, core became saturated and static water level rose to 88 m below land surface. Examination of core at and below this depth did not reveal a confining layer, but researchers noted an increase in structures described as "leached discontinuous fractures or possibly collapsed lithophysae" (Sample Management Facility, 1990).

Borehole discharge rates began to increase at a depth of 148 m. This increased discharge along with spontaneous potential and resistivity log data suggests penetration of a second separated saturated zone. Static water level remained constant at 88 m (Sample Management Facility, 1990).

After sealing off the upper 338 m of the borehole with cement, drilling continued through unsaturated rock beyond a third water-bearing zone, encountered at 448 m below land surface. Subsequent video logging revealed fracture discharge there that was estimated to be 1 gallon per minute (gpm) (Sample Management Facility, 1990).

Other wells and boreholes have been drilled into the tuff for mineralogical exploration or water-supply purposes. Much hydrologic data from this drilling were not originally recorded, has since been lost, or is of questionable accuracy, but existing data provide enough information for approximation of a depth to water map for parts of the study area. All available data related to this water-bearing zone are summarized in Table 5.3. Figure 5.6 shows available water level elevation data and an interpretation of the surface comprising those data points. The surface represents the uppermost extent of the uppermost perched saturated zone. Clearly, the local hydraulic gradient dips to the south with the aquifer discharging into Devil's Canyon.

Information about groundwater conditions in the area near Magma Mine, the field area proper, allows for only partial characterization of the system. A local water table has been defined by mine dewatering, pumping primarily at #9 shaft. Water levels are maintained below the 4100 level which is at an elevation of 162 m below sea level and 1432 m below ground surface at #9 shaft[1].

Prior to 1972, two springs issued from fractures into Queen Creek.[3] At elevations 1024 m and 1134 m above sea level, the springs are evidence of former surface interception of a local water table or communication with a deeper confined system. Upon construction of Never Sweat Tunnel and #9 shaft, both springs ceased flowing, indicating partial or total aquifer dewatering.

During drilling of #9 shaft, a water-bearing zone was encountered and subsequently sealed. The shaft was sealed between elevations 1020 m and 1041 m. Most water entered the shaft at 1031 m above sea level.

---

[3]Personal communication. Delbridge, W.G., 1990, Division Manager, Arizona Water Company, Superior, Arizona.

Table 5.3. Tabulation of All Known Water Level Data Related to the Shallow Perched Zone Within the Apache Leap Tuff. See Figure 5.6 for reference.

Well Identifier	Well Owner	Land Elevation (feet)	Elevation of Water Surface (Jmol)	Source of Data
34	ASLD	3000	2835	DWR
38	ASLD	3980	3281	DWR
31	ASLD	3900	3603	DWR
27	Asarco	4300	4003	DWR
25	ASLD	4160	3662	DWR
22	ASLD	4140	3540	DWR
19	Asarco	4200	3799	DWR
15	Asarco	4080	3721	DWR
DOE	DOE	4080	3721	SMF
16	Asarco	4210	3849	DWR
14	Asarco	5080	4689	DWR
13	Asarco	4720	4223	DWR
10	Asarco	4460	4108	DWR
9	Asarco	4420	4059	DWR
11	Asarco	4640	3888	DWR
1	Knight	4600	4400	DWR
R	Rotz	4445	4334	DWR[4]
S	Skousen	4445	4334	DWR[4]
W	Wiley	4450	4370	DWR[4]
B	Buckridge	4450	4337	DWR[4]
C2	Clary	4460	3809	Clary[5]
C1	Clary	4455	3806	Clary[5]
62	Reynolds	4560	4210	DWR
84	Asarco	4800	4410	DWR
96	Asarco	4720	3855	DWR

[1] ASLD - Arizona State Land Department
[2] DOE - U.S. Department of Energy
[3] DWR - Arizona Department of Water Resources Well Registry Report, 9/21/90
[4] DWR - Arizona Department of Water Resources Well Driller Report for Paul Buckridge, 8/14/90
James L. Rotz - 6/6/90
C.R. Skouser - 6/6/90
Molan A. Wiley - 7/18/90
[5] Clary - Thomas A. Clary, written communication (1991)

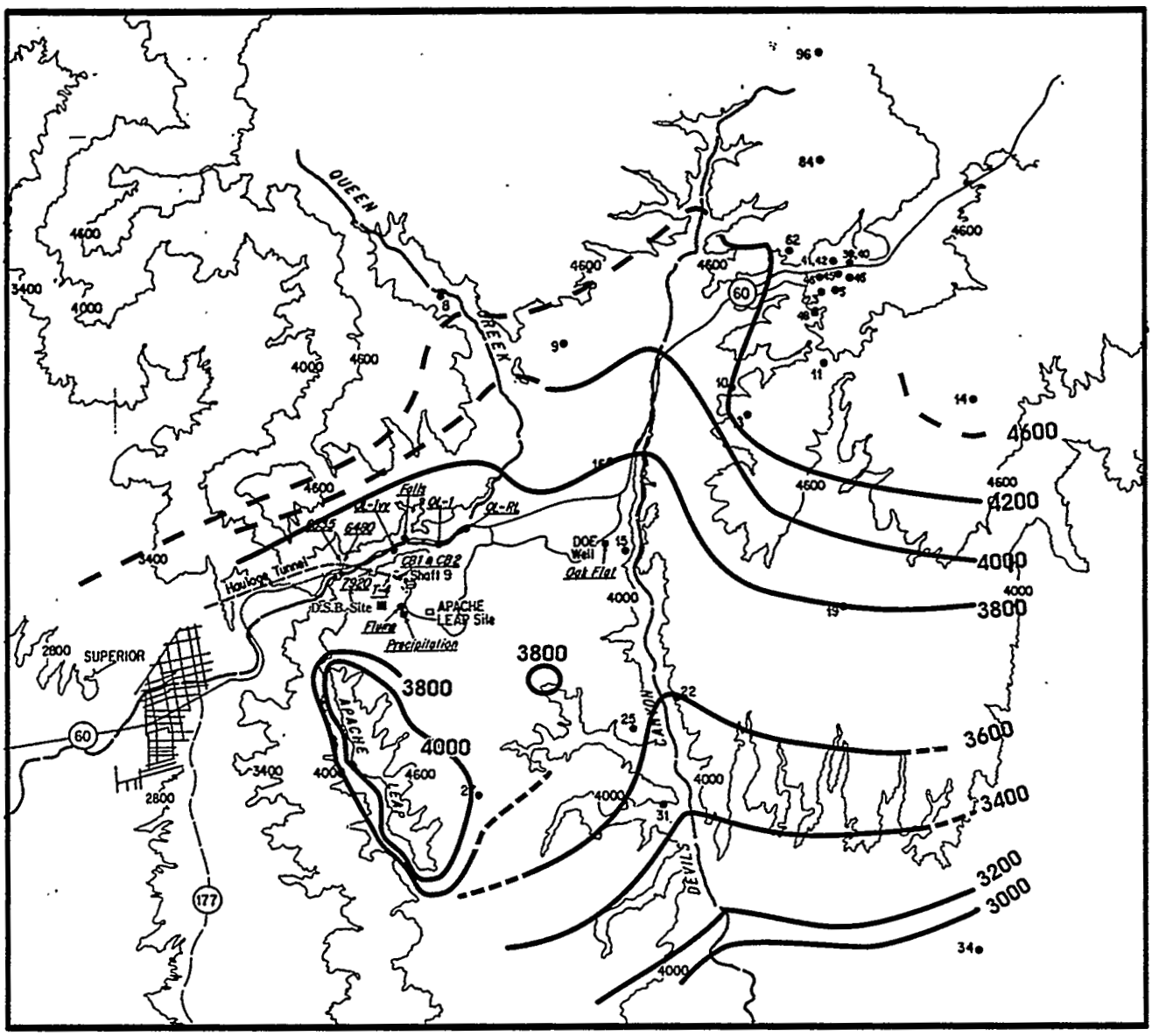

Figure 5.6. Regional water level map based on reports of first encounter of water from all drilling in the regional (data from Table 5.3) (Elevations in feet).

5.4.3 Communication Between Surface Water and Groundwater

An instructive set of pumping records has been located which can be used to correlate inflow of water to the Magma Mine derived most likely from flow in Queen Creek. Unfortunately, the historical record is only for the time period from 1975-1980.

The relationship between precipitation, Queen Creek discharge, and influx to Magma Mine demonstrates communication between surface water and groundwater. Although historical data for Queen Creek discharge and influx to the mine do not exist, information has been recorded for conditions that directly relate to those data.

The relative magnitude of discharge in Queen Creek is approximated by the volume of water pumped from #1 dam in Queen Creek, 0.4 km downstream from the contact between tuff and underlying limestone. Number 1 dam, operated by Arizona Water Company, is one component of Superior's municipal water supply. An intermittent source, creek water from the dam, augments the town's more dependable groundwater supplies when it is available.[3] Pumping is initiated at the onset of creek flow and ceases when the supply is exhausted. Thus, the volume of water pumped during a month is directly proportional to the combined duration of flows during that month. Because duration of flow is roughly proportional to discharge for this intermittent stream, #1 dam pumping records reflect discharge in Queen Creek.

Relative influx to Magma Mine is approximated by mine dewatering. Mine operators continuously pump water from one or more stations as needed to maintain a water level below active mine workings. Numerous factors determine the volume of water pumped, including the desired water level and mechanical malfunctions, but influx to the mine is a primary factor.[1] Thus, mine pumping data reflect relative influx of groundwater to Magma Mine.

Figure 5.7 shows a distinct correlation between the occurrence of precipitation and surface water and the volume of water pumped from Magma Mine. Six peaks in mine pumping are clearly associated with peaks in precipitation and surface runoff. Additionally, mine pumping peaks show a slight delay compared to surface runoff and precipitation, as is expected for a cause-and-effect relationship.

Semiquantitative information about travel times between surface and mine may be inferred from the magnitude of peak displacement. For the period represented in Figure 5.7, monthly mine and creek pumpage peaks show response times that range from zero to three months when measured from the onset of one peak to the onset of an affiliated peak. The delay suggests that travel times for water flowing from the surface to the upper portion of the mine are in the order of weeks or months, at least for the higher discharge fractures draining into the mine.

5.5 WATER CHEMISTRY

Water samples from the Apache Leap area were collected over a 14-month period to determine representative chemical compositions and variation of composition over time. Samples were taken repeatedly from precipitation, surface water, subsurface fracture flow, and groundwater sources.

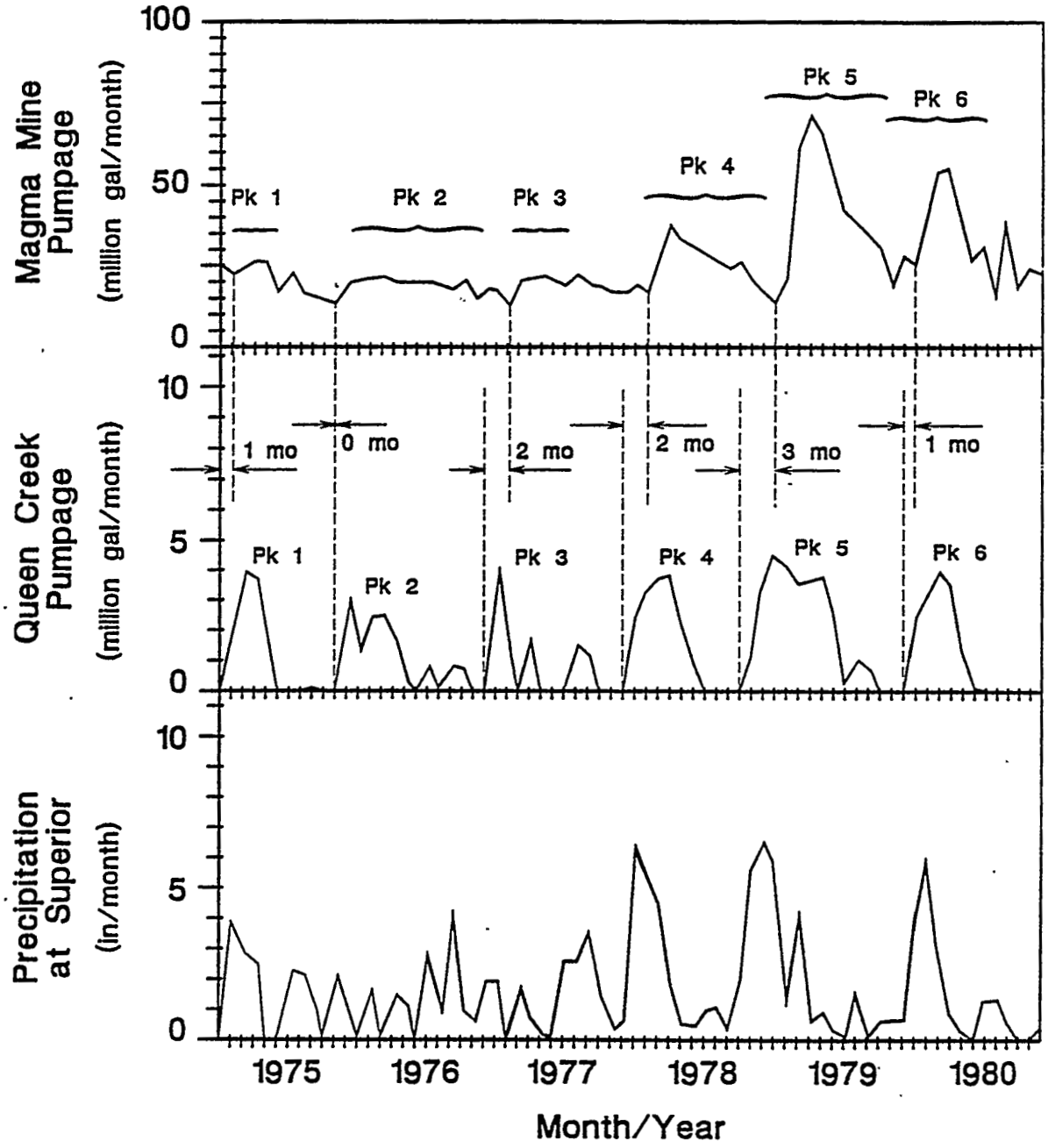

Figure 5.7. Correlation between precipitation, pumping in Queen Creek, and pumping of the mine works by Magma Copper Co. Delay in response time is a crude indication of travel time from land surface into the mine works.

5.5.1 Sample Sites

Sample collection sites are shown in Figures 5.2(a-e) and 5.6. Precipitation was sampled 0.5 km south of Magma Mine's #9 shaft. Surface water samples were collected at five sites, representing runoff within a subbasin in the Queen Creek watershed, one Queen Creek tributary, and three locations along Queen Creek. The flume sample site refers to the primary drainage in a 0.24 ha basin that is within the larger Queen Creek watershed. Although most of the creek bed is exposed bedrock, water flows over and through sandy alluvium at the collection site. Much of the basin is exposed tuff, but a thin soil zone covers about 50% of the watershed (Rasmussen et al., 1990). The falls sample site is at a tributary to Queen Creek about 30 m north of its confluence with the creek. Queen Creek sample sites are, from upstream to downstream, QC-RC, QC-1, and QC-Ivy. Most tributaries to Queen Creek enter at or below QC-1; thus, flow at QC-1 and QC-Ivy is in rapid response to precipitation events. At QC-RC, response to precipitation is more delayed and discharge is lower.

Groundwater was sampled two times at Oak Flat. One sample was taken from the upper water-bearing zone. A second, however, was sampled at a level within the second zone, but not isolated from discharge from the first. Thus, the second sample is a mixture of waters from two aquifers. Subsurface fracture seeps were sampled in Magma Mine's Never Sweat Tunnel. Although fracture traces are ubiquitous in the tunnel, most are dry or visibly damp without observable flow. Samples were taken from only those fractures with sufficient discharge for collection into an open container. At two sample sites, CB1 and CB2, discharge was not from discernible fractures but from boreholes drilled into the tunnel walls at oblique angles.

5.5.2 Field and Analytical Methods

Precipitation was sampled using an Aerochem Metrics automatic sensing wet/dry precipitation collector, Model 301. The collector is equipped with two polyethylene buckets secured to a bench, a horizontal lid which covers one or the other bucket, and a moisture sensor that triggers movement of the lid from one bucket to the other. Normally, the lid covers the "wet precipitation" bucket. At the onset of precipitation, however, the lid is shifted to expose that bucket, then returned after precipitation ceases. Samples were retrieved from the collector as soon as possible after a storm. Surface water was sampled by taking grab samples. A plastic beaker was dipped into the stream at a point of visible current.

Groundwater from Oak Flat was sampled while borehole drilling was in progress during interruptions in the drilling/coring process. As a part of the drilling process, cuttings and formation water were continuously purged by circulation of the drilling fluid, compressed air. Thus, during drilling interruptions, water in the borehole was assumed to be groundwater that had entered the borehole since drilling had ceased. Samples were retrieved with a Timco 3- liter polyvinyl chloride (PVC) bailer.

Fracture waters were sampled by collection into a plastic beaker held as near the fracture as possible. In most cases, collections were at the fracture surface, but for one sample, T-4, samples were collected as dispersed drops falling three meters from the tunnel ceiling. The boreholes that were sampled were fitted with hoses and pipes to divert discharge to a reservoir. Samples were collected by disconnecting those hoses and filling a plastic beaker.

Because of their instability, the parameters, temperature, pH, and alkalinity were measured at the sample collection site. Temperature was measured with a mercury thermometer and pH was measured using an Orion portable pH meter, Model SA 250. Alkalinity was determined by titration into a filtered sample using .0121 N HCl.

Samples were preserved for future laboratory analysis. Each sample was filtered through a 0.45 μm membrane, then transferred to 1-liter polyethylene bottles. One liter of sample, for analysis of cations, was acidified by addition of one ml concentrated nitric acid. One liter was left unacidified for analysis of anions and silica concentrations. Samples were stored in a cool, dark place until laboratory analysis at a later time. Surface water samples were refrigerated.

Chemical analyses were done at The University of Arizona and by two independent laboratories. In general, one analyst performed selected analyses on an entire subgroup of samples, but duplicated analyses verified results by different analysts and methods.

Concentrations of the major anions, chloride (Cl), nitrate (NO_3), and sulfate (SO_4) were determined by ion chromatography. At The University of Arizona, analyses were done using an ion chromatograph (IC) equipped with a 50-ml sample loop, a Dionex Ion Pac AS4A separator column, and a Dionex conductivity detector. Selected precipitation samples were analyzed at the United States Geological Survey (USGS) National Research Laboratory in Arvada, Colorado. Filtered, unacidified samples were analyzed for anion concentrations.

Analyses of the major cations, calcium (Ca), magnesium (Mg), sodium (Na), and potassium (K) were done primarily at The University of Arizona using atomic absorption spectrometry. A Perkin Elmer atomic absorption spectrometer (AA) equipped with an acetylene/air flame burner was employed. For Ca and Mg analyses, a lanthanum oxide solution was added to samples to alleviate interferences. Some precipitation samples were analyzed for major cations at the USGS National Research Laboratory by the inductively coupled plasma (ICP) method. Cation concentrations were measured using filtered acidified samples.

Determination of minor and trace metals was done at the USGS National Research Laboratory using an ICP coupled with a mass spectrometer (ICP-MS). Filtered, acidified samples were analyzed.

At The University of Arizona, silica concentrations were determined colorimetrically by the molybdosilicate method (American Public Health Association et al., 1985) using a Beckman DU-40 spectrophotometer. Selected samples were analyzed by ICP at Skyline Labs, Inc. in Tucson, Arizona.

5.5.3 Chemical Composition of Water Samples

Chemical composition of precipitation samples shows variation from storm to storm and within individual storm systems. Table 5.4 shows chemical composition of four precipitation samples. On an equivalent basis, dominant cations vary, but calcium or sodium are usually most abundant. Sulfate and nitrate are consistently dominant anions. In general, the water is dilute. Computed estimates of total dissolved solids (TDS) (Hem, 1985) for most samples are less than 2 mg/l. The waters are acidic, about pH 5. Silica concentrations are generally below a detection limit of 0.04 mg/l as SiO_2.

Surface water chemistry varies according to sample location. Table 5.5 gives a representative chemical composition for each sample site. Flume samples collected after different storms are similar in chemical composition. For four samples, values for pH range from 5.6 to 6.0, with calcium and sulfate the dominant cation and anion. Silica concentrations vary more than other constituents, ranging from 6 to 24 mg/l as SiO_2. Falls composition is similar to that of Flume, but pH and TDS are higher. Waters from QC-1 and at QC-Ivy have pH values that range from 6.5 to 7.2, and water type is either Ca-SO_4 or Ca-HCO_3, reflecting fluctuation in alkalinity more so than in sulfate concentration. Silica concentrations range from 18 to 32 mg/l as SiO_2. QC-RC samples are of pH 6.8 to 8.0. Consistently, calcium and bicarbonate are dominant, although alkalinity varies considerably over time. Silica concentrations range from 28 to 32 mg/l as SiO_2.

Table 5.4. Chemical Composition of Four Precipitation Samples from the Apache Leap Study Area. Concentration in units of mg/L unless otherwise noted; "nd" indicates no data available.

Constituent/Property	Rain 11-21-89	Snow 1-18-90	Snow/Rain 1-18-90	Rain 2-1-90
T (°C)	11.4	nd	nd	3.0
pH	4.8	~5	~5	5.3
Alkalinity (HCO_3)	<.5	<.5	<.5	<.5
SO_4	0.62	0.14	0.38	0.74
NO_3	0.71	0.17	0.35	0.78
Cl	0.17	0.09	0.18	0.49
Na[a]	<.006	0.026	0.063	0.273
K[a]	0.13	<.05	<.10	<.10
Ca[a]	0.148	0.016	0.126	0.203
Mg[a,b]	9.3	3.2	9.8	39.5
Al[a,b]	1.3	5.0	nd	4.2
Fe[a,b]	<5	<5	<5	<5
SiO_2[a]	<0.04	<0.04	<0.04	<0.04

[a] Laboratory analyses by John Garbarino, U.S. Geological Survey, National Research Laboratory, Arvada, Colorado

[b] units of μg/L

Groundwater sampled at Oak Flat is Ca-HCO_3 dominant. The water is basic, pH 8.4 for the upper aquifer, and silica concentration is about 65 mg/l. Table 5.5 gives chemical composition for one sample from the upper aquifer.

Thirty-eight samples have been collected in Never Sweat Tunnel. Although water has been sampled from seven different sites, some pairs of samples are clearly duplicates. Like chemical compositions and physical proximity indicate that samples T-6335 and T-6340 are two samples from one source as are samples CB1 and CB2. Considering these pairs one sample each renders five tunnel sample sites.

Table 5.5. Chemical Compositions of Five Surface and One Groundwater Sample from the Apache Leap Study Area. Concentration is in units of mg/L unless otherwise noted; "nd" indicates no data available. The headings "QC", "Flume" and "Falls" refer to Queen Creek, the watershed and a waterfall resulting from a major storm which emptied into Queen Creek.

Constituent/ Property	QC-RC 8-17-90	QC-IVY 8-17-90	QC-1 1-9-90	Flume 1-18-90	Falls 4-4-90	Oak Flat[b] 4-4-90
T (°C)	25.0	19.8	5.0	5.2	13.4	21.2
pH	8.0	7.0	6.6	6.0	7.7	8.4
Alkalinity (HCO_3^-)	90.4	35.1	12.6	0.7	7.8	164.8
SO_4	26.4	27.6	46.9	17.4	34.4	12.7
NO_3	nd	nd	nd	nd	nd	16.6
Cl	4.6	3.6	3.5	1.7	5.1	15.1
Na	7.0	6.1	7.4	3.7	6.8	24.8
K	3.1	1.9	1.4	0.9	1.5	3.0
Ca	27.5	15.4	14.6	4.2	8.8	36.0
Mg	7.0	3.9	3.8	1.0	2.6	8.3
Al[a]	17.1	36.1	45.0	nd	nd	68.1
Fe[a]	11.9	41.7	19.8	32.8	nd	29.6
SiO_2	32.0	28.0	19.0	15.3	34.0	65.0

[a]Laboratory analyses of Al and Fe by John Garbarino, U.S. Geological Survey, National Research Laboratory, Arvada, Colorado.
[b]Groundwater sample collected with bailer during drilling.

Table 5.6 shows chemical composition of two sets of tunnel water samples. Chemical compositions vary according to location and, at the western portion of the sampled section of the

tunnel, they vary with time. In general, values for pH range from 7.1 to 8.1. Bicarbonate is the dominant anion in all samples, and calcium is generally the dominant cation, although sodium is equally abundant in samples from one fracture. Silica concentrations range from 41 to 65 mg/l as SiO_2. The chemical analyses of all samples collected to date are listed in Appendix D.

Table 5.6. Chemical Compositions of Waters Sampled from Never Sweat Tunnel at the Apache Leap Study Area (after Lyons, in preparation). Concentration units given in mg/L unless otherwise noted.

Constituent/ Property[a]	T-6335 2-27-90	T-6340 2-27-90	T-6480 2-27-90	T-7920 2-27-90	T-4 2-27-90	T-CB2 2-27-90	T-CB1 2-27-90
T (°C)	19.4	19.6	21.0	21.5	19.2	24.0	24.0
pH	7.3	7.1	7.5	8.14	8.0	8.0	8.0
Alkalinity (CHO_3^-)	68.5	69.4	92.4	138.2	141.8	137.6	138.2
SO_4	35.6	36.0	33.3	5.3	35.2	15.7	16.6
NO_3	4.1	4.2	5.0	2.9	9.4	3.2	2.6
Cl	3.7	3.9	5.5	5.3	9.8	6.7	6.7
Na	13.3	13.3	17.5	26.5	25.3	21.5	21.0
K	0.57	0.57	0.72	0.57	0.88	0.81	0.82
Ca	22.8	23.0	25.0	20.5	36.0	28.2	29.2
Mg	4.2	4.2	4.8	3.8	6.2	5.0	5.2
Al[b]	8.1	11.2	9.3	9.2	13.0	8.2	7.1
Fe[b]	<5.0	<5.0	<5.0	<5.0	2.4	<5.0	<5.0
SiO_2	41.8	42.4	54.4	62.4	63.1	63.0	62.7

[a]Laboratory analyses of Al and Fe by John Garbarino, U.S. Geological Survey, National Research Laboratory, Arvada, Colorado. All others by Elizabeth Lyons, Department of Hydrology and Water Resources, University of Arizona, Tucson, Arizona.
[b]units of μg/L

Examination of variation between tunnel waters reveals distinct patterns defined by incremental changes in chemical composition of waters sampled along the length of the tunnel. Two parameters share a trend in which constituent concentrations increase from the western end, T-6335/6340, to midway, T-7920, then remain relatively constant to the eastern end, CB1/2. As illustrated in Figures 5.8 and 5.9, mean alkalinity and mean silica concentrations follow this pattern.

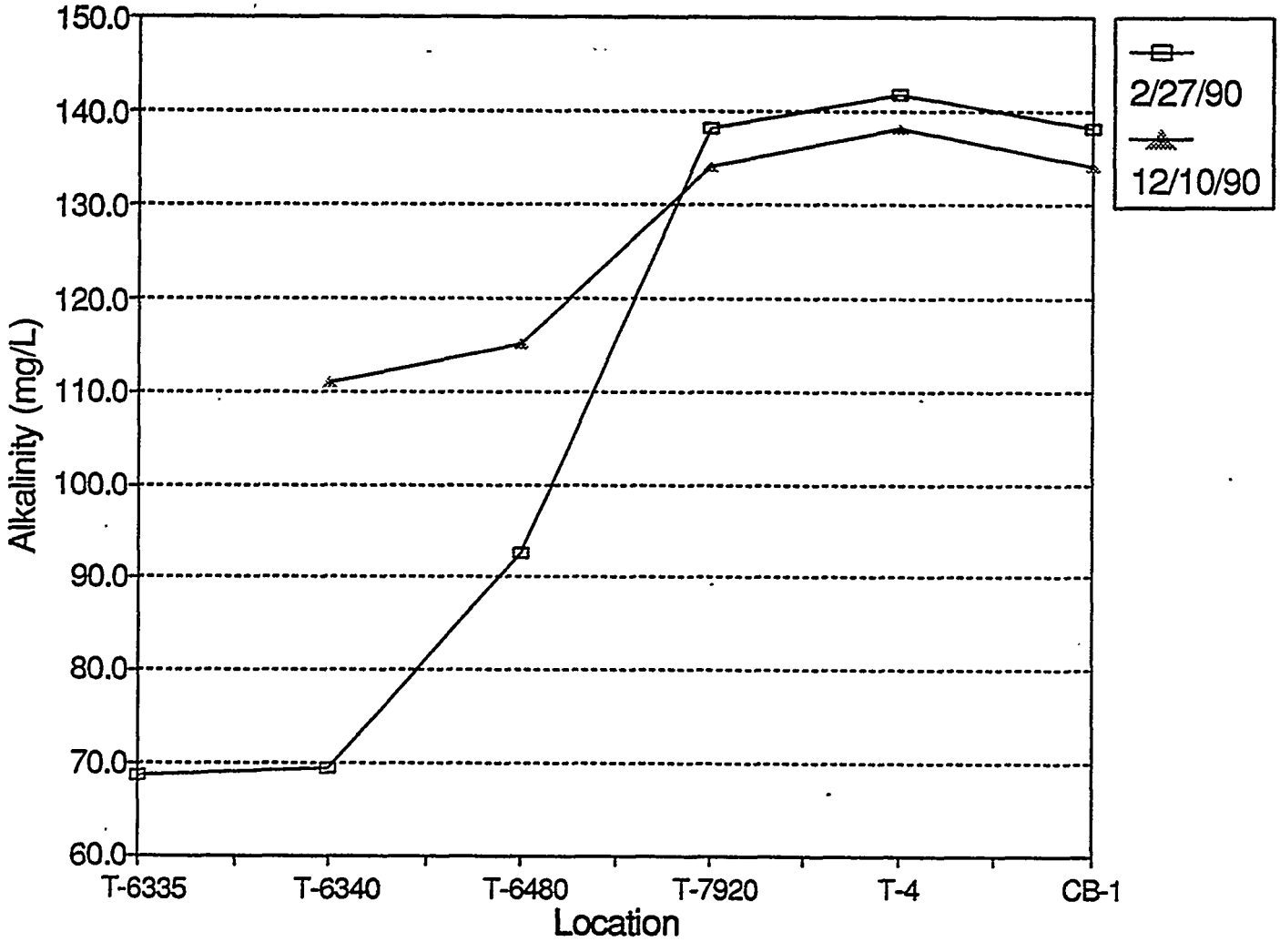

Figure 5.8 Change in alkalinity values of water draining fracture located in Never Sweat Tunnel

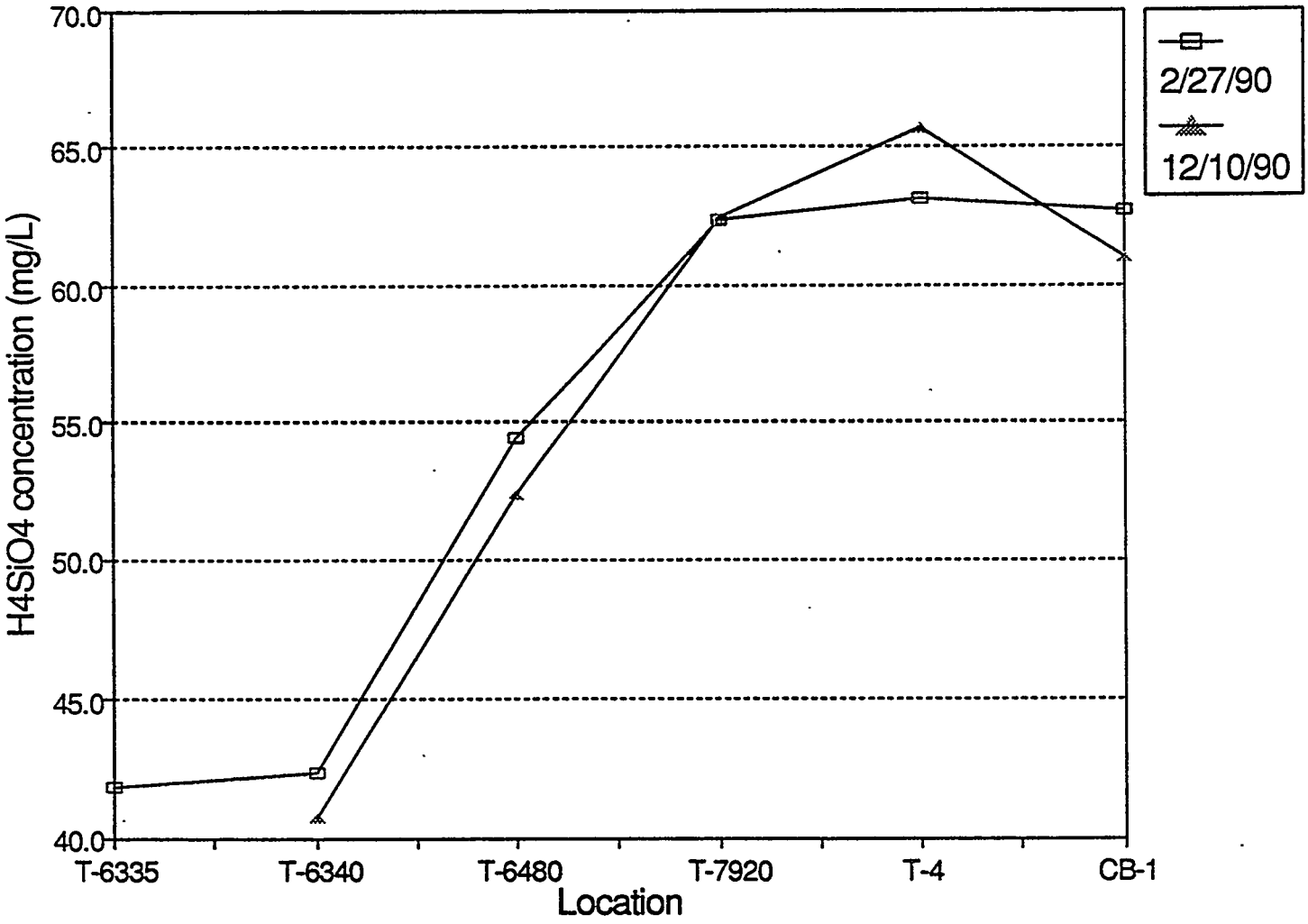

Figure 5.9 Change in concentration of dissolved silica in water draining fractures in Never Sweat Tunnel

Another pattern is evident when ratios of sulfate to chloride and calcium to sodium are plotted against distance into the tunnel. Mean SO_4:Cl decreases incrementally from T-6335/6340 to CB1/2 with an interruption in the pattern at T-7920. Mean Ca/Na behaves similarly, although the trend is more subtle.

For most parameters examined, Queen Creek waters resemble west end tunnel waters, and Oak Flat waters are more similar to east end tunnel waters. In some cases, chemical parameters of Queen Creek and Oak Flat waters serve as endmembers in the trends previously defined for tunnel water chemical composition.

5.6 TRAVEL TIME STUDIES

The movement of water and solute through fractured unsaturated tuff is being investigated in detail using both the Never Sweat Tunnel Research Site and the new Deep Slant Borehole Site. The following approaches are being employed to examine the fundamental characteristics of solute travel time in a fractured environment and are discussed in subsequent sections.

Never Sweat Tunnel Research Site

- Automated monitoring of electrical conductivity in Queen Creek and in fluid that discharges from fractures into the tunnel at two specific locations.
- Stable and radioactive isotopic composition of water discharging from fractures.
- Mass transfer modeling of the evolution of water composition in the tunnel.

Deep Slant Borehole Research Site

- Borehole data
- Stable and radioactive isotope data

5.6.1 Never Sweat Tunnel Research Site

5.6.1.1 Automated Monitoring

Initial sampling in the Never Sweat Tunnel was done by conducting day-long sampling trips during which time samples were obtained from discharge from several fractures. Once it was determined that there was indeed variation in the water chemistry, the need for a continuous monitoring capability was obvious. In May 1991, three Campbell Scientific CR10 dataloggers were installed: one was placed at the surface to monitor conductivity of water in Queen Creek, and two others were placed in the Never Sweat Tunnel. One unit was installed in the tunnel at the fracture designated T-6340 to monitor seepage from Queen Creek; the second was placed at the east end of the tunnel to monitor flow from fractures most likely draining the perched water table. Chemical analyses of samples from the east end of the tunnel confirm that the water composition is relatively constant over time, further supporting the hypothesis that a perched zone is present.

The period of record for monitoring conductivity at all three locations is now sufficiently long, May 1991-present; that influence of variable composition of Queen Creek recharge into the

fractures has been detected in the discharge from fractures in the tunnel. Queen Creek is an intermittent stream which is dry most of the year. Following storm events, the composition of Queen Creek is variable, initially more dilute; then, with evaporation and diminishing flow, the conductivity increases rapidly, and eventually the stream returns to dryness (Figure 5.10). The conductivity and flow rate of water discharging from fractures at the east end of the tunnel tends to stabilize at some background value, which is probably the composition of the perched water table located between the tunnel and the land surface (Figure 5.10). In contrast, the conductivity of the water which is draining the fractures located below Queen Creek is directly affected by changing water compositions in the Creek. The record of conductivity changes as shown in Figure 5.10 indicates that there may be a travel time on the order of weeks between recharge of flow in Queen Creek to discharge into the tunnel over a distance of approximately 150 meters. The details of the flow system, the potential for matrix and fracture interaction, and our ability to simulate this process with a variably saturated transport code is the subject of a Masters Thesis currently underway.

An important component of the simulation of transport through the fracture system is the frequency, quantity, and duration of flow events in Queen Creek. At present, no stream gauging is done on this portion of Queen Creek. Correlations may be made to the rainfall quantity data and data on the discharge from the watershed, especially after storm events. These data are displayed in Figure 5.11. The simulation of flow and transport will provide the best estimate of travel time for movement of solute along this extensive fracture network. The data describe the scenario of intermittent surface-derived flow over significantly longer distances than previously considered in the fractured unsaturated tuff environment.

5.6.1.2 Isotopic Studies

Stable and radioactive isotopes are being used to identify water source, determine travel time, and quantify reaction progress for fluid that passes through the unsaturated tuff section. To date, samples have been collected and analyzed for stable isotopic composition (δD, δ^{18}O, and δ^{13}C); in addition, the tritium and ^{14}C content for a small number of samples determined.

Deuterium and Oxygen

Samples have been collected and analyzed for deuterium and oxygen stable isotopic values from rainfall and snow, surface runoff, Queen Creek, and the Never Sweat Tunnel (Figures 5.12 to 5.16). The results are plotted along with the meteoric water line (MWL) of Craig (1961), and they plot close enough to the line to be considered meteoric. The majority of the samples indicate no major reaction pathway which would pull the plotted data away from the line other than evaporation, which is visible in the watershed and subsequently is reflected in the Queen Creek and Never Sweat Tunnel water samples. This seems to be particularly true for the tunnel samples collected in the portion of the tunnel most affected by Queen Creek seepage (Figure 5.17).

Tunnel samples all plot in a small cluster, ranging in values for deuterium of from -74 to -59‰ and for oxygen -10.2 to -4.8‰. The rainfall samples exhibit much greater variation with values for δD more than 40‰ on either side of the mean for tunnel δD; the δ^{18}O behaves in a parallel fashion. Rainfall amounts will be compared with isotopic signature in the future when all the outstanding samples have been analyzed to determine if there is a correlation between water from major storm events, which is likely to be recharged with isotopic signature. The early data indicate, however, that the vadose zone water is an integrated value for storm waters over the seasons. It

(a)

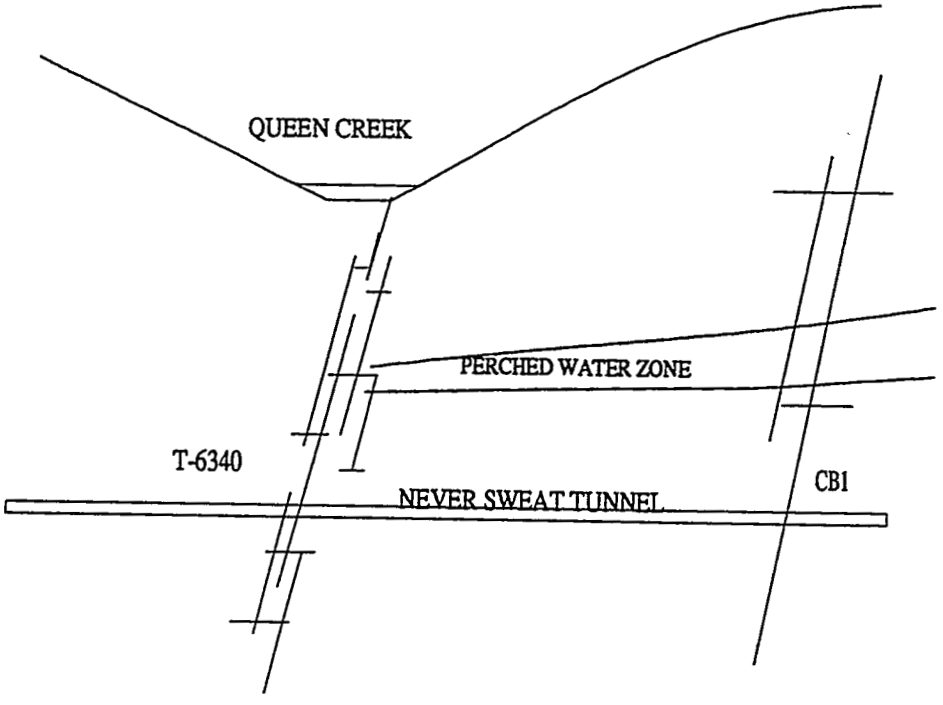

(b)

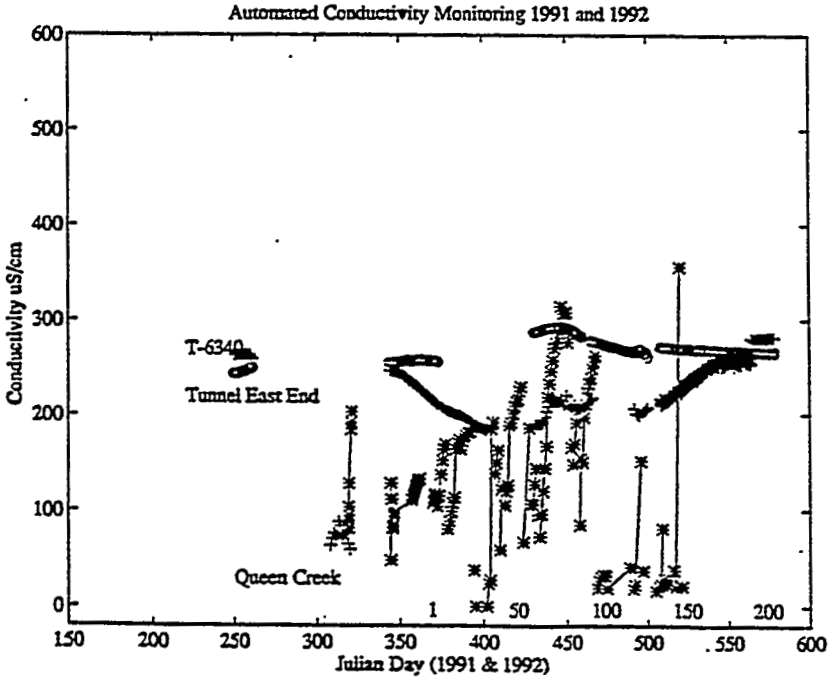

Figure 5.10. (a) Schematic representation of fracture network linking Queen Creek with Never Sweat Tunnel. Flow path is approximately 150 m. (b) Record of conductivity values from the Tunnel East End (o), the tunnel at T-6340 (+) and Queen Creek (*).

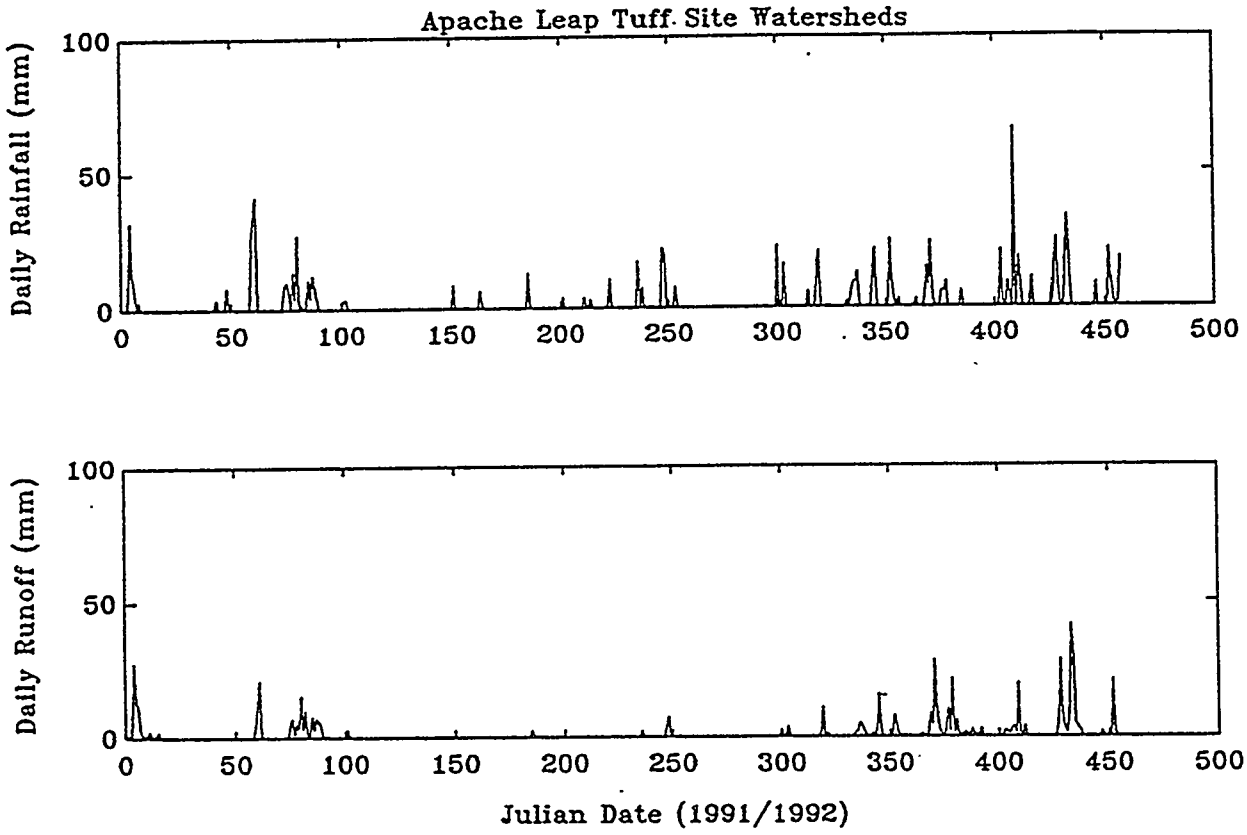

Figure 5.11. Data for rainfall and runoff at the instrumented watershed.

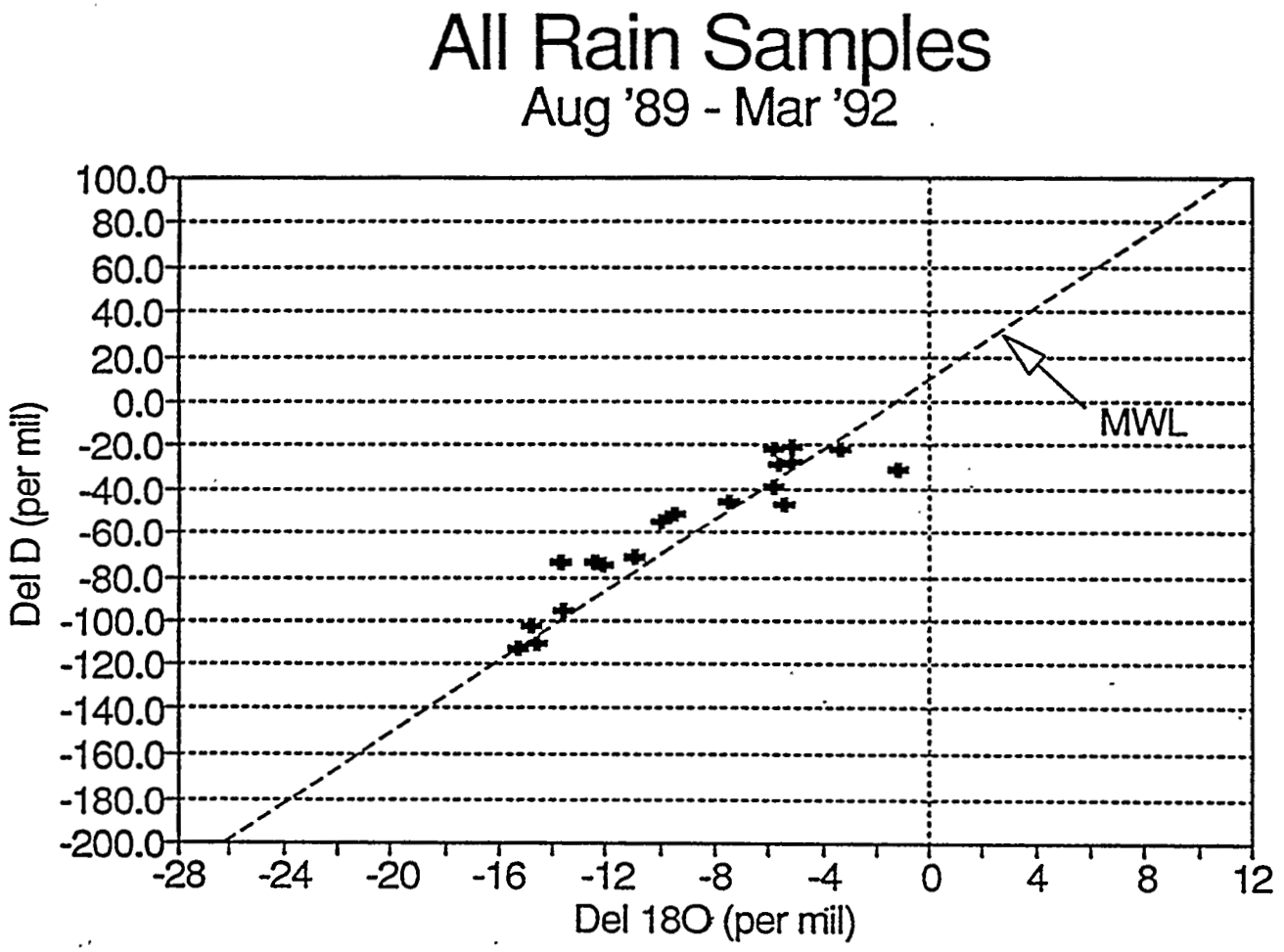

Figure 5.12. The hydrogen vs. oxygen stable isotope values of rainfall samples collected at the Apache Leap Research Site. Data are compared to the meteoric water line (MWL) of Craig (1961, © AAAS)

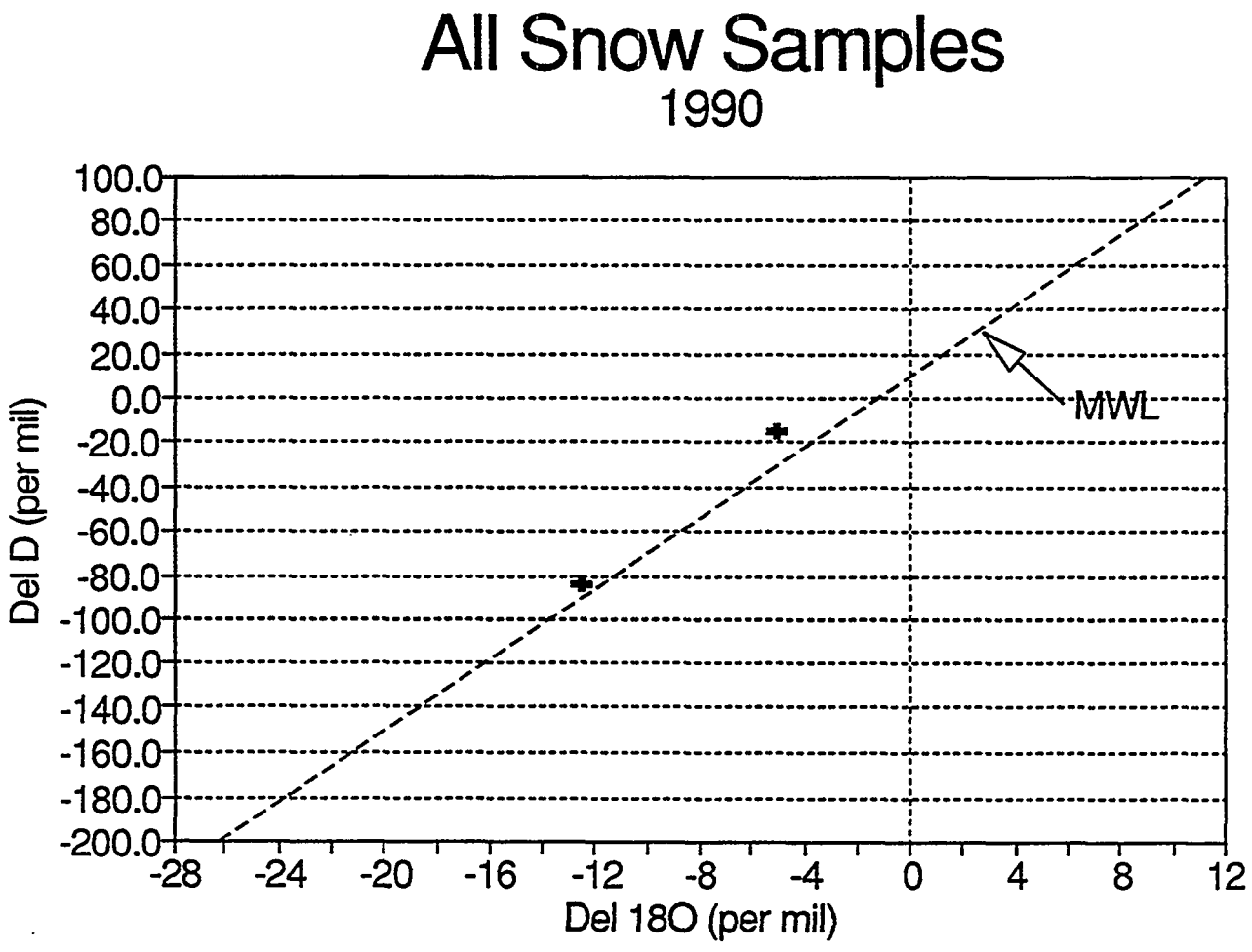

Figure 5.13. The hydrogen and oxygen stable isotopic values of snow samples collected at the Apache Leap Research Site. Data are compared to the MWL.

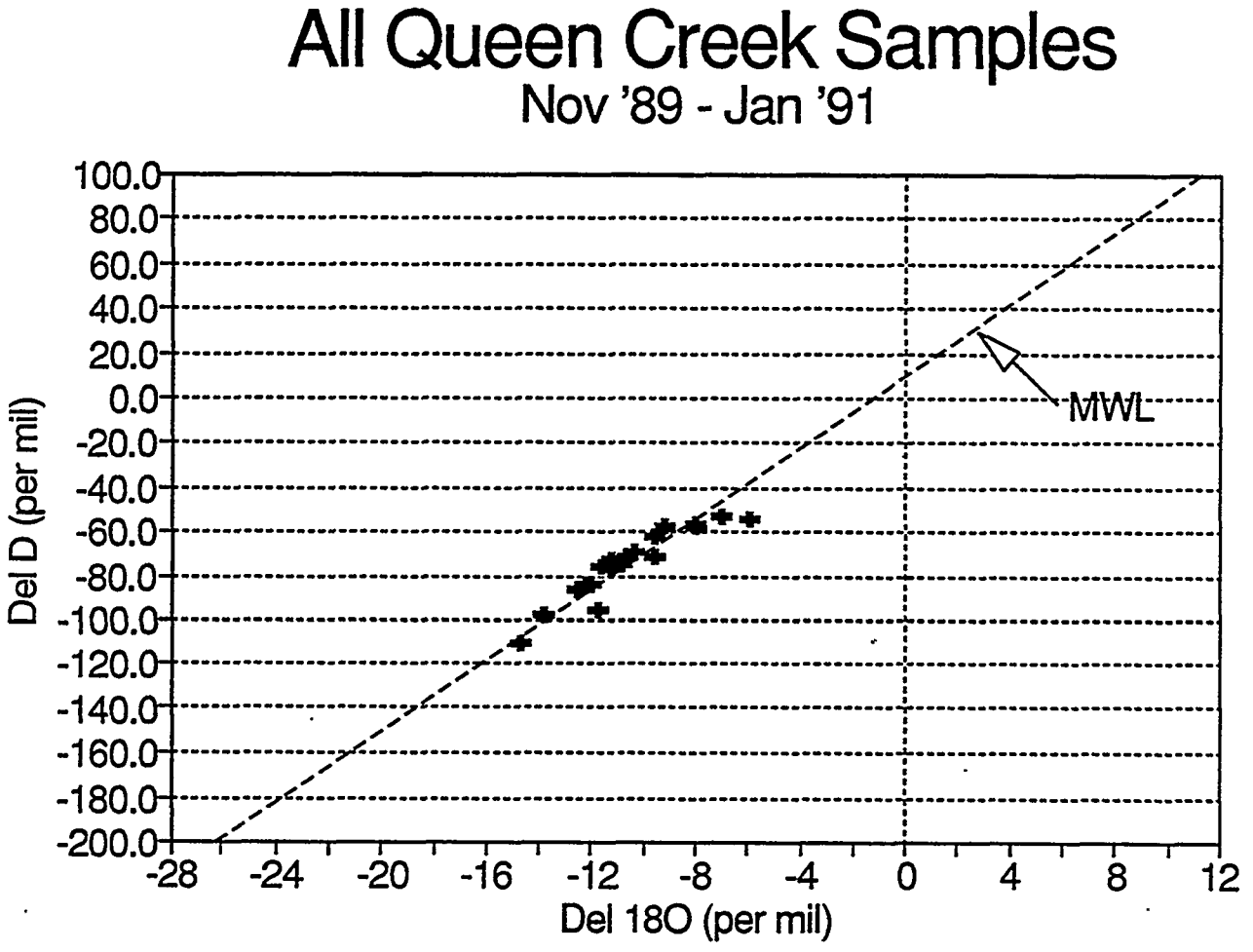

Figure 5.14. The hydrogen and oxygen stable isotopic values of samples collected from Queen Creek at the Apache Leap Research Site. Data are compared to the MWL.

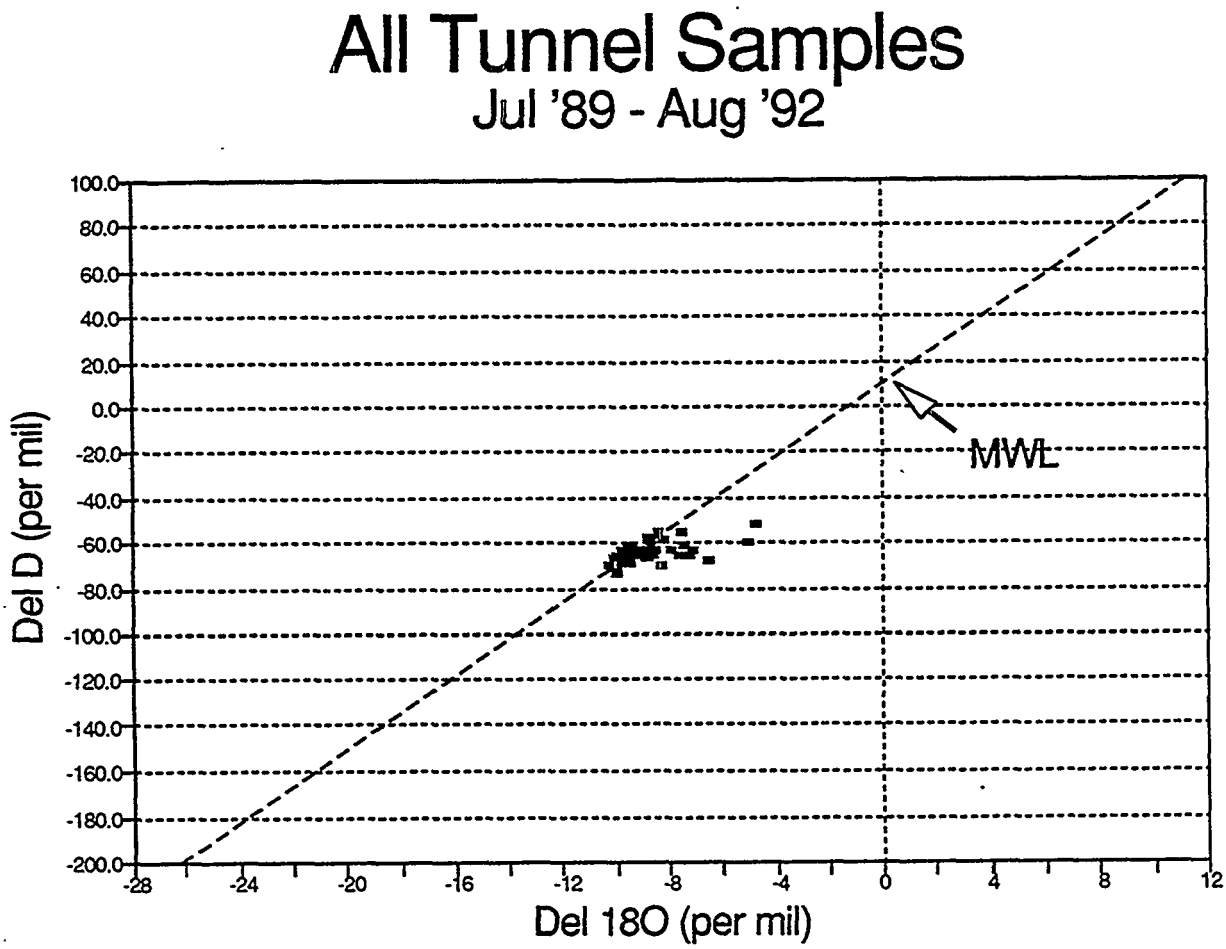

Figure 5.15. The hydrogen and oxygen stable isotopic values of samples collected from fracture discharge within the Never Sweat Tunnel near the Apache Leap Research Site. Data are compared to the MWL.

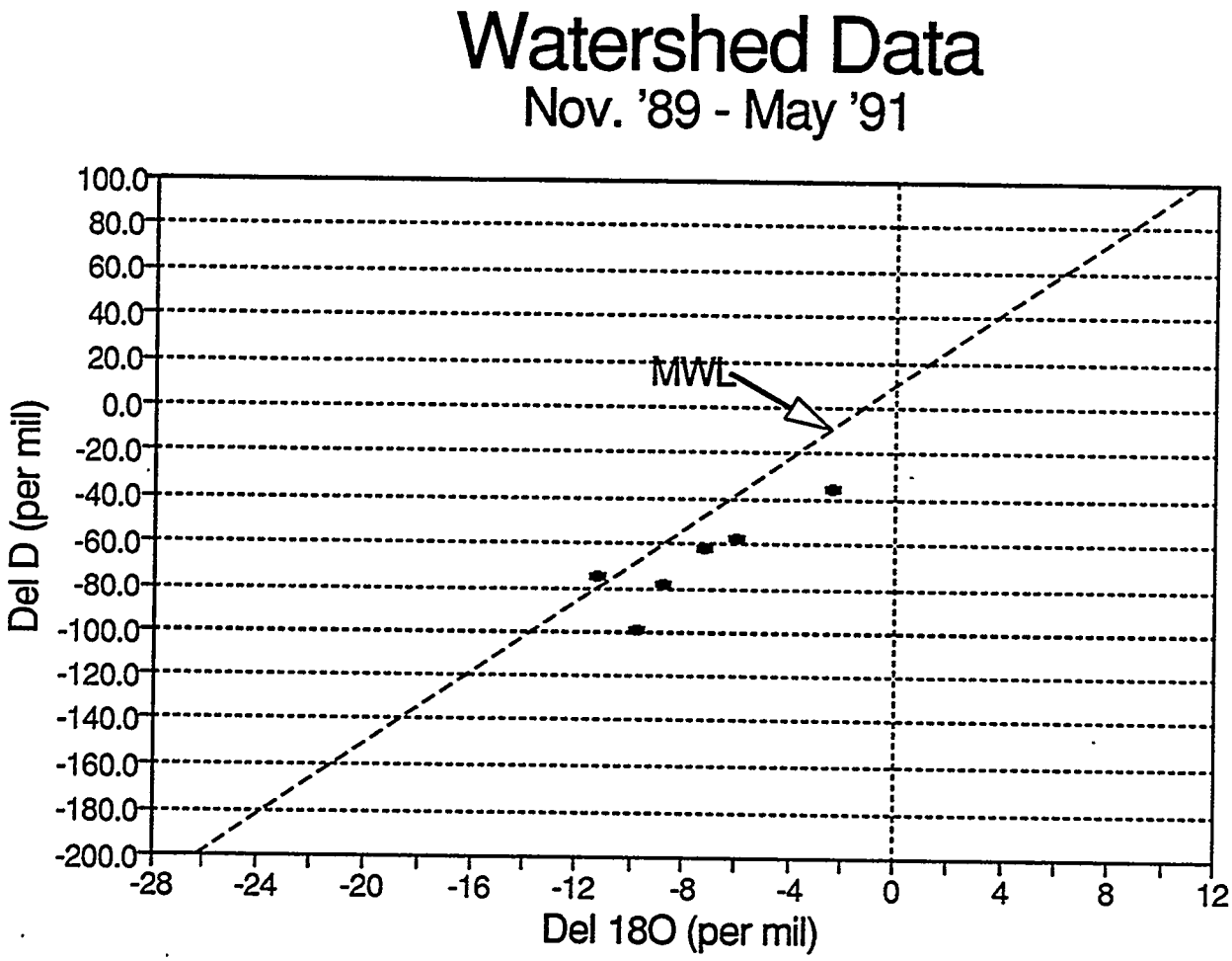

Figure 5.16. The hydrogen and oxygen stable isotopic values of samples collected from the watershed near the Apache Leap Research Site. Data are compared to the MWL.

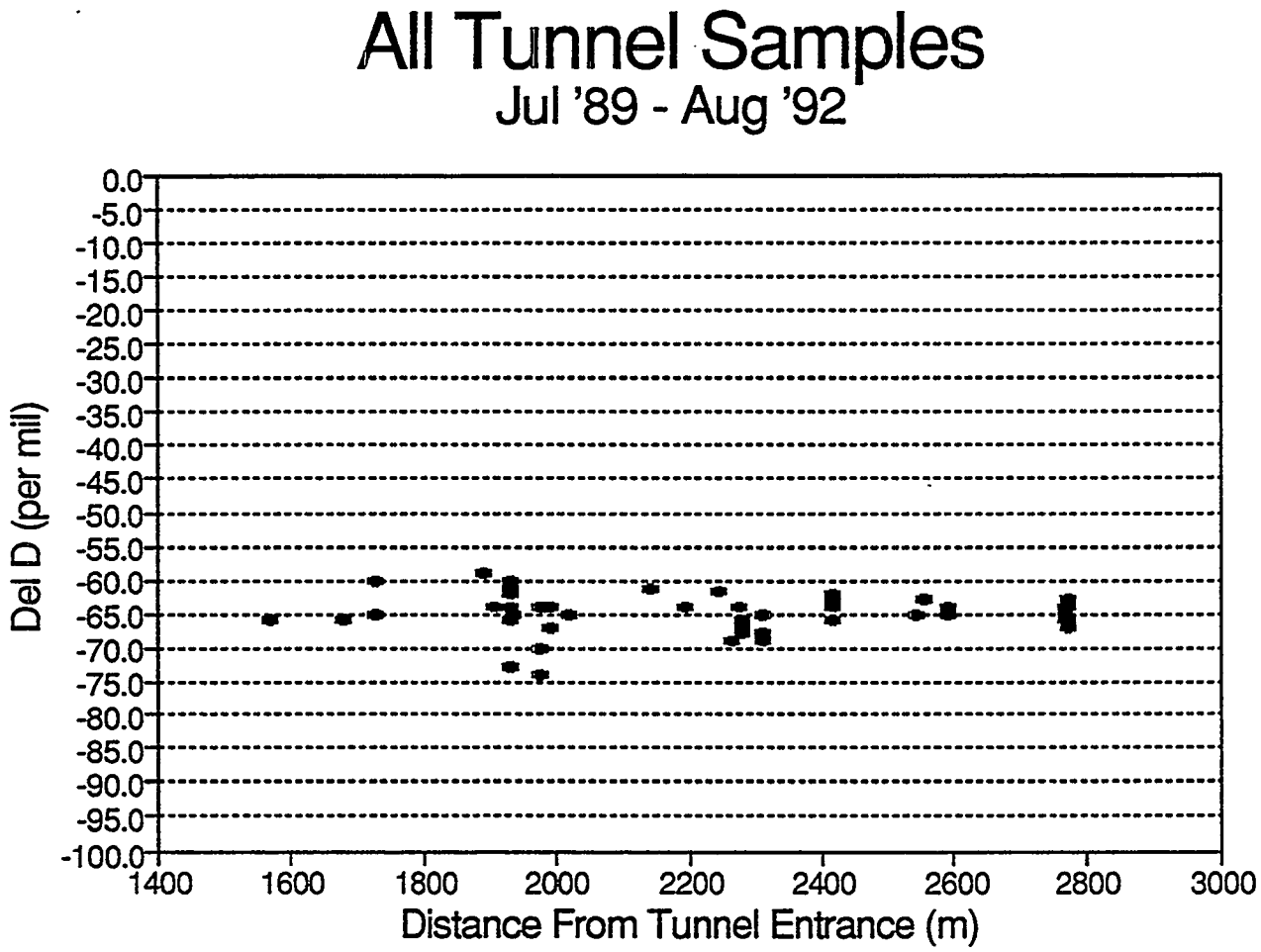

Figure 5.17. Variation in the SD isotopic signature along the tunnel length; highest variation exists in water samples from fractures influenced by Queen Creek.

is not clear at which point the evaporation is occurring. Possibly the evaporation occurs in the soil zone; then, during rainfall events, the flushed soil water is mixed with precipitation, altering the final composition. More likely is the scenario that most of the evaporation occurs over the days after the rainfall events, in the soil, shallow fractures, tributaries, and creeks themselves. Water samples collected in Queen Creek or in the tunnel will reflect the variable extent of evaporation on the water sample.

Isotopic analyses are available at present for five instances in which both rainfall and Queen Creek water samples could be collected (Figures 5.18 to 5.22). The samples are clearly different between different storm events, but the values cluster for any given storm; this will be useful in monitoring the travel time of the signature of any given storm through the fracture network from Queen Creek to the Never Sweat Tunnel. Additional samples have been collected, and analyses are pending.

The most significant indicator of travel time and the variability of the flow path is observed by plotting all available δD values against tunnel location (Figure 5.17). Clearly there is the greatest variability in the section of the tunnel which is most affected by Queen Creek seepage, whereas water from the perched zone, which integrates recharge over a broad area of the tuff, is much less variable. Interestingly, the mean values are actually quite similar. Presumably, the variability is correlative with major storm events which generate flow in Queen Creek and can range at least as much as 80 per mil δD in one week, as was observed in the rainfall samples for March 1991. The amount of mixing and dilution occurring as the water migrates down the fracture network must be minimal. In contrast, the perched water table integrates values over many years.

Carbon Isotopic Signature

The dissolved carbonate content of vadose zone water or perched water, as well as the carbon calcite deposited in the soil or the unsaturated portion of the tuff, probably originated from four possible sources: atmospheric carbon dioxide, soil-generated carbon dioxide, soil organic carbon, and carbonate from the limestones. The $\delta^{13}C$ value for water from the perched zone has been determined; samples were collected from water entering the east end of Never Sweat Tunnel and from the DOE Oak Flats well (Table 5.7). The variation is rather small, and the values tend to cluster between -12 and -15 per mil, with one low value of -9.3 for a tunnel sample collected during August.

The analyses useful for determining the apparent travel time have been received and are listed in Table 5.8. The tritium values indicate that the connection between Queen Creek and the Never Sweat Tunnel must be rapid because the tritium activity is essentially the same value. This is approximately what would be expected for surface water in this part of the continent. The DOE well and the CB2 sample are still registering some tritium activity, but significantly lower than that of waters influenced by Queen Creek. Future sampling will be aimed at determining whether the tritium content is the result of mixing with younger water or perhaps is sampling contamination, e.g., from bailing or collection from fractures in an open tunnel. More definitive studies can be performed in the deep slant borehole where hydraulic constraints are better defined.

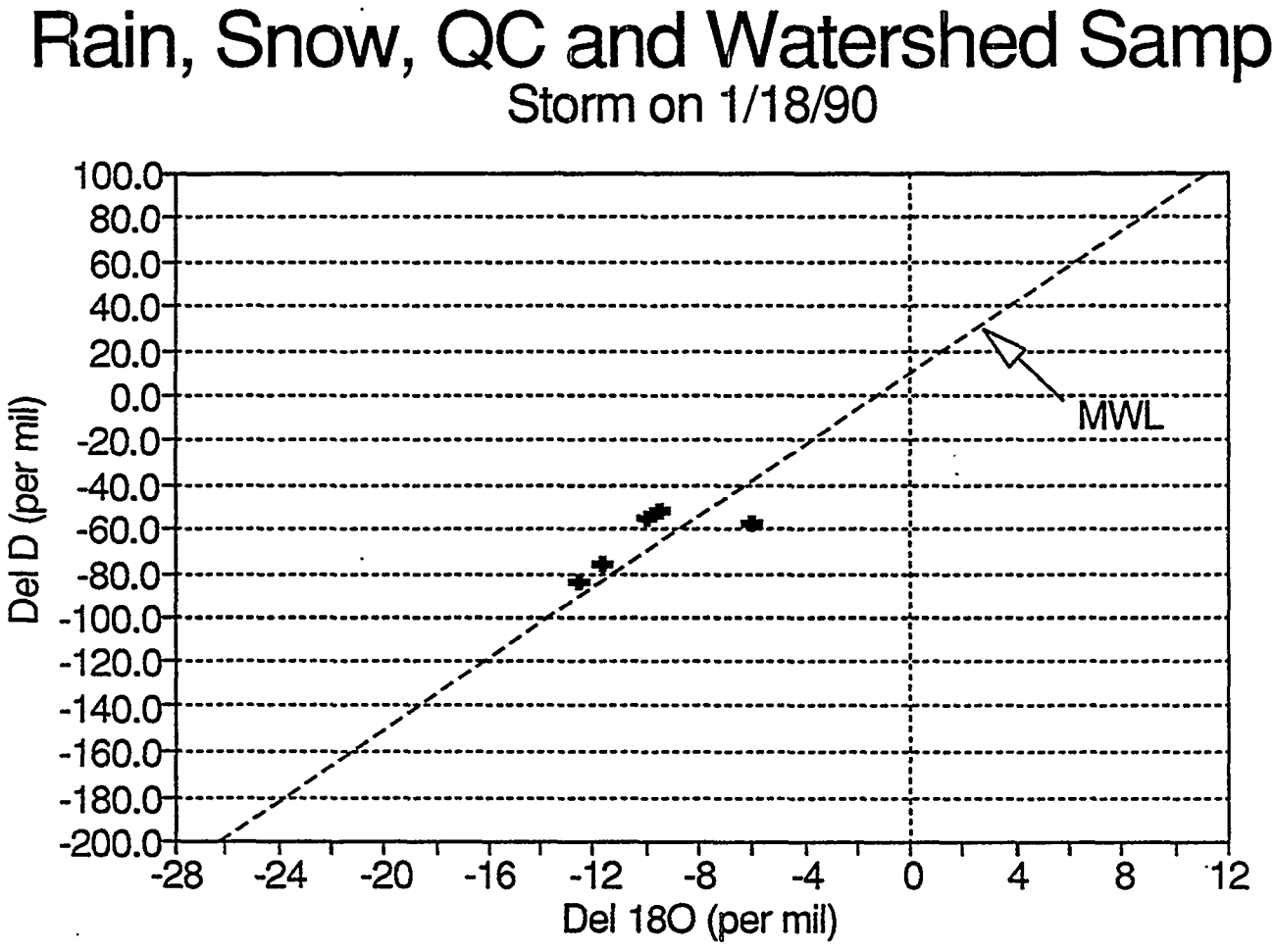

Figure 5.18. Range of values for hydrogen and oxygen isotopic composition for the rain, watershed, and Queen Creek for a storm event on 1/18/90.

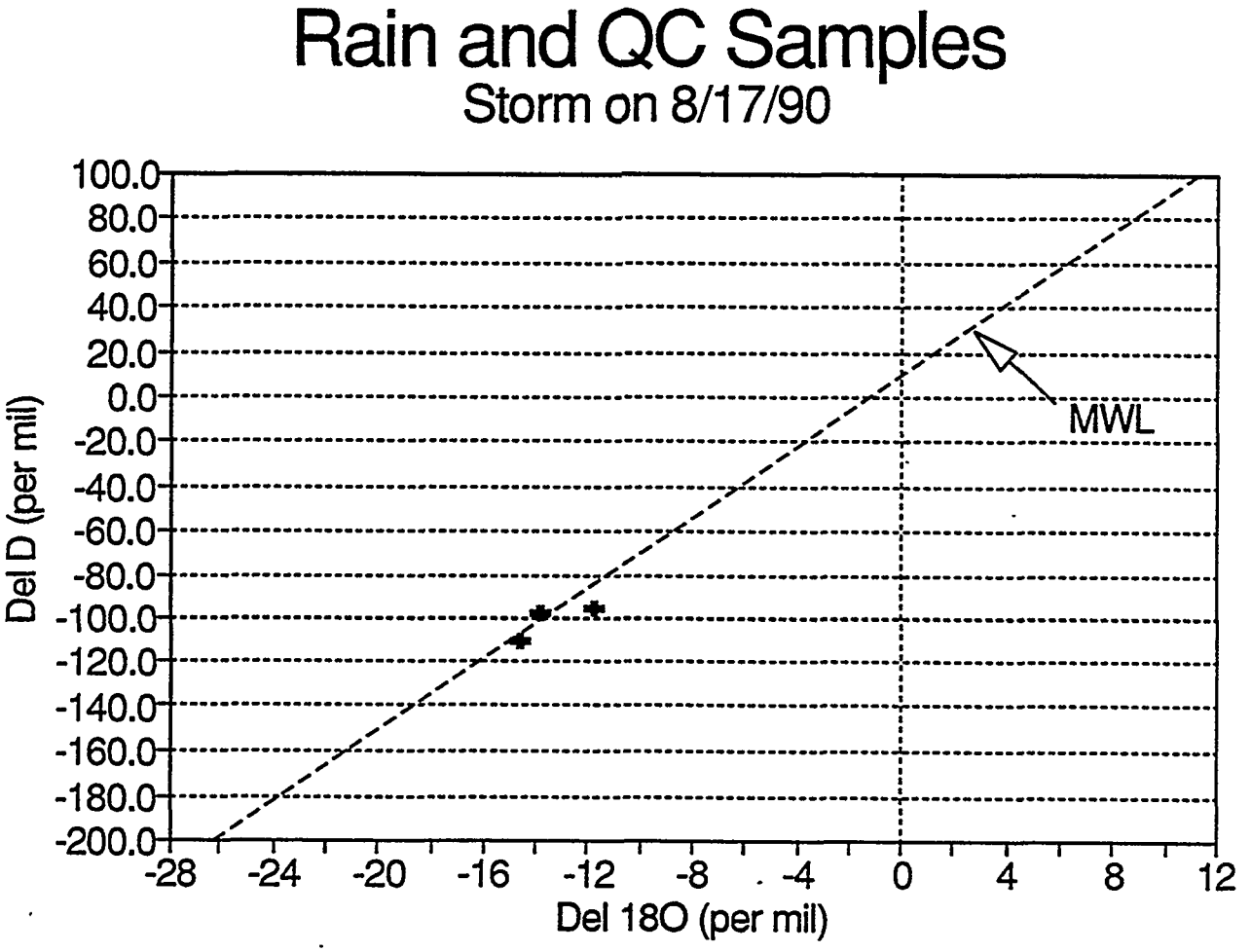

Figure 5.19. Range of values for hydrogen and oxygen isotopic composition for the rain and Queen Creek for a storm event on 8/17/90.

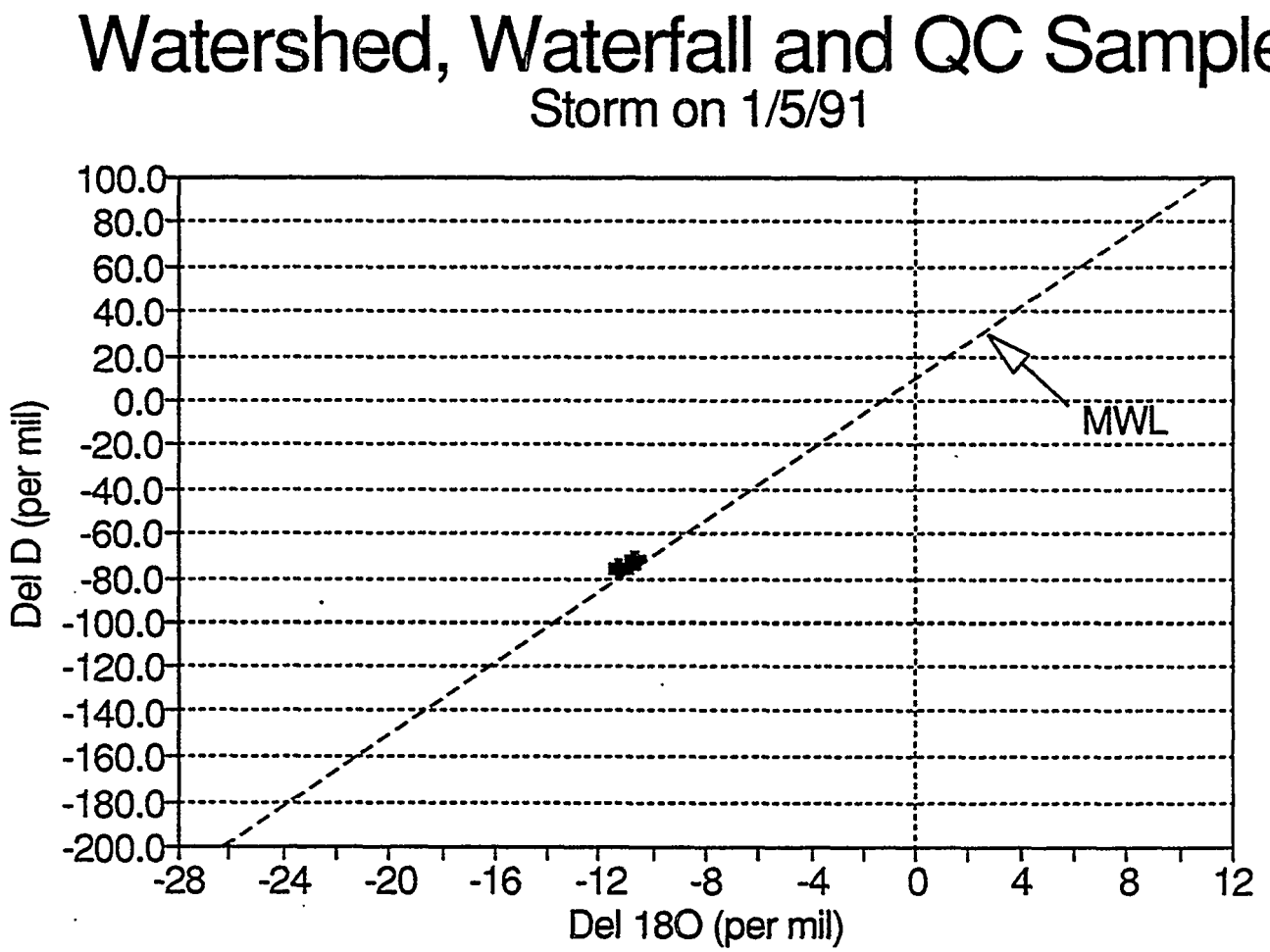

Figure 5.20. Range of values for hydrogen and oxygen isotopic composition for the watershed, waterfall and Queen Creek for a storm event on 1/5/91.

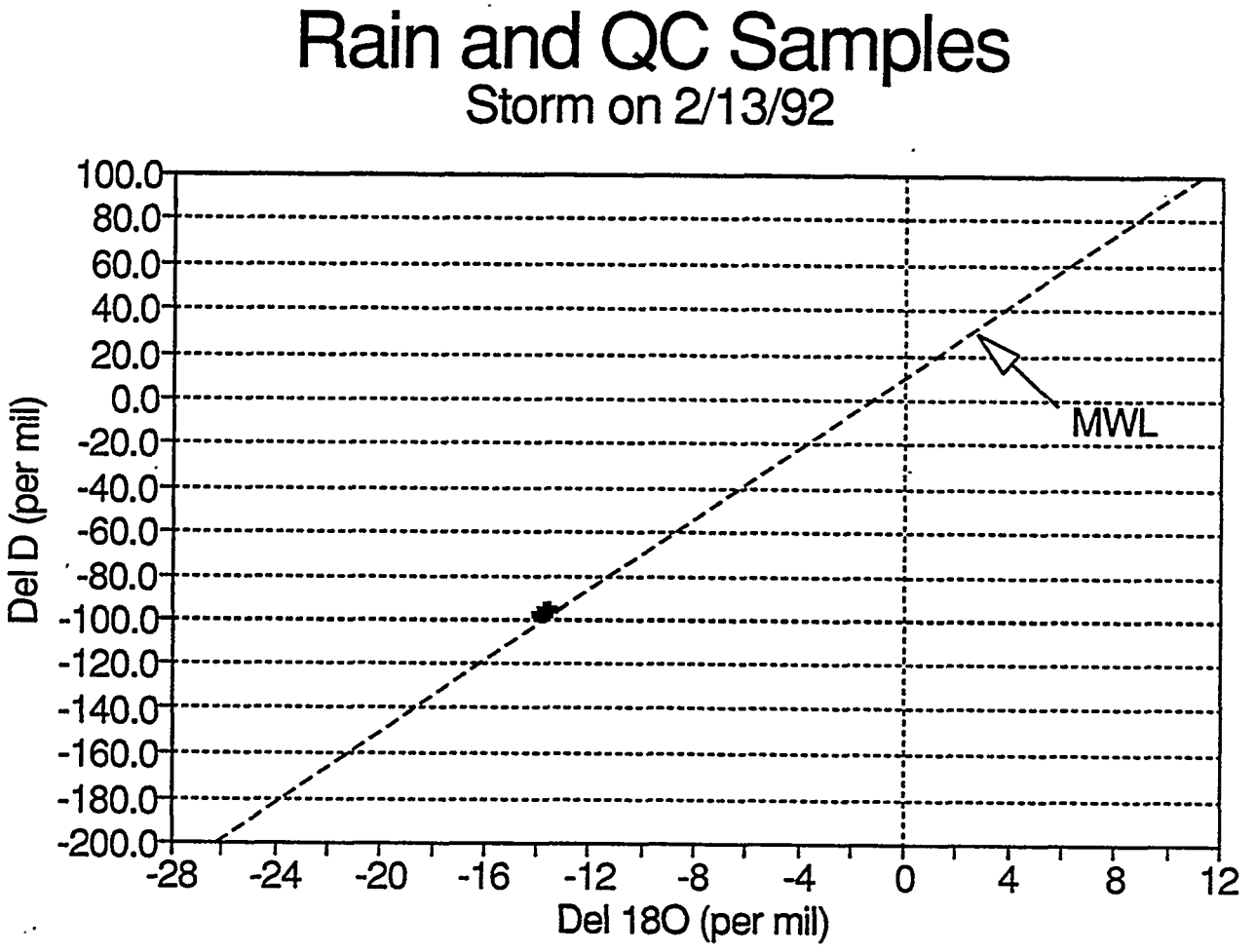

Figure 5.21. Range of values for hydrogen and oxygen isotopic composition for the rain and Queen Creek for a storm event on 2/13/92.

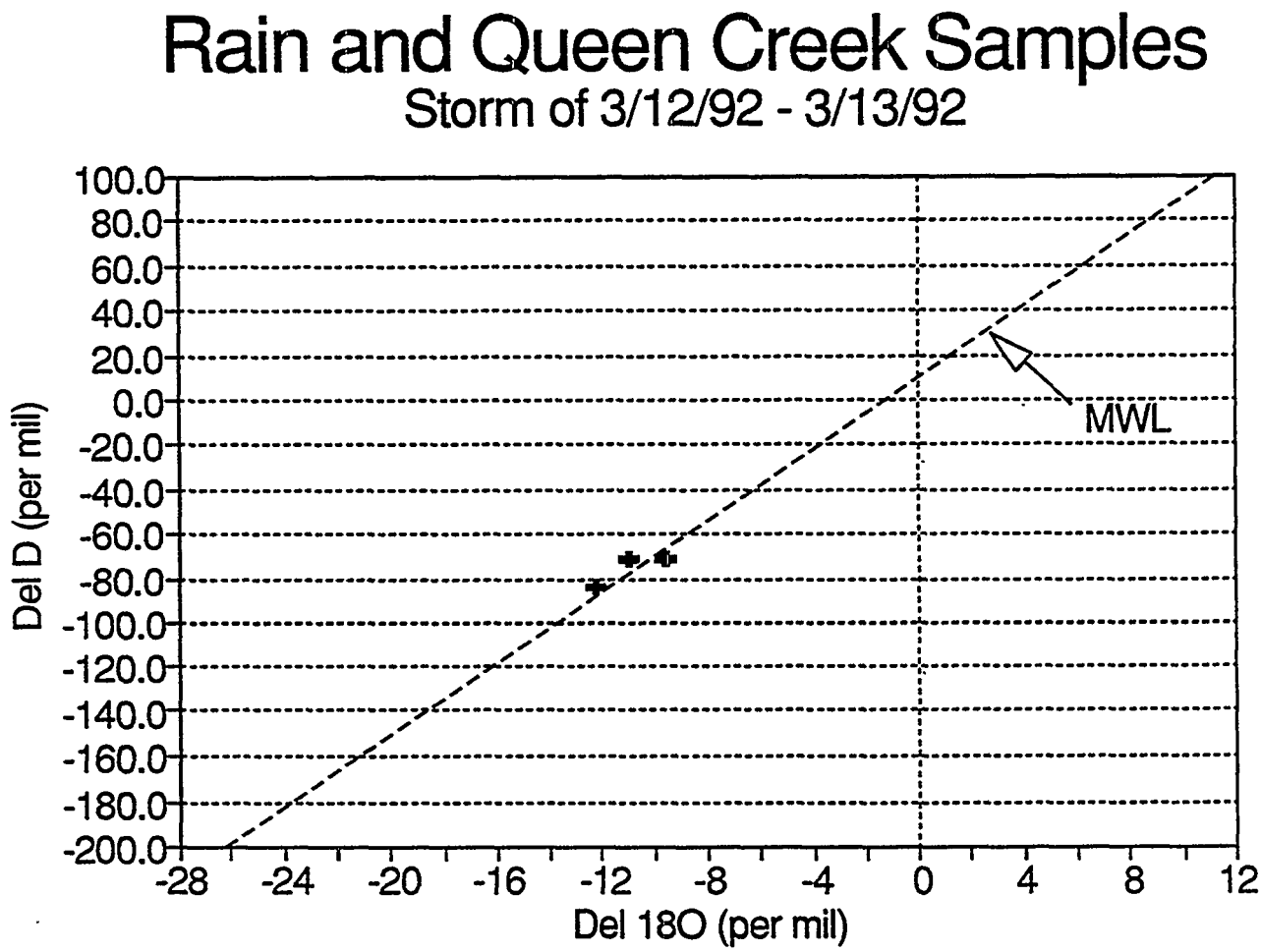

Figure 5.22. Range of values for hydrogen and oxygen isotopic composition for the rain and Queen Creek for a storm event on 3/12/92-3/13/92.

Table 5.7. Carbon Stable Isotope Measurements for Samples Collected to Date from Never Sweat Tunnel and the DOE Oak Flat Well.

Location	Date	$\delta^{13}C$
T-6335	2/27/90	-14.2
	8/17/90	-9.3
	9/14/90	-14.2
T-6480	2/27/90	-14.4
	8/17/90	-15.0
	9/14/90	-14.2
T-7920	2/27/90	-12.4
T-4	2/27/90	-14.3
CB-1	2/27/90	-13.6
DOE Well	4/27/90	-11.9

Table 5.8. Results of Tritium and Radiocarbon Analyses for Water Samples in Key Locations Along the Flow Pathways.

Sample Location	^{14}C Age	Years BP	PMC		Tritium (TU)	
CB-2	3,119	131	0.6885	0.0044	1.20	0.41
DOE Well	3,067	130	0.6827	0.0046	1.85	0.22
Queen Creek	na	na	na	na	5.58	0.27
T-6340	na	na	na	na	5.16	0.38

The ^{14}C analysis was done here at The University of Arizona on the Tandem Accelerator Mass Spectrometer (TAMS); the tritium values are from the Rosenstiel School of Marine and Atmospheric Sciences at the University of Miami. The first ^{14}C sample dated is from the east end of the Never Sweat tunnel; flow at this point is continuous, and it is suspected that the discharge is derived from a perched water table (Figures 5.2 and 5.3). The uncorrected age of this water is 3,119 $\pm$ 131 years BP (0.6885 $\pm$ 0.0044 PMC). The second sample was collected from the DOE Oak Flats well from the first perched water table encountered from 362-485 ft. The uncorrected age is 3,067 $\pm$ 130 years BP (0.6827 $\pm$ 0.0046 PMC).

These data are supportive of a rather long flow path from land surface to a perched zone with subsequent horizontal flow to the surface water discharge points such as the Devil's Canyon or Queen Creek Canyon. Water entering the tunnel on the east end is probably draining this perched

zone, perhaps lowering the head to the point that the zone no longer extends westward along the tunnel. This would allow water from Queen Creek to pass through fractures in the unsaturated zone and enter the middle portion of the tunnel without interacting with the perched zone.

The $\delta^{13}C$ values are given for a series of sampling points along the tunnel, from the zone most influenced by Queen Creek (T-6340) to the east end of the tunnel, at which point the flow is most likely from the perched zone (Table 5.9). The standard deviation of these tunnel samples is $\pm$ 0.77 (2σ) which is greater than the precision of the analysis reported to be $\pm$ 0.14 (2σ). The standard deviation is attributable almost entirely to one sample (T-7920). There is actually no statistically significant trend in the data; correlations with carbonate chemistry, however, are instructive. Using the chemical analysis for each of the tunnel samples and the sample from the DOE well, the partial pressure of CO_2 and the calcite saturation index was computed (Table 5.9). The water samples from T-6335 and T-6480 are influenced by Queen Creek, have lower alkalinities, and are clearly undersaturated with respect to calcite (Figure 5.23). The remaining samples have higher alkalinity, are in equilibrium with calcite, yet the $\delta^{13}C$ values are not significantly different, indicating that the reaction path for carbon may be similar as discussed below.

Table 5.9. Indicators of the Evolution of Carbonate Chemistry in Samples Collected from Never Sweat Tunnel in a Traverse from West to East.

Sample Location	$\delta^{13}C$	Alkalinity	pH	log P CO_2	$SI_{CALCITE}$
T-6335	-14.2	68.5	7.3	-2.496	-0.98
T-6480	-14.4	92.4	7.5	-2.560	-0.6
T-7920	-12.4	138.2	8.1	-3.031	0.14
T-4	-14.3	141.8	8.0	-2.896	0.19
CB-1	-14.3	138.2	8.0	-2.877	0.18
CB-2	-13.6	137.6	8.0	-2.879	0.16

The source of the carbon is undoubtedly soil gas; for desert soils in southern Arizona, one typically finds a soil water $\delta^{13}C$ of from -14 to -16 ‰ (Kalin, 1991, personal communication). The data available to date all seem to be in the -13 ‰ to -14 ‰ range.

Water with short residence time in the soil zone and short travel time to the tunnel will still reflect the soil zone P_{CO2} and $\delta^{13}C$ signature. This implies less reaction time for silicate + hydrolysis and thus less alkalinity and consequently the solution will not have sufficient reaction progress to reach saturation with respect to calcite. Longer flow path and reaction time, especially in a closed system, results in adequate time to reach the saturation point with calcite.

The most interesting observation, however, is the fact that even though calcite is precipitating, there is no indication that the $\delta^{13}C$ value for the transmitted water has been altered. This indicates that the loss of carbon mass is small, and the quantification of this process is the subject of future

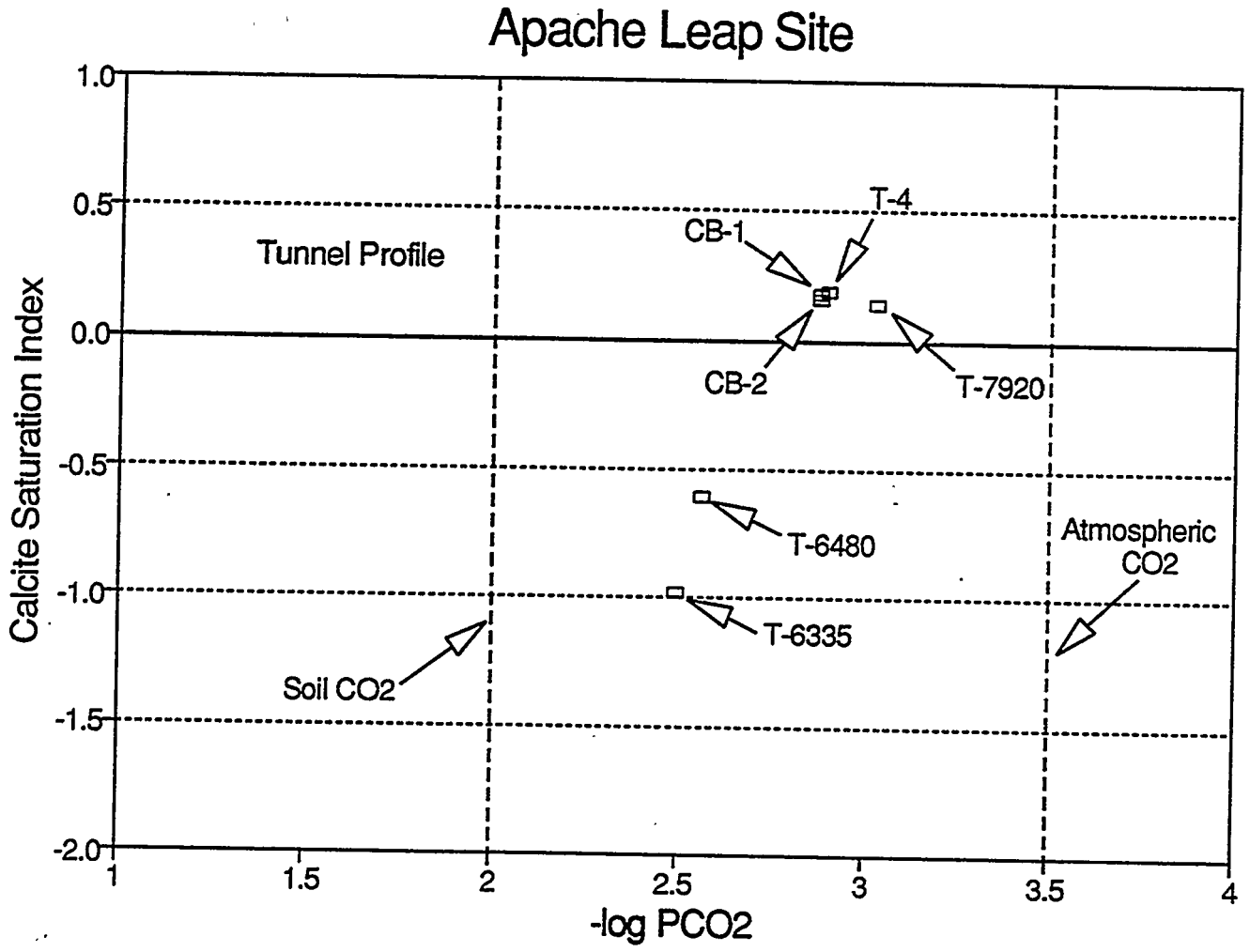

Figure 5.23. Saturation index for calcite correlated with computed partial pressure of CO_2 for samples collected along tunnel length.

work. It is essential to understand this process because it determines the extent to which apparent ^{14}C ages must be corrected to obtain a reliable value for travel time.

Boron and Sulfur Isotopic Data

Two additional stable isotopic tracers, sulfur ($\delta^{34}S$) and boron ($\delta^{11}B$), are now being investigated as being potentially useful for determining source, migration pathway, and potentially some indication of travel time of solute from the surface to the tunnel or to the perched water table through the unsaturated fractured tuff. We have just begun to use the isotopes of sulfur ($\delta^{34}S$) to distinguish old water from young. This is possible because of the atmospheric signature resulting from sulfur derived from the smelter in Superior only a few kilometers away. Much of the sulfur from the source is currently present in the soils of the region near the site. Sulfur isotopic analyses have been done for snowmelt, rainwater, surface runoff, Queen Creek, and tunnel discharge. These values are shown in Figure 5.24. It is likely that the light values which are seen in surface runoff in the watershed and Queen Creek can be correlated with recent atmospheric sources (< 100 years BP); whereas very old water present in the perched zone at Oak Flat (>3000 years BP), which could not have been influenced by the anthropogenic sources, is similar to dryfall and modern rainfall in the region no longer having input from the smelter. The mid-tunnel values are dominated by rapid recent fracture recharge, and the east end of the tunnel is apparently a mixture of old and recent water sources. This is especially intriguing because the east end has a radiocarbon date of several thousand years. This must be a mixed system, that illustrates the unreliability of radiocarbon when interpreted without other supporting isotopic values.

5.6.1.3 Reaction Path Modeling

Using the computer codes NEWBALANCE (Parkhurst, 1991, personal communication) and PHREEQE (Parkhurst et al., 1980), observed changes in chemical composition are simulated along a flow path that begins at Queen Creek and ends in Never Sweat Tunnel. Gains and losses of aqueous phase constituents are attributed to a series of processes that include dissolution of primary silicate minerals, formation of secondary minerals, and mixing.

There are at least two conceptual flow paths leading to Never Sweat Tunnel. For one path, precipitation falls within the Queen Creek watershed; flows as surface runoff, overland, and through soil zones to Queen Creek; flows in Queen Creek, then passes through the stream bed; enters fracture networks below and moves as fracture flow until discharge into Never Sweat Tunnel. A second path involves direct fracture recharge within local basins in the study area. Precipitation enters and passes through the soil zone; enters fracture networks below the soil zone; and flows through the tuff until discharge into Never Sweat Tunnel.

The westernmost tunnel samples, T-6335 and T-6340, appear to emerge from a flow path that most resembles the "Queen Creek" conceptual flow path, and the model for this reaction pathway is examined in greater detail here as an example.

5.6.1.4 Mineral Phases

Identification of mineral phases in the Queen Creek/T-6335 flow system is necessary for determining and quantifying the governing geochemical processes. A list of every mineral observed in the Apache Leap Tuff Site is presented in Table 5.10. This information is derived from earlier studies and from X-ray diffraction analysis conducted as part of this investigation.

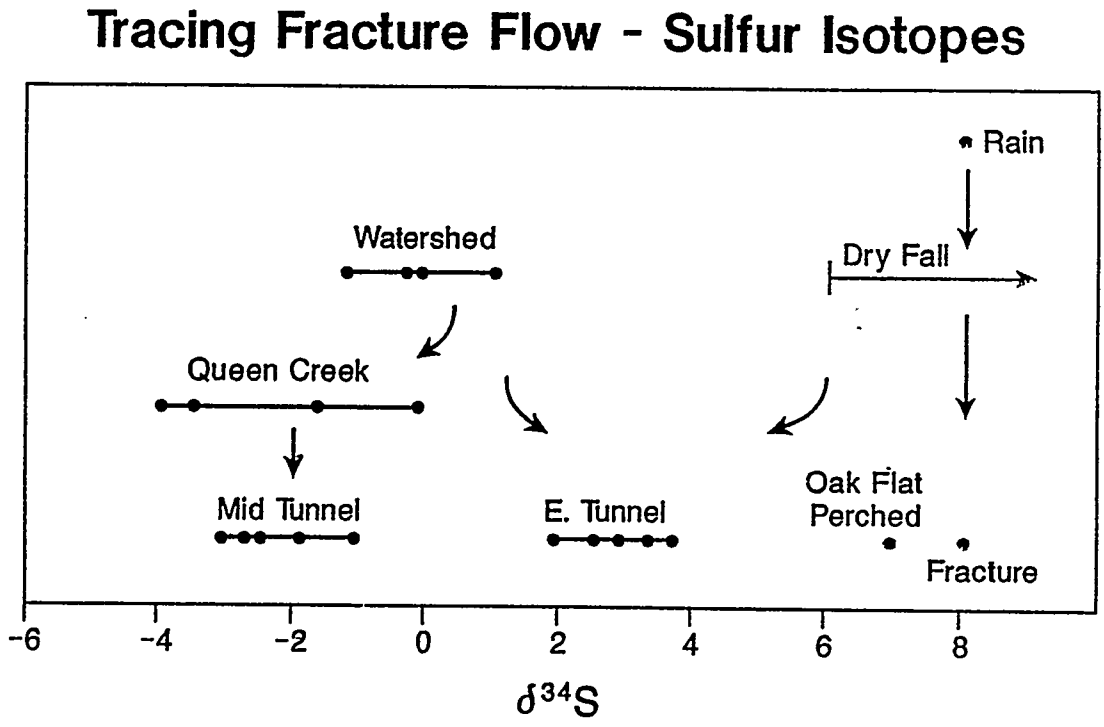

Figure 5.24. Range of $\delta^{34}S$ values for water samples collected at the Apache Leap Research Site.

Table 5.10. Minerals Associated with the Apache Leap Tuff.

Mineral	Relevance/Comment to T-6335 System	Source of Information
Plagioclase	An_{22-40}	P
Quartz		P,W
Biotite		P
Sanidine	Or_{84}-Ab_{16} to Or_{89}-Ab_{11}	P
Magnetite	Fe not considered in model	P
Hornblende		P
Sphene	Negligible quantity	P
Apatite	Negligible quantity	P
Zircon	Negligible quantity	P
Tourmaline	Negligible quantity	P
k-feldspar		P
Christobalite		P
Clinoptilolite	Negligible quantity	P
Tridymite	Negligible quantity	P
Opaline silica		W
Calcite	Undersaturated	W,S
Montmorillonite		W,A
Palygorskite-sepiolite	Undersaturated	W
Mixed layer illite-montmorillonite		W
Iron oxide	Fe not considered in model	S
Gypsum	Undersaturated	S
Mn oxide	Mn not considered in model	S
Silica		S
Zeolites	Undefined	S
Kaolinite		A
Chlorite		A
Gibbsite		O
Ferric hydroxide		O

Sources of Data: P = Peterson (1961); W = Webber (1985); S = Sample Management Facility (1990); A = this study; O = known to be present in weathered silicate rocks.

Peterson (1961) described the primary minerals that comprise the tuff. Additionally, he observed biotite partly altered to chlorite and a zeolite mineral that he believed to be clinoptilolite. Weber (1986) examined fracture-filling minerals by X-ray diffraction method, and DOE (Sample Management Facility, 1990) reported fracture-filling minerals identified from hand specimens.

For this study, X-ray diffraction methods were used to identify clay minerals isolated from soil samples and exposed fracture faces. Positively identified clays are smectite, kaolinite, and chlorite. Mixed layer illite-smectite was identified with uncertainty.

Although not explicitly identified, other minerals such as aluminum oxyhydroxide (gibbsite) are common weathering products of silicate rocks and are included in Table 5.10.

Assessment of potential relevance of the minerals listed in Table 5.10 to geochemical processes in the Queen Creek/T-6335 system is made with the following criteria: (1) Abundance of primary minerals--some are present in negligible quantities, and (2) thermodynamic feasibility--undersaturation of secondary minerals prohibits their formation under those conditions. Some mineral are not considered because their constituents are not relevant to this study, such as trace metal oxides and hydroxides.

5.6.1.5 Chemical Model

Water-rock interactions contribute negligible chloride to the aqueous systems in Apache Leap Tuff, an assumption supported by the research of Noble et al. (1967). Thus, chloride content in waters from the study area is ultimately derived from evaporative concentration of precipitation. Because western tunnel waters have greater chloride concentrations than the creek waters from which they derive, and evaporation within fracture networks is negligible, the increase must be attributable to mixing with more evaporated waters. The only feasible source of these waters is a perched water-bearing zone above Never Sweat Tunnel.

Model flow and reaction paths for this system are summarized as follows. Queen Creek waters enter fracture systems and move predominantly downward, toward Never Sweat Tunnel. Water-rock interaction produces dissolution of primary minerals and formation of secondary minerals. The sum of the reactions produces a net consumption of protons and conversion of carbonic acid to bicarbonate ions. Thus, pH and alkalinity increase. At one or more sections along the flow path, fracture waters mix with more evaporated groundwater. The mixture flows toward the tunnel and water-rock interaction continues, until discharge from fractures at T-6335.

It is assumed that sample QC-Ivy, the creek sample site nearest the tunnel, best represents chemical composition of creek waters, and that composition of the easternmost tunnel sample, T-CB1, approximates that of waters in the perched zone. Chemical compositions of waters used for modeling are given in Table 5.11.

The reaction path is quantified by solving all the appropriate mass balance equations simultaneously. Mixing is simulated at a ratio that produces the desired chloride concentration. Concentrations of other constituents in the simulated mixed solution are then compared to the desired final solution and discrepancies attributed to transfer to and from mineral phase components.

Table 5.11. Chemical Composition of Waters Used in Queen Creek/T-6335 Chemical Model. All units of concentration in mg/L unless otherwise noted.

Constituent/ Property[a]	QC-Ivy 8/17/90	T-CB1 8/17/90	T-6335 8/17/90	Model Simulated T-6335 9/14/90
T (°C)	19.8	25.0	20.0	21.0
pH	7.0	7.9	7.2	7.5
Alkalinity (HCO_3)	35.1	137.6	73.7	77.1
SO_4	27.6	15.6	31.5	24.9
NO_3	nd[b]	3.6	4.3	--
Cl	3.6	6.3	4.2	4.2
Na	6.1	21.1	13.0	13.0
K	1.9	0.81	0.57	0.57
Ca	15.4	28.2	22.2	22.2
Mg	3.9	5.0	4.0	4.0
Al[a]	36.1	7.1[c]	8.1[c]	4.0
Fe[a]	41.7	nd		
SiO_2	2.0	62.5_c	40.6	40.7
Charge Balance (%)[d]	5.71	-1.06	-0.85	

[a] Laboratory analyses of Al and Fe by John Garbarino, U.S. Geological Survey, National Research Laboratory, Arvada, Colorado. All other analyses by Elizabeth Lyons, Dept. of Hydrology and Water Resources, The University of Arizona, Tucson, Arizona.
[b] nd = no data
[c] Estimated value
[d] Charge balance (%) =

$$\frac{\Sigma \text{ cations}\left(\frac{meq}{\ell}\right) - \Sigma \text{ anions}\left(\frac{meq}{\ell}\right)}{\Sigma \text{ cations}\left(\frac{meq}{\ell}\right) + \Sigma \text{ anions}\left(\frac{meq}{\ell}\right)} \times 100\%$$

(Hem, 1989)
[e] units of μg/L

Table 5.12 gives five mass balance solutions for mixed creek water and groundwater evolving to T-6335. Variations between solutions are minor. Each assemblage includes dissolution of plagioclase, CO_2, and hornblende, with formation of illite and chlorite. Solution "a", however, appears to reflect the physical system more nearly than solutions "b" through "e". It includes biotite weathering with a similar quantity of chlorite formation, reflecting an expected rapid rate of biotite alteration to chloride.

PHREEQE (Parkhurst et al., 1980) is a code designed to model geochemical reactions, including equilibration of solutions with mineral and gas phases, ion exchange, and temperature changes. For the Queen Creek/T-6335 model, it simulated the mixing as prescribed by BALANCE. Computed results of the simulation yield a final pH of 7.27 (measured 7.0) using mass balance solution "a." A complete description is given in Lyons (1993).

5.6.2 Deep Slant Borehole Project Site

5.6.2.1 Borehole Data

The borehole was completed in December 1992, and the core has been preserved for study. Testing which consists initially of geophysical logging, followed by extraction of gas from specific locations in the unsaturated zone for chemical and isotopic analysis is now underway. Gas and liquid "apparent ages" and subsequent implications for travel times will be based on precise measurements of the following radioactive isotopes: radon, tritium, ^{39}Ar, ^{85}Kr, and ^{14}C. Similarly, samples of water squeezed from the core will be analyzed for both chemical and isotopic composition (tritium and radiocarbon). These data will provide indications of fluid and gas flow paths. Additionally, the gas and liquid flow pathways, as well as fracture and matrix interactions, will be simulated using flow and transport codes such as NEFTRAN.

The percentage core recovery was excellent and the recovery with respect to depth is given in Table 5.13.

5.6.2.2 Isotopic Studies

Carbon Isotope Geochemistry

The primary objective of this research is to determine how water and vapor move through an unsaturated, fractured tuff by studying the carbon isotope geochemistry. The carbon system is ideally suited as a tool for this investigation because it is common in the gas, aqueous, and mineral phases. Interactions between these phases can be traced by examining the stable carbon isotopic ratios of each phase, and information on rates of travel can be determined using ^{14}C activities if appropriate corrections are applied.

To accomplish this subtask, a small basin at the Apache Leap was chosen, and monitoring stations were set up in and around the basin. Monitoring of soil gas and surface water was initiated in the fall of 1991. Individuals directly involved in this subtask are R.L. Bassett and G.R. Davidson.

Table 5.12. Five Potential Mass Transfer Solutions for Queen Creek/T-6335 Chemical Model.

Mineral/Gas Phase	Reaction Quantity (mole/kg solution)			
	(a)	(b)	(c)	(d)
Plagioclase	0.1688×10^{-3}	0.1688×10^{-3}	0.1688×10^{-3}	0.1688×10^{-3}
Biotite	0.0533×10^{-3}			
Kaolinite		-0.0437×10^{-3}		
CO_2	0.2428×10^{-3}	0.2824×10^{-3}	0.2824×10^{-3}	0.2824×10^{-3}
Smectite			0.1345×10^{-3}	
SiO_2	-0.1314×10^{-3}		-0.3903×10^{-3}	-0.3499×10^{-3}
Gibbsite				-0.1749×10^{-3}
Hornblende	0.0283×10^{-3}	0.0283×10^{-3}	0.0283×10^{-3}	0.0283×10^{-3}
Illite	-0.1330×10^{-3}	-0.0455×10^{-3}	-0.0455×10^{-3}	-0.0455×10^{-3}
Chlorite	-0.0454×10^{-3}	-0.0165×10^{-3}	-0.0031×10^{-3}	-0.0165×10^{-3}
Sanidine/k-feldspar				0.0931

Table 5.13. Recovery Data for the Deep Slant Borehole (data recording began at 100 feet depth).

Start (feet)	End (feet)	Length (feet)	Recovered (feet)	Lost (feet)
100.7	110.5	9.8	9.0	0.8
110.5	120.2	9.7	10.2	-0.5
120.2	130.4	10.2	10.3	-0.1
130.4	140.8	10.4	10.2	0.2
140.8	150.3	9.5	10.2	-0.7
150.3	161.1	10.8	10.3	0.5
161.1	171.6	10.5	9.7	0.8
171.6	181.0	9.4	10.3	-0.9
181.0	191.1	10.1	10.3	-0.2
191.1	201.6	10.5	?	?
201.6	210.5	8.9	8.5	0.4
210.5	220.3	9.8	10.1	-0.3
221.0	231.3	10.3	10.3	0.0
231.3	241.4	10.1	10.3	-0.2
241.4	251.8	10.4	10.1	0.3
251.8	261.3	9.5	9.6	-0.1
261.3	271.4	10.1	10.0	0.1
271.4	281.3	9.9	10.3	-0.4
281.3	291.6	10.3	9.7	0.6
291.6	301.5	9.9	10.3	-0.4
301.5	311.6	10.1	10.1	0.0
311.6	321.9	10.3	10.3	0.0
321.9	331.3	9.4	9.1	0.3
331.3	341.3	10.0	9.2	0.8
341.3	350.4	9.1	10.1	-1.0
350.4	354.1	3.7	4.2	-0.5
354.1	363.2	9.1	8.2	0.9

363.2	373.3	10.1	10.2	-0.1
373.3	383.3	10.0	9.9	0.1
383.3	393.3	10.0	9.7	0.3
393.3	403.3	10.0	10.2	-0.2
403.3	413.3	10.0	9.7	0.3
413.3	423.3	10.0	10.0	0.0
423.3	433.3	10.0	10.3	-0.3
433.3	443.3	10.0	10.2	-0.2
443.3	453.3	10.0	9.7	0.3
453.3	463.3	10.0	9.7	0.3
463.3	473.3	10.0	9.7	0.3
473.3	483.3	10.0	9.7	0.3
483.3	493.3	10.0	9.6	0.4
493.3	503.3	10.0	10.0	0.0
503.3	513.3	10.0	10.0	0.0
513.3	517.2	3.9	4.2	-0.3
517.2	524.3	7.1	7.3	-0.2
524.3	533.2	8.9	8.0	0.9
533.2	543.6	10.4	7.2	3.2
543.6	551.5	7.9	8.5	-0.6
551.5	561.2	9.7	9.0	0.7
561.2	564.4	3.2	2.0	1.2
564.4	574.1	9.7	2.8	6.9
574.1	578.0	3.9	2.6	1.3
578.0	579.6	1.6	1.6	0.0
579.6	584.3	4.7	3.3	1.4
584.3	593.3	9.0	3.2	5.8
593.3	593.8	0.5	0.0	0.5
593.8	594.3	0.5	0.9	-0.4
594.3	599.3	5.0	4.3	0.7

599.3	602.3	3.0	2.7	0.3
602.3	606.6	4.3	3.2	1.1
606.6	612.0	5.4	6.3	-0.9
612.0	617.1	5.1	4.7	0.4
617.1	624.3	7.2	4.3	2.9
624.3	627.2	2.9	2.3	0.6
627.2	629.8	2.6	2.4	0.2
629.8	632.2	2.4	2.5	-0.1
632.2	641.7	9.5	6.0	3.5
641.7	644.3	2.6	2.7	-0.1
644.3	647.3	3.0	2.5	0.5
647.3	647.8	0.5	0.5	0.0
647.8	651.3	3.5	3.2	0.3
651.3	653.3	2.0	1.8	0.2
653.3	653.4	0.1	0.1	0.0
653.4	662.1	8.7	7.9	0.8

Total lost (feet): 32.7

Estimated percent recovery 8-100': 100.0
Percent recovery 100-200': 100.1
Percent recovery 200-300': 100.0
Percent recovery 300-400': 99.4
Percent recovery 400-500': 98.6
Percent recovery 500-600': 78.4
Percent recovery 600-622': 84.3

Total percent recovery: 94.9

5.7 CURRENT STATUS

5.7.1 Soil-Gas Carbon Isotope Chemistry

The carbon isotopic chemistry of most shallow unsaturated zones is controlled by plant respiration and decomposition. CO_2 generated by these processes builds up in the soil zone, resulting in a concentration gradient upward and downward. As a result, very little of the isotopically heavy atmospheric CO_2 passes very deeply into the unsaturated zone. This knowledge is important when using $\delta^{13}C$ analyses to trace the history of gas and water interactions with depth.

Dominance by biogenic CO_2 in the near-surface unsaturated zone could not be immediately assumed, however, at the Apache Leap. Soil cover is limited to weathered fractures and depressions and to the banks of small ephemeral streams. Highly fractured tuff is exposed over as much as 50% of the surface. Because of the patchy nature of the soil cover, often without visible vegetation, and the abundance of fractures open directly to the atmosphere, there is a possibility that atmospheric CO_2 could dominate in this system.

A series of soil gas sampling sites was established to examine this question. Results have so far been obtained for four sampling runs representing the fall of 1991, and the winter, spring, and summer of 1992. The results are tabulated in Table 5.14.

Table 5.14. $\delta^{13}C$ (‰) Results for Soil Gas Sampled at Apache Leap.

Sample	11/4/91	1/18/92	4/23/92	9/1/92	Description
LNB-1	-20.3	ns	ns	ns	stream deposit
CON-1	-20.9	ns	ns	ns	wet area, grass-covered
SG-L	-22.0	-18.2	-20.2	-22.1	stream deposit
		-20.3	-19.8		
SG-C	-20.0	-13.2	-19.3	ns	fracture fill, manzanitas
SG-MS	-18.1	-21.7	-20.4	ns	fracture fill
SG-MN	ns	-12.8	-17.2	-21.6	fracture fill
				-16.7	
SG-U	ns	-20.0	-22.0	-19.9	fracture fill
		-19.0*			
CHK-1	-9.7	ns	ns	ns	atmospheric sample

ns = not sampled or sample lost
* SG-U sampled on 1/14/92

Sample sites were selected at several different elevations in one subbasin. Sample locations are shown in Figure 5.25. For most sites, a plastic sheet was placed over a patch of soil free of vegetation. Two sites were not free of vegetation. At one site (CON-1), plastic was placed over a patch of short grass. At the second site (SG-C), plastic was sealed around the bases of three manzanita shrubs growing in a fracture. After allowing several days for soil CO_2 to build up beneath the plastic, gas samples were collected by inserting a soil probe into the ground through the plastic, pumping out several probe volumes of gas, and then drawing a sample into an evacuated 10-liter steel cannister.

It is clear from the $\delta^{13}C$ results that the soil at Apache Leap is permeated with biogenic CO_2 in spite of the many open fractures and discontinuous nature of the soil cover. Narrow soil-filled fractures and large areas with no surface vegetation still have characteristic $\delta^{13}C$ values for biogenic CO_2. The isotopically heavy values obtained for samples SG-C and SG-MN on 1/18/92 are the result of atmospheric contamination due to sampling errors.

The -17.2‰ value for SG-MN on 4/23/92 also probably contains an atmospheric CO_2 fraction. SG-MN is a fracture with a 10 cm aperture at the surface and a sampling depth no greater than 8 cm. It is possible that a 10 liter gas sample depletes the soil gas and draws in atmospheric air. To test this, a 4 liter sample was drawn first on 8/26/92 followed immediately by a 10-liter sample. The initial small sample had a $\delta^{13}C$ value of -21.6‰, consistent with the values observed at the other sites. The second 10-liter sample had a value of -16.7‰, confirming the suspicion that atmospheric air is being drawn into the larger gas sampling cannisters. It is significant that for even a very narrow and shallow strip of soil, biogenic CO_2 is still controlling the subsurface system.

Short-term isotopic fluctuation of soil CO_2 and sampling variability were tested by repeat sampling at two sites. At site SG-U, a sample was taken on 1/14/92 and again on 1/18/92. At site SG-L, two samples were collected at the same time on both 1/18/92 and 4/23/92. The duplicates from 4/23/92 are within the analytical uncertainty of $\pm$0.5‰, but the duplicates from 1/18/92 are different by 2‰. Within this range of variation, the $\delta^{13}C$ changes observed in Table 5.14 for different sites and different sampling dates may simply reflect sampling variability rather than fluctuating soil gas conditions. Similar results from borehole sampling by others (Yang et al., 1985; Thorstenson et al., 1990), however, may suggest that there are small-scale spatial and temporal fluctuations in the $\delta^{13}C$ of soil CO_2, but with a consistent mean value. The mean for the four sampling dates, excluding the contaminated samples, are -20.3, -19.8, -19.8, and -21.2‰ for 11/4/91, 1/18/92, 4/23/92 and 9/1/92, respectively (the 9/1/92 mean represents only three points). The overall mean is -20.3‰.

As a first step toward understanding what relationships exist between gas, aqueous, and mineral phases in the tuff, calculations were made to determine what should be expected if the entire unsaturated zone were in isotopic equilibrium with biogenic CO_2. According to Figure 5.26, a 7-8‰ difference can be expected between CO_2 gas and aqueous carbonate at isotopic equilibrium for a temperature range of 20-30°C, and an aqueous pH greater than 7.5. If the results of the soil gas analyses are averaged, as above, to approximate the long-term soil gas $\delta^{13}C$ value, a water in equilibrium with this gas at the temperature and pH described should have a $\delta^{13}C$ of -12 to -13‰. These numbers match quite well with those results obtained from the Oak Flats well on 4/27/90 (-11.9‰) and from some of the mine tunnel samples. Preliminary results hence suggest that the perched water is in isotopic equilibrium with biogenic CO_2 produced in the soil zone.

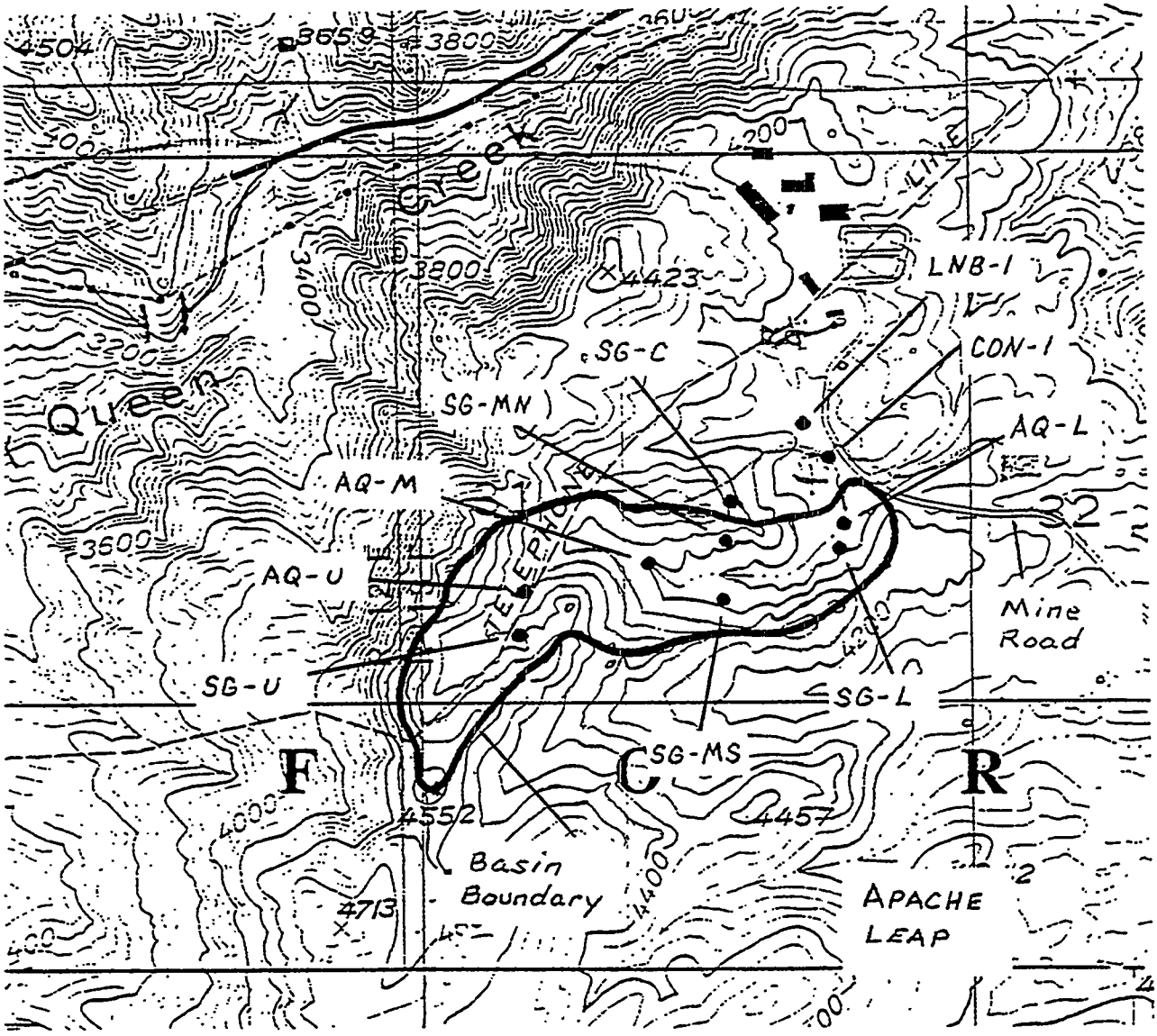

Figure 5.25. Topographic map of the Apache Leap study site with soil gas and surface water sampling sites marked.

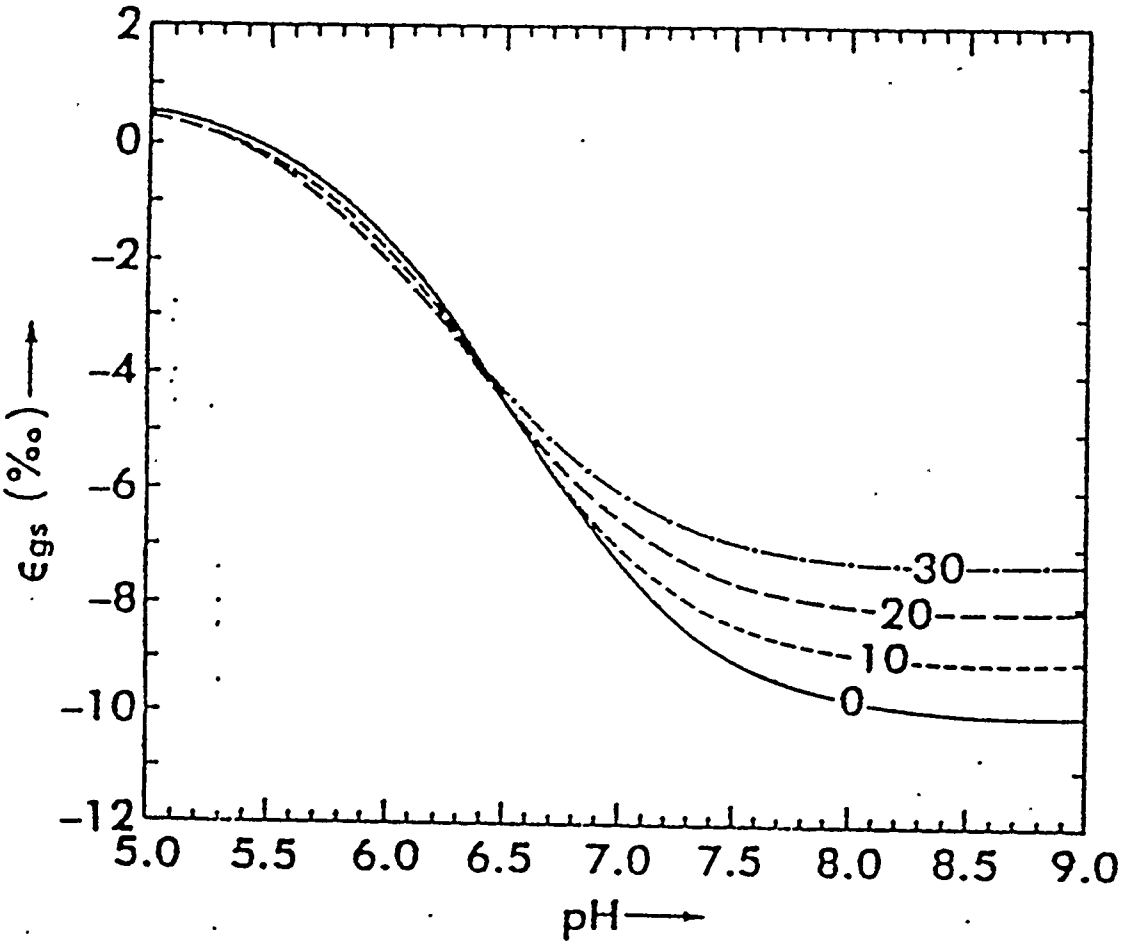

Figure 5.26. Equilibrium ^{13}C fractionation between calcite and a carbonate solution for various temperatures (°C) as a function of pH. (Reprinted from Geochim. Cosmochim. Acta 42, Wigley, T.M.L., L.N. Plummer, and F.J. Pearson, Mass-transfer and carbon isotope evolution in natural water systems, pp. 1117-1139, Copyright 1978, with kind permission from Elsevier Science Ltd, The Boulevard, Langford Lane, Kidlington OX5 1GB, UK.)

No data will be available for unsaturated zone water until sampling is begun from the slant borehole, but it is still possible to obtain some information on the soil-gas/pore-water relationship by investigating calcite precipitates. If the pore water is in isotopic equilibrium with biogenic CO_2, then calcites precipitated from the pore water may also have a $\delta^{13}C$ value that reflects those phenomena.

A few select samples from the DOE Oak Flats core have been obtained from the Sample Management Facility at the Nevada Test Site. Core samples ranging from 20 feet down to 460 feet have been analyzed using X-ray diffraction (XRD), scanning electron microscopy (SEM), and acid reaction tests to determine the existence of calcite. Using these methods, no calcite has been identified above 240 feet, although it should be noted that we do not have any core between 180 and 240 feet. Calcite is common in core below 240 feet. The perched water table is about 50 feet below the first appearance of calcite in these samples.

Using Figure 5.26, a pore water with a temperature between 10 and 20°C and a pH between 6.0 and 8.5 in isotopic equilibrium with Apache Leap biogenic CO_2 should have a $\delta^{13}C$ ranging from -18.5 to -12.0‰. Using Figure 5.27, a calcite in equilibrium with this pore water should have a $\delta^{13}C$ ranging from about -9 to -10‰. So far, only one fracture calcite from the Oak Flats core has been analyzed for a carbon isotopic signature. A sample from 240 feet was -9.5‰. In addition, Weber (1986) reported $\delta^{13}C$ values for two calcite samples above the perched water table at the Apache Leap. These values were -9.4 and -9.6‰. Again, preliminary data suggest that all phases in the unsaturated zone are in isotopic equilibrium with modern biogenic CO_2.

A matrix sample was randomly selected above 240 feet to determine if any calcite was present that was not identified using XRD, SEM, or acid-reaction tests. A 1.2 Kg sample from 125 feet was crushed and added to an acid bath to dissolve any carbonate. CO_2 from the dissolution was captured and analyzed for its carbon isotopic ratio. A very small mass of carbonate was observed by this process, but the resulting $\delta^{13}C$ value makes its origin suspect. A value of -15.9‰ was obtained for this sample.

According to calculations assuming 14% saturation, 17% porosity, and an alkalinity of the pore water of 80 mg/l as HCO_3^-, it is very possible that all the observed calcite was a result of evaporating pore water when the core was dried. Under such conditions, the resulting calcite would not reflect an equilibrium relationship with the pore water, but might instead match the $\delta^{13}C$ value of the pore water because of a complete transfer of mass.

If true, one possible interpretation is that infiltrating water traveled rapidly to this depth shortly before the sample was cored. This tentative conclusion is based on the fact that a water with a $\delta^{13}C$ of about -16‰ that is in equilibrium with soil CO_2 must have maintained a pH less than 7.0. A water that either traveled slowly or that traveled fast but sat for a long period of time at depth should have a higher pH as a result of silicate hydrolysis. A ^{14}C analyses of this sample to be performed using the tandem accelerator should help answer this question.

Efforts are currently being made to determine if the measured $\delta^{13}C$ values for soil gas match expected values based on dominant plant types. Identification of all the major plant species was performed in February 1992. A few deciduous shrubs and young perennials were also noted that were not identifiable at that time. Table 5.15 lists the plants by dominance and provides a tentative matching of the metabolism type which each species fits into (Smith, 1982).

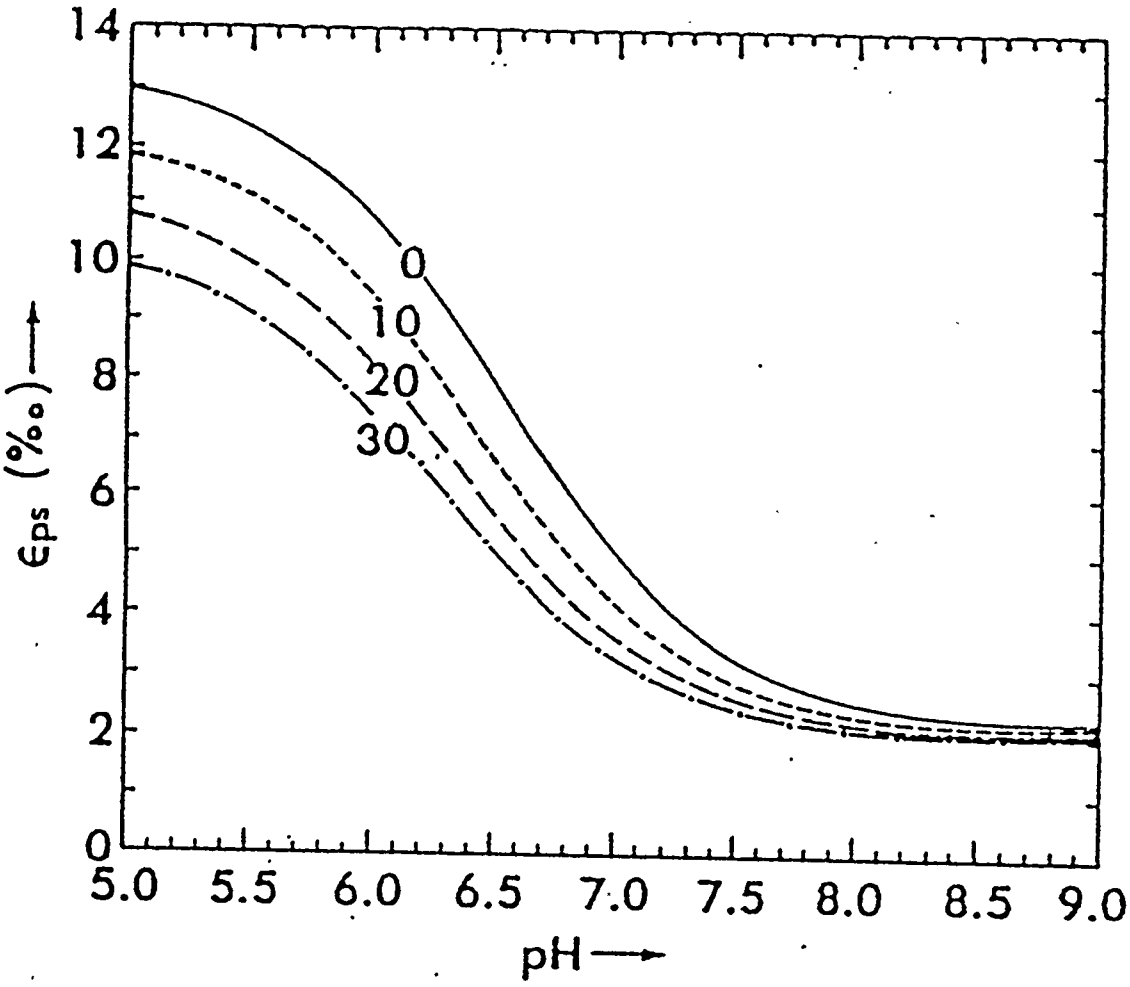

Figure 5.27. Equilibrium ^{13}C fractionation between a CO_2 gas phase and a carbonate solution for various temperatures (∞C) as a function of pH. (The 30∞ curve below pH 6.3 lies between the 10 and 20∞ curves.) (Reprinted from Geochim. Cosmochim. Acta 42, Wigley, T.M.L., L.N. Plummer, and F.J. Pearson, Mass-transfer and carbon isotope evolution in natural water systems, pp. 1117-1139, Copyright 1978, with kind permission from Elsevier Science Ltd, The Boulevard, Langford Lane, Kidlington OX5 1GB, UK.)

Table 5.15. Identified Plant Species at the Apache Leap Site and Metabolism Type.

		Metabolism Type
DOMINANT		
Scrub oak	*(Quercus turbinella)*	C_3
Point-leaf manzanita	*(Arctostaphylos pungens)*	C_3
VERY COMMON		
Sawtooth sotol	*(Dasylirion wheeleri)*	CAM
Agave	*(Agave palmeri)*	CAM?
Bear grass	*(Nolina microcarpa)*	CAM
Mountain mahogany	*(Cercocarpus betuloides)*	C_3
COMMON		
Toumey oak	*(Quercus toumeyi)*	C_3
Salt bush	*(Atriplex spp.)*	C_4
Yucca	*(Yucca spp.)*	C_3 or CAM
Wild lilac	*(Ceanothus greggii)*	?
LESS COMMON		
Alligator juniper	*(Juniperus deppeana)*	C_3
Wright silktassel	*(Garrya wrightii)*	C_3
Singleleaf pinyon	*(Pinus monophylla)*	C_3
Mistletoe	*(Phoradendron coryae)*	C_3
Utah juniper	*(Juniperus osteosperma)*	C_3
Grease bush	*(Glossopetalon spinescens)*	C_3
Muhly grass	*(Muhlenbergia spp.)*	C_4
RARE		
Prickly pear	*(Opuntia spp.)*	CAM
Cholla	*(Opuntia imbricata)*	CAM

5.7.2 Surface Water Chemistry

Runoff samples were collected from three elevations on 1/18/92 and 8/26/92. Sample locations are shown in Figure 5.25. Table 5.16 gives the results of the chemical analyses. For each sample, sulfate makes up half the weight of the dissolved solids. The high sulfate relative to other dissolved species is probably a result of continued leaching of smelter fallout. If this is the case, sulfur isotopes may serve as a useful tool to see how deep smelter-derived sulfate has penetrated into the unsaturated zone.

Although the soil is limited in its coverage, as discussed above, the $\delta^{13}C$ results for the aqueous samples indicate that runoff in this region is near equilibrium with soil gas CO_2 rather than atmospheric. A comparison is provided in Table 5.17 between the measured results and those expected if the water was in isotopic equilibrium with the soil gas, assuming a soil CO_2 value of -20.3‰. Three of the four measured values are nearly the same as the calculated values. Only the runoff sample for AQ-L on 1/18/92 is significantly different. The difference for this sample may simply be due to an inaccurate pH measurement. If the pH was actually about 6.2, the measured and calculated values will be the same. These results indicate that isotopic equilibration between soil gas and runoff is rapid and only marginally influenced by continued contact with the atmosphere.

5.8 SUMMARY AND CONCLUSIONS

Detailed studies of temperature, flow rate, and electrical conductivity of water discharging from fractures in the Never Sweat Tunnel have provided data on travel time for fracture- transmitted solute transport in unsaturated tuff.

Table 5.17. Calculated and Measured Stable Carbon Isotope Results for Runoff Samples. Calculated values are based on Figure 5.27 and assume isotopic equilibrium with a soil gas of -20.3‰.

Sample	pH	Temperature	Calculated $\delta^{13}C$	Measured $\delta^{13}C$
AQ-U (1/18/92)	6.17	3.5	-17.9	-17.9
AQ-L (1/18/92)	5.75	8.5	-19.3	-17.3
AQ-U (8/26/92)	6.00	23.3	-18.5	-18.9
AQ-L (8/26/92)	5.50	28.1	-20.1	-19.9

Deuterium and ^{18}O isotopic composition of rainfall, surface waters, and tunnel water has indicated the source and travel pathway for water entering the tunnel and appears to be a tool useful in delineating the various flow paths in the tuff.

Sulfur and boron isotopic compositions are systematically different, depending on the source of the recharging water. Recent contributions of sulfur to the surface water can be correlated with

Table 5.16. Chemical Composition of Runoff Samples. Concentrations are in mg/l.

	AQ-U 1/18/92	AQ-M 1/18/92	AQ-L 1/18/92	AQ-U 8/26/92	AQ-M 8/26/92	AQ-L 8/26/92
SO_4^-	17.6	19.4	17.8	16.8	19.0	17.2
Cl-	2.8	2.4	2.3	1.8	2.5	2.0
HCO_3^-	4.2	2.3	1.9	3.7	1.9	2.3
NO_3	bd	bd	bd	bd	bd	bd
Br^-	bd	bd	bd	bd	bd	bd
F^-	bd	bd	bd	bd	bd	bd
Ca^+	4.9	4.4	3.9	5.9	5.9	5.1
Mg^+	1.4	1.4	1.3	1.5	1.6	1.3
Na^+	4.0	3.8	3.7	3.7	3.8	3.4
K^+	1.2	1.0	0.9	1.3	1.7	1.6
Fe^{2+}	0.01	0.06	0.08	na	na	na
Al^{3+}	0.2	0.2	0.2	na	na	na
Si	12.9	13.9	13.9	14.7	17.4	13.9
pH	6.17	5.78	5.75	6.00	5.96	5.50
Temperature (°C)	3.5	7.5	8.5	23.3	27.3	28.1
TDS	49.2	48.9	46.0	49.4	53.8	46.9
Charge Balance (%)	-2.4	2.9	17.0	24.6	21.7	17.8

bd = below detection limit of 0.25 mg/l
na = not analyzed
charge balance = $((\Sigma cat-\Sigma an)/\Sigma cat)(100\%)$

mining activities, whereas older water or water traversing longer flow paths does not show this isotopic signature.

A perched water table has been identified within the tuff section. This hydrologic feature will now be studied in detail to determine recharge rates, head vaariation, and hydraulic and physical properties within the tuff that create permeability boundaries sufficient to support such a water table.

Samples of the perched water table have an uncorrected radiocarbon age of near 3000 years BP. This age is based on radiocarbon dating which has not been validated for unsaturated hydrologic systems such as this. Similar dating techniques are used at the Yucca Mountain site and may have the same limitations. The radiocarbon ages will be further defined by dating gas samples from within the tuff section using both radiocarbon and noble gas isotopes.

Drilling of a slant borehole through the tuff to the perched water table is completed. The corehole penetrated numerous potentially transmissive fractures. More than 90% core recovery was obtained for the 620 lineal foot corehole drilled along a 45° angle. Essentially, the entire core was preserved for future analyses for water content, water chemistry, mineralogy, and fracture studies.

Background ^{13}C soil gas samples have been collected from several locations which indicate that, even though the vegetation is sparse and the soil zone is extremely thin to non-existent, the plant-derived carbon dioxide is abundant in the unsaturated zone and the isotopic value is consistent and homogeneous throughout the upper few meters of the tuff. This is extremely important in calibrating the radiocarbon values in both gas and aqueous phases.

Based on preliminary data, it appears that biogenic CO_2 generated in the near-surface zone permeates the unsaturated zone and is in isotopic equilibrium with all phases. Further research must be done to validate these findings, but the implication is that there is not a significant degree of atmospheric penetration into the tuff. If true, this removes one potential complexity from the system, thus making it easier to interpret the results of radiometric dating techniques.

6. TASK V: INTRAVAL STUDIES

by R.L. Bassett

In support of the INTRAVAL project team, three experiments are being conducted which will provide characterization data and experimental results for model validation exercises. Characterization data sets and experimental results are being obtained for a nonisothermal transport experiment in a laboratory core as described under Task 1. These data will allow model validation exercises to be conducted which include nonisothermal transport of liquid and solute at the laboratory scale. Characterization data and experimental results are also being obtained for an isothermal fractured block experiment as described under Task 7. The simulation objective of this problem is to reproduce the movement of a wetting front of water in single horizontal fracture in an unsaturated block. At the field scale, multiscale estimates of pneumatic permeability are being obtained at the Apache Leap Site for testing models of gas phase flow and transport in unsaturated fractured tuff as described under Task 3. Two types of experiments will be conducted in the boreholes at the site which will provide observations for comparison with model results. These are cross-borehole pneumatic tests and gas tracer tests.

Presentations were made by University of Arizona representatives at an INTRAVAL working group meeting in December 1991 at Lawrence Berkeley Laboratory and in November 1992 in San Antonio, Texas. These presentations covered the description of the background, approach, and current status of the laboratory core and block experiments, field pneumatic tests, and determination of travel times through the two hydrologic regimes identified at the Apache Leap Site. The INTRAVAL data sets will be available in NUREG in the near future.

7. TASK VI: INFILTRATION, DEEP PERCOLATION, AND RECHARGE STUDIES

by Todd C. Rasmussen and Daniel D. Evans

The Apache Leap Tuff Site was used as a platform to study processes related to the vertical movement of water across the Earth's surface (infiltration) through the unsaturated zone (percolation) to the water table (recharge). The site is useful for these analyses because of its location in a semi-arid climate in unsaturated, fractured volcanic tuff. Of specific interest is the migration of water through the bulk rock which is composed of both a porous matrix microporosity and a fracture macroporosity. Laboratory and field experiments were conducted to evaluate the relative contribution to flow by both porosities.

Water budget analyses conducted on precipitation events during the study period indicate that most of the precipitation for large storms, and all of the precipitation for small storms, infiltrates on the watershed and is available for deep percolation. Some of the deep percolation may migrate to the surface at a lower elevation, while another component may be exhausted to the atmosphere in the vapor phase. Any residual deep percolation component which transits the entire thickness of the unsaturated zone will contribute to ground-water recharge. Evaluation of the disposition of the infiltration will be an important aspect of evaluating the magnitude of recharged water.

One portion of the study at the Apache Leap Tuff Site focused on water infiltration characteristics of an exposed fractured tuff site as a future approach for defining the upper boundary condition for unsaturated zone water percolation and contaminant transport modeling. The results of this study have been accepted for publication in the *Soil Science Society of America* journal. Two adjacent watersheds at the Apache Leap Tuff Site were selected for examination. The two watersheds had areas of 0.24 and 1.73 ha with slopes up to 45% instrumented for measuring rainfall and runoff. Fracture density was measured from readily observable fracture traces on the surface.

Three methods were employed to evaluate the rainfall-runoff relationship. The first method used the annual totals and indicated that only 22.5% of rainfall occurred as runoff for the 1990-1991 water year, which demonstrates a high water intake rate by the exposed fracture system. The second method employed total rainfall and runoff for individual storms in conjunction with the commonly used U.S. Soil Conservation Service Curve Number method developed for wide ranges of soils and vegetation. Curve Numbers between 75 and 85 were observed for summer and winter storms with dry antecedent runoff conditions, while values exceeded 90 for wet conditions.

The third method used a mass balance approach for four major storms, which indicated that water intake rates ranged from 2.0 to 7.3 mm hr^{-1}, yielding fracture intake velocities ranging from 122 to 293 m hr^{-1}. The three analyses show the complexity of the infiltration process for fractured rock. However, they contribute to a better understanding of the upper boundary condition for predicting contaminant transport through an unsaturated fractured rock medium.

7.1 WATERSHED-SCALE INFILTRATION PROCESSES

Additional studies related to watershed-scale infiltration processes have been examined to evaluate alternate conceptual models of infiltration processes. Of specific concern are the two models of watershed response, the Horton overland-flow model and the Dunne contributing-area model. The U.S. Soil Conservation Service (SCS) Curve Number method is commonly employed

to describe the cumulative storm rainfall-runoff-abstraction relationship. The SCS method uses the following formulations:

$$Q/P = F/S \tag{7.1}$$

$$F = P - Q \tag{7.2}$$

$$S = 1000/CN - 10 \tag{7.3}$$

where:

Q = runoff depth, inches;
P = precipitation depth, inches;
F = abstraction depth, inches;
S = potential storage depth, inches; and
CN = SCS Curve Number.

It should be noted that the value of P used here has been corrected for the initial abstraction, which is usually taken to be 0.2 S; thus, $P = P_{obs} - 0.2S$. The standard practice is to employ units of inches in the SCS Curve Number method. To avoid the requirement of using English units, Equations (7.1) and (7.2) are converted to a nondimensional form:

$$Q_s = Q/S \tag{7.4}$$

$$P_s = P/S \tag{7.5}$$

$$F_s = F/S \tag{7.6}$$

so that:

$$Q_s/P_s = F_s \tag{7.7}$$

$$F_s = P_s - Q_s \tag{7.8}$$

Solving Equations (7.7) and (7.8) yields:

$$Q_s = P_s^2/(1 + P_s) \tag{7.9}$$

$$P_s = F_s/(1 - F_s) \tag{7.10a}$$

or:

$$1/P_s = 1/F_s - 1 \tag{7.10b}$$

The time rate of change of the rainfall, runoff, and abstraction volumes are computed by letting:

$$q = dQ_s/dt \tag{7.11a}$$

$$p = dP_s/dt \tag{7.11b}$$

$$f = dF_s/dt \tag{7.11c}$$

which yields:

$$f = p(1 + P_s)^{-2} = p(1 - F_s)^2 \tag{7.12}$$

$$q = p - f = p[1-(1-F_s)^2] = p[1-(1+P_s)^{-2}] \tag{7.13}$$

The contributing area concept employs the following assumptions:

p	precipitation rate constant with space, variable with time
s_i	point storage depth variable with space, constant with time
f_i	point abstraction depth variable with space and time
q_i	point runoff depth variable with space and time

$$f_i = \begin{cases} 0 & \text{for } P_s > s_i \\ p & \text{for } P_s < s_i \end{cases} \tag{7.14}$$

$$q_i = \begin{cases} p & \text{for } P_s > s_i \\ 0 & \text{for } P_s < s_i \end{cases} \tag{7.15}$$

Integrating the point values over the entire watershed yields:

$$f = \int f_i da = \int 0 d\alpha + \int p d(1-\alpha) = p(1-\alpha) \quad (7.16)$$

$$q = \int q_i da = \int p d\alpha + \int 0 d(1-\alpha) = p\alpha \quad (7.17)$$

where a is the proportion of total area, and α is the proportion of area contributing to runoff. Solving for α as a function of the total precipitation and abstraction yields:

$$\alpha = q/p = 1 - (1+P_s)^{-2} = 1 - (1-F_s)^2 \quad (7.18)$$

The total abstraction, F_s, is related to the sum of the filled storage in the contributing area, S_i, plus the filled storage in the noncontributing area, or:

$$F_s = S_i + P_s(1-\alpha) \quad (7.19)$$

rearranging yields:

$$S_i = F_s - P_s(1-F_s)^2 = F_s^2 = (1+1/P_s)^{-2} \quad (7.20)$$

The area of filled storage as a function of total precipitation is obtained from Equation (7.18):

$$S_i = P_s = (1-\alpha)^{1/2} - 1 \quad (7.21)$$

Equation (7.21) provides a relationship between the watershed area and the storage depth distribution. A value of 0.2 is added to the storage depth to account for the initial abstraction depth on the watershed. The median storage depth (a = 0.5) is approximately 0.6, indicating that half of the watershed area has a maximum storage of approximately 0.6 S, while the remaining half exceeds this value. The mean depth is observed at the (a = 0.70) level, meaning that approximately 70% of the land area has a maximum storage depth less than S, while the remaining 30% of the area has a maximum storage depth exceeding S.

7.2 FRACTURE-MATRIX INTERACTION FOLLOWING FRACTURE IMBIBITION

Studies addressing the infiltration of atmospheric precipitation into fractured rock surfaces highlight the importance of fracture flow. Of increasing concern is the effect of matrix-fracture interaction in the attenuation of fracture flow with depth. Processes related to this interaction are addressed in the following section entitled "Laboratory Fractured Block Experiments". Results of these investigations are directly relevant to the migration of fluids from the surface through discrete fractures.

7.3 SUMMARY AND CONCLUSIONS

This task used field data from the Apache Leap Tuff Site to investigate the migration of fluids from each atmosphere interface through unsaturated fractured rock. Specific accomplishments included the collection of over three years of hourly rainfall, runoff, and infiltration data at two small watersheds at the Apache Leap Tuff Site. In addition, new field methods for obtaining

characterization data were developed to provide sufficient accuracy, precision, and reliability so that meaningful interpretations of the potential migration of liquids through the subsurface could be determined. The experiments yielded data that demonstrated only a small proportion of the limited precipitation which occurs as overland runoff and streamflow, even though the site is primarily devoid of vegetation and soil and possesses very steep slopes with only bare rocks exposed at the surface. These experiments also demonstrated that substantial quantities of water were imbibed into fractures and provided the potential for rapid migration to great depths in the fractured rock. The importance of long-duration, low-intensity precipitation on the potential for large volumes of infiltration was identified as a critical parameter controlling net movement through the unsaturated zone.

8. TASK VII: LABORATORY FRACTURED BLOCK MEASUREMENTS

by Todd C. Rasmussen

This section summarizes recent experiments related to the investigation of the behavior of unsaturated fractured rock. A series of tests were performed to characterize the water and air transport properties of fractures and the rock matrix for a range of matric suctions. The tests were conducted on a block of Apache Leap Tuff (white unit) with a single discrete fracture. Fractures and other macropores provide conduits of high conductivity for flow through saturated rock. Because flow velocities through fractures may be orders of magnitude greater than matrix velocities, the confinement capability of fractured rock for wastes may be compromised. Fractures in unsaturated rock may not provide these pathways, however, because large asperities are empty except when positive fluid pressures are present or for matric suctions very near zero.

8.1 BACKGROUND

High-permeability conduits such as fractures substantially affect the movement of fluids, including water, air, and other gases. Conceptual, mathematical, and numerical models are required to investigate the behavior of flow and transport through fractured rock or any geologic media containing macropores. The objective is to find a parsimonious and rigorous formulation of the flow and transport behavior that is computationally efficient and physically justifiable.

The complex phenomena associated with fracture flow have been systematized by Rasmussen and Evans (1989) using a hierarchical scale (Figure 8.1). At the lowest scale are processes related to flow in individual fractures, termed intrafracture flow processes. Processes associated with this scale include aperture variability and continuity. A larger scale focuses on flow through networks of discrete fractures, termed interfracture flow processes. At this scale, fracture orientations and interconnectivity are important. A final scale incorporates the effects of the porous rock matrix on flow behavior, termed suprafracture flow. Fracture surface sealing and matrix permeability introduce additional complexities at this scale.

This study focuses on two aspects of the behavior of fluid flow through a discrete fracture embedded in porous tuff. The first aspect of the experiment described here emphasizes fluid flow through a discrete fracture in the absence of matrix flow, which is related to the physics of infrafracture flow processes. Water, air, and gas flow through the fracture is not significantly affected by flow into or through the rock matrix when the rock matrix is saturated with water. In this case, fluid flow through the fracture is greatly dependent upon the rock fracture geometry. Fracture flow experiments were performed to investigate the behavior of water and three gas mixtures: air, air plus a helium gas tracer, and air plus an argon gas tracer. Fracture apertures were estimated based on transmissivities and hydraulic conductivities, tracer breakthrough times, and air-entry potentials. These apertures provide useful information for determining the influence of fracture geometry on fluid and solute transport behavior at the intrafracture scale.

A second aspect of this experiment focuses on coupled fracture-matrix fluid flow. For a fractured dry rock block, the imbibition of water into the fracture and uptake and migration of water into and through the rock matrix bounding the fracture is useful for describing the physics related to suprafracture flow processes. A conceptual and mathematical model has been proposed by Nitao and Buscheck (1991) that hypothesizes three stages in the fracture imbibition process. The first stage consists of rapid water imbibition into a dry fracture in response to a specified head

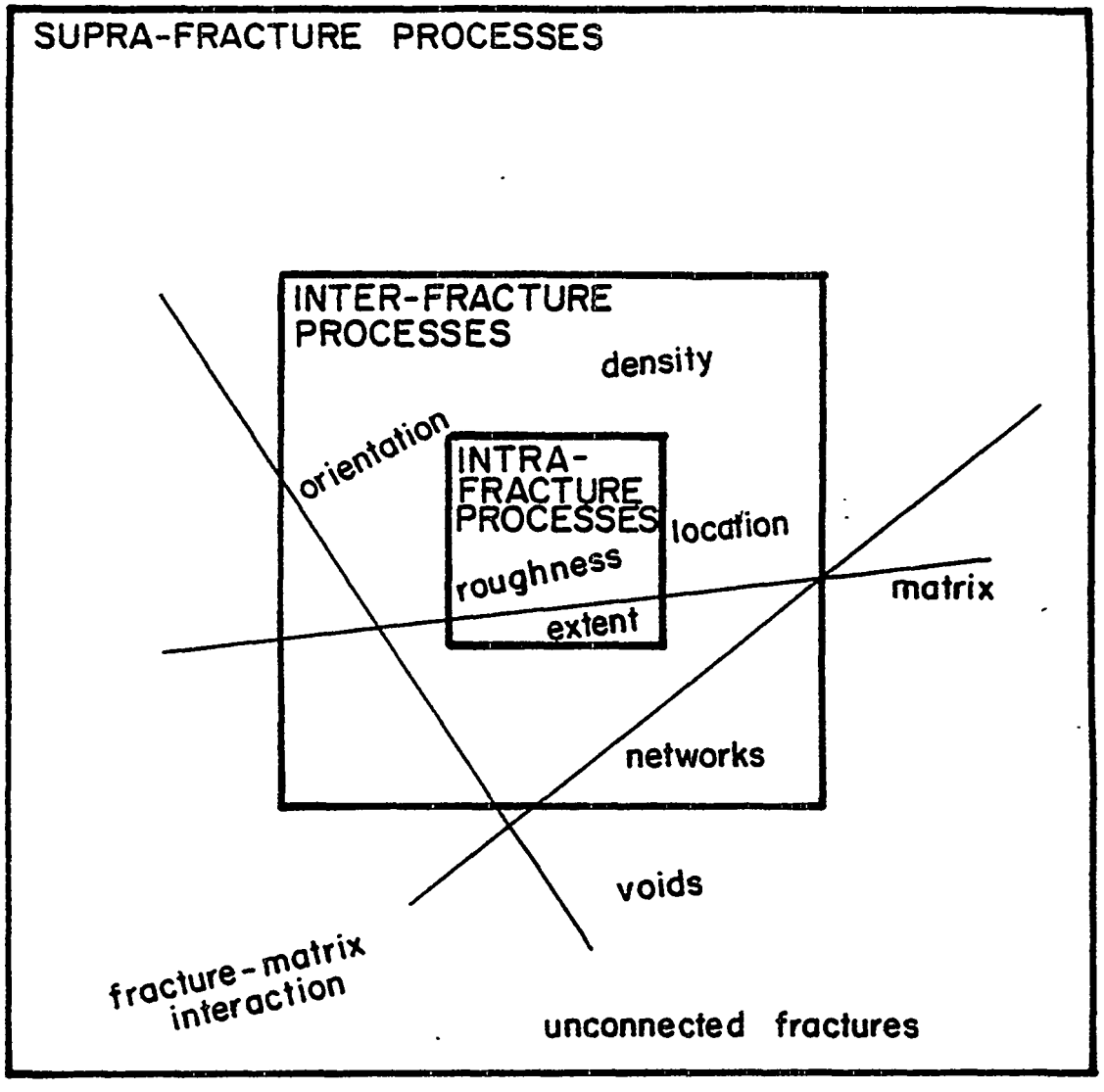

Figure 8.1. Hierarchical structure of fracture flow and transport processes.

or flux at one end of the fracture. The initial rapid intake slows in the second phase as water advances in both the rock matrix and fracture. The final phase begins when the water wetting front in the rock matrix encounters an axis of symmetry resulting from the existence of nearby fractures or an impermeable rock matrix boundary parallel to the fracture.

An evaluation of the hypothesized model of Nitao and Buscheck (1991) is presented here. The evaluation consists of two components, verifying the existence of the three proposed stages and verifying the parametric form of the prediction equation. The hypothesized parametric equation is evaluated by independently estimating material properties of the rock matrix and fracture. Characterization data sets are presented and used to construct a prediction model of the behavior of the fracture imbibition experiment. One measure of model performance is the comparison of the time series of predicted imbibition volumes with observed volumes. A second measure of model performance is the comparison of the time series of the predicted wetting front with the visual wetting front observed during the experiment.

8.2 EXPERIMENTAL PROCEDURE

A rock block measuring 20.2 cm wide, 92.5 cm long, and 21.0 cm high and containing a single discrete horizontal fracture was used for the experiments described here. The fracture was stabilized in the field using rock bolts cemented in place to prevent fracture movement. Two metal manifolds were constructed and attached to either end of the block to provide water injection capability into the rock fracture. The manifolds were attached with a thin rubber gasket between the manifolds and the rocks and tightened with all-threaded rods. The exposed fracture surface not covered by the manifolds was sealed using clay caulking. All surfaces of the block were covered with sheets of transparent vinyl adhesive to prevent evaporation and seepage. The block was air-dried at an average humidity of approximately 30%. Figure 8.2a illustrates the fractured block experimental apparatus.

8.3 ROCK VOLUME AND POROSITY

The rock porosity, consisting predominantly of the rock matrix porosity plus the less important fracture porosity, was obtained using a pycnometer with a volume of 3634.2 cm^3 attached to one of the injection manifolds with the manifold closed on the opposite end. The porous volume of the block was determined by placing a partial vacuum on the block, venting the pycnometer to the atmosphere, and then venting the pycnometer to the block. Figure 8.2b illustrates the experimental apparatus. The initial pressures of the block and pycnometer and the final pressure of the two vented to each other are used to calculate the block volume assuming isothermal ideal gas behavior:

$$v_b = -v_p \Delta p_p / \Delta p_b \qquad (8.1)$$

where:

v_b = block porous volume;
v_p = pycnometer volume;
Δp_b = pressure change in rock; and
Δp_p = pressure change in pycnometer.

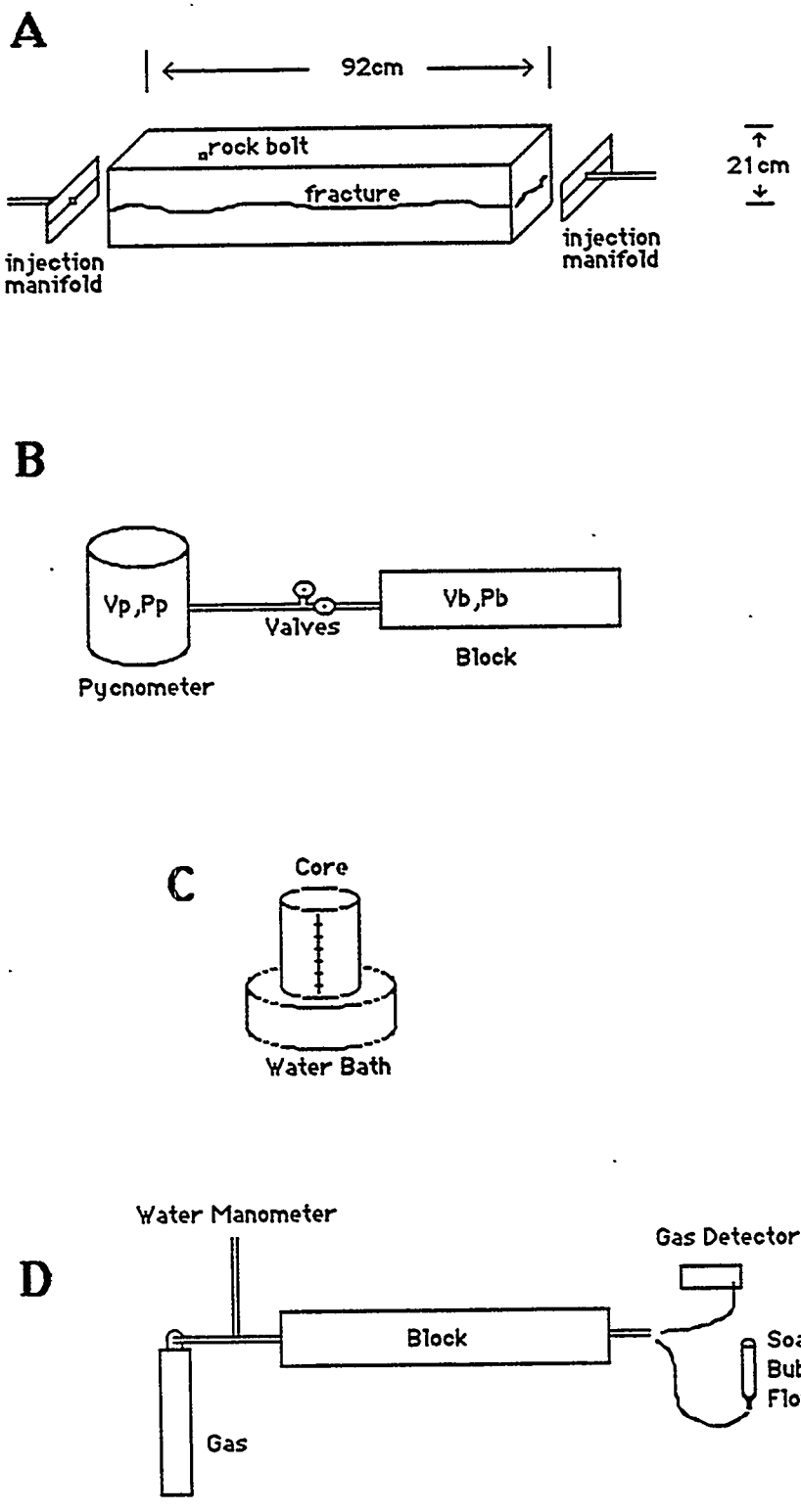

Figure 8.2. Experimental setups: (A) Block dimensions and manifold, (B) Pycnometer configuration, (C) Rock matrix water diffusivity experiment, and (D) Gas permeability and breakthrough curve experimental configuration.

Pycnometer measurements yielded a total rock porosity of 4635 $\pm$ 120 cm^3 (mean $\pm$ standard deviation of mean). The block porosity is calculated by subtracting the fracture volume and then dividing the block porous volume by the dimensions of the block. Given the matrix block dimension of approximately 39,240 cm^3, the block effective porosity is 11.5 $\pm$ 0.3 percent.

8.4 HYDRAULIC DIFFUSIVITY COEFFICIENT

The hydraulic diffusivity was estimated using a rock matrix core obtained from an excess rock fragment located immediately next to the block. The diffusivity was determined by placing the air-dried rock core on a water surface and measuring the advancement of the wetting front with time along four vertical profiles. Figure 8.2c presents the experimental configuration. The core imbibition experiment was conducted under conditions similar to that expected to occur during the block imbibition experiment, i.e., the core was at the same initial water content and water was applied at near zero pressure. The rock matrix water diffusivity was calculated assuming negligible gravitational forces using:

$$D_m = \pi y^2/4t \qquad (8.2)$$

where:

D_m = rock matrix water diffusivity coefficient;
y = height of rise of visual wetting front; and
t = observation time.

Rock matrix sorptivity experiments yielded a mean water diffusivity of 3.61 $\pm$ 0.28 $cm^2\ hr^{-1}$. Figure 8.3 presents the laboratory rock matrix imbibition data along with least squares model fits of the data. It is evident from the figure that significant diffusivity variation is present, even in the same core, leading to substantial uncertainty in this parameter.

8.5 GAS DIFFUSION COEFFICIENT

Argon gas movement through the rock matrix due to advective transport of the gas through the fracture was observed by maintaining a constant pressure gradient between the two manifolds and measuring the outflow concentration of gas using a thermal conductivity detector. Figure 8.2d presents the laboratory experimental arrangement. Gas diffusion into the dry rock matrix resulting from the advection of gas through the fracture and Fickian diffusion into the matrix on either side of the fracture is predicted using:

$$C* = (C - C_i)/(C_o - C_i) = \mathrm{erfc}[nD_g^{1/2}\tau/b(t-\tau)^{1/2}] \qquad (8.3)$$

where:

C^* = normalized tracer concentration;
C = measured tracer concentration;
C_i = initial tracer concentration in rock;
C_o = new injection tracer concentration;
n = matrix porosity;
D_g = matrix gas diffusion coefficient;
b = fracture aperture;

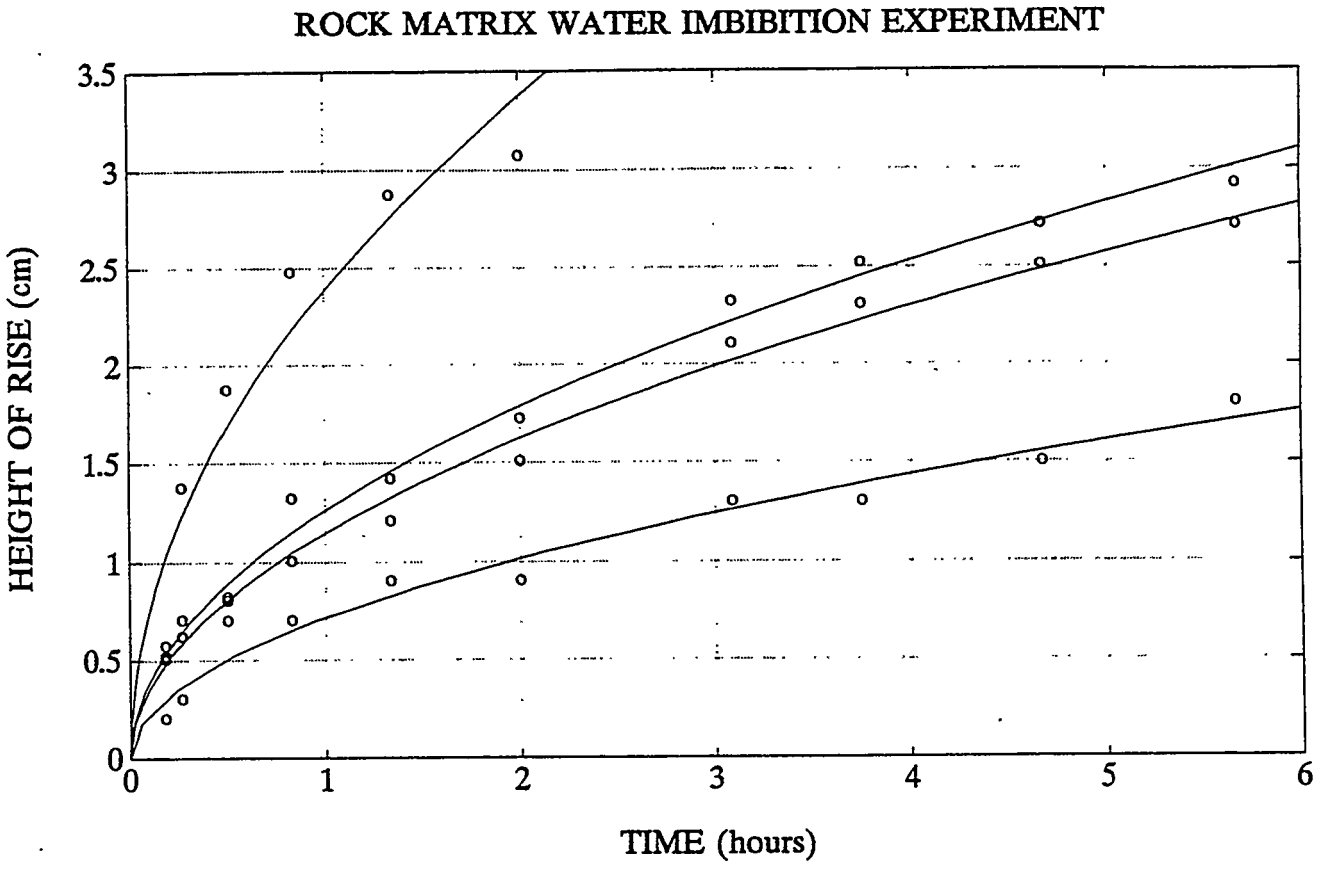

Figure 8.3. Observed and fitted height of water rise in core.

t = time since injection; and
τ = time of travel along block.

Equation (8.3) was inverted to solve for the matrix gas diffusion coefficient:

$$D_g = (t-\tau)\ (b\ \text{ierfc}[C*]/\tau n)^2 \qquad (8.4)$$

where ierfc is the inverse complementary error function. For pure argon gas flowing past the dry rock matrix, the value of D_g was estimated to be 31.0 $\pm$ 0.94 $cm^2\ hr^{-1}$. Figure 8.4 presents plots of three observed breakthrough curves along with the estimated breakthrough using the calculated matrix gas diffusion coefficient value.

8.6 FRACTURE VOLUME

Three methods were employed to determine the fracture volume. In one case, pycnometer tests of fracture volume were obtained once the rock matrix was saturated with water. Because the rock matrix pores were saturated with water, the fracture porosity could be determined without the complicating factors of matrix diffusion and storage. Results of pycnometer tests using a pycnometer volume of 108.4 cm^3 indicated a fracture volume of 142.3 $\pm$ 4.0 cm^3.

In a second experiment, argon and helium gases were used as air-phase tracers to determine the fracture volume. A steady flow of gas was established and then connected to one end of the rock fracture. A gas leak detector was used to measure the arrival time of the gas tracer. The flow rate of gas through the fracture was measured using a bubble flowmeter. The pressure gradient was also recorded. The fracture volume was determined by multiplying the gas flow rate by the arrival time of the gas. For dry rock, the initial arrival time was used to calculate the fracture volume because the diffusion of gas into the rock matrix substantially diminishes subsequent concentrations. The fracture volume calculated using the volumetric flux and the observed travel time was 100.2 $\pm$ 13.2 cm^3.

A final experiment was conducted using tracer tests through an open fracture embedded in a saturated rock matrix. The average travel time was used to determine the fracture volume. For the helium and argon gas tracer tests past a saturated rock matrix, the fracture volume was estimated to be 143.0 $\pm$ 12.6 cm^3, which is very similar to the estimate presented above for the volume estimated using the pycnometer. Estimates of fracture volume using tracer tests through the dry rock are less than the estimate based on the wet rock tracer and pycnometer tests due in part to the use of the initial arrival time.

8.7 FRACTURE TRANSMISSIVITY

The rock fracture transmissivity was determined before and after the imbibition test using air flow, tracer, and water injection experiments. For these experiments, a steady fluid flow was established, the flow rate was measured using a bubble flowmeter for gas and a graduated cylinder for liquid, and the pressure head gradient was measured. Figure 8.2d presents the experimental conditions. The fracture transmissivity was calculated using:

$$T = (Q/w)/(\Delta h/L) = q/i \qquad (8.5)$$

where:

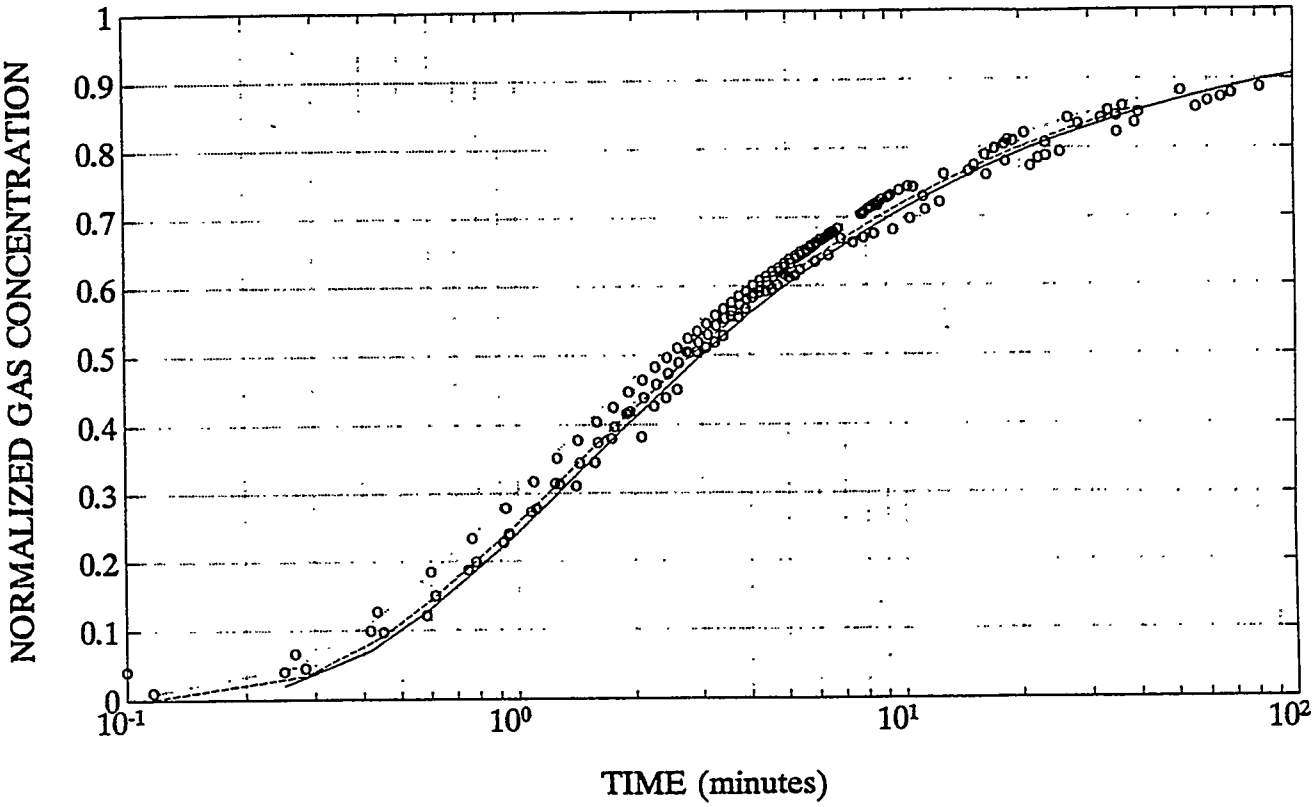

Figure 8.4. Observed and fitted argon gas breakthrough curves.

T = fracture transmissivity;
Q = flow rate;
w = fracture width;
Δh = freshwater manometer pressure head drop;
L = fracture length;
q = flow rate per unit fracture width (Q/w); and
i = freshwater pressure head gradient.

The freshwater manometer pressure head drop is defined here to provide consistent estimates of fracture transmissivity, irregardless of the fluid viscosity. To adjust for variable viscosity, the observed head is multiplied by the water viscosity and divided by the test fluid viscosity (i.e., $\Delta h = \Delta h_o \mu_w/\mu_g$). This formulation allows disparate fluids to be compared for wide ranges of pressure head gradients.

The fracture transmissivity calculated using water as the test fluid is 410 cm^2 hr^{-1}. The mean fracture transmissivity calculated using data for air flow through dry rock is higher at 457 cm^2 hr^{-1}, while the value for wet rock is slightly lower at 266 m^2 s^{-1}. Using argon gas flow through dry rock yields a value of 389 cm^2 hr^{-1}, which is close to the estimated value using water. The value using mixtures of air with helium and argon gases through the wet rock was larger, 598 cm^2 hr^{-1}. Using all data resulted in a mean fracture transmissivity of 490 $\pm$ 25.2 cm^2 hr^{-1}. Figure 8.5 presents the fracture transmissivity data as a function of the pressure gradient for air, mixtures of air with argon and helium gases, and water. The effects of slip-flow are not apparent, which is consistent with the large pore sizes present.

8.8 FRACTURE HYDRAULIC CONDUCTIVITY

An effective fracture hydraulic conductivity was obtained using data from the helium and argon tracer tests through the fracture embedded in a saturated rock matrix. The velocity of the tracer was calculated as the straight-line travel path divided by the observed arrival time. The mean velocity was obtained by averaging over all measured arrival times. The effective hydraulic conductivity was determined by dividing the mean velocity for each test by the mean freshwater gradient, adjusted for each test using the viscosity of the fluid. The observed effective fracture hydraulic conductivity was observed to be 9650 $\pm$ 504 cm hr^{-1}.

8.9 FRACTURE AIR-ENTRY VALUE

The air-entry value for the fracture is the suction head at which the fracture saturation allows the passage of air from one manifold to the other. The air-entry value was obtained by placing a vacuum on the fracture, flooding the fracture with water, dissipating the vacuum and allowing the water to saturate the fracture, disconnecting the water source, venting one manifold to the atmosphere, lowering the outlet of an outflow tube connected to the other fracture manifold, and observing the suction head at which air was observed in the outflow tube. An air-entry suction head of 13.5 $\pm$ 0.7 cm was required to drain the fracture at 20°C.

8.10 INTERPRETATION OF GAS BREAKTHROUGH CURVES

For a single component advection-diffusion model, the matrix gas diffusion coefficient combines the effects of flow due to partial and total gas pressure head gradients (adapted from Massmann and Farrier, 1992, Eqn. 11):

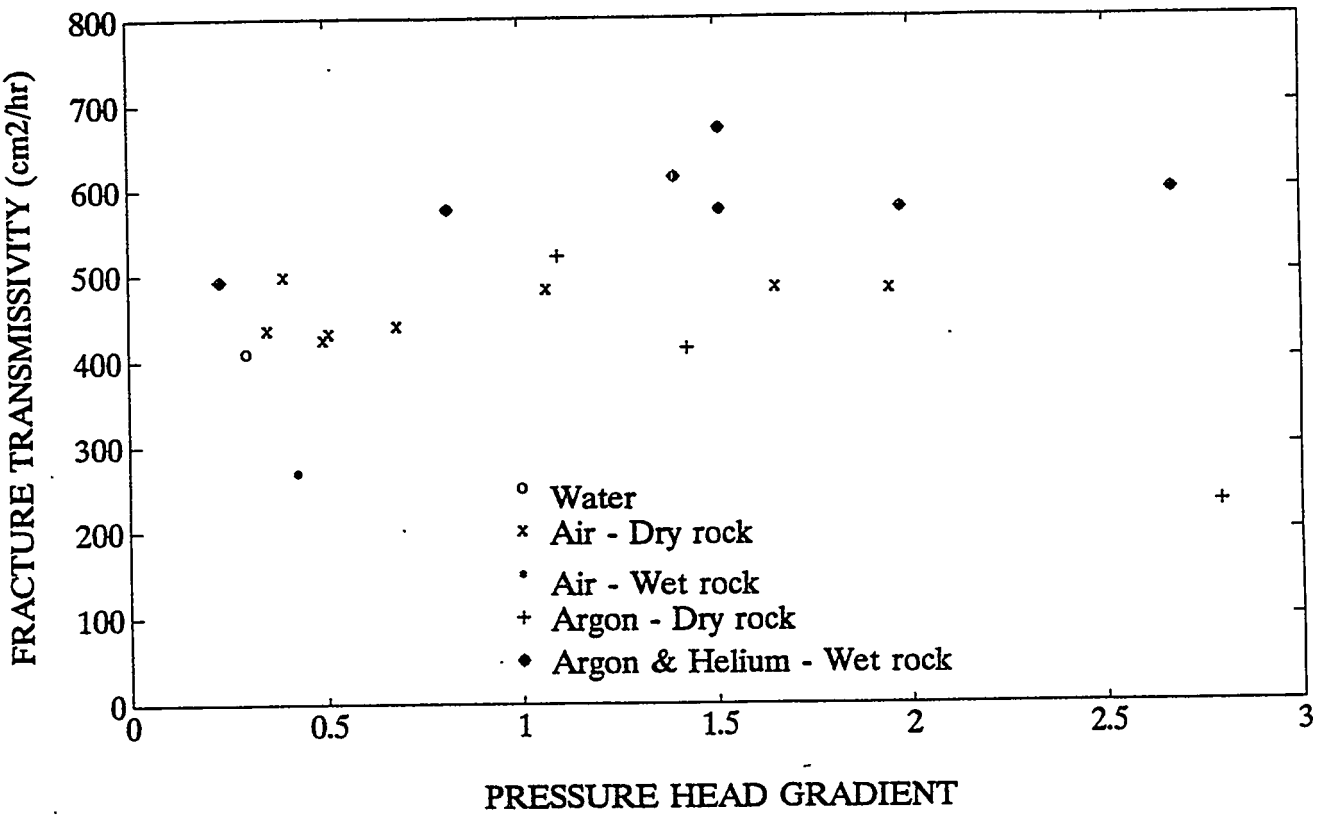

Figure 8.5. Observed fracture transmissivities.

$$D_g = D_j + k/\mu p_j \nabla h/\nabla h_j \quad (8.6)$$

where:

D_j = effective diffusion coefficient for gas j;
k = rock matrix permeability;
μ = gas mixture viscosity;
p_j = mean gas pressure head;
∇h = total pressure head gradient; and
∇h_j = partial pressure head gradient.

Massmann and Farrier (1992) further showed the validity of the single-component model for conditions where the permeability of the rock matrix is greater than approximately 0.01 μm^2. The mean rock matrix permeability of the Apache Leap Tuff is approximately 0.002 μm^2, or near the limit of the applicability of the single-component model. For conditions where the single-component model is not appropriate, Massmann and Farrier presented a simultaneous equation method for solving multicomponent gas mixture flow and diffusion problems.

Advantage can be taken of variations in the gas diffusion coefficient to determine the gas porosity of fractured rock or geologic materials with both micro- and macro-porosities. The volume of air-filled microporosity determines the reduction in breakthrough time for a gas with low diffusion rates compared to the time of a gas with higher diffusion rates. Breakthrough curves for gases of variable diffusivity are denoted by (C_i,t_i), where C_i is the observed concentration at time t_i for gas i with diffusion coefficient D_i.

Gases with variable diffusion coefficients are used to determine the travel time through the fracture, τ, by noting that, for conditions of steady flow, homogenous rock matrix porosity, and variable travel path lengths between the injection source and the observation, there will exist n pairs of observations where the gas concentrations for two gases are equal, i.e., $C_1 = C_2$. The fracture travel time for the specified concentration is:

$$\tau_i = (t_1 - \alpha t_2)/(1 - \alpha) \quad (8.7a)$$

where α is the diffusivity ratio, D_1/D_2. Inserting the estimated value of τ_i into Equation (8.3) yields an estimate of the rock matrix porosity-fracture aperture ratio for each travel path:

$$(n/b)_i = \text{ierfc}(C_1)\ (t_1 - \tau_i)^{1/2}/\tau_i D_1^{1/2} \quad (8.7b)$$

For a specified travel distance, L, with a steady and uniform velocity along the streamline:

$$(b/L)_i = (12\mu/\gamma \Delta h \tau_i)^{1/2} \quad (8.7c)$$

where:

μ = gas viscosity;
γ = manometer fluid specific weight; and
Δh = pressure head difference along the streamline from source to observation point.

The hydraulic conductivity distribution for each streamline can also be determined using:

$$K_i = L^2/\Delta h \tau_i \qquad (8.7d)$$

For one-dimensional steady fracture flow, the values of μ, γ, L, and Δ h are constant and known, providing unique estimates of the distribution of fracture hydraulic conductivity, fracture apertures, and rock matrix porosity.

8.11 ANALYSIS OF FRACTURE APERTURES

Six methods for determining the fracture aperture are presented. Three of the methods provide estimates of the volume of the fracture, two methods arrive at an equivalent frictional aperture using Poiseuille's law, and one method uses capillary theory to estimate an equivalent aperture. (Volumetric apertures are denoted with the symbol b, frictional apertures with the symbol e, and capillary aperture with the symbol c.) Pycnometer estimates of fracture volume were used to estimate the mean fracture aperture:

$$b_1 = V/A \qquad (8.8)$$

where:

V = fracture volume;
A = fracture surface area; and
b_1 = volumetric aperture.

Poiseuille's law is commonly employed to relate the fracture permeability to the fracture aperture for the case of fluid flow through smooth-walled fractures.

$$T = b_2 K = b_2 k\gamma/\mu = b_2 e_1^2/12\gamma/\mu \qquad (8.9)$$

where:

T = fracture transmissivity;
b_2 = volumetric aperture;
k = intrinsic permeability;
γ = specific weight of manometer fluid; and
e_1 = Poiseuille aperture.

Applying Equation (8.9) to rough-walled fractures underestimates the mean aperture due to inertial and friction effects. The assumption is often made that $b_2 = e_1$, i.e., that the mean cross-sectional area equals the Poiseuille aperture, yielding the so-called cubic equation:

$$k_f = e_2^3/12 \qquad (8.10)$$

where:

k_f = fracture intrinsic permeability; and
e_2 = Poiseuille aperture estimated using the cubic equation.

$$\sigma_x^2 \approx 2\ b^2\ \ln\ (E[b]/E[e]) \qquad (8.17)$$

Inserting the values of b_1 and e_1 from Table 8.1 yields an estimate of the fracture aperture standard deviation of 1.3 mm, which is consistent with the fracture surface roughness standard deviation of 1.8 $\pm$ 0.8 mm obtained from profiling six fracture surfaces (three matched pairs) located immediately adjacent to the rock matrix block investigated here (Vickers, 1990). Inserting a value of b_1 and e_2 from Table 8.1 yields a slightly smaller fracture aperture standard deviation of 1.1 mm. While the fracture aperture standard deviation is expected to decrease for mated fracture surfaces, a reduction in the fracture surface roughness standard deviation would reduce the gap between the calculated and observed standard deviations.

8.12 IMBIBITION EXPERIMENT

A water imbibition experiment was initiated by opening a valve connected to one of the fracture manifolds and a Marriotte bottle maintained at a pressure head of 1 cm of water. The fracture manifold at the opposite end of the fracture was open to the atmosphere. The total pressure head at the wetting front of the fracture is the applied pressure head plus the capillary pressure head, estimated previously to be 13.5 cm, yielding a value of 14.5 cm. Water intake into the fracture was measured using a graduated Marriotte bottle. Table 8.2 provides the cumulative fracture imbibition volume for various times.

Visual wetting fronts were monitored at various times by marking the position onto the clear plastic surface covering the rock matrix. Figure 8.7 presents the visual wetting front position at several times. It is apparent from the figure that the wetting front in the fracture advanced rapidly and irregularly for the first ten hours. Isolated zones of saturation were observed along the length of the fracture that finally coalesced at about ten hours, after which time the advancement of the wetting front along the fracture slowed, and most of the water movement appeared to be in the matrix perpendicular to the fracture, with some exceptions. At about 46 hours, rapidly growing fingers of saturation in the rock matrix intersected both the top and bottom boundaries. These fingers expanded laterally in size until about 146 hours, when most of the block was saturated and the fracture wetting front appeared to intersect the far end of the block. Full saturation was not observed until approximately 221 hours.

Nitao and Buscheck (1991) proposed the following predictive equations for the water imbibition rate into a single horizontal fracture bounded by porous rock:

$$\phi_m\ \Delta S_f/2\ (D_f/\pi t)^{1/2} \quad t < t_b$$

$$q_f \approx \Gamma(5/4)/\Gamma(3/4)\ \phi_m\ \Delta S_f(2D_f/\pi)^{1/2}\ (t\ t_b)^{-1/4} \quad t_b < t < t_a \qquad (8.18)$$

$$\phi_m\ \Delta S_f/2\ (D_f(1+\lambda)/\pi t)^{1/2} \quad t_a < t$$

and:

Tracer studies provided additional estimates of fracture aperture. A direct estimate used the arrival time of a conservative tracer in conjunction with the flow rate and the assumption of piston flow:

$$b_3 = V/A = Qt_a/A \tag{8.11}$$

where:

b_3 = volumetric aperture from tracer arrival times;
Q = volumetric flow rate; and
t_a = tracer residence time.

The tracer velocity was also used to estimate the fracture permeability:

$$k = v\gamma/\mu i = L\gamma/\mu i t_a \tag{8.12}$$

where:

v = tracer velocity;
i = pressure head gradient; and
L = fracture length.

The tracer velocity estimate of fracture permeability is used to estimate two additional fracture apertures: the Poiseuille aperture from Equation (8.8) and the mean aperture using Equation (8.10) and knowing the fracture transmissivity:

$$b_2 = T/K = e_2^3/e_1^2 \tag{8.13}$$

The negative pressure head required to drain the fracture is the air-entry value and can be related to a fracture aperture using:

$$c = 2\tau\cos\beta/\gamma\Delta z \tag{8.14}$$

where:

c = capillary aperture;
τ = air-water surface tension;
β = air-water-solid contact angle;
γ = water specific weight; and
Δz = air-entry pressure head.

For this experiment, the specific weight of water was 9806 pa m^{-1}, and the surface tension was 0.07275 Pa m. A contact angle of 0° was assumed.

Table 8.1 summarizes the experimental estimates of the Poiseuille, volumetric, and capillary aperture estimates. Figure 8.6 presents a comparison of the six fracture aperture estimates. The volumetric apertures obtained from the pycnometer and tracer experiments, b_1 and b_3, appear similar, while the volumetric aperture obtained from permeability and tracer velocities, b_2, is signifi-

cantly smaller. The apertures estimated using the permeability equations are smaller yet, due undoubtedly to surface effects. The smallest observed aperture is the capillary aperture, c. The order of fracture apertures is:

$$c < e_1 < e_2 < b_2 < b_1 \leq b_3 \tag{8.15}$$

Table 8.1. Fractured Block Aperture Estimates.

	Mean	Standard Deviation
Poiseuille's Aperture:		
e_1 $(12\mu K/\gamma)^{1/2}$	181	41 μm
e_2 $(12\mu T/\gamma)^{1/3}$	255	95 μm
Volumetric Aperture:		
b_1 V/A	762	.21 μm
b_2 T/K	507	403 μm
b_3 Q t_a/A	765	67 μm
Capillary Aperture:		
c 2τ cos/γ Δz	112	21 μm

This ranking of fracture apertures is consistent with the model of Tsang (1992). Silliman (1989) noted that the fracture aperture obtained from permeability estimates can be a function of the geometric mean, while the volumetric mean is the arithmetic mean of the fracture aperture. For an unknown spatial distribution of fracture apertures, x, the geometric mean, exp(E[ln(x)]), can be related to the arithmetic mean, E[x], using:

$$E[e] = \exp(E[\ln(x)]) = \exp(E[\ln(E[x]) + \ln(1+a)]) \tag{8.16}$$

where a = x/E(x) - 1. Knowing that:

$$\ln(1+a) = a - a^2/2 + a^3/3 \ldots \text{for } -1 < a < 1$$

yields the following relationship between the mean volumetric aperture b and the mean permeability aperture, e:

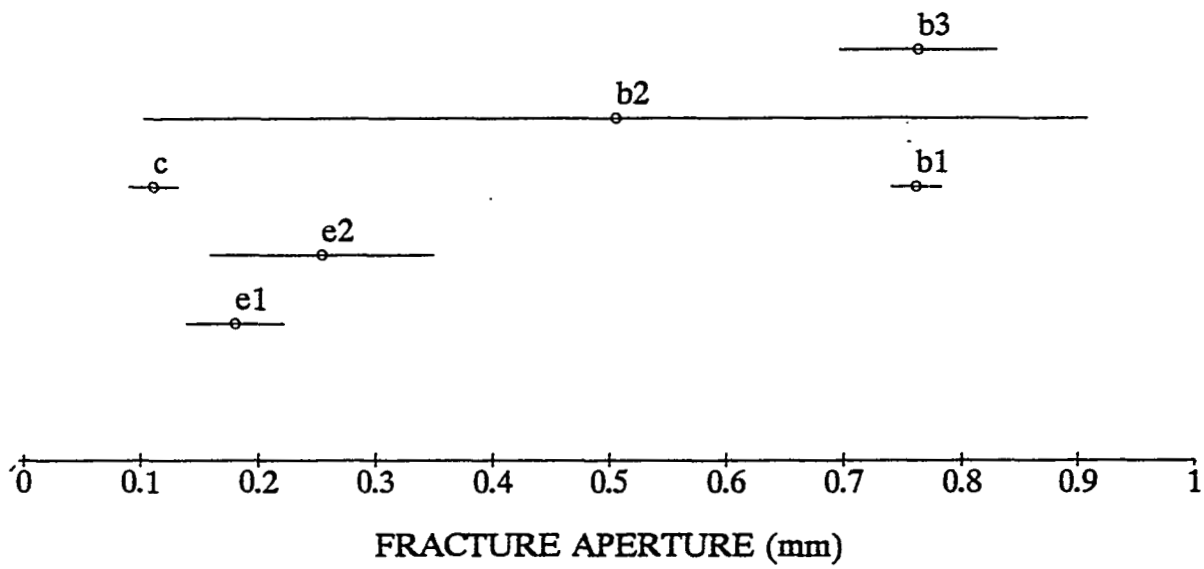

Figure 8.6. Mean $\pm$ one standard deviation fracture apertures.

Table 8.2. Fracture Block Imbibition Volumes.

Time (minutes)	Volume (cm^3)	Time (minutes)	Volume (cm^3)	Time (minutes)	Volume (cm^3)
2	15	135	202	1892	1348
3	20	155	212	1899	1348
4	25	165	235	2797	1678
5	28	180	250	2887	1711
7	31	195	270	4556	2271
9	35	210	280	4597	2313
11	39	225	293	4704	2313
13	41	240	312	4708	2323
15	46	255	328	4758	2333
19	52	285	342	4794	2342
22	57	300	360	5966	2896
25	60	340	407	5986	2911
30	70	360	430	6017	2911
35	73	390	463	6026	2924
40	80	420	485	7303	3588
45	90	452	500	7450	3649
50	93	465	506	7507	3671
55	99	508	528	7573	3696
60	107	552	577	7633	3720
65	116	586	598	8546	4041
70	126	596	601	8883	4122
75	132	600	607	9058	4157
80	140	771	711	10108	4337
85	144	1344	1034	10587	4390
90	150	1440	1126	11677	4511
95	157	1519	1168	12035	4551
100	163	1676	1301	12882	4679
105	169	1801	1309	13248	4717
120	190	1825	1317		

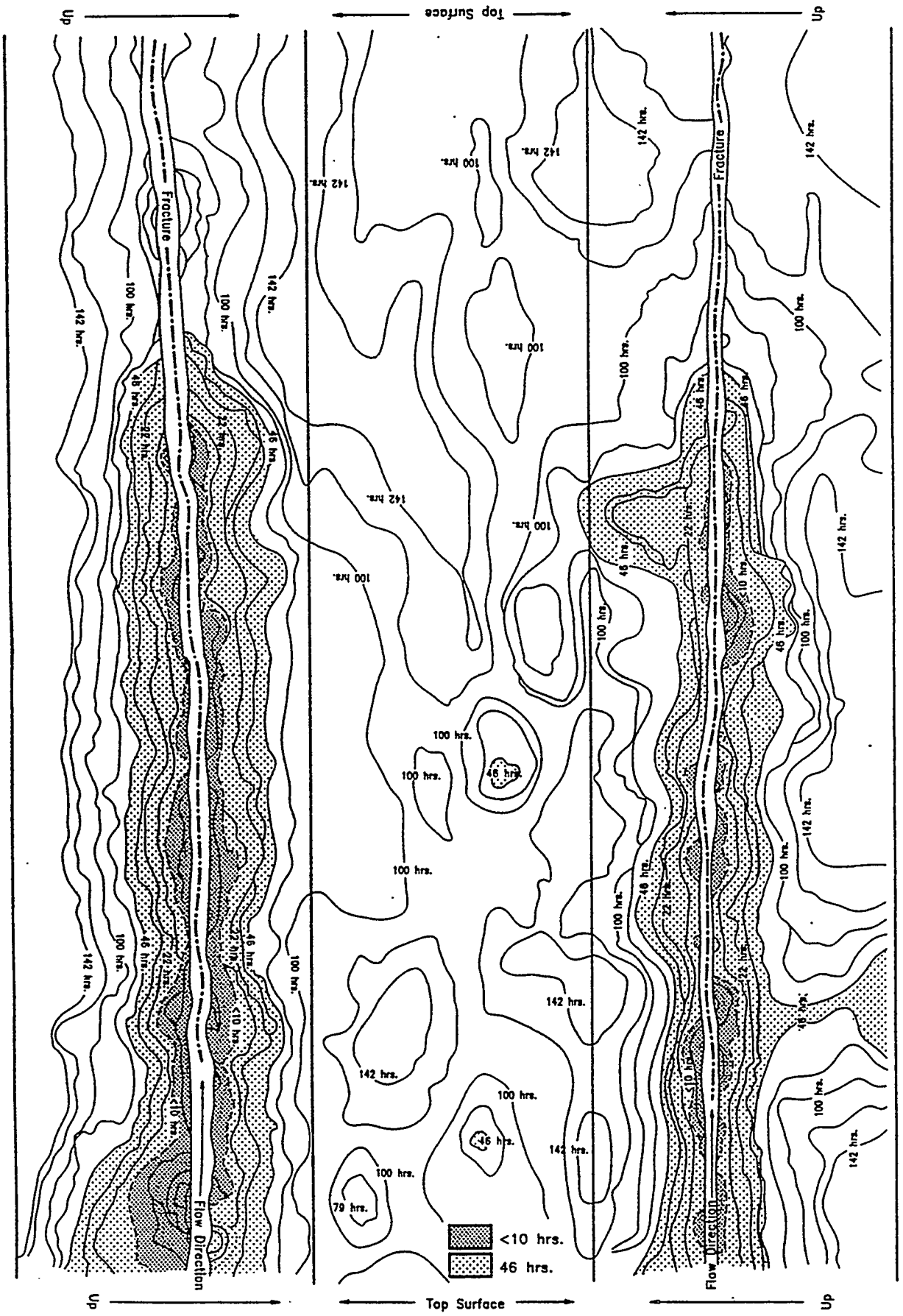

Figure 8.7. Observed wetting front positions.

$$t_a = a^2 \pi / D_m \tag{8.19a}$$

$$t_b = [b\Delta S_f / \phi_m \Delta S_m]^2 \pi / D_m \tag{8.19b}$$

$$\lambda = a\Delta S_m \phi_m / b\Delta S_f = V_m / V_f = (t_a / t_b)^{1/2} \tag{8.19c}$$

$$D_f = 2\pi K_f p_o / \phi_f \Delta S_f \tag{8.19d}$$

where:

q_f = flow rate into fracture;
ϕ_f = fracture porosity;
ϕ_m = matrix porosity;
ΔS_f = change in fracture saturation across the wetting front;
ΔS_m = change in matrix saturation across wetting front;
D_f = fracture diffusivity coefficient;
D_m = matrix diffusivity coefficient;
a = half-distance between parallel fractures;
t = time from beginning of imbibition;
V_m = matrix volume;
V_f = fracture volume;
K_f = fracture hydraulic conductivity; and
p_o = pressure head.

According to this model, the initial stage of flow corresponds to fracture imbibition, the second to another imbibition rate into the fracture and rock matrix, and a final stage corresponds to an imbibition rate where the parallel fractures interfere and limit the lateral migration of flow away from the fracture.

Parameters in Equations (8.19a-d) were estimated using three methods. The first method employed data obtained from characterization studies, termed prediction parameters. The second method used the observed imbibition flux to calculate optimal parameter values, termed calibration parameters. The third method used the observed fracture wetting front position to determine the fracture water diffusivity.

Table 8.3 presents the mean and standard deviation of the observed values of the estimated characterization properties of the rock matrix and embedded fracture. Several parameters, including the liquid saturation changes across the wetting front in the fracture and rock matrix, are assumed values. The fracture porosity is incorporated in the fracture hydraulic conductivity value due to the manner in which the hydraulic conductivity was determined. The prediction parameters required in Equation (8.18) (i.e., t_a, t_b, λ, and D_f) were obtained from these characterization data. Table 8.4 presents the estimates of the prediction parameters using data from Table 8.3. Figure 8.8 presents a comparison of model predictions with observed data. As is evident in the figure, the model approximates the transition times between the three periods and reproduces the slope of the

Table 8.3. Fractured Block Characterization Properties.

		Mean	Standard Deviation
Rock Matrix Properties:			
V	Rock volume	39,240	0 cm^3
V_t	Pore plus fracture volume	4,635	120 cm^3
V_m	Matrix pore volume	4,493	127 cm^3
ϕ_m	Matrix porosity	0.115	0.003
ΔS_m	Liquid saturation change	1[1]	--
D_m	Water diffusivity coefficient	3.61	0.28 $cm^2\ hr^{-1}$
D_g	Gas diffusion coefficient	31.0	0.94 $cm^2\ hr^{-1}$
Rock Fracture Properties:			
V_f	Volume	142.3	41.7 cm^3
w	Width	20.2	0 cm
a	Fracture-boundary distance	10.5	3 cm
b	Half-aperture	381	11 μm
L	Fracture length	92.5	0 cm
ϕ_f	Porosity	1[2]	--
ΔS_f	Liquid saturation change	1[1]	--
K_f	Hydraulic conductivity	9650	504 cm hr^{-1}
T_f	Fracture transmissivity	490	25.2 $cm^2\ hr^{-1}$
Boundary Condition:			
p_o	Pressure head:		
	with capillarity	14.5	0 cm
	without capillarity	1.0	0 cm

[1] Value assumed
[2] Value incorporated in K_f

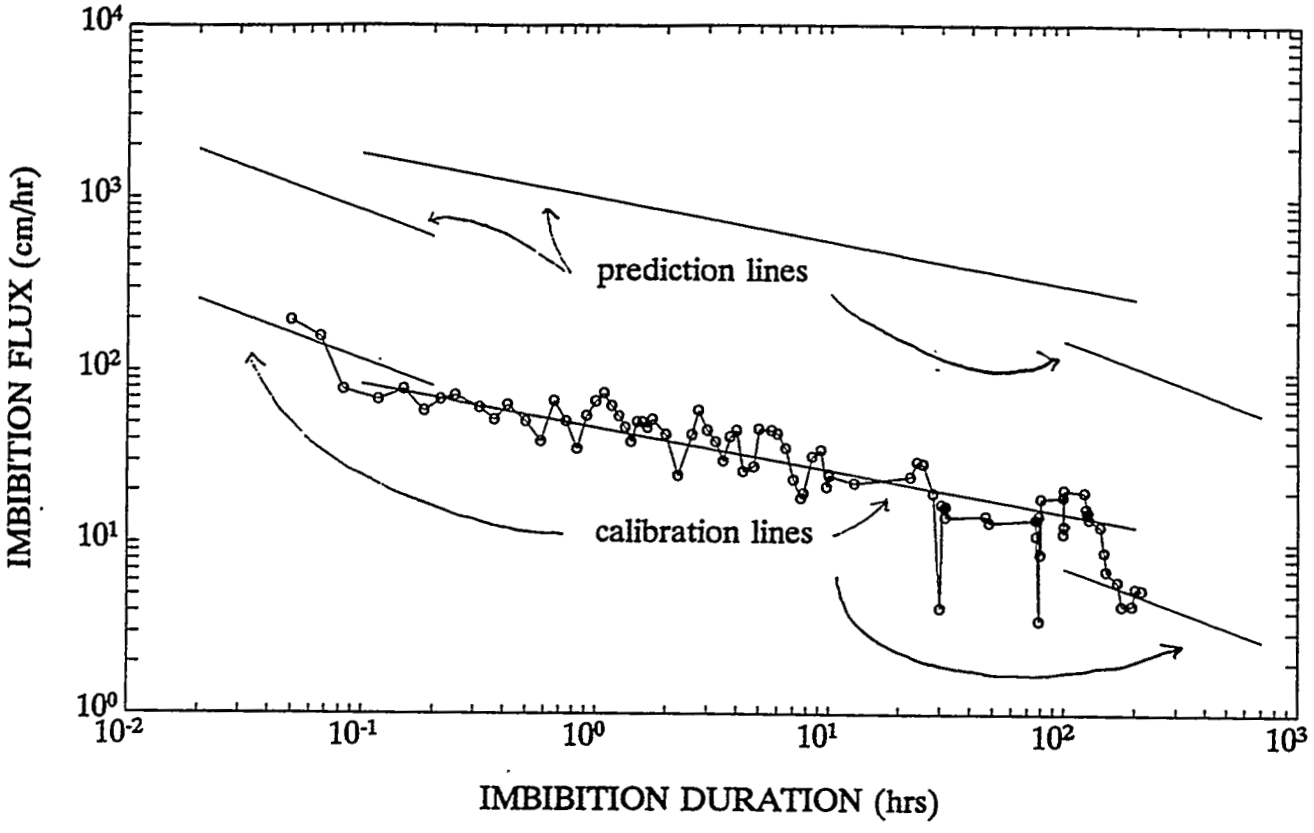

Figure 8.8. Observed, predicted and calibrated water imbibition rates.

observed data. On the other hand, the prediction equation overestimates the observed imbibition flux during all periods.

Calibration parameters were obtained using the inverted form of Equation (8.18) and the observed imbibition rates as a function of time. The values of t_b and λ were set equal to the prediction values, while t_a was estimated by observing the time at which a distinct change occurred in the slope of the q_f curve. The calibrated value of this parameter, as noted in Table 8.4, cannot be rejected at the $\alpha = 0.05$ level. The difference between the calibrated and predicted value of t_a can be attributed to the spatial variability of the hydraulic diffusivity, as well as the possibility of entrapped air retarding the advance of the wetting front in the rock matrix. Values of the calibration parameters are presented in Table 8.4. All values of D_f estimated in the regression model are statistically different from the values computed by Equation (8.19d).

Table 8.4. Fractured Block Prediction and Calibration Parameters

	Prediction		Calibration	Reject
t_a (hr)	96.1	71.3	195.0	No
t_b (hr)	0.1	0.1	0.1[1]	No
λ	31.6	8.19	31.6	No
D_f (cm^2 hr)	897,000	47,000		
Imbibition Rate:				
Phase 1			16,800	Yes
Phase 2			1,970	Yes
Phase 3			1,990	Yes
Wetting Front Position:				
Phase 2			13,000	Yes

[1] Equal to prediction value

The position of the wetting front in a single horizontal fracture embedded in a porous rock is predicted using (Nitao and Buscheck, 1991, similar to Eqns. 72-74):

$$x(t) \approx \begin{cases} (D_f t/\pi)^{1/2} & t < t_b \\ (2D_f)^{1/2} (t\, t_b)^{1/4}/\pi t_b & t_b < t < t_a \\ (D_f t/\pi\ (1+\lambda))^{1/2} & t_a < t \end{cases} \qquad (8.20)$$

where x(t) is the fracture wetting front position as a function of time. The fracture wetting front advance was observed by noting the farthest advance of wetting along the fracture-matrix interface. Wetting front position data are only available during the second phase. The observed fracture wetting front position is indicated in Figure 8.9 along with prediction and calibration positions. It is evident from the figure that the prediction parameters overestimate the observed wetting front advance. If the value of t_b is assumed to equal the prediction value during Phase 2, then the value of D_f can be calculated. This value is also shown in Table 8.4. Like the calibration parameters obtained from imbibition flux data, the wetting front value of D_f is substantially less than the prediction value, although not as low as the calibration values.

The wetting front advance data were also used to estimate the change in fracture saturation behind the wetting front, ΔS_f. Estimates of ΔS_f were obtained by visually noting the length of saturated rock matrix immediately adjacent to the fracture and dividing by the furthermost extent of wetting along the fracture. Figure 8.10 presents a plot of the fracture saturation as a function of imbibition duration. As can be noted in the figure, for very early time, the saturation is approximately 10%, but increased rapidly to near saturation for most of the experiment. The appropriate value of ΔS_f for most of Phase 2 and all of Phase 3 is clearly 1.0, while a lower value is required for Phase 1. Thus, the importance of ΔS_f can be neglected for most of Phase 2 and all of Phase 3.

A porous block of volcanic tuff with an embedded fracture was used to perform characterization studies of water and gas flow. Equivalent fracture apertures were obtained using six types of experiments. Three volumetric fracture aperture values were obtained by using a pycnometer, tracer breakthrough volumes, and the ratio of fracture transmissivity to fracture hydraulic conductivity. Two Poiseuille apertures were obtained using a cubic aperture equation applied to gas and water flow rates and by using quadratic aperture equation gas breakthrough velocities. A final estimate of fracture aperture was obtained using the air-entry potential of the saturated fracture.

The volumetric apertures estimated using the pycnometer and the tracer breakthrough volumes were closely related. The volumetric aperture determined using the ratio of fracture transmissivity to hydraulic conductivity was less, followed by the apertures determined using the cubic and quadratic equations, respectively. The smallest aperture observed was the capillary aperture. This progression is consistent with the hypothesis that fracture roughness will decrease the effective flow area for the Poiseuille flow and induce an ink bottle effect at fracture constrictions.

A horizontal fracture imbibition experiment was also conducted using water as a fluid imbibed into an initially dry fractured rock. The imbibition rate was reproduced using a model developed by Nitao and Buscheck (1991). The form of the model was found to provide a good fit to the shape of the observed data, but the model overestimated the fracture imbibition volume by a factor of 20 and the fracture wetting front advance by a factor of eight. The noted reduction in water

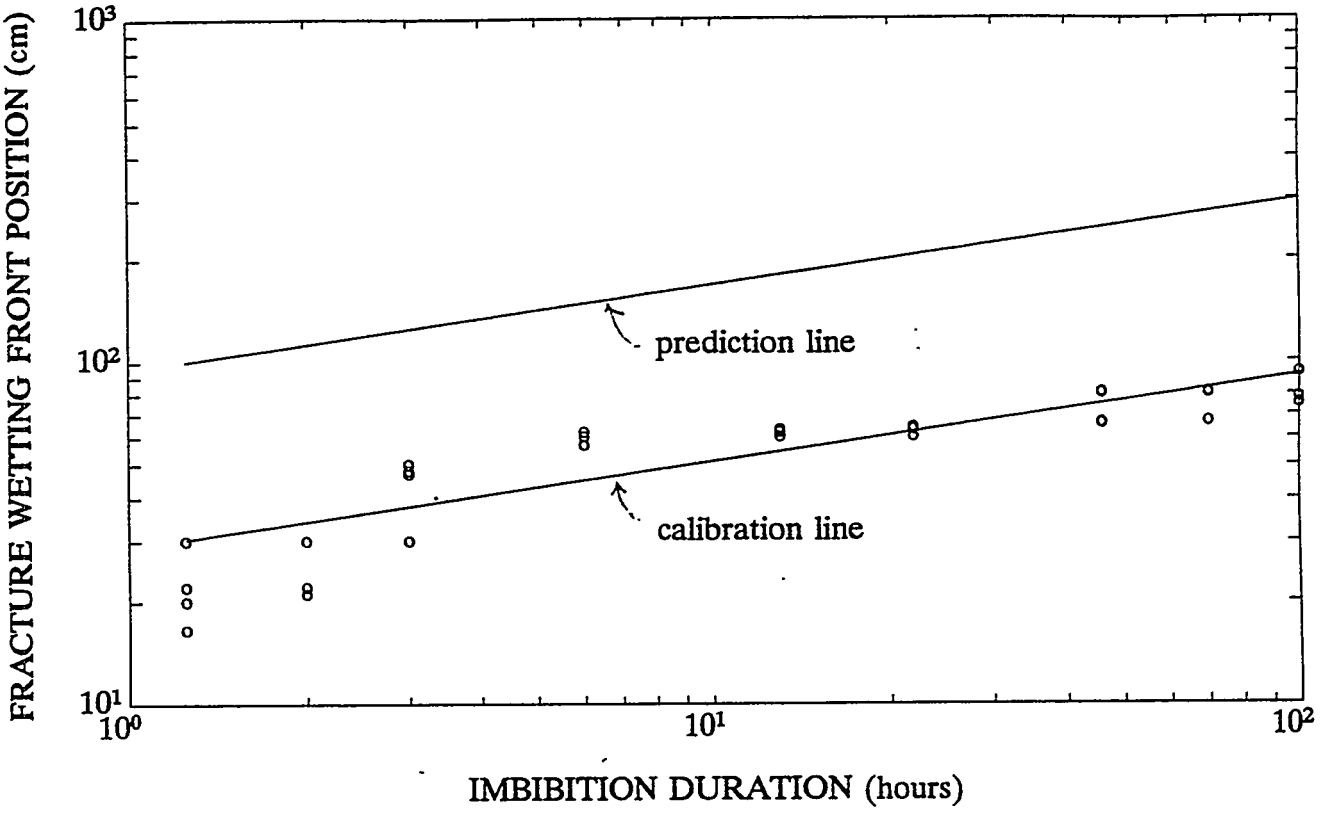

Figure 8.9. Observed, predicted and calibrated fracture wetting front position.

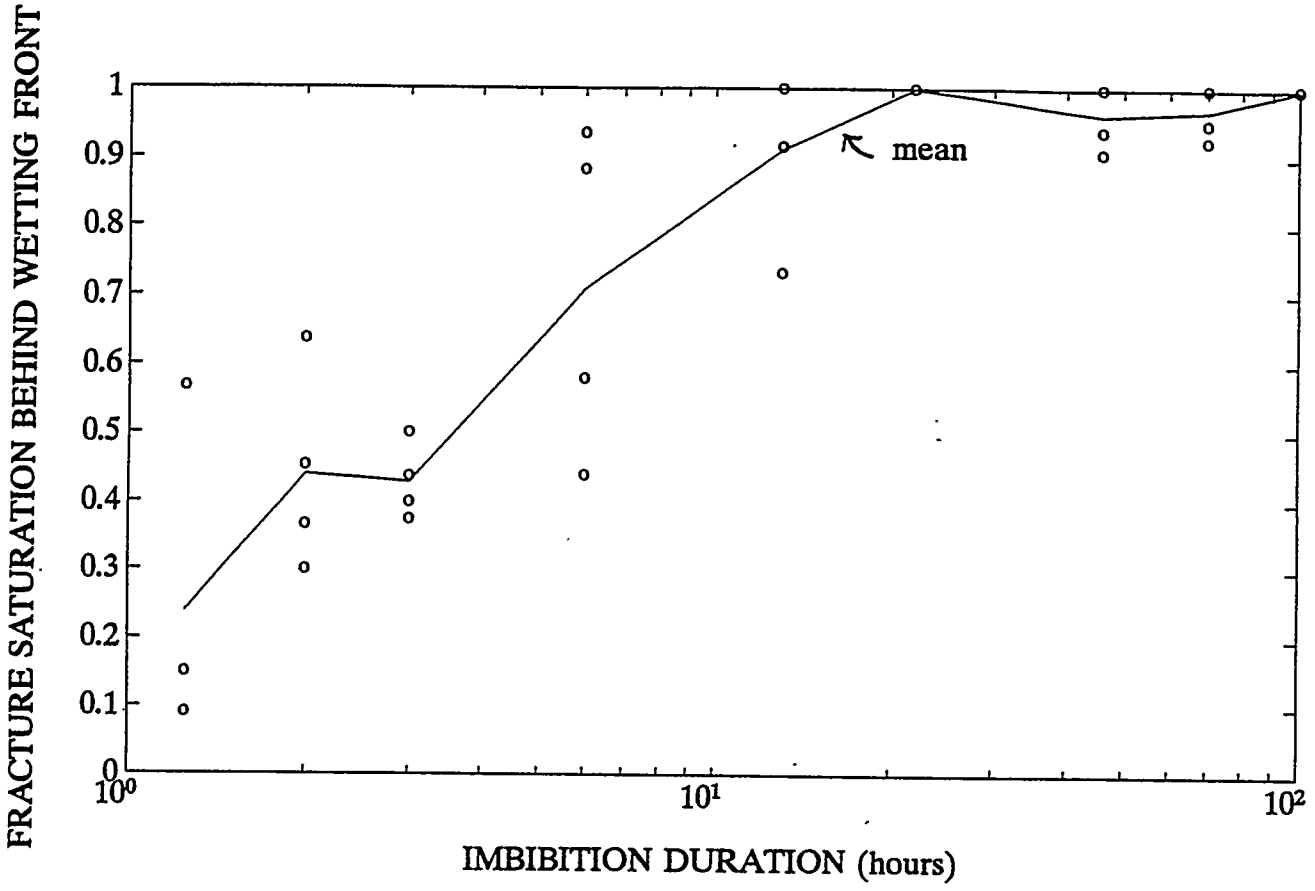

Figure 8.10. Observed and mean fracture saturation behind wetting front.

inflow may be due to phenomena neglected in the theoretical model, such as fracture surface coatings or enhanced surface weathering, and the inability to accurately determine fracture physical properties *a priori*, such as the fracture water diffusivity. It was shown that fracture saturation behind the wetting front initially is very low, perhaps 10%, but increases to complete saturation during the course of the experiment. This may indicate that fingers of saturation exist within the fracture during early time which expand laterally and dissipate over time.

8.13 SUMMARY AND CONCLUSIONS

Laboratory experiments were conducted using a block of Apache Leap Tuff with a natural fracture embedded along the long axis of the block. The fracture experiments were designed in conjunction with Tasks 3 and 6, which focused on the mechanics of fluid flow through fractured rock on field scales. Important research results related to fractured block experiments included the development of fractured rock characterization methods for parameters relevant to high- level waste transport, including fracture transport apertures, transmissivity, matrix porosity, and fracture wetting from propagation velocities. In addition, an evaluation of analytic and numeric models for representing fluid flow and transport through fractured rock under isothermal conditions was performed. It was shown that current analytic methods are unsuitable for predicting both the imbibition rate and the wetting front propagation velocity. Relevant characterization parameters were also identified. It was shown that existing characterization techniques focus on parameters which may not be relevant for field scale transport through fractured rock. In particular, the fracture water diffusivity coefficient was shown to be the parameter that most accurately indicates the fracture wetting front migration. The characterization of this parameter has not yet received attention to date.

9. TASK VIII: WORKSHOPS ON FRACTURE FLOW AND TRANSPORT

by R.L. Bassett

Workshop V was organized by The University of Arizona, U.S. Geological Survey, and the U.S. Nuclear Regulatory Commission and was convened in Tucson, Arizona in January 1991. More than 70 scientists attended, giving presentations and participating in the open discussions. A field trip was conducted to the Apache Leap Tuff Site at which time technical presentations were made by the students, faculty, and staff of The University of Arizona. Summaries of the papers are published in a NUREG report (in press). The workshop was highly successful and future workshops were recommended.

Workshop VI was held in Tucson, Arizona, January 25-28, 1993, organized by The UA, NRC, and the Center for Nuclear Waste Regulatory Analyses (CNWRA). Technical presentations addressed the more focused theme of using borehole data and core analysis in evaluating flow and transport in unsaturated fractured rock. Technical presentations were given in a new format which allowed for much more discussion. Abstracts were not required, and scientists were encouraged to bring their latest research. The discussions were excellent. In addition, this workshop allowed time for video presentations of research sites, e.g., Apache Leap activities, video of the drilling of the new deep slant borehole, and a video from the Las Cruces Trench site. This format was instructive and will be continued in future meetings.

10. REFERENCES

American Public Health Association, American Water Works Association, and Water Pollution Control Federation, 1985, Standard Methods for the Examination of Water and Wastewater, 16th Ed., American Public Health Association, 1268 pp.

Arizona Department of Water Resources, 9-21-90, Well Registry Report.

Ashworth, E. and T. Ashworth, 1990, A rapid method for measuring thermal conductivity of rock core and its preliminary use for finding the thermal resistance of cracks, in Hustrum and Johnson (eds.), Rock Mechanics Contributions and Challenges, Balkema, Rotterdam.

Bassett, R.L., T.C. Rasmussen, G. Davidson, and A.G. Guzman, 1992, Validation studies for assessing unsaturated flow and transport through unsaturated fractured rock: experimental research plan, letter report to Tom Nicholson.

Campbell, G.S. and G.W. Gee, 1986, Water potential: miscellaneous methods, in A. Klute (ed.), *Methods of Soil Analysis*, Part I, 2nd Ed., Agron. Monogr. 9. ASA and SSSA, Madison, Wisconsin, pp. 619-633.

Carslaw, H.S. and J.C. Jaeger, 1959, Conduction of Heat in Solids, Oxford Press, p. 100.

Clauser, C., 1992, Scale effects on permeability measurements on crystalline rocks, *EOS*.

Craig, H., 1961, Isotopic variations in meteoric waters, *Science*, 133, 1702-1703, AAAS.

Cushman, J.H., 1984, On unifying concepts of scale, instrumentation, and stochastics in the development of multiphase transport theory, *Water Resources Research*, (20)11, pp. 1668-1676.

Deer, W.A., R.A. Howie, and J. Zussman, 1966, An Introduction to the Rock-Forming Minerals, Longman Group Limited, London, 528 p.

DeSorcy, G.J. (Ed.), 1978, Theory and Practice of the Testing of Gas Wells, 3rd Ed., Energy Resources Conservation Board, Calgary, Canada.

Dixon, J.B. and S.B. Weed, 1977, *Minerals in soil environments*, Soil Science Society of America, 948 pp.

Donohue, D.A.T. and T. Ertekin, 1982, *Gas well testing; theory, practice and regulation*. International Human Resources Development Co., Boston, Massachusetts, 214 pp.

Dranchuck, P.M. and L.J. Kolada, 1968, Interpretation of steady linear visco-inertial gas flow data. *Journal of Canadian Petroleum Technology* (Jan.-March), pp. 36-40.

Dranchuck, P.M. and J.G. Flores, 1973, Non-Darcy transient radial gas flow through porous media. Paper SPE 4595, 48th Meeting of AIME, Las Vegas, Nevada.

Ershagi, I. and J.J. Woodbury, 1985, Examples of pitfalls in well test analysis, *Journal of Petroleum Technology*, (Feb.), pp. 335-341.

Estes, R.K. and P.F. Fulton, 1956, Gas slippage and permeability measurements. *Trans. Am. Inst. Min. Metall. Pet. Eng.* 207, pp. 338-342.

Evans, D.D. and T.J. Nicholson, 1987, *Flow and Transport Through Unsaturated Fractured Rock*, Geophysical Monograph 42, American Geophysical Union, Washington, D.C.

Forchheimer, P., 1901, Wasserbewegung durch boden, *Zeitschrift Des Verines Deutsch Ing.* 45, pp. 1736-1749.

Freeze, R.A., L.G. Everett, G.E. Grisak, J.W. Mercer, R.W. Nelson, S.S. Papadopulos, and M.Th. van Genuchten, 1991, Unsaturated zone hydrology peer review record memorandum. U.S. Dept. of Energy, OCRWM, Yucca Mountain Site Characterization Project, June 24.

Fritz P., J-Ch. Fontes, S.K. Frape, D. Louvat, J-L. Michelot, and W. Balderer, 1989, The isotope geochemistry of carbon in groundwater at Stripa. *Geochim. Cosmochim. Acta* 53, pp. 1765-1775.

Guzman, A.G., M.J. Sully, and S.P. Neuman, 1992, Spatial structure of air permeability estimates in unsaturated fractured tuff. Program and Abstracts, AGU 1992 Joint Spring Meeting, May 11-16, Montreal, Canada.

Guzman, A.G., S.P. Neuman, and C. Lohrstorfer, Determination of pneumatic permeability in unsaturated fractured rock, in preparation to be submitted to *Water Resources Research.*

Guzman, A.G., S.P. Neuman, C. Lohrstorfer, and Bassett, R.L., 1992, Air permeability determinations: scale effects. Third INTRAVAL Phase-2 Workshop, Nov., San Antonio, Texas.

Guzman, A.G., M.J. Sully, S.P. Neuman, and C. Lohrstorfer, 1991, Determination of pneumatic permeability in unsaturated fractured rock using steady state analysis. Program and Abstracts, AGU 1991 Fall Meeting, Dec. 9-13, San Francisco, California.

Guzman, A.G., M.J. Sully, S.P. Neuman, and C. Lohrstorfer, 1992, Validation studies for assessing unsaturated flow and transport through fractured rock at the Apache Leap Tuff Site: in-situ pneumatic permeability tests, Hydrology Research Meeting, Center for Nuclear Waste Regulatory Analyses, San Antonio, Texas.

Guzman, A.G., M.J. Sully, and S.P. Neuman, 1991, Three-dimensional characterization of pneumatic permeabilities in unsaturated fractured tuff at the Apache Leap Tuff Site. First INTRAVAL Phase-2 Workshop, Seattle, Washington.

Guzman, A.G., 1994, Air permeability determinations in unsaturated porous rocks, Ph.D. dissertation, University of Arizona.

Haas, H., D.W. Fisher, D.C. Thorstenson, and E.P. Weeks, 1983, $^{13}CO_2$ and $^{14}CO_2$ measurements on soil atmosphere in the subsurface unsaturated zone in the Western Plains of the U.S. *Radiocarbon* 25, pp. 301-314.

Hammer, D.F. and R.N. Webster, 1960, Some geologic features of the superior area, Pinal County, Arizona, in Robert H. Weber and H. Wesley Peirce (Eds.), Guidebook of the Mogollon Rim Region, East-Central Arizona, New Mexico Geological Society, pp. 148-153.

Hem, J.D., 1985, Study and interpretation of the chemical characteristics of natural water, U.S. Geological Survey Water-Supply Paper 2254, 264 p.

Hiles, J. and R.A. Mott, 1974, *Fuel* 24: 135, 1945 in Scheidegger.

Hsieh, P.A., S.P. Neuman, and E.S. Simpson, 1983, Pressure testing of fractured rocks: a methodology employing three-dimensional cross-hole tests, U.S. Nuclear Regulatory Commission, NUREG/CR-3213.

Huijbregts, Ch.J., 1991, Reconstitution du variogramme ponctuel a partir d'un variogramme experimental regulirise. Rep. N-224, Cent. Morphol. Math., Ecole des Mines de Paris, Fontainebleau.

Hvorslev, M.J., 1951, Time lag and soil permeability in groundwater observations, Bulletin 36, U.S. Army Engineer Water Ways Experiment Station, Vicksburg, Michigan.

Jakubick. A.T., 1983, Vacuum logging for measurement of the integrity of the near-excavation zone. Inter. Symp. on Field Meas. in Geomech. (Sept.), pp. 163-175.

Katz, D.L., D. Cornell, R. Kobayashi, F.H. Poettmann, J.A. Vary, J.B. Elenbaas, and C.F. Weinaug, 1959, Handbook of Natural Gas Engineering, McGraw-Hill, New York, 802 p.

Klinkenberg, L.J., 1941, The permeability of porous media to liquids and gases, Am. Pet. Inst., Drilling and Production Practice, pp. 200-213.

Klute, A. 1986, Water retention: laboratory methods, in A. Klute (ed.), *Methods of soil analysis*, Part I, 2nd ed., Agron. Monogr. 9. ASA and SSSA, Madison, Wisconsin, pp. 635-662.

Klute, A., 1964, Water diffusivity, in *Methods of soil analysis*, Part 1, Am. Soc. Agron., Soil Sci. Soc. Am., pp. 262-272.

Klute, A. and C. Dirksen, 1986, Hydraulic conductivity and diffusivity: laboratory methods, in A. Klute (Ed.), *Methods of soil analysis*, Part I, 2nd ed., Agron. Monogr. 9. ASA and SSSA, Madison, Wisconsin, pp. 687-734.

Lee, J., 1982, Well Testing, Society of Petroleum Engineers of AIME, New York.

Massmann, J. and D.F. Farrier, 1992, Atmospheric pressures on gas transport in the vadose zone, *Water Resources Research*, 28(3), pp. 777-791.

Missbach, A., 1937. Listy Curkrovar, 1937. 55: 293 in Scheidegger 1974.

Montazer, P., 1982. Permeability of unsaturated, fractured metamorphic rocks near an underground opening, Ph.D. Dissertation, Colorado School of Mines.

Neuman, S.P. and S. Orr, 1992, Prediction of steady-state flow in nonuniform geologic media by conditional moments: exact local formalism, effective conductivities, and weak approximation, *Water Resources Research*, Vol. 29, No. 2, pp. 341-364.

Neuman, S.P., 1990, Universal scaling of hydraulic conductivities and dispersivities in geologic media, *Water Resources Research*, 26(8), pp. 1749-1758.

Neuman, S.P. and J.S. Depner, 1988, Use of variable-scale pressure test data to estimate the log hydraulic conductivity covariance and dispersivity of fractured granites near Oracle, Arizona. *Journal of Hydrology*, 102, pp. 475-501.

Nitao, J.J. and T.A. Buscheck, 1991, Infiltration of a liquid front in an unsaturated, fractured porous medium, *Water Resources Research*, 27(8), pp. 2099-2122.

Noble, D.C., V.C. Smith, and L.C. Peck, 1967, Loss of halogens from crystallized and glassy silicic volcanic rocks, *Geochimica et Cosmochimica Acta* 31, pp. 215-223.

Parkhurst, D.L., D.C. Thorstenson, and L.N. Plummer, 1980, *PHREEQE: a computer program for geochemical calculations*, U.S. Geological Survey Water Resources Investigations 80-96, 146 p.

Peterson, D.W., 1961, Dacitic ash-flow sheet near Superior and Globe, Arizona, Ph.D. Dissertation, Stanford University; U.S. Geological Survey Open-File Report, April 3, 1961, 130 p.

Peterson, D.W., 1968, Zoned ash-flow sheet in the region around Superior, Arizona, in Spencer R. Titley (Ed.), Southern Arizona Guidebook III, Geological Society of America, pp. 215-223.

Peterson, D.W., 1969, Geologic Map of the Superior Quadrangle, Pinal County, Arizona, U.S. Geological Survey.

Rasmussen, T.C. and D.D. Evans, 1989, Fluid Flow and Solute Transport Modeling Through Three-Dimensional Networks of Variably Saturated Discrete Fractures, U.S. Nuclear Regulatory Commission, Washington, D.C, NUREG/CR-5239.

Rasmussen, T.C. and D.D. Evans, 1992, Nonisothermal hydrologic transport experimental plan, NUREG/CR-5880, U.S. Nuclear Regulatory Commission, Washington, D.C.

Rasmussen, T.C. and D.D. Evans, 1993, Water Infiltration-Percolation for Exposed Fractured Rock Surfaces, Accepted for publication in *Soil Sci. Soc. of Am. J.*, Vol. 57, No. 2, pp. 324-329.

Rasmussen, T.C., D.D. Evans, P.J. Sheets, and J.H. Blanford, 1990, Unsaturated fractured rock characterization methods and data sets at the Apache Leap Tuff Site, NUREG/CR-5596, U.S. Nuclear Regulatory Commission, Washington, D.C.

Rawlins, E.L. and M.A., Schellhardt, 1936, Backpressure data on natural gas wells and their application to production practices. Monograph 7, U.S. Bureau of Mines.

Sample Management Facility, 1990, *Geologic summary of borehole USW UZP-4 phase 1e prototype drilling, Apache Leap, Arizona*, Draft Report prepared for U.S. Department of Energy Yucca Mountain Project, Science Applications International Corporation, 10 p.

Scheidegger, A.E., 1974, The Physics of Flow Through Porous Media, 3rd Ed., University of Toronto Press, Toronto, Ontario, Canada, 353 p.

Silliman, S.E., 1989, Interpretation of the difference between aperture estimates derived from hydraulic and tracer tests in a single fracture, *Water Resources Research*, 25(10), pp. 2275-2283.

Smith, R.L., 1960, *Zones and zonal variations in welded ash flows*, U.S. Geological Survey Professional Paper 354-F, 159 p.

Smith, B.N., 1982, General characteristics of terrestrial plants (agronomic and forests) - C_3, C_4, and crassulacean acid metabolism plants, in O.R. Zaborsky, A. Mitsui and C.C. Black (Eds.), CRC Handbook of Biosolar Resources, Vol. 1, Part. 2, CRC Press, Inc., Boca Raton, Florida, pp. 99-118.

Stonestrom, D.A. and J. Rubin, 1989, Air permeability and trapped-air content in two soils. *Water Resources Research*, 25(9), pp. 1959-1969.

Sully, M.J., T.E. Detty, and A.G. Guzman, 1992, Effect of liquid saturation on slip flow and inertial flow in an unconsolidated porous material, Program and Abstracts, AGU 1992 Joint Spring Meeting, May 11-16, Montreal, Canada.

Sully, M.J., A.G. Guzman and S.P. Neuman, 1991, In-situ pneumatic permeability test at the Apache Leap Tuff Site, First INTRAVAL Phase-2 Workshop, Seattle, Washington.

Sully, M.J., A.G. Guzman, and D.B. Stephens, 1991, Characterizing permeability to gas in the vadose zone. Symposium on Soil Venting, Robert S. Kerr Environmental Research Laboratory and National Center for Groundwater Research, Houston, Texas.

Sully, M.J., A.G. Guzman, and S.P. Neuman, 1991, Effect of measurement scale on in-situ pneumatic permeability measurements on unsaturated fractured rock, Program and Abstracts, AGU 1991 Fall Meeting, Dec. 9-13, San Francisco, California.

Thornburg, T.M., 1990, Electrical resistivity of unsaturated, fractured tuff: influence of moisture content and geologic structure, M.S. Thesis, University of Arizona, 196 p.

Thorstenson, D.C., E.P. Weeks, H. Haas, and J.C. Woodward, 1990, Physical and chemical characteristics of topographically affected airflow in an open borehole at Yucca Mountain, Nevada, in *Nuclear Waste Isolation in the Unsaturated Zone*, Focus '89, La Grange Park, Illinois, Amer. Nucl. Soc. Proc., pp. 256-270.

Thorstenson, D.C. and D.W. Pollock, 1989, Gas transport in unsaturated porous media: the adequacy of Fick's law, *Review of Geophysics*, 27(1), pp. 61-78.

Thorstenson, D.C., E.P. Weeks, H. Haas, and D.W. Fisher, 1983, Distribution of gaseous $^{12}CO_2$, $^{13}CO_2$ and $^{14}CO_2$ in the subsoil unsaturated zone of the western U.S. Great Plains, *Radiocarbon*, 25, pp. 315-346.

Tsang, Y.W., 1992, Usage of "equivalent apertures" for rock fractures as derived from hydraulic and tracer tests, *Water Resources Research*, 28(5), pp. 1451-1455.

Vickers, B.C., 1990, Aperture configuration of a natural fracture in welded tuff, Unpublished M.S. Thesis, Department of Hydrology and Water Resources, The University of Arizona, Tucson, 132 p.

Vogt, G.T., 1988, Porosity, pore-size distribution and pore surface area of the Apache Leap Tuff near Superior, Arizona using mercury porosimetry, M.S. Thesis, University of Arizona, Tucson, 130 p.

Weber, D.S., 1986, Stable isotopes of authigenic minerals in variably-saturated fractured tuff, M.S. Thesis, University of Arizona, Tucson, 128 p.

Weeks, E.P., D.E. Earp, and G.M. Thompson, 1982, Use of atmospheric fluorocarbons F-11 and F-12 to determine the diffusion parameters of the unsaturated zone in the southern high plains of Texas, *Water Resources Research*, 18, pp. 1365-1378.

Wentworth, C.K., 1944, *American Journal of Science*, Vol. 242, 478

Wigley, T.M.L., 1976, Effect of mineral precipitation on isotopic composition and ^{14}C dating of groundwater, *Nature* 263, pp. 219-221.

Wigley, T.M.L., L.N. Plummer, and F.J. Pearson, 1978, Mass-transfer and carbon isotope evolution in natural water systems, *Geochim. Cosmochim. Acta* 42, pp. 1117-1139.

Yang, I.C., H.H. Haas, E.P. Weeks, and D.C. Thorstenson, 1985, Analysis of gaseous-phase stable and radioactive isotopes in the unsaturated zone, Yucca Mountain, Nevada. In: Proceedings of Conference on Characterization and Monitoring of the Vadose (Unsaturated) Zone, National Water Well Association, Denver, Colorado, pp. 488-506.

APPENDIX A: SINGLE BOREHOLE AIR-INJECTION TEST FIELD OPERATING PROCEDURE

by Amado Guzman, Michael J. Sully, and Charles Lohrstorfer

A.1 SINGLE BOREHOLE TEST (INJECTION)

The single borehole test is designed to determine in-situ pneumatic permeability of a geologic formation. The general procedure of this test is similar to the Conventional Test of the gas industry. As such, the test is a step-wise sequence of increasing injection rates followed by a recovery test. A straddle packer is used to isolate an interval along the wellbore. Injection is performed with the help of an air compressor. During a typical test, pressure, flow rate, relative humidity, and temperature in the injection interval are recorded as a function of time. The necessary equipment and procedure are as follows:

A.2 EQUIPMENT

A schematic representation of the straddle-packer system is presented in Figure A.1. The essential parts of the system, besides hoses and valves, listed from the air compressor to the computer terminal along this schematic are:

(1) Air compressor (1,000 kPa and 200 lt) with pressure regulator
(2) Air filter and on-line desiccator
(3) Electronic flow controller
(4) Absolute pressure transducer (0-15 psia)
(5) Thermistor (0.1,°C)
(6) Two rotameters (0-1.5 slm and 0-20 slm)
(7) Mass flow meters (0-0.2, 0-2, and 0-20 slm)
(8) Straddle-packer assembly
(9) Thermistor (0.1,°C)
(10) Gauge pressure transducer (15 psig)
(11) Relative humidity sensor
(12) Campbell Scientific data-logger unit and PC-Interface
(13) Personal computer
(14) Field book

A.3 PROCEDURE

(1) Write down in the field notebook relevant information about the test; date, time, borehole, distance along the borehole, operator(s), and any other pertinent data (e.g., rain, snow, locations of other boreholes packed off);

(2) Place straddle packer so the center of the injection-extraction interval coincides with the desired elevation;

(3) Set pressure regulator for the injection line at approximately 45 psig (gauge) near the compressor tank and the pressure regulator by the flow meters to 35 psig;

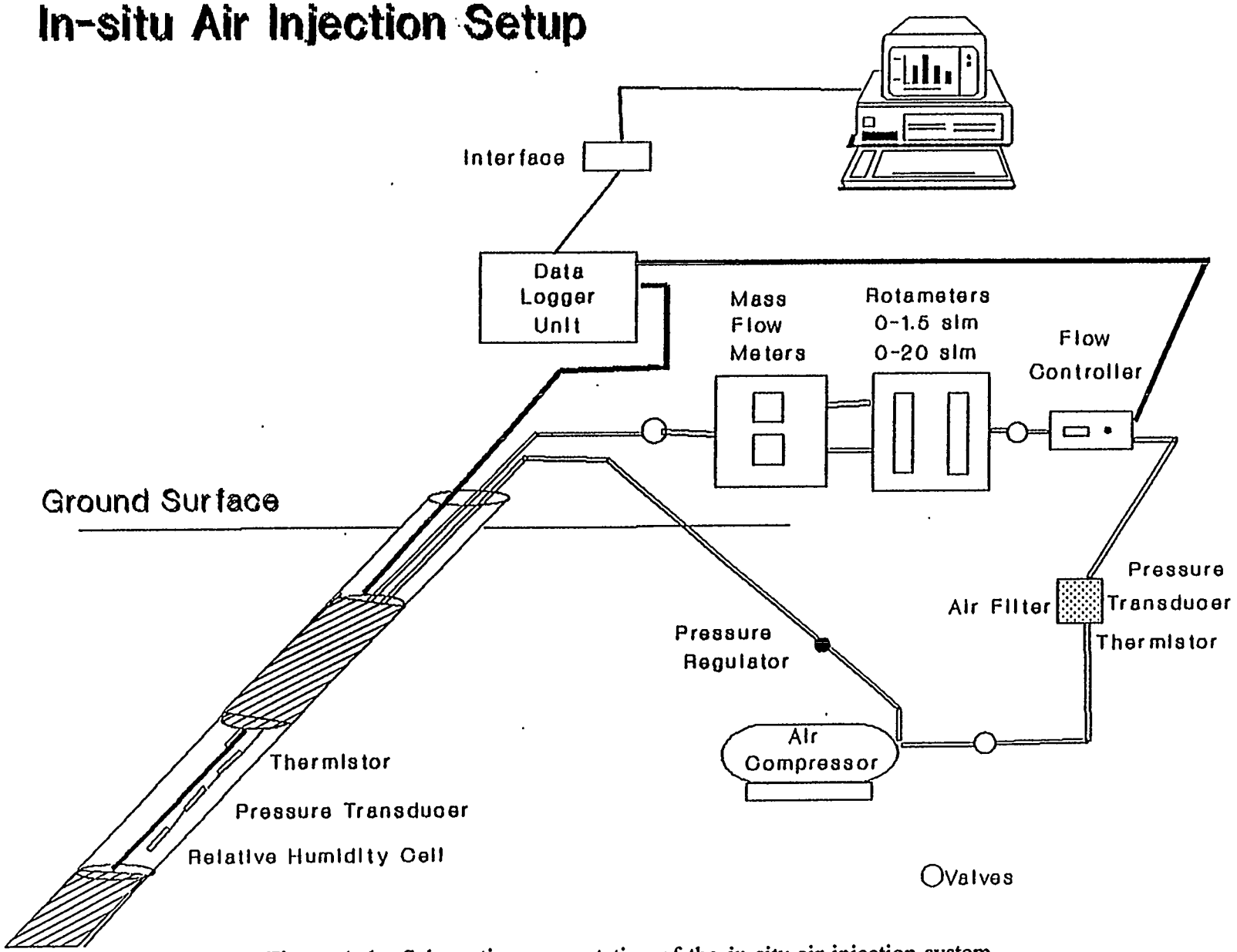

Figure A.1. Schematic representation of the *in situ* air injection system.

(4) Connect the injection line to the desiccator box and then to the pressure regulator by the air compressor;

(5) Turn on the system and allow 15 minutes for instrument stabilization. Download the program SINGLE.DLD to the data logger by means of the data logger software TERM.COM. If necessary, zero flow meters and PTs. Close the valves to isolate the interval from atmospheric pressure;

(6) Set pressure regulator for the packer line to 60 psig and inflate the straddle packer. As the straddle packer is inflated, a slight positive pressure will be registered by the PT at the injection interval, P(p). If this pressure does not stabilize or the stabilized value is greater than three centimeters of mercury, deflate packer and check for leakage in the body of the straddle packer around the interval using bubble solution. Otherwise, open the exhaust valve and allow for pressure dissipation. Then continue with next step;

(7) With the outlet of flow meter open to the atmosphere, set the flow to desired rate, and allow enough time (5 minutes at least) for pressure stabilization in the transducer located in the flow meter housing, p(f). When setting the discharge, proceed as follows: (a) open rotameter and shut-off valves completely, (b) open three-way valve to select the appropriate rotameter; immediately after, open valve downstream of flowmeter, (c) set the flow controller to "SET" and turn the knob for the appropriate flow meter to select the desired flow rate, and (d) switch the flow controller to the "READ" mode;

Monitor discharge until a stable reading of flow is obtained. Once the discharge reading is constant, make sure that the information in the field book contains all relevant data for the test about to start;

(8) Record initial time and switch the valve from "exhaust" to "test" to start the injection test. Continue test until a "steady state" pressure is obtained. "Steady state" is considered if a change of 1 mm Hg or less occurs within a 30-minutes time period. If stabilization is not achieved, continue the test for at least 300 min. In order to get a good definition throughout the test duration, measurements should be collected at small time intervals during early stages of the test and then at progressively larger intervals as the test advances to steady state. Table A.1 outlines the suggested time intervals and the times at which the "scan rate" should be modified;

Every time the sampling interval (scan rate) is changed in the data logger, write down in the notebook the following information: (a) new scan rate in seconds, (b) pressure at the active interval, (c) pressure upstream of the flow meters, (d) temperature at the active interval and upstream of the flow meters, (e) barometric pressure, (f) relative humidity and, during injection, and (g) reading in the mass flow meter and rotameter. Continue test until stabilization or up to 300 minutes, which ever occurs first. After the first hour, collect these data every 30 minutes;

(9) Once pressure in the injection interval has stabilized, switch the flow controller to "SET" mode and select the new, higher flow rate using the following steps: (a) write down the steady-state data for the previous flow rate, (b) step up the flow rate by switching the control knob to "set" and by slowly turning the adjustment knob to the new flow rate

Table A.1. Suggested Scan Rates

Time Span (min)	Table 1 Scan Rate (sec)	Table 2 Scan Rate (sec)
0-3	3	20
3-7	6	20
7-15	10	20
15-25	15	30
25-40	30	60
40-60	60	120
60-120	120	240
> 120	240	480

without going over it, and (c) reset the scan rate to three seconds and 20 seconds for Tables 1 and 2, and proceed collecting data at the intervals suggested in Table A.1,

(10) Repeat steps (8) to (9) with at least another flow rate. When performing these additional injection tests, remember that flow rate should be kept as constant as possible. The magnitudes of these flow rates will depend on the maximum pressure change obtained within the first flow rate. The objective when running these different flow rates is to cover completely the available pressure span. Thus, set the test flow rates so that the resulting steady-state pressures span the available range of the pressure transducer (approximately 76 cm Hg). Although the Druck pressure transducers are able to handle ten times their rated pressure, try to keep the maximum change in the test interval to less than 75 cm Hg;

(11) If pressure stabilization is not achieved during any of these constant discharge tests, an extended discharge test will be necessary. The extended test should be started right after the pressure drawdown of the last constant (maximum) discharge test has been allowed to recover to within a few millimeters of mercury from initial atmospheric conditions. At this time, the valves should be opened and Q set between the two largest flow rates used in step (10). The extended discharge test should be continued until "steady-state" pressure is achieved. After a steady pressure response is recorded, injection is suspended, and the formation is allowed to recover. Recovery data for this extended flow rate need not be monitored;

(12) The complete data set (3 or 4 injection and 1 recovery stages versus time) should be downloaded into a floppy diskette. A duplicate of this file should be made and stored into the subdirectory C:\air in the personal computer. The floppy disk should be labeled, clearly noting date, borehole, and exact location of the test. The file name for this file contains the following; interval code (JK, EM, JN, etc.), the date (mmdd), and a letter indicating the test sequence (a, b, c, etc.). The data should be downloaded into permanent storage (floppy or hard disk) at least once a day.

A.4 NOTES

Periodic runs of the "zero permeability" procedure will provide a means to correct and maintain good quality field data. Quality assurance runs should be done at least every two weeks or after 15 tests have been completed, which ever occurs first.

APPENDIX B: ZERO PERMEABILITY TEST FIELD OPERATING PROCEDURE

by Amado Guzman and Charles Lohrstorfer

B.1 ZERO PERMEABILITY TEST

The zero permeability test is designed to determine air leakage rate out of a straddle packer system under static positive gauge pressure. This leakage rate could be used to correct the measurements obtained during the in-situ permeability tests. The necessary equipment and procedure are as follows:

B.2 EQUIPMENT

(1) Air compressor (1,000 kPa and 200 lt) with pressure regulator
(2) Air filter and on-line desiccator
(3) Absolute pressure transducer (0-15 psia)
(4) Thermistor (0.1,°C)
(5) Straddle-packer assembly
(6) Thermistor (0.1,°C)
(7) Gauge pressure transducer (15 psig)
(8) Relative humidity sensor
(9) Campbell Scientific data-logger unit and PC-Interface
(10) Personal computer
(11) 4" I.D./20' PVC pipe
(12) Soap solution
(13) Field book

B.3 PROCEDURE

(1) Record in the field book the date and name of the person(s) conducting the test.

(2) Rid straddle packer of large debris along the rubber bladders and place it into PVC pipe.

(3) Connect the injection line from the compressor to the desiccator box and then into the flowmeter outlet to the active interval.

(4) Download the program SINGLE.STN into the data logger by means of the data logger software (TERM.COM). If necessary, zero flow meters and PTs.

(5) Connect packer line to air compressor and inflate packer to 60 psig (gauge). As the packer is inflated, a slight positive pressure will be registered by the PT at the test interval. If this pressure does not stabilize or the stabilized value is greater than two centimeters of mercury, deflate packer and check for leakage along the body of the straddle packer using soap solution. Otherwise, open three-way flow controlling and shut-off valves and allow pressure to dissipate. Then continue with step (6).

(6) Record initial time and open valves to start the injection into the test interval. Allow for pressure buildup until a pressure of 75 cm of mercury is achieved in the test interval. Close all valves to isolate the straddle-packer system from atmospheric pressure.

(7) After all the valves are closed, record the time and the maximum pressure reached inside the test interval. The time at which the pressure reaches this maximum marks the beginning of the zero permeability test. During the next one hour, write down in the notebook the following information at 10-minute intervals: (a) time, (b) pressure at the active interval, (c) temperature at the interval, (d) barometric pressure, and (e) relative humidity.

(8) The rate at which pressure is being lost (leak) from the system should be approximately linear for most of the duration of the test. Use the following equation to translate this rate of pressure decay to a standard flow rate:

$$Q(\text{sccm}) = \frac{[P_1T_1 - P_2T_2]}{T_1T_2} \frac{VT_{s_c}}{P_{s_c}\Delta t} \qquad \text{(B.1)}$$

where:

V = total system volume (cm^3)'
P_1 = absolute pressure at time one (cm Hg);
P_2 = absolute pressure at time two (cm Hg);
P_{sc} = absolute pressure at standard condition (76.0 cm Hg);
T_1 = absolute temperature at time one (K = °C+273);
T_2 = absolute temperature at time two (K = °C+273);
T_{sc} = temperature at standard conditions (20°C, 293 K); and
Δt = time interval; t_2-t_1 (minutes);

(9) Starting with the second 10-minute reading, use Equation (B.1) to compute the leakage rate over the given period of time. Write down in the field book the time and the computed leakage rate. If the leakage rate is greater than 15 sccm at any given interval, stop test and find leak. Once the leak(s) has been found, repeat the zero permeability test.

(10) After the test is completed, download test information from data logger (use TELCOM.EXE) to a file ZPdate.RAW (date is composed of six digits as follows: 01-day, 01-month, and 90-year). Copy this file to the subdirectory C:\air and to a floppy disk. Write down the file name on the cover of the floppy.

APPENDIX C: DERIVATION OF EQUATION (4.2)

The governing partial differential equation representing flow of a real gas through a porous medium is (Katz et al., 1959; DeSorcy, 1978):

$$\nabla^2 p^2 = \frac{\Phi \mu C_g}{k} \frac{\partial p^2}{\partial t} \tag{C.1}$$

where k is the intrinsic permeability, μ is the gas viscosity, Φ is the porosity, p is the pressure, and C_g is the gas compressibility factor defined as:

$$C_g = \frac{1}{p} + \frac{1}{Z} \frac{dZ}{dp} \tag{C.2}$$

here, Z is the real gas compressibility (indicates the extent to which a given gas behaves as an ideal gas, $Z \leq 1$). Equation (C.2) was derived assuming that the gas density can be represented by:

$$\rho = \frac{M}{RT} \frac{p}{Z} \tag{C.3}$$

where M is the molecular weight of the real gas, and R is the universal gas constant.

To simplify the derivation of the solution of Equation (C.1), let us consider a fully penetrating line source in a homogeneous, isotropic, confined reservoir of infinite lateral extent. Mass continuity under steady-state flow conditions requires that:

$$\rho Q = \text{constant} \tag{C.4}$$

where Q is the volumetric gas flow, and ρ is the gas density at reservoir pressure and temperature. Darcy's equation in radial coordinates is expressed as:

$$Q = -2\pi r b \frac{\kappa}{\mu} \frac{ap}{dr} \tag{C.5}$$

for a reservoir with thickness b. Combining Equations (C.3) through (C.5) and assuming isothermal conditions, the mass continuity Equation (C.4) can be written as:

$$Qp = -2\pi r b \frac{\kappa}{\mu} p \frac{dp}{dr} \tag{C.6}$$

Due to the gas compressibility, it is better to express the volumetric flow Q in terms of a set of standard conditions. Commonly, these standard conditions (sc) are assumed to be determined by p_{sc} equal to 1 atmosphere and T_{sc} equal to 20°C. As such, a volumetric flow Q under a pressure p and temperature T can be transformed to standard conditions using the following equation:

$$Q_{sc} = \frac{T_{sc} p}{T p_{sc} Z} Q \qquad (C.7)$$

Substitution of this equation into Equation (C.6) and integrating from r_w, the well radius, to r yields:

$$Q_{sc} = \frac{\pi k b [p^2(r) - p_w^2]}{\mu Ln(r/r_w)} \frac{T_{sc}}{T p_{sc} Z} \qquad (C.8)$$

where p_w is the pressure at the well. Assuming the radius of influence (the distance at which the pressure disturbance can be considered negligible) to be of the order of the thickness b results in Equation (4.2).

APPENDIX D: TABULATION OF ALL CHEMICAL ANALYSES OF WATER SAMPLES COLLECTED AND ANALYZED FOR THIS PHASE OF THE CONTRACT

by E. Lyons, R. Bassett, and Gregg Davidson

	T °C	pH[a]	$(HCO_3)^c$	SO_4	NO_3	Cl	Na	K	Ca	Mg	SiO_2
Highway 177											
Rain 8/3/89	26.2	4.7	6.6	0.90	1.71	0.29	0.170	0.07	0.584	0.0400	0.12
Apache Leap Precipitation											
Rain 11/21/89	11.4	5.00		0.62	0.71	0.17	<0.006	0.13	0.148	0.0093	<0.04
Snow 1/18/90		5.00		0.14	0.17	0.09	0.026	<0.05	0.016	0.0032	<0.04
Snow/Rain 1/18/90		5.00		0.38	0.35	0.18	0.063	<0.10	0.126	0.0098	<0.04
Rain 2/1/90	3.0	5.35		0.74	0.78	0.49	0.273	<0.10	0.203	0.0395	<0.04
Rain 6/10/90		5.00		3.10	1.50	0.15	0.090	<0.10	0.200	0.0270	
T-CB1											
7/6/89	25.1	7.85	138.5	15.6	3.9	6.0	22.5	0.89	28.0	5.2	62
2/27/90	24.0	8.00	138.2	16.6	2.6	6.7	21.0	0.82	29.2	5.2	62
8/17/90	25.0	7.93	137.6	15.6	3.6	6.3	21.1	0.81	28.2	5.0	
6/7/92		8.07	134.0[d]	17.5	4.49	15.4	22.5	1.08	25.9	5.41	58
12/10/92	24.6	7.91[b]		16.7	4.33	7.24	20.9	<1.0	24.6	5.16	61
		7.64									
T-CB2											
7/6/89	25.1	7.76	136.1	15.7	4.2	6.3	22.8	0.90	27.5	5.0	62
2/27/90	24.0	7.98	137.6	15.7		6.7	21.5	0.81	28.2	5.0	63
8/17/90	25.0	7.92	137.0	14.8	4.0	6.5	21.5	0.81	27.5	4.8	
9/14/90	25.0	7.90	136.2	16.5	4.0	7.0	21.8	0.86	25.0	5.0	
T-4											
7/6/89	21.0	7.55	132.7	60.8	27.6	17.0	30.1	1.15	46.6	8.3	65
2/27/90	19.2	8.03	141.8	35.2	9.4	9.8	25.3	0.88	36.0	6.2	63
8/17/90	23.8	7.90	139.3	36.4	12.0	10.3	25.3	0.87	37.7	6.3	62
9/14/90	24.0	7.85	139.3	46.5	14.5	11.7	26.3	0.92	40.8	6.8	62
6/7/92		8.17[b]	145.0[d]	63.9	19.5		31.5	1.16	55.4	9.63	62
12/10/92	nd	7.78	138.0	62.1	20.6	27.5	29.4	<1.0	47.2	9.01	65
		nd[b]									
T-8380		8.13*									
6/7/92			144[a]	29.3	5.70	30.0	37.3	<1.0	27.0	4.75	60

	T °C	pH[a]	(HCO$_3$)[c]	SO_4	NO_3	Cl	Na	K	Ca	Mg	SiO_2
T-7920											
7/6/89	21.9	7.79	137.4	7.8	3.6	5.3	29.1	0.64	20.5	4.0	60
2/27/90	21.5	8.14	138.2	5.3	2.9	5.3	26.5	0.57	20.5	3.8	62
8/17/90	23.2	8.11	136.6	4.4	3.3	5.3	24.3	0.57	21.2	4.0	61
9/14/90	23.0	8.02	139.1	4.3	2.8	5.2	24.0	0.57	21.3	4.0	62
6/7/92		8.23[b]	123.0[a]	5.89	3.61		24.0	<1.0	19.8	4.72	59
12/10/92	22.6	8.01[b]		5.09	3.49	5.80	22.6	<1.0	18.7	4.35	62
		6.88	134.0								
T-7480											
6/7/92		8.09[b]	143.0[a]	46.8	6.79	18.4	28.9	1.01	39.0	4.78	49
12/10/92		7.9[b]	141.0	43.5	6.49	8.61	27.1	<1.0	34.7	4.44	52
T-7040											
12/10/92		7.92[a]	138.0	40.3	5.79	7.87	31.9	<1.0	28.8	3.99	51
		nd[b]									
T-6480											
2/27/90	21.0	7.52	92.4	33.3	5.0	5.5	17.5	0.72	25.0	4.8	54
8/17/90	20.5	7.48	105.2	26.6	7.5	5.1	17.5	0.76	27.0	5.3	50
9/14/90	20.5	7.48	114.5	29.3	6.1	5.5	17.8	0.78	28.3	5.5	52
6/7/92		7.94[b]	128.0[a]	29.5	6.55		19.7	1.02	29.3	6.73	51
12/10/92		7.7[b]	115.0	28.2	8.72	6.36	18.6	<1.0	26.1	6.03	52
T-6340											
7/6/89	20.5	7.40	98.3	32.2	3.9	4.5	18.4	0.78	26.3	4.6	46
2/27/90	19.6	7.10	69.4	36.0	4.2	3.9	13.3	0.57	23.0	4.2	42
6/7/92		7.59[b]	105[a]	48.1	5.11	13.4	16.3	1.15	32.8	6.92	38
12/10/92		7.6[b]		38.4	6.84	5.66	14.6	<1.0	29.6	6.30	40
T-6335											
2/27/90	19.4	7.33	68.5	35.6	4.1	3.7	13.3	0.57	22.8	4.2	41
8/17/90	20.5	7.30	84.8	33.0	5.3	4.4	14.0	0.62	25.3	4.5	41
9/14/90	20.0	7.16	73.7	31.5	4.3	4.2	13.0	0.57	22.2	4.0	40
T-6262											
6/7/92		7.69*	138.0[a]	48.8	3.84		32.3	<1.0	30.5	4.58	59

	T °C	pH[a]	$(HCO_3)^c$	SO_4	NO_3	Cl	Na	K	Ca	Mg	SiO_2
Magma Tunnel Sample											
9/11/78		7.50	138.0	11	---	6.7			28.8	5.1	62
Oak Flat-DOE Borehole											
4/4/90	21.2	8.42	164.8	12.7	16.6	15.1	24.8	3.0	36.0	8.3	65
4/27/90	22.0	nd	152.2	7.5	9.8	18.2	28.3	2.9	29.3	6.2	70
H Well-BU											
6/17/86	24.5	7.70	349.2	49.0	2.0	12.2	38.5	0.77	69.3	8.1	66
H Well-LS											
6/17/86	26.0	7.90	656.0	98.2	<0.6	8.3	30.5	0.42	108.0	52.0	50
QC-Ivy											
4/27/90	11.8	nd	47.9	26.2		3.5	6.5	1.9	16.0	4.1	28
8/17/90	19.8	6.99	35.1	27.6		3.6	6.1	1.9	15.4	3.9	28
QC-Road Crossing											
4/4/90	15.8	7.88	126.4	35.4		5.0	7.4	2.3	36.0	1.9	28
4/29/90	16.8	6.78	185.3	28.6		5.1	8.4	2.8	46.2	2.4	29
8/17/90	25.0	7.98	90.4	26.4		4.6	7.0	3.1	27.5	7.0	32
QC-1											
11/21/89	13.8	6.50	4.1	6.0		1.7	1.4	2.5	3.5	1.2	4
1/9/90	5.0	6.60	12.6	46.9		3.5	7.4	1.4	14.6	3.8	19
1/18/90	5.0	6.70	19.6	46.3		3.5	7.4	1.5	15.0	3.9	18
4/1/90	12.8	7.20	31.1	34.4		4.1	7.1	1.4	15.0	3.9	25
4/29/90	16.0	6.78	62.0	28.3		3.7	6.7	1.8	21.3	1.2	32
Flume Creek											
11/21/89	12.8	5.70	<0.7	10.4		1.1	2.5	1.1	3.8	0.9	6
1/9/90	12.0	5.70	0.5	19.8		1.9	4.0	1.1	4.3	1.1	17
1/18/90	5.2	6.00	0.7	17.4		1.7	3.7	0.9	4.2	1.0	15
4/1/90	19.0	5.60	0.7	19.0		2.5	4.4	1.3	4.6	1.1	23
Falls											
4/4/90	13.4	7.65	7.8	34.4		5.1	6.8	1.5	8.8	2.6	34
Trib Creek											
4/4/90	11.4	6.60	38.1	32.7		5.5	6.4	1.6	17.0	4.2	26

	T °C	pH[a]	$(HCO_3)^c$	SO_4	NO_3	Cl	Na	K	Ca	Mg	SiO_2
Trib Spring											
6/17/86	28.5	7.2	57	33	4.5	6	13.0	3.5	12.8	4.6	33
Queen Creek Surface--#1 Dam											
4/17/85		7.90	171	43	0.2	5	11		55	10	
5/2/83		7.90	129	72	0.2	<3	10		49	11	
12/14/81		8.20	178	49	1.5	6	11		50	12	
1/77		7.50	44	44	<1	5	7		24	5	
11/71		7.80	85	94	<1	7	15		44	11	
4/69			138	77	2	5	8		44	8	
4/72			180	42	1	9	14		60	6	
Spring/Queen Creek Surface--#2Dam											
4/69			88	76	<1	6	7		32	13	
8/62			176	7	<1	6	17		36	8	
Spring--#3Dam											
4/69		7.60	117	82	<1	6	9		49	15	
8/62			171	56	1	8	12		48	11	
Spring-3mi E											
5/2/58			32	73	2	4	11		26	6	
10/18/56			200	17	1	10	15		46	9	
Queen Creek											
2/18/88		7.50	129	40	0.2	<3	7.8		38	6.7	
Pump Station											
12/14/81			146	49	1.5	6	11.0		50	12	
Watershed Runoff Sample											
AQ-U 1/18/92	3.5	6.17	4.2	17.6	bd	2.8	4.0	1.2	4.9	1.4	
AQ-M 1/18/92	7.5	5.78	2.3	19.4	bd	2.4	3.8	1.0	4.4	1.4	
AQ-L 1/18/92	8.5	5.75	1.9	17.8	bd	2.3	3.7	0.9	3.9	1.3	
AQ-U 8/26/92	23.3	6.00	3.7	16.8	bd	1.8	3.7	1.3	5.9	1.5	
AQ-M 8/26/92	27.3	5.96	1.9	19.0	bd	2.5	3.8	1.7	5.9	1.6	
AQ-L 8/26/92	28.1	5.50	2.3	17.2	bd	2.0	3.4	1.6	5.1	1.3	

[a] Field pH measurement

[b] Laboratory pH measurement

[c] Alkalinity by titration

[d] Alkalinity from TIC

nd = Not determined

bd = Below detection limit

APPENDIX E: CALCULATION OF SAMPLE STATISTICS

$$\mu_x = E(x)$$
$$\sigma_x = (E(x)^2 - E^2(x))^{1/2}$$
$$CV_x = \sigma_x / \mu_x$$

$$\mu_{1/x} \approx (1 + CV_x^2) / \mu_x$$
$$\sigma_{1/x} \approx (CV_x^2 - CV_x^4)^{1/2} / \mu_x$$
$$CV_{1/x} \approx CV_x (1 - CV_x^2)^{1/2} / (1 + CV_x^2)$$

$$\mu_{x*y} = \mu_x \mu_y$$
$$\sigma_{x*y} = (\mu_y^2 \sigma_x^2 + \mu_x^2 \sigma_y^2 + \sigma_x^2 \sigma_y^2)^{1/2}$$
$$CV_{x*y} = (CV_x^2 + CV_y^2 + CV_x^2 CV_y^2)^{1/2}$$

$$\mu_{x/y} \approx (1 + CV_y^2) \mu_x / \mu_y$$
$$\sigma_{x/y} \approx (CV_x^2 + CV_y^2 - CV_y^4)^{1/2} \mu_x / \mu_y$$
$$CV_{x/y} \approx (CV_x^2 + CV_y^2 - CV_y^4)^{1/2} / (1 + CV_y^2)$$

$$\mu_{\ln(x)} \approx \ln(\mu_x) - CV_x^2/2$$
$$\sigma_{\ln(x)} \approx ((\ln(\mu_x))^2 + \mu_x CV_x^2)^{1/2}$$
$$CV_{\ln(x)} \approx ((\ln(\mu_x))^2 + \mu_x CV_x^2)^{1/2} / (\ln(\mu_x) - CV_x^2/2)$$

$$\mu_{\exp(x)} \approx 1 + \mu_x + \sigma_x^2/2$$
$$\sigma_{\exp(x)} \approx (1 + 2\mu_x + 2\sigma_x^2)^{1/2}$$
$$CV_{\exp(x)} \approx (1 + 2\mu_x + 2\sigma_x^2)^{1/2} / (1 + \mu_x + \sigma_x^2/2)$$

Assumptions:

1. x and y are uncorrelated random variables
2. moments greater than second order are neglected
3. CV < 1

NRC FORM 335 (2-89) NRCM 1102, 3201, 3202

U.S. NUCLEAR REGULATORY COMMISSION

BIBLIOGRAPHIC DATA SHEET

(See instructions on the reverse)

1. REPORT NUMBER (Assigned by NRC, Add Vol., Supp., Rev., and Addendum Numbers, if any.)

NUREG/CR-6203

2. TITLE AND SUBTITLE

Validation Studies for Assessing Unsaturated Flow and Transport through Fractured Rock

3. DATE REPORT PUBLISHED

MONTH: August YEAR: 1994

4. FIN OR GRANT NUMBER

L1282

5. AUTHOR(S)

R.L. Bassett, S.P. Neuman, T.C. Rasmussen, Amado Guzman, G.R. Davidson, and C.F. Lohrstorfer

6. TYPE OF REPORT

7. PERIOD COVERED *(Inclusive Dates)*

11/13/89 - 11/12/92

8. PERFORMING ORGANIZATION — NAME AND ADDRESS *(If NRC, provide Division, Office or Region, U.S. Nuclear Regulatory Commission, and mailing address; if contractor, provide name and mailing address.)*

Department of Hydrology & Water Resources
University of Arizona
Tucson, Arizona 85721

9. SPONSORING ORGANIZATION — NAME AND ADDRESS *(If NRC, type "Same as above"; if contractor, provide NRC Division, Office or Region, U.S. Nuclear Regulatory Commission, and mailing address.)*

Division of Regulatory Applications
Office of Nuclear Regulatory Research
U.S. Nuclear Regulatory Commission
Washington, D C 20555-0001

10. SUPPLEMENTARY NOTES

11. ABSTRACT *(200 words or less)*

The objectives of this contract are to examine hypotheses and conceptual models concerning unsaturated flow and transport through heterogeneous fractured rock and to design and execute confirmatory field and laboratory experiments to test these hypotheses and conceptual models. Important new information is presented such as the application and evaluation of procedures for estimating hydraulic, pneumatic, and solute transport coefficients for a range of thermal regimes. A field heater experiment was designed that focused on identifying the suitability of existing monitoring equipment to obtain required data. A reliable method was developed for conducting and interpreting tests for air permeability using a straddle-packer arrangement. Detailed studies of fracture flow from Queen Creek into the Magma Copper Company ore haulage tunnel have been initiated. These studies will provide data on travel time for transport of water and solute in unsaturated tuff. The collection of rainfall, runoff, and infiltration data at two small watersheds at the Apache Leap Tuff Site enabled us to evaluate the quantity and rate of water infiltrating into the subsurface via either fractures or matrix. Characterization methods for hydraulic parameters relevant to high-level waste transport, including fracture apertures, transmissivity, matrix porosity, and fracture wetting front propagation velocities, were developed.

12. KEY WORDS/DESCRIPTORS *(List words or phrases that will assist researchers in locating the report.)*

air permeability, fracture flow, tuff, unsaturated fractured rock, vapor phase transport, isotopes, radio carbon, matrix flow, computer models, water balance

13. AVAILABILITY STATEMENT

unlimited

14. SECURITY CLASSIFICATION

(This Page) unclassified

(This Report) unclassified

15. NUMBER OF PAGES

16. PRICE